DEPARTMENT OF PHYSICS
INDIAN INSTITUTE OF TECHNOLOGY
MADRAS
CHENNAI-600 036

Measurement of CKM angle ϕ_3 from $B^\pm \to D(K_S^0 h^- h^+)h^\pm$ decays at Belle and Belle II

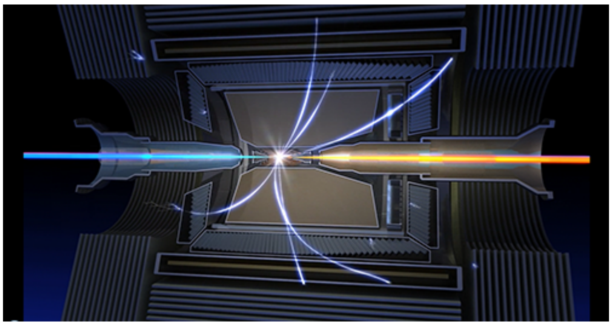

A thesis

submitted by

NIHARIKA ROUT

For the award of the degree

Of

DOCTOR OF PHILOSOPHY

January, 2022

Dedicated to my parents..

THESIS CERTIFICATE

This is to certify that the thesis titled **Measurement of CKM angle ϕ_3 from $B^\pm \to D(K^0_S h^- h^+)h^\pm$ decays at Belle and Belle II**, submitted by **NIHARIKA ROUT**, to the Indian Institute of Technology Madras, for the award of the degree of **Doctor of Philosophy**, is a bonafide record of the research work done by her under my supervision. The contents of this thesis, in full or in parts, have not been submitted to any other Institute or University for the award of any degree or diploma.

Place: Chennai

Date: 5th April 2022

Prof. Jim Libby
Research Guide
Professor
Dept. of Physics
IIT Madras, 600 036

List of Publications

1. J. Libby, N. Rout and K. Trabelsi with the Belle II collaboration "*Combined analysis of Belle and Belle II data to determine the CKM angle* $\boldsymbol{\phi_3}$ *using* $\boldsymbol{B^+ \to D(K^0_S h^- h^+) h^+}$ *decays*"; J. High. Energ. Phys. **02**, 063 (2022). [arXiv:2110.12125].

2. N. Rout *et al.* (8 primary authors and the Belle II Collaboration), "*Study of* $B \to D^{(*)}h$ *decays using 62.8 fb*$^{-1}$ *of Belle II data*", [arXiv:2104.03628].

3. N. Rout (on behalf of the Belle II collaboration), "*First results of* $B \to DK$ *decays at Belle II*", presented at 11th Internal conference on CKM unitarity triangle, Melbourne, Australia, Nov, 2021, Proceedings of Science (PoS) is in preparation.

4. N. Rout (on behalf of the Belle II collaboration), "*Measurement of* ϕ_3 *(*γ*) and first results on* CP *violation at Belle II*", PoS (ICHEP2020) **416** (2020).

5. N. Rout (on behalf of the Belle and Belle II collaboration), "*Determination of CKM angle* ϕ_3 *at Belle and Belle II*", XXIV DAE-BRNS High Energy Physics symposium (2020), Springer Proceedings in Physics.

6. E. Ganiev, N. Rout and B. Wach (on behalf of the Belle II collaboration), "*Hadronic* B *decay reconstruction in early Belle II data*", PoS (Beauty2019) **062** (2019).

7. N. Rout (on behalf of the Belle II collaboration), “*Measurement of CKM angle ϕ_3 at Belle II*", in Proceedings of the 17th Conference on Flavor Physics and CP Violation, 2019, eConf **C190506** (2019).

8. N. Rout (on behalf of the Belle II collaboration), “*Rediscoveries from the first data of Belle II*", XXIII DAE-BRNS High Energy Physics symposium (2018), Springer Proceedings in Physics **261** (pages 101-107).

9. Author of 43 papers in refereed journals as listed in `https://inspirehep.net/authors/N.Rout.1` as a member of Belle and Belle II collaboration.

ACKNOWLEDGEMENTS

I want to use this opportunity to express my gratitude to all the people without whose encouragement and support this thesis would not have been possible. First and foremost, I'd like to express my thankfulness to Prof. Jim Libby, my PhD supervisor, for his guidance and support throughout my PhD tenure. This thesis would not have been possible without his dedicated supervision, advice and constructive criticisms. I consider myself privileged to have worked with him. I owe him a debt of appreciation for encouraging and patiently mentoring me over the last five and half years. I also thank him for providing me with an outstanding opportunity and resources to work with the Belle and Belle II collaborations.

I was delighted to work with Dr. Karim Trabelsi from IJCLab, Orsay, for the data analysis. I genuinely appreciate his continual support and discussions. I was astonished by his sincerity and enthusiasm, and it was an honour to work with him. I also feel privileged to have worked with Dr. Diego Tonelli from INFN, Trieste. I would also like to thank my analysis review committee: Dr. Pavel Krokovny, Dr. Frank Meier and Dr. Makoto Uchida, for reviewing my analysis and their constructive comments and suggestions. I want to thank the Belle and Belle II collaboration for allowing me to work at KEK and providing me with financial assistance during my visits. A special thanks to Nakao-san for being the host for me for the ATHENA program. Also, it was a great pleasure to work with my collaborators Eldar, Fernando, Eiasha, Chiara and Yi. I want to acknowledge all the members of the Belle India Group who have motivated and supported me during my PhD. The Belle Analysis Workshops helped me comprehend

numerous technical elements of the analysis procedures, and the physics talks provided me with a thorough understanding of many experimental and theoretical parts of particle physics.

The work was made possible by the Department of Physics, IIT Madras, which supplied excellent infrastructure, facilities and resources. I'd want to express my gratitude to all the faculty members and staff for their assistance. I am grateful to Dr. Suresh Govindarajan, Dr. Prasanta K. Tripathy, Dr. Chandra Kant Mishra, and Dr. Rahul Sinha, members of my doctorate committee, for their insightful remarks and ideas during my PhD.

I thank my colleagues Anita and Ansu for their support. A special thanks to my seniors Resmi and Krishnakumar for all the technical help, supports and discussions, for which I am very grateful to you guys. I also thank my Belle II colleagues Minakshi, Renu and Soumen for all the physics discussions. I am thankful to all my friends, Ankita, Basudev, Karishma, Rashmi, Smhruti, Snigdha, Sushanta, Tanim and Wafa, for their constant love and affection, and for being there for me whenever I need them. I am grateful to Sagarika, Bibek, Subash and Nisha for making my stay on campus memorable. Anubhab, I owe you a huge debt of gratitude for being my closest friend for the last 13 years and for being there for me wherever I go. I can't thank you enough! I'm at a loss for words to express my gratitude to Amit for being my emotional support during the difficult times. Thank you for being there all the time, for looking after me, and for tolerating all my craziness.

I would like to express my thankfulness to my school, college and university teachers for their guidance, without which I wouldn't have discovered my passion for physics.

I have no words to express my gratefulness to my all-time support system, my elder sister, Sagarika, and my brother-in-law, Jyotirmaya. You have worked hard to keep me out of all the burdens, so that I can pursue my dream; I can never thank you enough for that. I am deeply indebted to my parents Snehalata and Gokulananda, for their unwavering support and encouragement throughout my life. Nothing will ever be able to replace their selfless love. I want to thank all my family members and relatives for their support. A special thanks to my one and only Chua Maa for her love and blessings. Above all, I am greatly thankful to the Supreme Soul for all I have today.

ABSTRACT

This thesis reports the measurement of the CKM unitarity triangle angle ϕ_3 using a model-independent Dalitz plot analysis of $B^{\pm} \rightarrow D(K_S^0 h^+ h^-)K^{\pm}$ ($h = \pi$ or K) decays, where D can either be a D^0 or a $\bar{D}^0$, which currently provides the best sensitivity. The D phase space is divided into bins based on the phase-difference of D^0 and $\bar{D}^0$ at each point of the phase space. The decay rates of $B^{\pm}$ in the i^{th} bin are given as

$$\Gamma_i^{\pm} \propto F_i + r_B^2 \overline{F}_i + 2\sqrt{F_i \overline{F}_i}(c_i x_{\pm} + s_i y_{\pm}),$$

where $(x_{\pm}, y_{\pm}) = r_B(\cos(\pm\phi_3 + \delta_B),\ \sin(\pm\phi_3 + \delta_B))$. Here, F_i and $\overline{F}_i$ are the fraction of events in the i^{th} bin of a flavour tagged D^0 and $\bar{D}^0$ decays and are obtained from $B^{\pm} \rightarrow D(K_S^0 h^+ h^-)h^{\pm}$ sample. The values of the amplitude-averaged strong-phase difference parameters, c_i and s_i, are taken from combined measurement of BESIII and CLEO-c data. This is the first measurement that simultaneously uses Belle and Belle II data, combining samples corresponding to integrated luminosities of 711 fb^{-1} and 128 fb^{-1}, respectively. All data were accumulated from energy-asymmetric e^+e^- collisions at a centre-of-mass energy corresponding to the mass of the $\Upsilon(4S)$ resonance. The ϕ_3 value is measured to be $(78.4 \pm 11.4 \pm 0.5 \pm 1.0)^{\circ}$, where the first uncertainty is statistical, the second the experimental systematic and the third is from the uncertainties on the strong-phase difference parameters.

This thesis also reports the measurement of the beam energy in the centre-of-mass frame for the Belle II detector using fully reconstructed neutral and charged B decays from various final states. An accurate determination of the beam energy is crucial for many physics analyses and detector calibrations. The reported shift is of the order of 0.5 MeV from the nominal beam energy value.

TABLE OF CONTENTS

Page

3 Selection of $B^{\pm} \to D(K_S^0 h^- h^+)h^{\pm}$, $h = K, \pi$ events at Belle and Belle II **62**

LIST OF TABLES

Table **Title** **Page**

LIST OF FIGURES

CHAPTER 1

Introduction

The Standard Model (SM) of particle physics [1, 2, 3] has been confirmed by many experimental results and is presently the best-known explanation of the fundamental elements of nature and their interactions; the building blocks are the quarks and leptons, and the fundamental forces that bind them together are strong, weak and electromagnetic interactions. Despite its tremendous success, there are still a few unanswered questions that are not explained by the theory, such as the matter-antimatter asymmetry, mass and flavour hierarchy of the quarks and leptons, and no explanation for the very fundamental force of nature, gravity, which keeps our feet on the ground. However, despite these shortcomings, the SM is the best-tested theory so far.

In the SM, there are a total of six quarks and six leptons, which are fermions, and are organised in three generations, as shown in Table 1.1. Various spin-1 gauge bosons mediate their interactions, which are mentioned in Table 1.2. The strong interactions are mediated by gluons, which bind the quarks in mesons and baryons. The electromagnetic interaction is approximately 10^{-2} times weaker than the strong interaction and is mediated by photons. Gluons couple with themselves because of the colour charge, but photons cannot as they are electrically neutral. The weak interaction, which is nearly 10^{-10} times[1] weaker than the electromagnetic interaction, is mediated via the massive $W^{\pm}$ and Z^0 bosons. Mainly, the scalar Higgs boson is responsible for providing mass to

---

[1] This is valid at energies $q \simeq 1$ MeV, a typical nuclear scale.

Table 1.1: Fundamental fermions of the SM and their properties [8].

Type	Generation	Particle	Mass (MeV/c^2)	Electric charge (e)
Quarks	1	up (u)	$2.16^{+0.49}_{-0.26}$	$+\frac{2}{3}$
		down (d)	$4.67^{+0.48}_{-0.17}$	$-\frac{1}{3}$
	2	charm (c)	1270 ± 20	$+\frac{2}{3}$
		strange (s)	93^{+11}_{-5}	$-\frac{1}{3}$
	3	top (t)	172760 ± 300	$+\frac{2}{3}$
		bottom (b)	4180^{+30}_{-20}	$-\frac{1}{3}$
Leptons	1	electron (e)	0.511 ± 0.000	-1
		electron neutrino (ν_e)	$< 1.1 \times 10^{-6}$	0
	2	muon (μ)	105.658 ± 0.000	-1
		muon neutrino (ν_μ)	< 0.19	0
	3	tauon (τ)	1776.86 ± 0.12	-1
		tau neutrino (ν_τ)	< 18.2	0

Table 1.2: Fundamental vector bosons of the SM and their properties [8].

Particle	Interaction	Mass (GeV/c^2)	Electric charge (e)
Gluon (g)	Strong	0	0
Photon (γ)	Electromagnetic	$< 10^{-24}$	0
$W^\pm$	Weak	80.379 ± 0.012	± 1
Z^0	Weak	91.188 ± 0.002	0

the elementary particles via spontaneous symmetry breaking [4, 5]; after the discovery of the Higgs boson in 2012 [6, 7], the SM picture is complete.

Many physicists at various experiments are looking for physics effects beyond the Standard Model (BSM). Despite this, no (statistically significant)[2] experimental data have been produced that lead to a viable replacement that would resolve the present theory's underlying issues.[3] Making measurements of the parameters in the flavour sector, which are the weak processes between the different types (flavours) of quarks and leptons, to see whether they deviate from the SM predictions is one way to look

---

[2] The $g-2$ results and flavour anomalies are at $3-4\sigma$ range, but 5σ observation has not been achieved so far.

[3] The observed non-zero neutrino masses can be accounted for by several plausible SM extensions. However, these extensions are unlikely to overcome the issues outlined earlier [8].

for BSM physics. Experimental flavour physics observations, particularly the meson mixing and CP-violation results, give constraints on BSM physics at energy scales of the order of 10^4 TeV, from the possible inclusion of massive new physics particle in the loops [9]. This is a considerably higher energy scale which is impossible to achieve in present and prospective near-future particle colliders [10].[4]

This thesis represents the precise measurement of the CP-violating phase ϕ_3, a key parameter that defines the sole source of matter-antimatter asymmetry within the SM. The remainder of this chapter is as follows. The discrete symmetries and their violation are described in Sec. 1.1, the source of CP violation and its SM picture are explained in Sec. 1.2. The extraction of the CKM angle ϕ_3 is presented in Sec. 1.3.

1.1 THE *C, P* AND *T* SYMMETRIES AND THEIR VIOLATION

Symmetry plays a crucial role in modern physics; they lead to conservation laws in physics according to Noether's theorem [11]. For example, invariance of a system under translational or rotational transformation results in the conservation of linear and angular momentum, respectively. The interactions and dynamics within the SM follow a local $U(1) \times SU(2) \times SU(3)$ gauge symmetry [12]; however, the SM fails to explain the evident lack of symmetry in our present matter-dominated universe. Hence, it is crucial to understand the underlying symmetries of our universe and to what extent they are broken.

In particle physics generally we encounter two different types of symmetries:

---

[4] These limitations do not exclude out NP at lower energy scales, but they do place strict constraints on any NP model's potential flavour structure at the $< 10^4$ TeV scale [10].

continuous and *discrete*. The translational or rotational transformations are the most common example of continuous symmetries. The three important discrete symmetries are the parity operator P, the charge-conjugation operator C and the time-inversion operator T.

The operator P inverts the spatial dimensions of space-time: $\vec{x} \to -\vec{x}$ without changing any other quantum numbers. As a result, it transforms left-handed particle fields into right-handed particle fields and vice versa. Fermions and anti-fermions have opposite intrinsic parity with unit magnitude. So, a meson formed from a quark and anti-quark will have an intrinsic parity of -1 because of the multiplicative property of the parity quantum number. Until 1956 parity was considered to be an exact symmetry of nature. The first evidence of parity violation in weak interactions was observed by Wu *et al.* [14] through β decay of ^{60}Co. Further experiments proved that the weak interaction violates parity maximally, which is contained in the SM by the $W^{\pm}$ boson coupling exclusively to the left-handed fermions. However, it is conserved in strong and electromagnetic interactions

The operator C conjugates the internal quantum numbers of the quantum state of the particle, such as baryon number, lepton number, and charge; but it does not affect the handedness of the particle. Similar to the parity operator, it is also conserved in strong and electromagnetic interactions but maximally violated in the weak interaction [14, 15]. For example, a left-handed ν becomes a left-handed $\bar{\nu}$ upon the implementation of C operator, which does not exist in the SM assuming ν mass to be zero.

All the fundamental interactions were believed to be invariant under CP symmetry, a simultaneous operation of charge conjugation and parity. It converts a particle to its antiparticle; a left-handed ν become a right-handed $\bar{\nu}$ with the CP operation. However, CP symmetry violation was first observed in the neutral kaon system in 1964 [16]. Cronin and Fitch observed that long-lived kaons, which mainly decay to the CP-odd three-pion final states, could also decay to the CP-even two-pion final states. After that it has been established in various systems, in both charged and neutral B meson decays by the BaBar, Belle and LHCb collaboration [17, 18, 19, 20], in D^0 decays by the LHCb collaboration [21]; the most recent evidence for CP-violation in the neutrino sector has been reported by the T2K collaboration [22].

CP-violation can be classified into three categories.

1. *CP-violation in decay*, where $|A/\bar{A}| \neq 1$ for a decay amplitude A and $\bar{A}$ being the amplitude of the CP-conjugate mode. This results in different decay rates of the two decays

   $$\Gamma(M \to f) \neq \Gamma(\bar{M} \to \bar{f}). \tag{1.1}$$

   The CP violation in the decay of $B^+ \to DK^+$ and its CP conjugate decay $B^- \to DK^-$ is the main focus of this thesis.

2. *CP-violation in mixing*, which represents the case where the mixing rates between two CP-conjugate states, M^0 and $\bar{M}^0$, differ:

   $$\Gamma(M^0 \to \bar{M}^0) \neq \Gamma(\bar{M}^0 \to M^0). \tag{1.2}$$

   This has been observed in the neutral kaon system.

3. *CP-violation in interference between mixing and decay*, which comes into picture when a neutral initial state M^0 and its CP conjugate state $\bar{M}^0$ decay to the same final state f. An interference term between the two amplitudes, amplitude for a direct $M^0 \to f$ decay and amplitude after mixing $M^0 \to \bar{M}^0 \to f$, is included in the decay rate. Even in the absence of the two previous effects, the decay rates, $\Gamma(M^0 \to f)$ and $\Gamma(\bar{M}^0 \to f)$, might differ due to the presence of the interference term. The CP-asymmetry in the decay $B^0 \to J/\psi K$ is an example of this type of CP violation [23].

The time-inversion operator T inverts the temporal dimension of space-time: $t \to -t$. The three operators are connected by the CPT theorem [24], which states that any Lorentz-invariant Quantum Field Theory (QFT) must be symmetric when all three operators are applied simultaneously, and assures that the particles and their anti-particles have the same mass and lifetime. So far, no experimental evidence of CPT symmetry breaking has been reported.

According to Sakarov's conditions [13], CP-violation is required the universe to be matter dominated. One can refer to the baryon-to-photon ratio to measure this dominance, which is of the order of 10^{-9} with the present day temperature $T_{CMB} = 2.73$ K; but the SM + SM cosmology predicts this ratio as 10^{-18} unless there were additional sources of CP-violation in the early universe [8]. Hence, the discussion of the SM picture of CP-violation is provided in the next section.

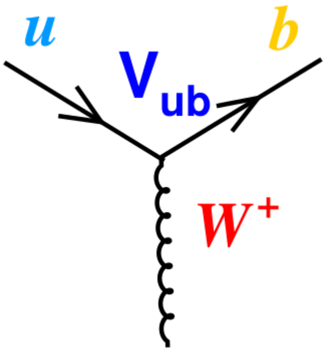

Figure 1.1: A $b \to u$ quark transition where the vertex factor element is proportional to V_{ub}.

1.2 CP VIOLATION IN THE STANDARD MODEL

After the observation of CP violation in neutral kaon system, it took almost 10 years to figure out the place of CP violation in the developing structure of the SM. In 1973, Makoto Kobayashi and Toshihide Maskawa pointed out that in the case of three quark generations the number of degrees of freedom in the SM naturally gives rise to the CP violating complex phase in the 3×3 quark mixing matrix, currently known as the Cabibbo-Kobayashi-Maskawa (CKM) matrix [25, 26]. It is to be noted that, in 1973, only the u, d and s quarks were known.[5]

At present the SM contains three generation of quarks, each having an up-type quark (u, c and t) and a down-type quark (d, s and b). The mixing of quarks take place with the emission or absorption of $W^{\pm}$ boson, which exchanges an up-type quark into a down-type quark and vice-versa. The difference between the quark-mass eigenstates and the weak eigenstates causes this flavor-changing charged current transitions. The mass eigenstates and the weak eigenstates (denoted by primes) are related via the Cabibbo-

---

[5] The existence of charm (c) quark was first predicted by Glashow, Iliopoulos and Maiani and was introduced for the first time through the suppressed flavour-changing-neutral-current (FCNC) interactions via GIM mechanism in 1970 [27]. Later it was experimentally discovered through J/ψ meson, a $c\bar{c}$ bound state, confirming the GIM mechanism in 1974 [28].

Kobayashi-Maskawa (CKM) matrix, which is represented as

$$\begin{pmatrix} d' \\ s' \\ b' \end{pmatrix} = \begin{pmatrix} V_{ud} & V_{us} & V_{ub} \\ V_{cd} & V_{cs} & V_{cb} \\ V_{td} & V_{ts} & V_{tb} \end{pmatrix} \begin{pmatrix} d \\ s \\ b \end{pmatrix}, \tag{1.3}$$

where the elements V_{ij} reveals the strength of the corresponding quark transitions; an example has been shown in Fig. 1.1.

The SM Lagrangian terms representing the coupling of a $W^{\pm}$ boson with an up-type and down-type quark is

$$\mathcal{L}_{W^+} = -\frac{g}{\sqrt{2}} V_{ud} (\bar{u} \gamma^{\mu} W_{\mu}^{+} d) \qquad \mathcal{L}_{W^-} = -\frac{g}{\sqrt{2}} V_{ud}^{*} (\bar{d} \gamma^{\mu} W_{\mu}^{-} u), \tag{1.4}$$

where *g* is the weak coupling constant, γ_μ are the Dirac matrices, and *u* and *d* are the left-handed components of the physical quark states.

The CKM matrix is unitary by nature; hence, it can be parametrized by $3^2 = 9$ independent and real parameters, which are described by three rotation angles and six phases. One can eliminate five out of six phases by proper re-phasing of the quark states, both weak and mass eigenstates. Thus, the CKM matrix is described by four physical parameters: three mixing angles and an irreducible phase. According to the

Chau and Keung parametrization [8], the CKM matrix can be written as

$$\begin{aligned} V_{\mathrm{CKM}} &= \begin{pmatrix} 1 & 0 & 0 \\ 0 & c_{23} & s_{23} \\ 0 & -s_{23} & c_{23} \end{pmatrix} \begin{pmatrix} c_{13} & 0 & s_{13}e^{-i\delta} \\ 0 & 1 & 0 \\ -s_{13}e^{-i\delta} & 0 & c_{13} \end{pmatrix} \begin{pmatrix} c_{12} & s_{12} & 0 \\ -s_{12} & c_{12} & 0 \\ 0 & 0 & 1 \end{pmatrix} \\ &= \begin{pmatrix} c_{12}c_{13} & s_{12}c_{13} & s_{13}e^{-i\delta} \\ -s_{12}c_{23} - c_{12}s_{23}s_{13}e^{i\delta} & c_{12}c_{23} - s_{12}s_{23}s_{13}e^{i\delta} & s_{23}c_{13} \\ s_{12}s_{23} - c_{12}s_{23}s_{13}e^{i\delta} & -c_{12}s_{23} - s_{12}c_{23}s_{13}e^{i\delta} & c_{23}c_{13} \end{pmatrix}, \end{aligned} \tag{1.5}$$

where $s_{ij} \equiv \sin\theta_{ij}$ and $c_{ij} \equiv \cos\theta_{ij}$ represent the sine and cosine of the three rotation angles, $\theta_{12} = \theta_c$ is the Cabibbo angle [25] and δ is the complex phase; the phase changes sign when a *CP* operation is performed, which indicates symmetry violation.

The diagonal elements of the CKM matrix are approximately equal to one while the off-diagonal elements are smaller in magnitude, which indicates that the quark transition is preferred within the same generations. Then, according to Eq. 1.5, the elements s_{13}, s_{23} and s_{12} will follow the hierarchy $s_{13} \ll s_{23} \ll s_{12} \ll 1$. The Wolfenstein parameterisation [29], in which the elements are represented as power series in $\lambda \equiv \sin\theta_c \simeq 0.23$, which naturally integrates the hierarchy, is the most frequently used alternative parameterisation. There are four independent parameters of the same order, λ, A, ρ and η, that define the elements s_{ij} and δ:

$$s_{12} \equiv \lambda, \qquad s_{23} \equiv A\lambda^2, \qquad s_{13}\mathrm{e}^{-i\delta} \equiv A\lambda^3(\rho - i\eta). \tag{1.6}$$

The values of c_{ij} can be obtained from the Taylor expansions in such a way that the matrix elements can be written as

$$V_{\mathrm{CKM}} = \begin{pmatrix} 1-\lambda^2/2 & \lambda & A\lambda^3(\rho - i\eta) \\ -\lambda & 1-\lambda^2/2 & A\lambda^2 \\ A\lambda^3(1-\rho-i\eta) & -A\lambda^2 & 1 \end{pmatrix} + \mathcal{O}(\lambda^4). \tag{1.7}$$

A non-zero value of η would suggest the complex phase of the matrix elements V_{ub} and V_{td}, which is the source of CP violation in the SM. The unitarity requirement $VV^\dagger = V^\dagger V = 1$ of the CKM matrix establishes the orthogonality relation between the matrix elements of the form

$$\sum_{i\in\{u,c,t\}} = V^*_{i\alpha} V_{i\beta} = \delta_{\alpha\beta}, \quad \alpha, \beta \in \{d, s, b\}, \tag{1.8}$$

There can be six distinct conditions for which the right-hand side of the Eq. 1.8 become zero and can be represented as a triangle in the complex plane. The area of each triangle is identical and measures the amount of CP violation in the SM. Out of these, the triangle that corresponds to the unitarity condition between the first and third columns of the CKM matrix is more significant as the sides are of the same order of magnitude, $\mathcal{O}(\lambda^3)$. It is commonly referred to as the Unitarity triangle and can be expressed in the form

$$\frac{V^*_{\mathrm{ub}} V_{\mathrm{ud}}}{V^*_{\mathrm{cb}} V_{\mathrm{cd}}} + 1 + \frac{V^*_{\mathrm{tb}} V_{\mathrm{td}}}{V^*_{\mathrm{cb}} V_{\mathrm{cd}}} = 0, \tag{1.9}$$

as shown in Fig. 1.2; the standard names of the three angles are also provided, which can be defined in terms of the matrix elements as

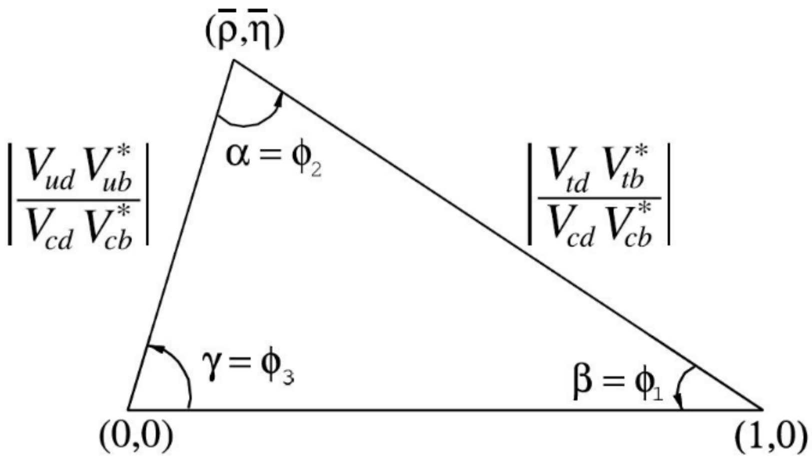

Figure 1.2: Unitarity triangle in the $\bar{\rho}-\bar{\eta}$ plane [8].

$$\alpha=\phi_2\equiv\arg\left(-\frac{V_{\mathrm{tb}}^*V_{\mathrm{td}}}{V_{\mathrm{ub}}^*V_{\mathrm{ud}}}\right),\quad \beta=\phi_1\equiv\arg\left(-\frac{V_{\mathrm{cb}}^*V_{\mathrm{cd}}}{V_{\mathrm{tb}}^*V_{\mathrm{td}}}\right),\quad \gamma=\phi_3\equiv\arg\left(-\frac{V_{\mathrm{ub}}^*V_{\mathrm{ud}}}{V_{\mathrm{cb}}^*V_{\mathrm{cd}}}\right). \tag{1.10}$$

An important test of the SM predictions is to overconstrain the unitarity triangle by taking individual measurements of all the sides and angles in as many distinct decay channels as possible. The current experimental measurements are consistent with SM predictions, as shown in Fig. 1.3.

This thesis is focused on the measurement of the angle ϕ_3, also known as γ. Among all the CKM parameters, the angle ϕ_3 is unique because it can be measured readily from the tree-level decays without considerable theoretical uncertainty, which is of $\mathcal{O}(10^{-7})$, and comes only due to the second-order electroweak corrections [31]. As ϕ_3 is an input parameter in the SM, it is not feasible to construct a theoretical expected value of ϕ_3 to which experimental measurements can be compared to. However, generally, BSM physics have minimal impact on the tree-level processes. Hence, direct measurements of ϕ_3 can serve as an SM benchmark, which can be compared to constraints based on measurements of other CKM parameters that are measured via

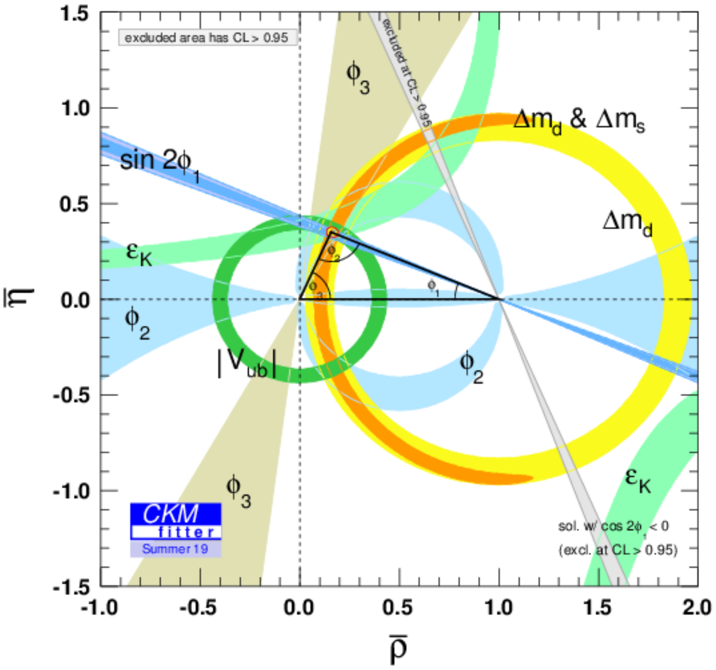

Figure 1.3: Constraints on the Unitarity Triangle parameters as determined by the CKMFitter group for the EPS 2019 conference [30].

loop-level decays and are more likely to be affected by BSM physics [32], also referred to as indirect extrapolation. These constraints are derived from the global fits based on the measurements of all CKM elements except for the angle ϕ_3, along with preserving the unitarity of the CKM matrix. The constraint on ϕ_3 mostly come from the value of ϕ_1 and the elements defining the side opposite to ϕ_3; all these measurements rely heavily on neutral B mixing processes shown in Fig. 1.4. If the BSM physics comes into picture in the loop-level decays, which have not been accounted for in the global fit, then it can provide a different value of ϕ_3 to that of the direct measurements. The current world average value of ϕ_3 coming from direct measurements is $(66.2^{+3.4}_{-3.6})^\circ$ [33] where as from indirect-extrapolation it is $(65.6^{+0.9}_{-2.5})^\circ$ [30]. To compare both these values, first it is necessary to reduce the uncertainty on the direct measurements to the level of indirect extrapolation. Hence, precision measurements of ϕ_3 are strongly motivated and one of

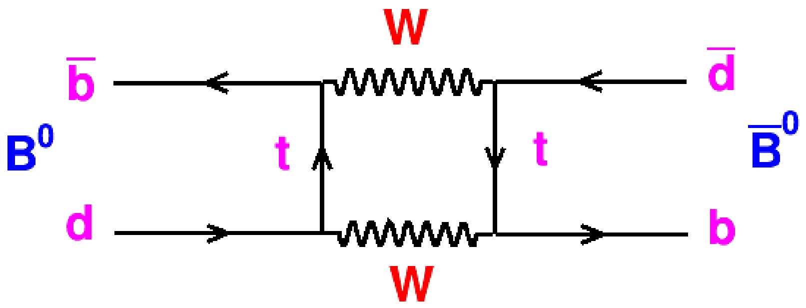

Figure 1.4: $B^0 - \bar{B}^0$ mixing process.

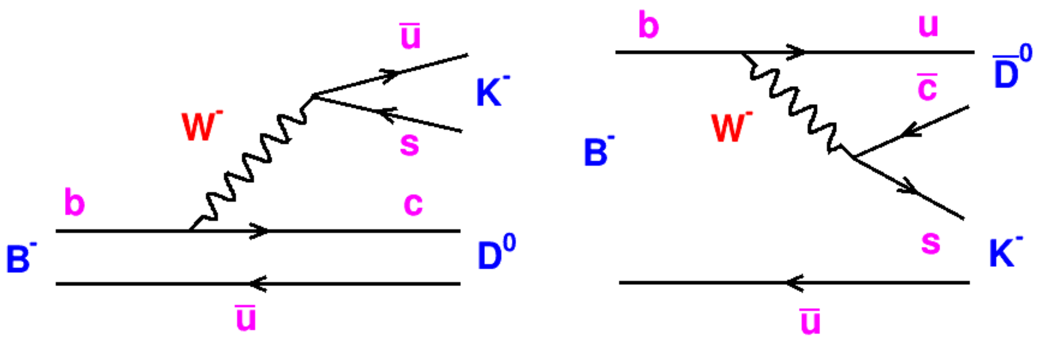

Figure 1.5: Quark-flow diagrams of colour-favoured (left) and colour-suppressed (right) decays of $B^- \to DK^-$ process.

these is the primary goal of this thesis. The theory behind the measurement is discussed in the next sections.

1.3 MEASUREMENT OF ANGLE ϕ_3 FROM TREE-LEVEL DECAYS

The angle ϕ_3 is measurable via the interference of the tree-level quark transitions $b \to c\bar{u}s$ and $c \to \bar{c}us$.[6] Hence, the classic decay channel used for this study is $B^+ \to DK^+$, where D is either a D^0 or $\bar{D}^0$ decaying to a common final state f. The quark-flow diagrams of these decays are shown in Fig. 1.5; out of these two, the mode $B^- \to D^0K^-$ is colour-favoured and $B^- \to \bar{D}^0K^-$ is colour-suppressed, the latter is also suppressed because of the dependency on V_{ub}.

---

[6] Throughout this thesis charge-conjugate processes are assumed unless explicitly stated otherwise.

The amplitudes for these two decays can be written as

$$\mathcal{A}(B^- \to D^0 K^-) \equiv A_B, \tag{1.11}$$

and

$$\mathcal{A}(B^- \to \bar{D}^0 K^-) \equiv A_B r_B e^{i(\delta_B - \phi_3)}, \tag{1.12}$$

where r_B is the ratio of suppressed-to-favoured B amplitude and δ_B represents the relative strong-phase difference between the suppressed and favoured amplitudes. The value of r_B can be approximated as

$$r_B = \frac{|V_{ub}||V_{cs}|}{|V_{us}||V_{cb}|} \times \frac{1}{3} \approx 0.1, \tag{1.13}$$

where the factor $\frac{1}{3}$ arises from the colour suppression. Since CP-violation is ascribed to the weak phase, the CP-conjugate decay amplitudes can be obtained from Eqs. 1.11 and 1.12 by changing the sign of the weak phase ϕ_3. Thus the decay rate of $B^- \to DK^-$ can be expressed as

$$\Gamma \propto |(B^- \to \tilde{D}K^-)|^2 = |\mathcal{A}(B^- \to D^0 K^-) + \mathcal{A}(B^- \to \bar{D}^0 K^-)|^2, \tag{1.14}$$

$$= A_B^2 + A_B^2 r_B^2 + 2A_B^2 r_B \cos(\delta_B - \phi_3). \tag{1.15}$$

Depending on the D final states, these equations can be utilised to extract various experimental observables related to ϕ_3.

If D decays to a CP eigenstate, for example the final state is $K^+K^-, \pi^+\pi^-$ or $K_S^0\pi^0$, the Gronau, London, and Wyler (GLW) method [34] is used. The observables related to ϕ_3 can be extracted via a measurement of the ratio and CP asymmetry of the decay rates of CP eigenstates and Cabibbo-favoured decays; these are

$$\begin{aligned} R^{\pm}_{CP} &= \frac{\mathcal{B}(B^- \to D_{CP\pm}K^-) + \mathcal{B}(B^+ \to D_{CP\pm}K^+)}{\mathcal{B}(B^- \to D^0K^-) + \mathcal{B}(B^+ \to \bar{D}^0K^+)}, && (1.16) \\ &= 1 + r_B^2 \pm 2r_B\cos(\delta_B)\cos(\phi_3). && (1.17) \end{aligned}$$

and

$$\begin{aligned} A^{\pm}_{CP} &= \frac{\mathcal{B}(B^- \to D_{CP\pm}K^-) - \mathcal{B}(B^+ \to D_{CP\pm}K^+)}{\mathcal{B}(B^- \to D_{CP\pm}K^-) + \mathcal{B}(B^+ \to D_{CP\pm}K^+)}, && (1.18) \\ &= \pm 2r_B\sin(\delta_B)\sin(\phi_3)/R^{\pm}_{CP}, && (1.19) \end{aligned}$$

where $D_{CP\pm}$ are the CP eigenstates with eigenvalues ±1. The sensitivity of these observables to the CP violation effect is limited by the small value of r_B. However, as these observables constrain $(\sin\delta_B\sin\phi_3)$ and $(\cos\delta_B\cos\phi_3)$, there is a eight-fold ambiguity for the solutions of (ϕ_3, δ_B). These ambiguities can be broken by measuring the same observables using the channels $B^- \to D^*K^-$ or $B^0 \to DK^{*0}$, which have the unique values of r_B and δ_B [34].

If the D final state is a doubly-Cabibbo-suppressed state, such as $K^+\pi^-$, $K^+\pi^-\pi^0$ or $K^+\pi^-\pi^+\pi^-$, then the Atwood, Dunietz, and Soni (ADS) method [35, 36] is used to extract the observables related to ϕ_3. In this method the B meson reaches to its final state either via the favored B decay ($b \to c$) followed by a doubly-Cabibbo-suppressed D decay ($D^0 \to f$ or $\bar{D}^0 \to \bar{f}$), or via the suppressed B decay ($b \to u$) followed by a Cabibbo-favored D decay ($D^0 \to \bar{f}$ or $\bar{D}^0 \to f$). Since these two interfering decay amplitudes are of same order of magnitude, substantial interference effects are expected, which increases the sensitivity to ϕ_3 by enhancing the CP violation effects. The related observables are

$$R_{\text{ADS}} = \frac{\mathcal{B}(B^- \to [f]_D K^-) + \mathcal{B}(B^+ \to [\bar{f}]_D K^+)}{\mathcal{B}(B^- \to [\bar{f}]_D K^-) + \mathcal{B}(B^+ \to [f]_D K^+)}, \tag{1.20}$$

$$= r_B^2 + r_D^2 + 2 r_B r_D \cos(\delta_B + \delta_D) \cos\phi_3, \tag{1.21}$$

and

$$A_{\text{ADS}} = \frac{\mathcal{B}(B^- \to [f]_D K^-) - \mathcal{B}(B^+ \to [\bar{f}]_D K^+)}{\mathcal{B}(B^- \to [f]_D K^-) + \mathcal{B}(B^+ \to [\bar{f}]_D K^+)}, \tag{1.22}$$

$$= 2 r_B r_D \sin(\delta_B + \delta_D) \sin\phi_3 / R_{\text{ADS}}, \tag{1.23}$$

where r_D is the ratio of the magnitude of the suppressed to favoured D decays and δ_D is the strong-phase difference between them; knowledge of these parameters are required for ϕ_3 extraction and can be measured independently [33]. The constraints from the ADS observables also suffer from ambiguities similar to the GLW case; however, each D decay mode provides an independent set of constraints because of the difference in D decay parameters.

If the D meson decays to a multibody self-conjugate final state, such as $K_S^0\pi^+\pi^-$ or $K_S^0 K^+ K^-$, then the Bondar, Poluektov, Giri, Grossman, Soffer, and Zupan (BPGGSZ) method [37, 38, 39] is used to extract the CP observables. These final states are more sensitive to ϕ_3 because of their rich resonant structure, which behaves like either GLW or ADS type modes in the phase space and provides a combined sensitivity from a single decay mode. Using this method, ϕ_3 extraction can be performed either in a model-dependent manner or in a model-independent way. The model-dependent process requires knowledge of the amplitudes of the intermediate resonances that contribute to the D phase space. However, the imperfect understanding of the phase of the amplitude can limit the precision of the ϕ_3 measurement. Furthermore, the systematic uncertainty calculation gets much more difficult with the model assumptions. It has been reported that the model-related systematics uncertainty range from $3.0° - 8.9°$ [40, 41]. The model-independent method measures the CP asymmetries in independent areas of the D phase space, referred to as bins [37, 38]. Compared to the model-dependent method, binning reduces statistical precision, but it removes the uncertainty associated with model assumptions by utilising measurements of average strong-phase differences within the bins.

This thesis describes the analysis of the $K_S^0 h^+ h^-$ final state in a model-independent manner.

1.3.1 Model-independent method to extract ϕ_3

Consider the decay mode $B^+ \to D(K_S^0 h^+ h^-)K^+$, the amplitude of the B decay is given by:

$$A_{B^+}\left(m_-^2, m_+^2\right) = \bar{A}\left(m_-^2, m_+^2\right) + r_B^{DK} e^{i\left(\delta_B^{DK} - \phi_3\right)} A\left(m_-^2, m_+^2\right) \;, \tag{1.24}$$

where, m_+^2 and m_-^2 are the Dalitz plot variables (the squared invariant masses of $K_S^0h^+$ and $K_S^0h^-$ combinations, respectively), $\overline{A}$ is the amplitude of $\bar{D}^0 \rightarrow K_S^0h^+h^-$ decay and A is the amplitude of $D^0 \rightarrow K_S^0h^+h^-$ decay. The probability density for events in the D-decay phase space can be written as the square of the amplitude as

$$
\begin{aligned}
P_B = |A_B|^2 = |\overline{A} + r_B \mathrm{e}^{i(\delta_B - \phi_3)} A|^2 && (1.25)\\
= |\bar{A}|^2 + r_B^2 |A|^2 + r_B \left(\bar{A}^* A \mathrm{e}^{i(\delta_B - \phi_3)} + \bar{A} A^* \mathrm{e}^{-i(\delta_B - \phi_3)} \right). && (1.26)
\end{aligned}
$$

Again,

$$\bar{A}^* A = |\bar{A}||A| \mathrm{e}^{i\Delta\delta_D}, \tag{1.27}$$

where $\Delta\delta_D$ represents the strong-phase difference between $D^0 \rightarrow K_S^0h^+h^-$ and $\bar{D}^0 \rightarrow K_S^0h^+h^-$ decays and is given by the equation

$$\Delta\delta_D \equiv \delta_D \left(m_-^2, m_+^2\right) - \delta_D \left(m_+^2, m_-^2\right). \tag{1.28}$$

After substituting this in Eq. 1.26,

$$
\begin{aligned}
\bar{A}^* A \mathrm{e}^{i(\delta_B - \phi_3)} + \bar{A} A^* \mathrm{e}^{-i(\delta_B - \phi_3)} &= |A||\bar{A}| \left(\mathrm{e}^{i\Delta\delta_D} \mathrm{e}^{i(\delta_B - \phi_3)} + \mathrm{e}^{-i\Delta\delta_D} \mathrm{e}^{-i(\delta_B - \phi_3)} \right)\\
&= 2|A||\bar{A}| \left(\cos\left(\Delta\delta_D + (\delta_B - \phi_3) \right) \right)\\
&= 2|A||\bar{A}| (\cos \Delta\delta_D \cos\left(\delta_B - \phi_3\right)\\
&\qquad - \sin \Delta\delta_D \sin\left(\delta_B - \phi_3\right)).
\end{aligned} \tag{1.29}
$$

Now, Eq. 1.26 becomes

$$\begin{aligned}P_B &= |\bar{A}|^2 r_B^2 |A|^2 + 2r_B|\bar{A}||A|\left(\cos\Delta\delta_D\cos\left(\delta_B-\phi_3\right)-\sin\Delta\delta_D\sin\left(\delta_B-\phi_3\right)\right)\\ &= |\bar{A}|^2 + r_B^2|A|^2 + 2\sqrt{P\bar{P}}(x_-C - y_-S),\end{aligned} \tag{1.30}$$

where $P(m_-^2, m_+^2) = |A|^2$ and $\bar{P}(m_-^2, m_+^2) = |\bar{A}|^2$; while

$$x_- = r_B\cos(\delta_B - \phi_3), \;\; y_- = r_B\sin(\delta_B - \phi_3); \tag{1.31}$$

and the functions $C = C(m_-^2, m_+^2)$ and $S = S(m_-^2, m_+^2)$ are the cosine and sine of the strong phase difference, $\delta_D(m_-^2, m_+^2) = \arg A - \arg\bar{A}$, between the $D^0 \to K_S^0h^+h^-$ and $\bar{D}^0 \to K_S^0h^+h^-$ decay amplitudes. For CP conjugate mode, $B^- \to DK^-$, the density can be written as

$$P_{\bar{B}} = |A|^2 + r_B^2|\bar{A}|^2 + 2\sqrt{P\bar{P}}(x_+C + y_+S), \tag{1.32}$$

where $x_+ = r_B\cos(\delta_B + \phi_3)$ and $y_+ = r_B\sin(\delta_B + \phi_3)$.

In the model-independent method, the D-decay Dalitz plot is divided into $2 \times \mathcal{N}$ bins that are indexed from $i = -\mathcal{N}$ to $i = \mathcal{N}$, with $i = 0$ excluded. The bins are defined symmetrically about $m_+^2 = m_-^2$, as shown in Fig. 1.6, such that if the point $\left(m_-^2, m_+^2\right)$ lies within bin i then point $\left(m_+^2, m_-^2\right)$ lies within bin $-i$; bins in which $m_-^2 > m_+^2$ are labelled with $i > 0$ and vice versa. The strong phase of the D^0-decay amplitude at a point $\left(m_-^2, m_+^2\right)$ is written as $\delta_D\left(m_-^2, m_+^2\right)$, from which the D-amplitude-weighted average of the cosine of the strong-phase difference between D^0 and $\bar{D}^0$ decays within

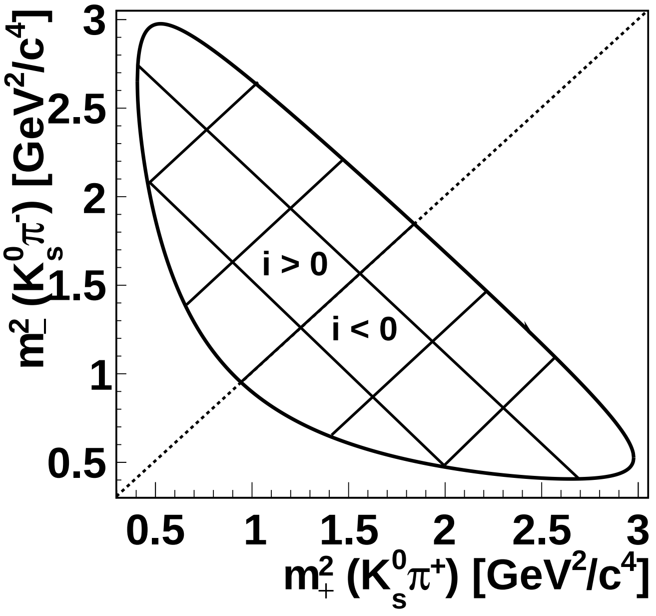

Figure 1.6: Illustration of the binning scheme used for the decay $D^0 \to K^0_S\pi^+\pi^-$ in BPGGSZ measurements: the bins are symmetric around the $m^2_+ = m^2_-$ diagonal, and numbered so that opposite bins have the same number, except with opposite sign.

bin i is defined as [37]

$$c_i = \frac{\int_i dm^2_- \, dm^2_+ \left|A_D\left(m^2_-, m^2_+\right)\right| \left|A_D\left(m^2_+, m^2_-\right)\right| \cos\left[\delta_D\left(m^2_-, m^2_+\right) - \delta_D\left(m^2_+, m^2_-\right)\right]}{\sqrt{\int_i dm^2_- \, dm^2_+ \left|A_D\left(m^2_-, m^2_+\right)\right| \int_i dm^2_- \, dm^2_+ \left|A_D\left(m^2_+, m^2_-\right)\right|^2}}\,, \tag{1.33}$$

where the integral is over the i-th bin. The D-amplitude-weighted average of the sine of the strong-phase difference within a bin s_i is defined in a similar manner. These definitions result in the conditions $c_i = c_{-i}$ and $s_i = -s_{-i}$. Here, no direct *CP*-violation for $D^0 \to K^0_S\pi^+\pi^-$ decays is assumed. Further, the A_{B^+} (A_{B^-}) amplitudes can be squared and integrated over each bin to give the expectation for the B^+ (B^-) yields in each bin N_i^+ $\left(N_i^-\right)$:

$$\begin{aligned}
N_i^+ = & \quad h_{B^+}\left[F_{-i} + \left\{\left(x_+^{DK}\right)^2 + \left(y_+^{DK}\right)^2\right\} F_i \quad + 2\sqrt{F_i F_{-i}}\left(x_+^{DK} c_i - y_+^{DK} s_i\right)\right] \ , \\
N_{-i}^+ = & \quad h_{B^+}\left[F_i \quad + \left\{\left(x_+^{DK}\right)^2 + \left(y_+^{DK}\right)^2\right\} F_{-i} + 2\sqrt{F_i F_{-i}}\left(x_+^{DK} c_i + y_+^{DK} s_i\right)\right] \ , \\
N_i^- = & \quad h_{B^-}\left[F_i \quad + \left\{\left(x_-^{DK}\right)^2 + \left(y_-^{DK}\right)^2\right\} F_{-i} + 2\sqrt{F_i F_{-i}}\left(x_-^{DK} c_i + y_-^{DK} s_i\right)\right] \ , \\
N_{-i}^- = & \quad h_{B^-}\left[F_{-i} + \left\{\left(x_-^{DK}\right)^2 + \left(y_-^{DK}\right)^2\right\} F_i \quad + 2\sqrt{F_i F_{-i}}\left(x_-^{DK} c_i - y_-^{DK} s_i\right)\right] \ ,
\end{aligned} \tag{1.34}$$

where $h_{B^\pm}$ are independent normalisation constants, $x_\pm^{DK} = r_B^{DK}\cos\left(\delta_B^{DK} \pm \phi_3\right)$, and $y_\pm^{DK} = r_B^{DK}\sin\left(\delta_B^{DK} \pm \phi_3\right)$.[7] Here F_i is the fractional yield in each bin for a pure sample of D^0 decays accounting for any experiment-specific efficiency variation over the Dalitz plot [42]:

$$F_i = \frac{\int_i dm_-^2\, dm_+^2 \left|A_D\left(m_-^2, m_+^2\right)\right|^2 \eta\left(m_-^2, m_+^2\right)}{\sum_j \int_j dm_-^2\, dm_+^2 \left|A_D\left(m_-^2, m_+^2\right)\right|^2 \eta\left(m_-^2, m_+^2\right)}, \tag{1.35}$$

where the sum in the denominator is over all $2\mathcal{N}$ bins and $\eta\left(m_-^2, m_+^2\right)$ is the acceptance profile over the Dalitz plot, which depends on both laboratory-frame decay kinematics and the experimental setup. The fractional yield in each bin for a pure sample of $\bar{D}^0$ decays, neglecting the CP-violation in D decays, is $\bar{F}_i = F_{-i}$.

The $4\mathcal{N}$ observables defined in Eqs. (1.34) depend upon $4\mathcal{N}+4$ parameters. Therefore, independent measurements of the $2\mathcal{N}$ strong-phase parameters c_i and s_i are used to determine the other parameters from these yields. Furthermore, the $2\mathcal{N}-1$ fractional

---

[7] *CP* violation in the total decay rate is negligible, i.e., when integrated over the full Dalitz plot [42]. Therefore, to avoid any bias due to detector asymmetry, independent normalisation constants are used for B^+ and B^- decays.

yields F_i can be constrained using the simultaneous analysis of $B^+ \to D\pi^+$ decays [42], which have a branching fraction an order of magnitude larger than $B^+ \to DK^+$ [8]. An analogous set of yields for $B^+ \to D\pi^+$ exist as those defined in Eq. (1.34), which depend upon $x_\pm^{D\pi} = r_B^{D\pi} \cos\left(\delta_B^{D\pi} \pm \phi_3\right)$ and $y_\pm^{D\pi} = r_B^{D\pi} \sin\left(\delta_B^{D\pm} \pm \phi_3\right)$, where $r_B^{D\pi}$ and $\delta_B^{D\pi}$ are the magnitude ratio and strong-phase difference between the Cabibbo and colour suppressed $B^+ \to D^0\pi^+$ amplitude and the favoured $B^+ \to \bar{D}^0\pi^+$ amplitude. The value of $r_B^{D\pi}$ is approximately twenty times smaller than r_B^{DK} so the sensitivity to *CP* violation is significantly reduced in comparison to that from $B^+ \to DK^+$ decays. Given the almost identical kinematic properties between $B^+ \to DK^+$ and $B^+ \to D\pi^+$, the F_i parameters are common for the two sets of yields within a single experiment. A parameterisation [43, 44] that utilises the common dependence on ϕ_3 of the $B^+ \to DK^+$ and $B^+ \to D\pi^+$ yields by introducing the single complex variable is adopted,

$$\xi^{D\pi} = \left(\frac{r_B^{D\pi}}{r_B^{DK}}\right) e^{i\left(\delta_B^{D\pi} - \delta_B^{DK}\right)} \, . \tag{1.36}$$

Defining $x_\xi^{D\pi} \equiv \mathrm{Re}\left(\xi^{D\pi}\right)$ and $y_\xi^{D\pi} \equiv \mathrm{Im}\left(\xi^{D\pi}\right)$ one can write

$$x_\pm^{D\pi} = x_\xi^{D\pi} x_\pm^{DK} - y_\xi^{D\pi} y_\pm^{DK} \ , \quad y_\pm^{D\pi} = x_\xi^{D\pi} y_\pm^{DK} + y_\xi^{D\pi} x_\pm^{DK} \, . \tag{1.37}$$

The values of $x_\pm^{DK}$, $y_\pm^{DK}$, $x_\xi^{D\pi}$, $y_\xi^{D\pi}$ and F_i are determined simultaneously from a fit to the $B^+ \to Dh^+$ candidates. The advantages of this parameterisation are the inclusion of the ϕ_3 sensitivity from $B^+ \to D\pi^+$ in the determination of $x_\pm^{DK}$ and $y_\pm^{DK}$ as well as much improved fit stability [42]. Further, the determination of F_i by simultaneously fitting $B^+ \to Dh^+$ removes a source of systematic uncertainty as compared to the similar analysis reported in Ref. [45], where the values of F_i were determined from a sample of $D^{*+} \to D^0\pi^+$ decays. The differing kinematic properties of the $B^+ \to D\pi^+$ and $D^{*+} \to D^0\pi^+$ decays resulted in different $\eta\left(m_-^2, m_+^2\right)$ acceptance functions for the two samples, which was a source of systematic uncertainty.

There are three different 2×8 binning schemes available for the $D^0 \to K_S^0\pi^-\pi^+$ decays, equal-strong-phase, optimal and modified optimal, out of which the optimal binning scheme is considered for our analysis; the bins are chosen in such a way that gives the maximum sensitivity to ϕ_3 [46]. The optimisation is performed assuming a strong-phase difference distribution as predicted by the BaBar amplitude model [47]. Similarly, for the $D^0 \to K_S^0 K^- K^+$ final state, three choices of binning schemes are available, containing 2×2, 2×3, and 2×4 equal-strong-phase bins, which use the BaBar model [48] for defining the bin boundaries. The 2×2 binning scheme is considered for this final state, as most of the sensitivity is covered by this scheme, and there might be a possibility of fit instability by addition of extra bins because of low statistics of the decay $B^+ \to DK^+$, $D \to K_S^0 K^+ K^-$. An example of binning choice for both $D \to K_S^0\pi^+\pi^-$ and $D \to K_S^0 K^+ K^-$ decays are given in Fig. 1.7.

1.3.2 Charm factory inputs

The strong-phase parameters c_i and s_i are measured at *charm* factories like CLEO and BESIII using quantum-correlated $D^0\bar{D}^0$ pairs produced at the $\psi(3770)$ $(c\bar{c})$ resonance in e^+e^- collisions. The $D^0\bar{D}^0$ pairs are called quantum-correlated as the quantum state of one D meson can be determined by observing the final products of other D decay. These parameters can also be measured using B data, but that will lead to loss of precision as

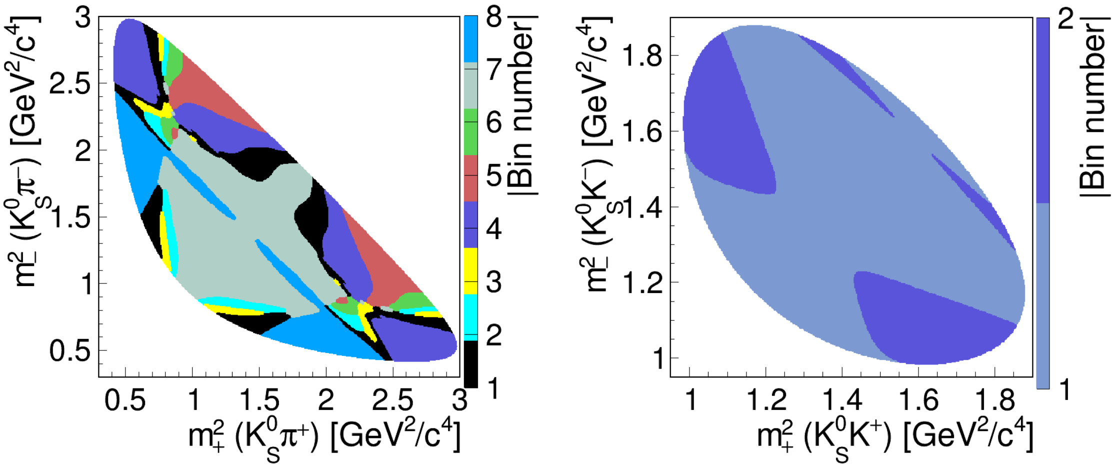

Figure 1.7: Binning schemes used for (left) $B^+ \to DK^+$, $D \to K^0_S\pi^+\pi^-$ decays and (right) $B^+ \to DK^+$, $D \to K^0_S K^+K^-$ decays.

the datasets are statistically limited.

These measurements are available in all binning schemes mentioned in the previous section; the values provided for optimal ($K^0_S\pi^-\pi^+$) and equal-strong-phase ($K^0_S K^-K^+$) binning are considered for our measurements. The measurements of c_i and s_i ignore the effects of D-mixing and assumes CP-conservation in D decay; generally the results have negligible bias with the ignorance of both these effects in the strong-phase and B analyses. The measurements presented in this thesis are based on a combination of the BESIII and CLEO results made by the BESIII collaboration [49, 50]. The results are tabulated in Tables 1.3 and 1.4, and are also presented in Figs. 1.8.

Table 1.3: Measured c_i and s_i parameters averaged over BESIII and CLEO results for $D^0 \to K^0_S\pi^-\pi^+$ decay [49].

Bin	c_i	s_i
1	-0.037 ± 0.049	-0.829 ± 0.097
2	0.837 ± 0.067	-0.286 ± 0.152
3	0.147 ± 0.067	-0.786 ± 0.154
4	-0.905 ± 0.021	-0.079 ± 0.059
5	-0.291 ± 0.041	1.022 ± 0.064
6	0.272 ± 0.082	0.977 ± 0.176
7	0.918 ± 0.017	0.184 ± 0.065
8	0.773 ± 0.033	-0.277 ± 0.118

Table 1.4: Measured c_i and s_i parameters averaged over BESIII and CLEO results for $D^0 \to K^0_S K^- K^+$ decay [50].

Bin	c_i	s_i
1	-0.713 ± 0.032	0.107 ± 0.132
2	-0.758 ± 0.037	0.394 ± 0.173

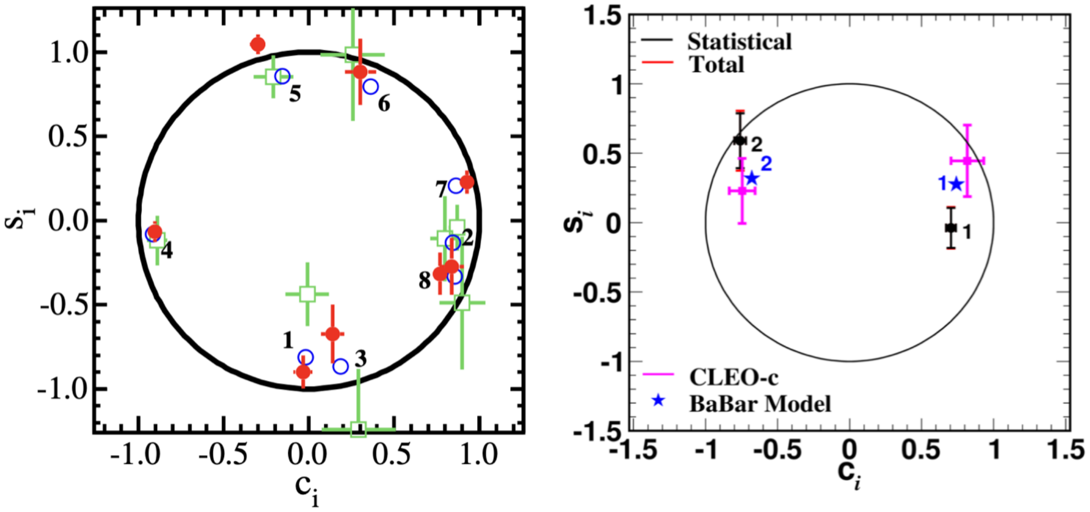

Figure 1.8: Measured c_i and s_i parameters from BESIII and CLEO experiment for $D^0 \to K^0_S\pi^-\pi^+$ (left) and $D^0 \to K^0_S K^- K^+$ (right) decays [49, 50]. The $D^0 \to K^0_S\pi^-\pi^+$ plot show the results obtained by (red) BESIII, (green) CLEO, and (blue) the model expectation using the model from Ref. [47] and the $D^0 \to K^0_S K^- K^+$ plot show the results obtained by (red) BESIII, (magenta) CLEO, and (blue) the model expectation using the model from Ref. [48].

The primary part of this thesis presents the measurement of angle ϕ_3 from the decay $B^+ \to Dh^+$, $D \to K^0_{\rm S}h^-h^+$ using the data samples collected at Υ (4S) resonance by the Belle and Belle II detector at KEKB and SuperKEKB accelerator, respectively. The remainder of this thesis is organized as follows: Chapter 2 gives the detailed description of Belle and Belle II detectors. The selection criteria and signal extraction procedures are discussed in Chapter 3 and 4, respectively. The results are summarized in Chapter 5. The secondary part of the thesis is the results of beam energy calibration work done for the Belle II experiment and is described in Chapter 6. Chapter 7 provides the conclusion and outlook.

CHAPTER 2

Belle and Belle II experiments

The analyses presented in this thesis are based on data samples collected by the Belle and Belle II experiments. The Belle detector was installed at the interaction region of the KEKB asymmetric-energy e^+e^- collider operating at $\Upsilon(4S)$ resonance. The Belle II detector is a substantial upgrade of the Belle detector and sits at the interaction point of the SuperKEKB accelerator. Both of these accelerators are situated at the High Energy Accelerator Research Organization (KEK) in Tsukuba, Japan. In this chapter the overview of these two accelerators and their corresponding detectors are discussed.

2.1 KEKB ACCELERATOR

A schematic of the KEKB accelerator complex is given in Fig. 2.1. The KEKB accelerator is an asymmetric-energy collider of 8 GeV electrons and 3.5 GeV positrons. It is made up of two storage rings: the High Energy Ring (HER) for the electrons and the Low Energy Ring (LER) for the positrons. The Lorentz boost generated from the asymmetric collisions benefit time-dependent *CP* violation measurements.

The two rings are approximately three kilometres in circumference, 11 metres below ground level, and built side-by-side in the TRISTRAN tunnel.[1] The electrons are produced from an electron gun and are accelerated through a LINAC to produce the beam. The positron beam is created with the help of a tungsten target in the path of the

---

[1] A symmetric electron-positron particle accelerator at KEK, Japan. This was built in 1981-1986 with the aim to search for $t\bar{t}$.

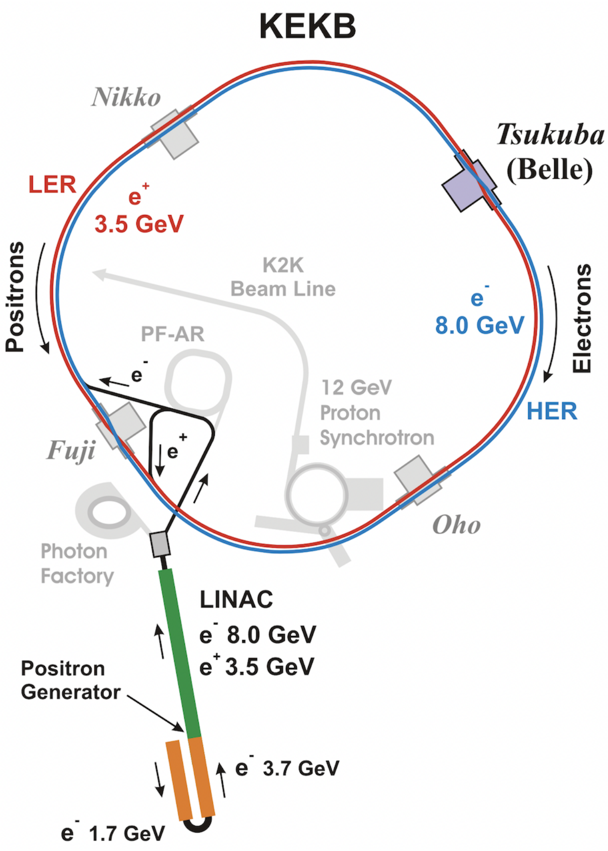

Figure 2.1: Schematic of the KEKB accelerator complex [51].

electron beam and is separated using a magnetic field. Then these two beams are fed into the storage rings and injected into KEKB in the Fuji area. The LER and HER can store currents up to 2.6 A and 1.1 A, respectively; they use an RF of 508.9 MHz to accelerate the beams [52]. With the aid of dipole, quadrupole, and sextupole magnets, the beams are made to circulate in trajectories that maximise the instantaneous luminosity. In order to compensate for the energy loss of the beams due to radiation as they circulate in KEKB, two kinds of RF cavities are installed: normal conductive cavities, which are accelerator resonantly coupled with energy storage, and superconducting cavities.

The two beams cross at the interaction point (IP) in the Tsukuba experimental hall at the center of the Belle detector. At the IP, the two beams collide with a finite

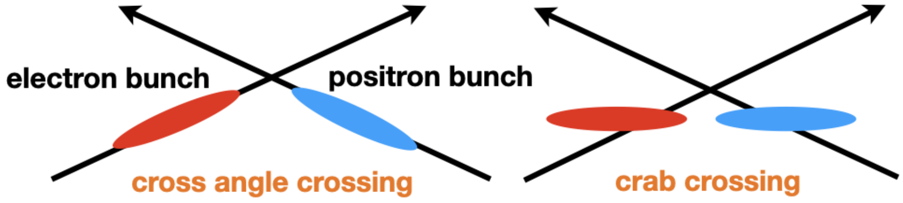

Figure 2.2: A schematic of cross-angle and crab crossings.

Table 2.1: Data collected at or near Υ resonances and their corresponding luminosities.

Data type	$\sqrt{s}$ (GeV)	Luminosity (fb^{-1})
Υ(4S) resonance	10.58	711
Υ(4S) off-resonance	10.52	89
Υ(5S) resonance	10.86	121
Υ(5S) scan	$10.58 < E_{\mathrm{CM}} < 11.02$	7
Υ(3S) resonance & off-resonance	10.35 & 10.32	2
Υ(2S) resonance & off-resonance	10.02 & 9.99	28
Υ(1S) resonance & off-resonance	9.46 & 9.43	8
Total		966

horizontal crossing angle of ± 11 mrad [53]. This angle eliminates the need for any separation-bend magnets, lowering the beam-related background level substantially. Two superconducting crab cavities are employed to kick the bunches into the horizontal plane in order to achieve the maximum luminosity [54, 55]. The crab cavities have a transverse RF that allows the bunches to spin and collide with the most overlap at the IP, as shown in Fig. 2.2.

The data samples were collected at or near centre-of-mass (c.m.) energies ($\sqrt{s}$) corresponding to different Υ resonances, as shown in Table 2.1. The total e^+e^- annihilation cross section as a function of the CM energy in the region of the Υ resonances are shown in Fig. 2.3. The data sample used in our analysis is corresponds to the sample collected at the Υ(4S) resonance, which is just above the threshold for decay into $B\bar{B}$ meson pairs. The highest instantaneous luminosity achieved by KEKB

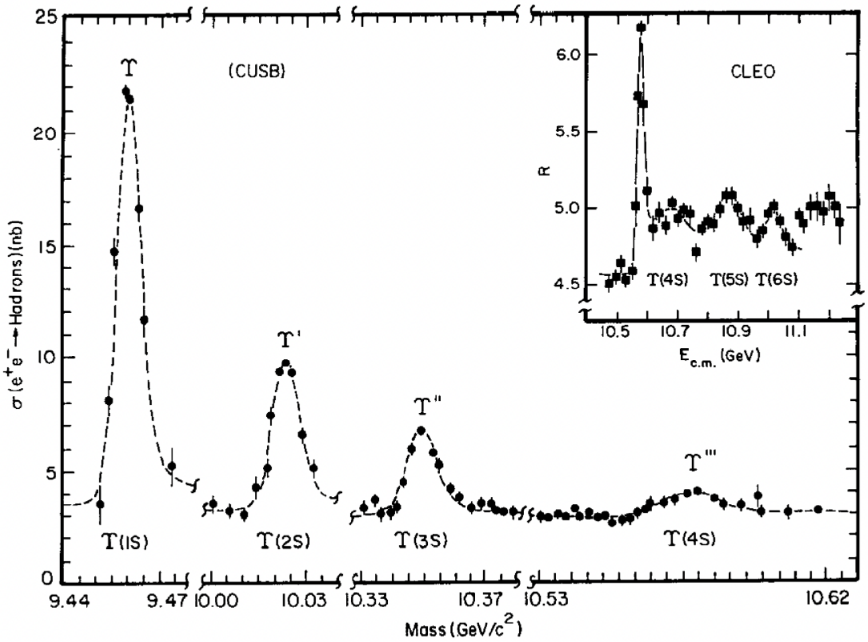

Figure 2.3: Various Υ resonances from e^+e^- collisions and their cross-sections [56].

was 2.11×10^{34} cm^{-2} s^{-1}, which was a world record until 2020 [57]. After the completion of the physics runs in 2010, the overall integrated luminosity was around 1 ab^{-1}.

2.2 BELLE DETECTOR

The Belle detector [58, 59] is a general purpose detector surrounding the IP to detect the particles coming from e^+e^- collisions. It has different sub-systems for various purposes. The schematic view of the Belle detector is shown in Fig. 2.4. The component at it's centre is the silicon vertex detector (SVD), which accurately determines particle decay vertices and measures charged particle tracks. The SVD is surrounded by the central drift chamber (CDC), which completes the tracking system. The CDC also performs ionisation-energy-loss (dE/dx) measurements that assist the differentiation between various particle species, along with the aerogel cherenkov counter (ACC) and

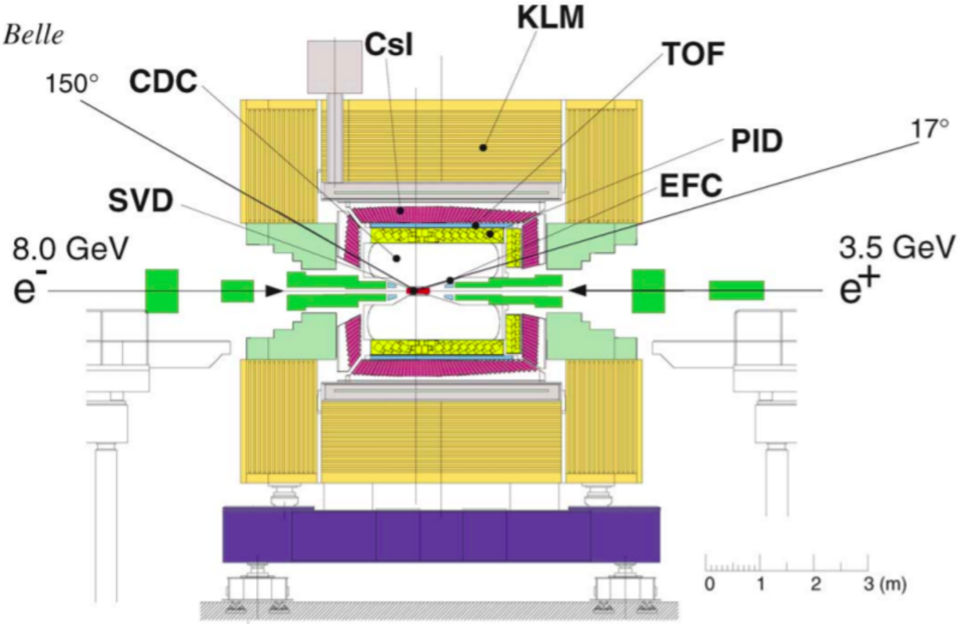

Figure 2.4: Side view of the Belle detector [58].

time-of-flight (TOF) counter subsystems. These three subsystems form the particle identification (PID) system at Belle, which plays a crucial role in identifying the most abundant hadrons after the collision: kaons and pions. The PID system is surrounded by a crystal calorimeter, which measures the energy deposited by electromagnetic interactions. The whole detector is surrounded by a superconducting solenoid, which generates a 1.5 T magnetic field. The K_{L}^0 and muon detection systems (KLM) are the outermost components.

Belle follows a right-handed coordinate system; the origin is the nominal IP position, the x-axis is horizontally aligned pointing outward from the centre of the KEKB ring, the y-axis is along the vertical direction (upward) and the z-axis is aligned opposite to the positron beam direction. The polar angle θ is measured relative to the positive z-axis and the azimuthal angel ϕ with respect to x-axis. Due to the boost of the Υ(4S) resonances, the components of Belle are asymmetric in z.

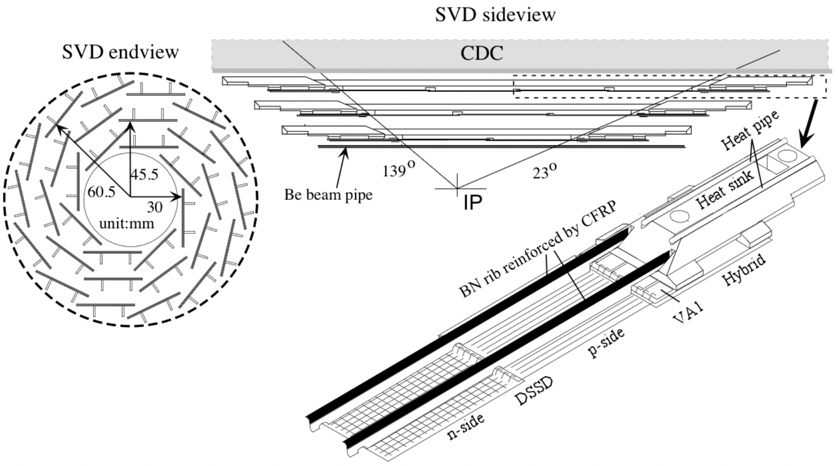

Figure 2.5: Schematic view of the SVD1 subsystem of Belle [60].

Each subsystems are discussed in detail in the following sub-sections.

2.2.1 Silicon Vertex Detector (SVD)

The primary purpose of the SVD is to determine the z-axis position of the B and D meson decay vertex, which is essential for time-dependent *CP* and meson-mixing analysis. The average distance between B and $\bar{B}$ meson decay vertices is around 200 μm; the SVD vertex separation measurement along the z direction is approximately 100 μm. SVD also helps in low momentum charged particle tracking. In Belle, there are two types of SVD sub-detectors used: a three-layer SVD1 until summer 2003, and a four-layer SVD2 until the end of data taking in 2010. SVD1 was replaced by SVD2 in 2003 as the former was damaged by the synchrotron radiation. The fraction of the total data set collected by SVD1 is 20% and by SVD2 is 80%. The schematic view of SVD1 and SVD2 are shown in Figs. 2.5 and 2.6, respectively.

SVD1 consists of three layers of double-sided silicon strip detectors (DSSD) that cover the region $23^\circ < \theta < 139^\circ$, which is 86% of the total solid angle. The three layers

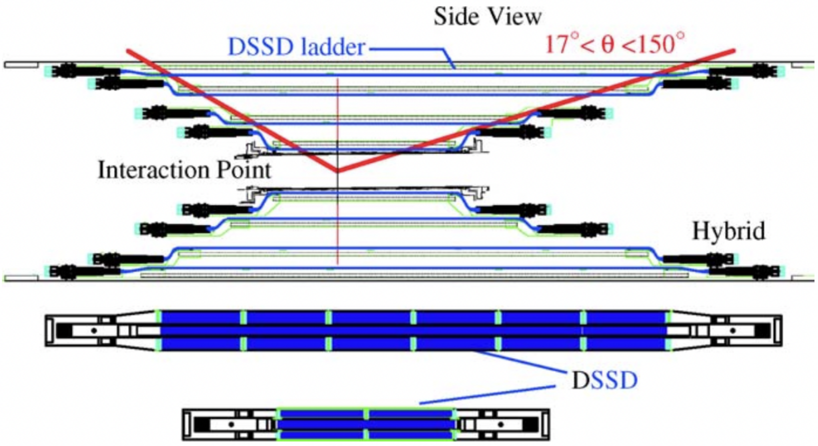

Figure 2.6: Schematic view of the SVD2 subsystem of Belle [61].

consist of eight, ten and 14 complete ladders for the inner, middle, and outer layers, respectively, around the beam axis. Each half-ladder has one or two DSSDs, and each full ladder is made up of two half-ladders. There are 32 ladders and 102 DSSDs in total. The DSSDs are diode-strip detectors that have been reverse-biased. They have a thickness of 300 μm and a surface area of 57.5×33.5 mm^2. Each DSSD contains 1280 sense strips and 640 readout pads. The signals from the DSSDs are read out by VA1 chips mounted on a ceramic hybrid [62, 63]. The momentum and angular dependencies, shown in Fig. 2.7, of the impact parameter (the closest approach of tracks to the IP) resolution are

$$\sigma_{xy} = 19 \oplus 50(p\beta \sin^{3/2}\theta)^{-1}\mu\text{m}, \qquad \sigma_z = 36 \oplus 42(p\beta \sin^{5/2}\theta)^{-1}\mu\text{m}, \tag{2.1}$$

where $\oplus$ indicates a quadratic sum. Here the momentum p is given in units of GeV/c and β is defined as the velocity of the particle divided by the speed of light. The impact parameter resolution for a 1 GeV track is around 55 μm.

Several improvements were made for SVD2. It has four layers and has a larger angular

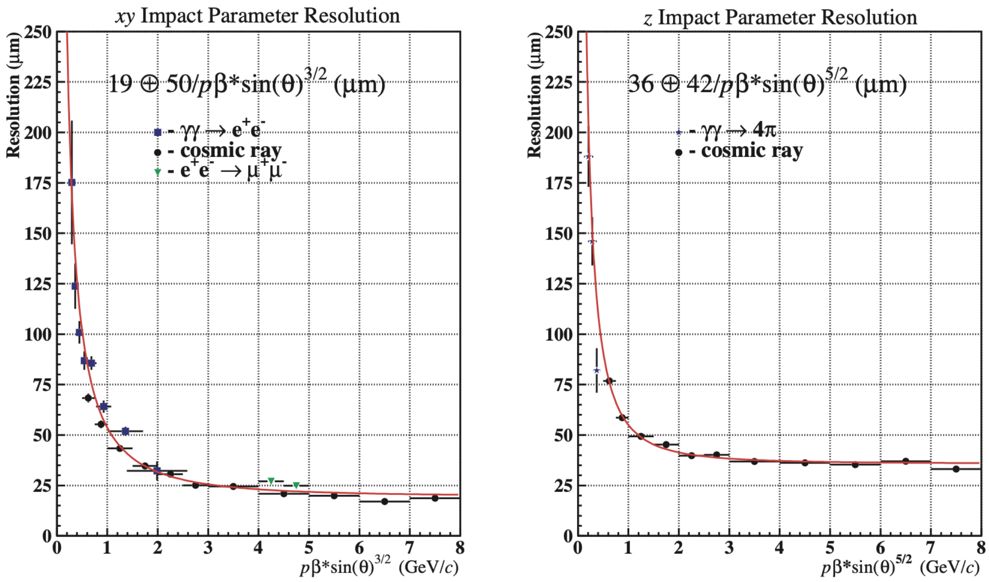

Figure 2.7: Resolution of the impact parameter measured by the SVD [58].

acceptance of $17^\circ < \theta < 150^\circ$. The innermost layer is closer to the primary interaction point at a distance of 2 cm. The four layers of SVD2 contain six, 12, 18 and 18 full ladders from the innermost layer to the outermost. Each half-ladder consists of one, two or three DSSDs. The DSSDs for SVD2 have 512 readout channels in both $r - z$ and $r - \phi$ planes, providing a total of 110,592 readout channels. The limited radiation tolerance of the VA1 front-end readout chips are replaced by the VA1TA chips [64] for SVD2.

2.2.2 Central Drift Chamber (CDC)

The principal purpose of CDC is to measure the momentum and dE/dx, which along with the SVD, comprises the tracking system of the Belle experiment. The dE/dx information is used for PID. The schematic view of the CDC sub-detector is shown in Fig. 2.8. The inner and outer radii of CDC are 83 and 874 mm, respectively, and the length is 2,400 mm. It has a polar angle range of 17° to 150°. The CDC is a tiny cell

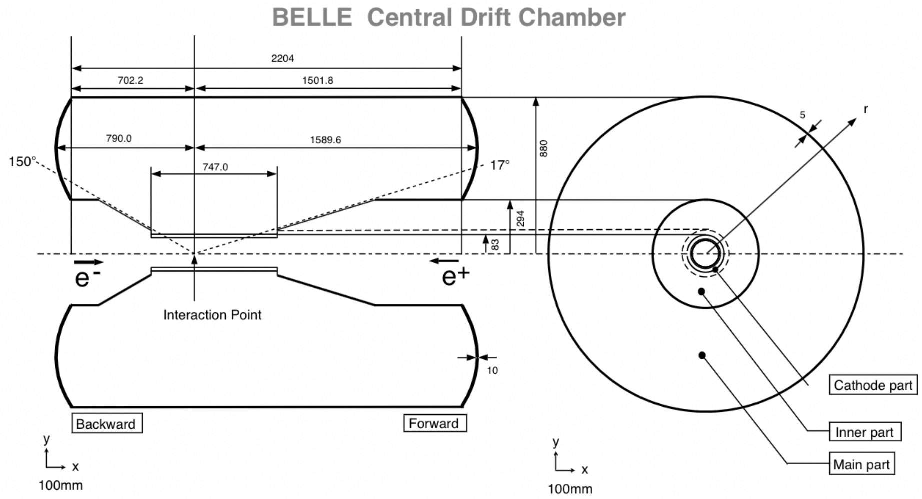

Figure 2.8: Schematic view of the CDC sub-detector of Belle [65].

drift chamber with 50 layers of anode sensing wire and three layers of cathode strip. The anode wires have 8,400 readout channels, whereas the cathode strips have 1792. The anode wires provide the three-dimensional track information.

In addition to tracking, CDC is an important component of the particle identification system. For a particle passing through the CDC, a measure of the mean energy deposition due to ionisation of the gas (dE/dx) may be derived from the pulse height at the anode wires. As the energy loss of a particle is proportional to its boost, dE/dx will vary depending on particle species for a given momentum value. To reduce the multiple Coulomb scattering contribution, the chamber is filled with a 1:1 mixture of helium and ethane. The pulse height and drift time of the ionization are measured to provide the information about the energy deposit and the distance from the sensor-wire, respectively. The distribution of dE/dx as a function of momentum in the CDC is shown in Fig. 2.9; the separation between different particles is clearly visible. The separation between kaons and pions is of relevance for our analysis.

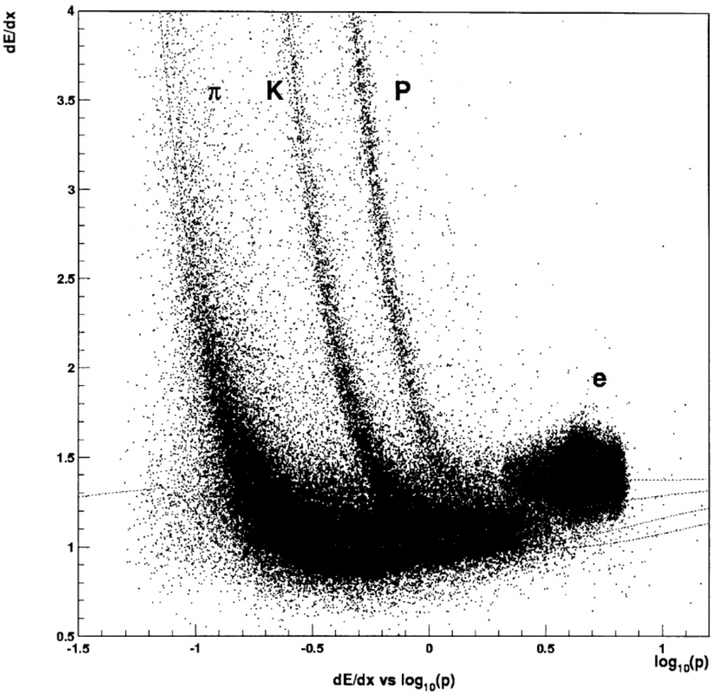

Figure 2.9: dE/dx measurements as a function of momentum for various particle types. [58].

2.2.3 Aerogel Cherenkov Counter (ACC)

The aerogel based Cherenkov counter [66] is designed for kaon and pion track separation; it works well in the momentum range 0.5 to 4 GeV/c. ACC detects the Cherenkov light generated by a particle when it moves faster than the speed of light in a medium. Cherenkov light is emitted for a material with refractive index n if the particle's velocity β meets the criterion

$$n > 1/\beta = \sqrt{1 + (mc/p)^2}, \tag{2.2}$$

where m and p are the mass and momentum of the particle, respectively. As a result, there is a range of velocity for which pions produce Cherenkov radiation but kaons do not, depending on the refractive index of the medium. This fact is exploited for the

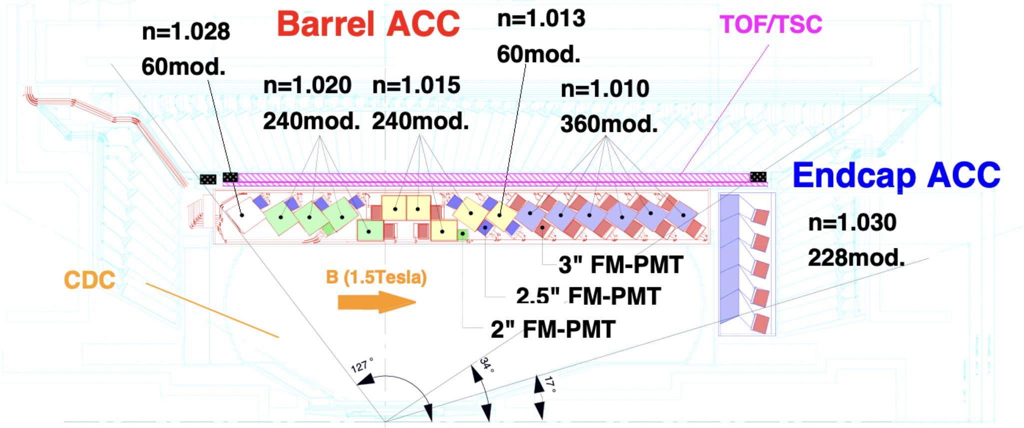

Figure 2.10: Schematic of ACC sub-detector of Belle [58].

particle identification technique with the ACC.

The barrel part is made up of 960 aerogel counter modules, which are further divided into 60 cells in the ϕ direction. The forward end-cap is made up of 228 modules organised in five concentric levels. Aerogel blocks having refractive indices of $n = 1.010,\ 1.013,\ 1.015,\ 1.020$, and 1.028 are organised according to polar angle in five distinct types. One or two fine mesh-type photomultiplier tubes are used to observe a standard counter module, which comprises of silica aerogel packed in 0.2 mm-thick metal boxes (FM-PMTs). The FM-PMTs are designed to perform well in the 1.5 T magnetic field. There are total 1560 readout channels in the barrel region and 228 in the end-cap. The arrangement of the ACC is shown in Fig. 2.10.

2.2.4 Time-of-Flight Counter (TOF)

The time-of-flight sub-detector [66] adds PID information for charged particles with momenta less than 1.2 GeV/c, where the K/π separation power of ACC and CDC are less effective. The TOF also provides fast timing signals for the trigger system, which

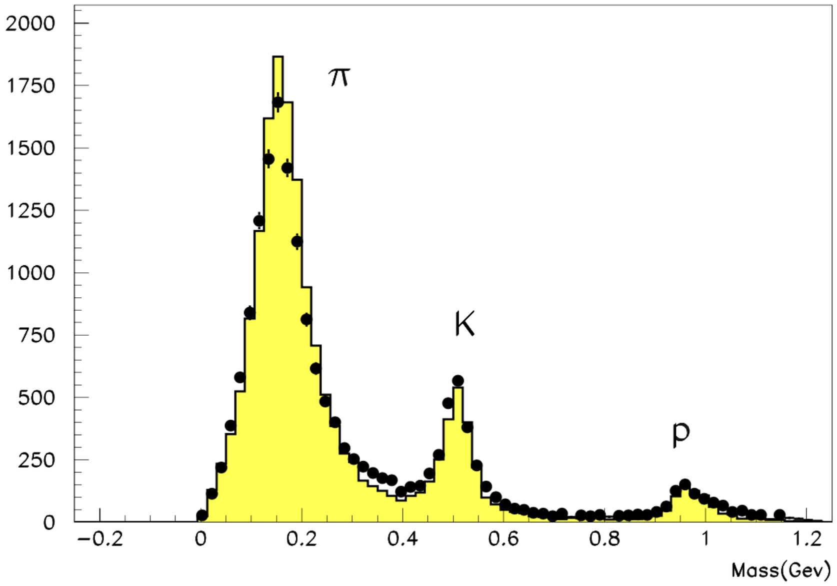

Figure 2.11: Hadron mass distributions calculated from TOF measurements for particles with momentum below 1.2 GeV/c. The black points represent data and the shaded histogram represents the simulation sample [67].

requires a timing resolution of the order of 100 ps. The TOF measures the amount of time it takes for a particle to reach TOF after the collision at the IP. Hence, the particle's mass can be calculated when combined with its measured momentum. This enables particle species to be distinguished by their measured flight time. The flight time, T , for a particle of mass m to travel a length L is given by

$$T = \frac{L}{c}\sqrt{1+\left(\frac{mc}{p}\right)^2}. \tag{2.3}$$

The mass distribution obtained from TOF measurements is shown in Fig. 2.11.

The TOF system consists of 128 TOF counters and 64 trigger scintillation counter (TSC) counters, which form 64 TOF modules positioned in the barrel region covering a polar angle range of 33° to 121°. One module comprises two TOF counters (4 cm thick) and a TSC (0.5 cm thick). The structure of a TOF module is shown in Fig. 2.12.

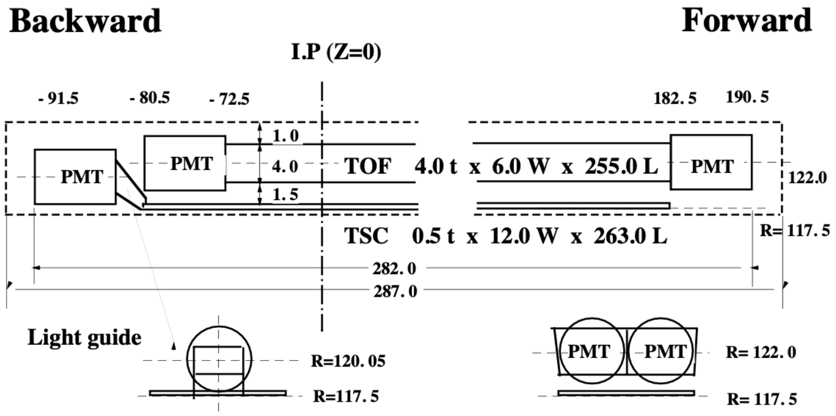

Figure 2.12: Schematic view of the TOF sub-sytem of Belle [58].

TOF counters and TSC are made of fast scintillators, and FM-PMTs mounted directly on the scintillators. Each TOF module is made up of two TOF counters, read out by two FM-PMTs attached at both ends, and one TSC, read out by one FM-PMT attached at the back end. TSC is utilised to generate trigger signals synchronised with the TOF counters to minimise the trigger hit rate. TOF scintillators have a time resolution of 100 ps.

Information from the TOF combined with the ACC and the dE/dx measurement from the CDC give the Belle detector more than a 3σ separation between charged kaons and pions over the whole momentum range up to 3.5 GeV/c.

2.2.5 Electromagnetic Calorimeter (ECL)

The electromagnetic calorimeter (ECL) measures the energy and position of photons from π^0 decays, as well as from radiative B decays, with high efficiency and good position resolution. It is also used for electron and positron identification. The ECL is composed of an array of tower-shaped CsI(Tl) crystals, which are arranged pointing towards the IP. The crystals are placed with a small tilt angle so that photons do not

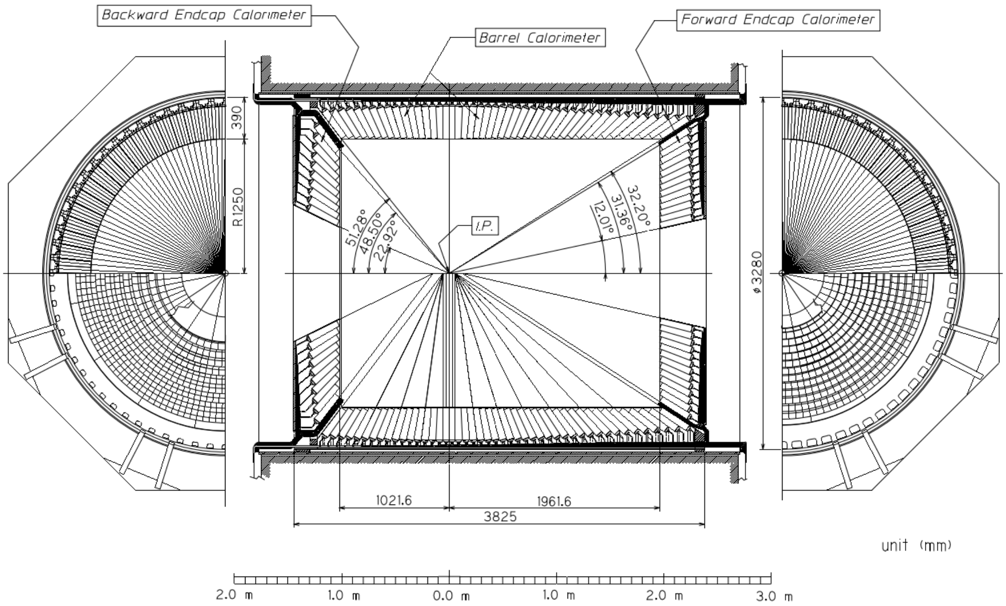

Figure 2.13: Schematic view of the ECL sub-sytem of Belle [58].

pass through a gap between the crystals without interacting. A schematic of the ECL is shown in Fig. 2.13. The geometrical configuration is summarized in Table 2.2. The length of each crystal is 30 cm, which corresponds to 16.2 radiation lengths, and it is read out by a pair of silicon PIN photodiodes.

Table 2.2: The geometrical configuration of the ECL of Belle.

	θ coverage (°)	# crystals	position (cm)
Forward endcap	$12.4 < \theta < 31.4$	1152	$z = 196$
Barrel	$32.2 < \theta < 128.7$	6624	$r = 125$
Backward endcap	$130.7 < \theta < 155.1$	960	$z = 196$

The energy resolution of the ECL is measured to be [68]

$$\frac{\sigma_E}{E} = \frac{0.0066}{E} \oplus \frac{1.53}{E^{1/4}} \oplus 1.18(\%), \tag{2.4}$$

where the energy E is measured in GeV. The first term comes from the contribution of electronic noise, whereas the second term and a portion of the third term originate from the electromagnetic shower's inadequate confinement. Systematic influences, such as the uncertainty of the calibration of the light output from each crystal, are also included in the third term. The spatial resolution is found to be $0.27 \oplus 3.4/\sqrt{E} \oplus 1.8/E^{1/4}$ mm.

The ECL is also crucial for electron identification, in addition to measuring photon and electron energy. A charged track that points towards an ECL cluster is recognised as an electron (or positron) provided the energy and momentum are consistent, among other requirements.

2.2.6 K_L^0 and muon detector (KLM)

The KLM detects K_L^0 mesons and muons with a momentum greater than 600 MeV/c. The detector is mounted outside the solenoid and comprises 15 layers of resistive plate chambers (RPC), with 14 layers of 4.7 cm thick iron plates in the barrel and 14 RPC layers in the endcap. One RPC super-layer contains two RPC planes to provide θ and ϕ information. The KLM covers the polar angle region of $20^\circ < \theta < 155^\circ$. Signals are read out from cathode strips in both θ and ϕ directions. There are 21,856 readout channels for the barrel detector and 16,126 for the two endcap detectors. The resolution for K_L^0 mesons is 30 mrad in both θ and ϕ directions, and the time resolution is of the order of a few nanoseconds.

All the material in the Belle detector up to the KLM equates to around one hadronic interaction length for K_L^0 mesons. The iron plates in the KLM provide a further 3.9 interaction lengths of material, which is necessary for detecting K_L^0 mesons with high efficiency. When the K_L^0 meson interacts with matter, it produces a shower of hadrons, which results in a cluster of hits in the KLM that is not associated with a charged track.

The KLM can distinguish muons from K_{L}^{0} mesons because they feature a charged track and a series of KLM hits instead of a shower pattern. The KLM has detection effectiveness of more than 90% for muons with a momentum of more than 1 GeV/c and a fake rate of less than 2% for muons with momentum more than 1 GeV/c (from non-interacting pions and kaons).

2.2.7 Trigger system

The purpose of the trigger is to determine when the Belle detector's different subsystems should record an event. When a certain particle collision meets the trigger conditions, data from all subsystems is retrieved and saved for later use. The term *event* is interchangeably used to describe either a physical particle collision or the data that represents the interaction. The choice to read out the events is based on carefully determined criteria that eliminate background events while efficiently preserving events of relevance. The major sources of background events are undesirable interactions between the electron-positron beams, collisions of a beam particle with a residual gas molecule or with the beam pipe, and synchrotron radiation from the beams. Events of interest are mainly hadronic ($e^+e^- \to q\bar{q}$ or $e^+e^- \to \Upsilon(4\mathrm{S}) \to B\bar{B}$) and QED events ($e^+e^- \to \ell^+\ell^-$), used for physics analyses as well as detector calibration and luminosity measurement. Only hadronic events are relevant to our analysis; thus, the next discussion will concentrate on the hadronic trigger. At a design luminosity of 10^{34} cm^{-2}s^{-1}, both physics and background events occur at roughly 100 Hz each; however, to accommodate potentially larger luminosities and beam backgrounds, the

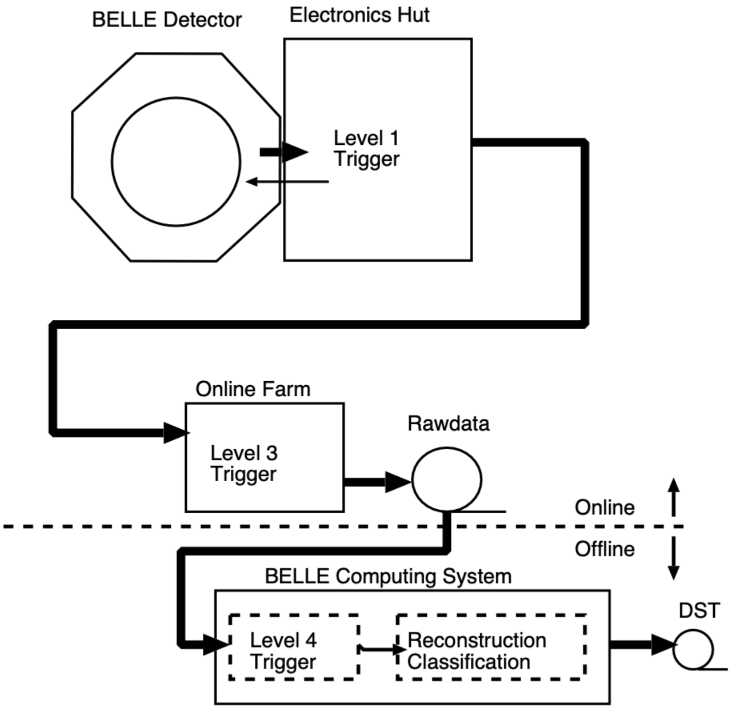

Figure 2.14: An overview of the Belle trigger system [69].

trigger is designed to function at 500 Hz.

The Belle trigger data flow is depicted in Fig. 2.14. It comprises of a level-1 (L1) hardware trigger, a level-3 (L3) software trigger implemented by an online computer farm, and a level-4 (L4) trigger that operates on the Belle computing system off-line and conducts more complex background reduction based on full event reconstruction.

The L1 trigger consists of the sub-trigger system and the central trigger system called global decision logic (GDL). All the subtrigger signals are designed to arrive at the GDL within 1.85 μs of the event taking place. The L1 final trigger signal is issued 2.2 μs after the event crossing. L1 receives a track trigger from the CDC, ACC, and TOF subsystems. Based on the energy deposition in the CsI(Tl) crystals, the energy trigger is acquired from the ECL. These are evaluated in parallel before being sent to

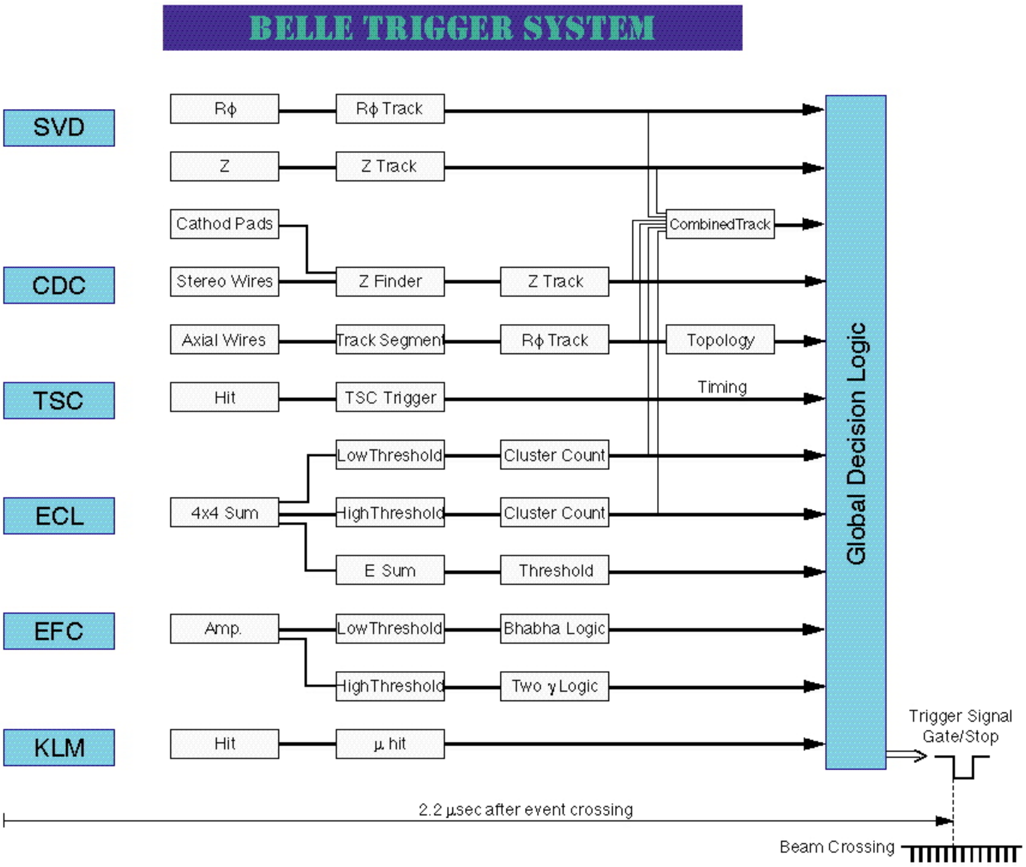

Figure 2.15: Belle level-1 (L1) trigger schematic [58].

the GDL. The timing of the trigger signals must be accurate since the trigger signal determines the readout timing. The timing of the final trigger is determined by the TOF trigger or in its absence by the ECL trigger. For hadronic events, the L1 trigger logic has a 98% efficiency; a schematic of the L1 trigger is shown in Fig. 2.15.

The aim of the L3 trigger is to minimize the number of events to be stored. The L3 trigger first verifies the L1 trigger information but passes some categories of events, such as Bhabha events and random trigger events. If an event does not belong to these categories, the L3 trigger performs a quick reconstruction and rejects the event if it has no track with $|z| < 5$ cm from the IP. A substantial fraction of the beam background events are eliminated by this procedure.

The L4 filters events just before the full event reconstruction takes place. The basic strategy of this trigger is to reject tracks that originate away from the IP. Events rejected by the L4 trigger still remain in the raw data. Thus, the L3 trigger (together with the L1 trigger) reduce the data size to be recorded, while the L4 trigger reduces only the CPU time for data summary tapes (DST) production. The L4 trigger rejects about 78% of triggered events while keeping nearly 100% of B meson events.

2.2.8 Data Acquisition system (DAQ)

The purpose of the DAQ system is to record events defined by the trigger up to a maximum of 500 Hz while maintaining the detector's dead-time fraction below 10%. A distributed-parallel system is used to do this. An overview of the Belle data acquisition system is shown in Fig. 2.16. To handle the data from each subdetector, the DAQ system is divided into seven subsystems. Most sub-detector signals pass via a charge-to-time (Q-to-T) converter before being processed by a time-to-digital converter (TDC). The multihit TDC digitises the timings of the leading edges of the pulse produced by the Q-to-T converter, which is proportional to the input charge. Only the SVD does not employ TDCs and instead uses flash analogue-to-digital converters (FADCs). As the pulse height does not give meaningful information, the KLM does not have a Q-to-T converter.

The readout sequence begins when the sequence controller (SEQ) sends a common stop signal to the TDCs after receiving a final trigger from the GDL. The event-builder combines the data from each sub-detector into a single event, converting *detector-by-detector* parallel data streams into *event-by-event* data. The event-output builder's data

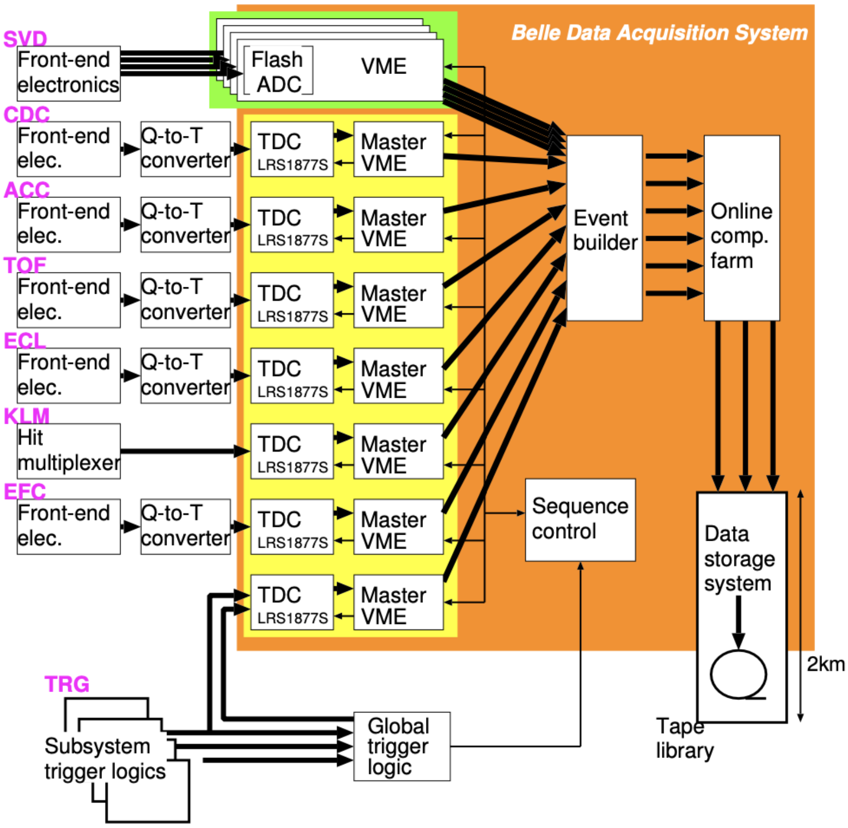

Figure 2.16: A schematic of the Belle DAQ system [58].

is sent to the online computer farm through the L3 trigger. The online data quality monitor (DQM) in the online farm that performs real-time monitoring of the data quality. Finally, the data is transferred by optical fibre to the KEK computing centre's mass storage system, where it is saved on tape. The maximum data transfer rate is 15 MB/s at a trigger rate of 500 Hz.

2.3 SUPERKEKB ACCELERATOR

The new generation of B-Factory is represented by the SuperKEKB accelerator, which is an upgrade of KEKB; the improvement programme began in 2010. The major objective of this upgrade is to raise the machine's instantaneous luminosity from 2.1×10^{34} cm^{-2}s^{-1} (KEKB) to 6×10^{35} cm^{-2}s^{-1} in order to meet the physics goals of the Belle II experiment. With the usage of the nano-beam scheme, this luminosity enhancement is achieved by employing a higher beam current and a smaller beam dimension at the IP, with the goal of keeping the beam emittance as low as possible [71].

SuperKEKB is an e^+e^- asymmetric collider, with an energy of 7 GeV (4 GeV) for the electron (positron) beam. The resulting center-of-mass energy in the relativistic limit is $\sqrt{s} = \sqrt{4E_{e^+}E_{e^-}} = 10.58$ GeV. The beam asymmetry generates a Lorentz boost of $\beta\gamma = 0.28$ of the B mesons in the laboratory frame, which results in their average flight distance being 130 μm. The electron and positron beams are produced in the same manner as of KEKB. The two beams collide at the IP with a large crossing angle and a unique nano-beam scheme (explained in the following section), which is essential to achieve the intended luminosity. The final focus system had to be redesigned to accommodate this new collision approach. To meet the luminosity requirements, there are some other structural modifications made to the accelerator: the electron injection and positron target are modified, the damping ring, the radio-frequency system, the optics, the beam pipe and the vacuum system were upgraded [71].

The data taking program of the SuperKEKB collider is subdivided in three main phases: Phase I (2016), where a preliminary run was conducted to assess the beam backgrounds using a dedicated detector [72]; Phase II (2018), which refers to a period of collisions at low luminosity used to calibrate and optimize the accelerator, as well as the detector response and with a partial Vertex Detector installed,[2] and Phase III (2019), which corresponds to the physics data taking with the complete Belle II detector at nominal luminosity.[3] The dataset used in the analysis presented in this thesis was collected in phase III.

2.3.1 The nano-beam scheme

The idea behind the nano-beam scheme is to increase the luminosity by reducing the beam size at the IP. Generally, the luminosity is defined as

$$\mathcal{L} = \frac{\gamma_{\pm}}{2er_e}\left(1+\frac{\sigma_y^*}{\sigma_x^*}\right)\frac{I_{\pm}\xi_{y\pm}}{\beta_{y\pm}^*}\cdot\frac{R_L}{R_{\xi_y}}, \tag{2.5}$$

where γ is the relativistic Lorentz factor, e is the absolute value of the electron charge, r_e is the classical radius of electron, σ_x^* and σ_y^* are the widths of the bunch at IP on the transvere plane, I is the current of the beam, β_y^* is the vertical betatron function at the IP, ξ_y is the vertical beam-beam parameter, R_L and R_{ξ_y} are the reduction factors of luminosity and the vertical beam-beam parameter due to non-vanishing crossing angle.

The nano-beam scheme significantly reduces the vertical betatron function while minimising the longitudinal size of the beam overlap at IP, as shown in Fig. 2.17.

---

[2] One single ladder per each layer of PXD and SVD detectors (equivalent to roughly one octant of the full vertex detector) was installed to check the beam background rate and tune the accelerator parameters for high luminosity runs.

[3] The second layer of PXD is currently incomplete; it consists of four sensor modules mounted on two ladders covering only one sixth of the azimuthal angle.

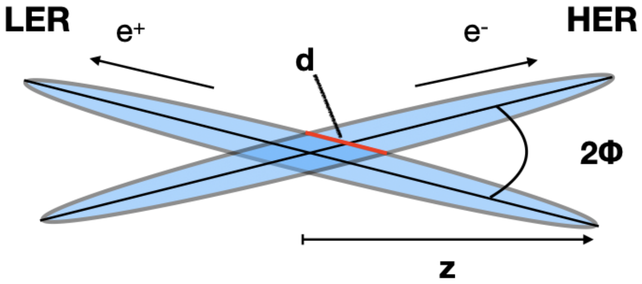

Figure 2.17: The geometry of the IP in the nano-beam scheme. The effective longitudinal overlap size d is highlighted in red.

The effective overlap region is $d \approx \sigma_y^*/\phi$, 2ϕ being the beam-crossing angle. As a result, the crossing angle at Belle II is 83 mrad, about four times that of the KEKB. In addition σ_y^* is reduced to the size of tens of nm to reach a beam size of 50 nm. To summarise, the betatron function β_y^* is lowered by a factor of 20 in comparison to KEKB using this technique, and since all other terms are have similar values for KEKB and SuperKEKB, the current of the beams need to be twice those of KEKB to provide the requisite luminosity.

2.4 BELLE II DETECTOR

The Belle II detector is a substantial upgrade of the Belle detector and sits at the interaction point of the SuperKEKB collider. It is a general-purpose experiment that can track charged particles efficiently even in the low momentum range (down to 50 MeV/c); it also includes a neutral-identification system based on efficient photon (γ) detection along with the multi-detector Particle Identification (PID) system. In addition, effective reconstruction of τ pairs and low multiplicity events is also possible at Belle II. To deal with the extreme background circumstances predicted at SuperKEKB, Belle II has high efficiency and trigger system.

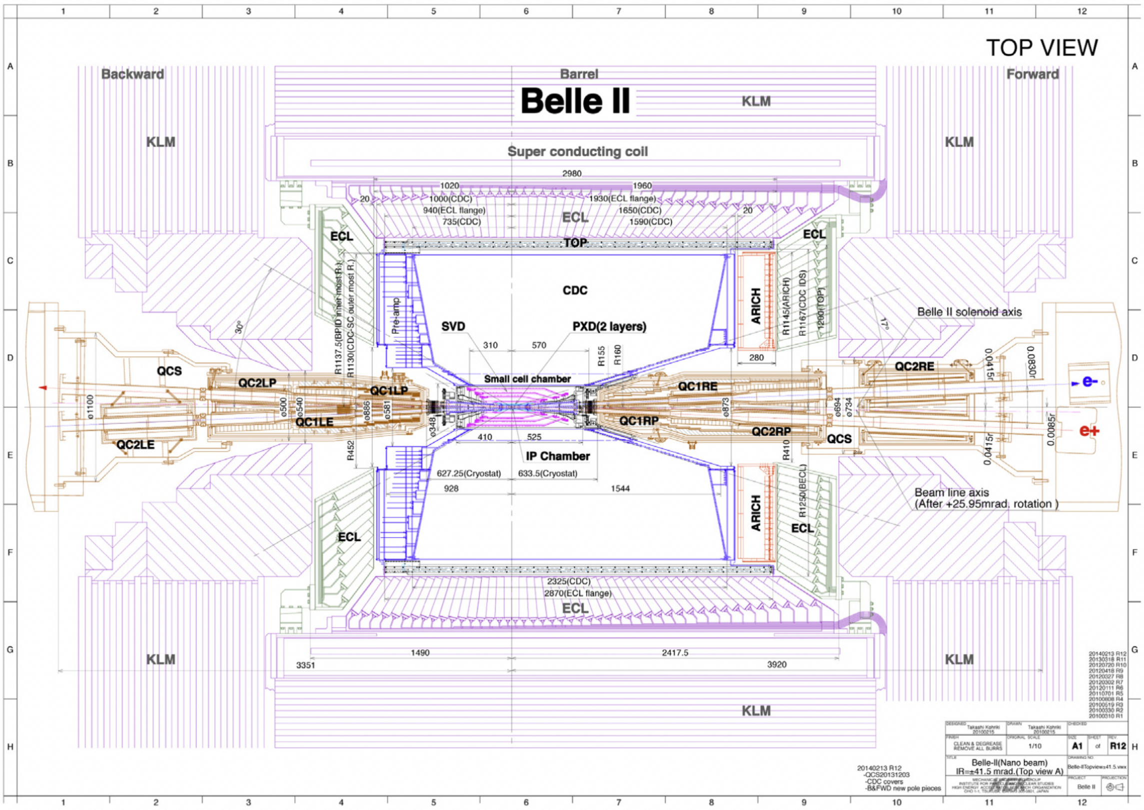

Figure 2.18: Structural view of the Belle II detector [73].

The Belle II detector geometry is similar to that of Belle. The detector has a roughly cylindrical symmetry around the symmetry axis of the solenoid, while it has a significant forward-backward asymmetry to improve the solid angle acceptance in the boost (forward) direction. The structure of the Belle II detector is shown in Fig. 2.18. The main changes in the subsystems with respect to the Belle detector are discussed in the following subsections.

2.4.1 Vertex Detector (VXD)

The VXD is the innermost subsystem of Belle II, that surrounds the beam pipe. It has total six layers: two layers of pixel detector (PXD) and four layers of silicon vertex detector (SVD). It is completely a new sub-detector in comparison to SVD of Belle.

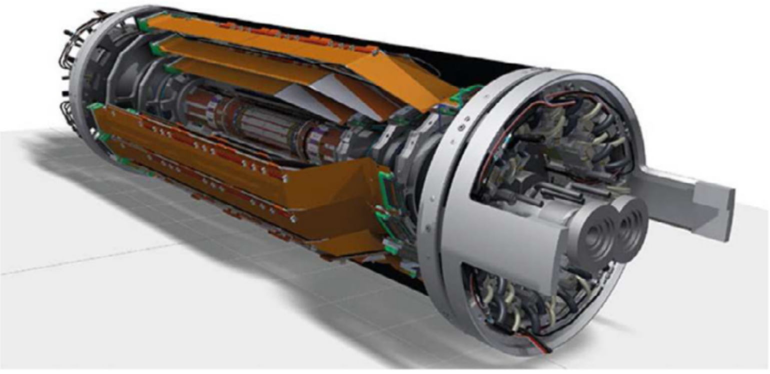

Figure 2.19: Belle II Vertex Detector: the beam pipe, PXD, SVD, and the shield material are assembled in a single structure [73].

The structure of the Belle II VXD is shown in Fig. 2.19.

The PXD is made up of two layers of pixelated sensors with depleted field effect transistor (DEPFET) technology [74]. It enables the use of ultra-thin pixels (50 μm) with readout components located beyond the acceptance regions, lowering the material budget thus reducing multiple scattering. The DEPFET sensors are arranged into rectangular modules, known as ladders, that make up the two levels of the PXD, with radii of 14 and 22 mm, respectively. The acceptance criteria of the detector establish the sensitivity lengths of each layer: a polar angular coverage of 17° to 155° is ensured. The PXD is made up of roughly eight million pixels that are arranged into arrays. Each DEPFET pixel is a cell, which is a monolithic structure with internal amplification, making it significantly smaller than other devices that require external amplification. The pixels have a typical size of 50×50 μm^2 and 50×75 μm^2 for the inner and outer layer, respectively. The readout time of each row of the sensors is 20 μs.

The SVD is made up of four layers of DSSDs with radii of 39 mm (layer 3), 80 mm (layer 4), 104 mm (layer 5) and 135 mm (layer 6). It has angular coverage of

$17^\circ < \theta < 150^\circ$. The double-sided sensors are positioned such that the *n* and *p* side strips are perpendicular and parallel to the beam direction, respectively, giving both x and y coordinates for the hits. The innermost SVD layer has small rectangular sensors of thickness 320 μm, whereas the other three layers have big rectangular (thickness of 320 μm) and slanted sensors (thickness of 300 μm) with a trapezoidal form that enhances acceptance and accuracy for forward boosted particles. The SVD readout electronics are based on the so-called APV25 chip [75], which was originally designed for the CMS experiment and provides fast readout with a modest integration time. In order to maintain a high signal-to-noise ratio, the signal line capacitance has to be as small as possible. Hence, the *Origami chip-on-sensor* concept was introduced in Belle II for the inner sensors [76], which has thinned APV25 readout ASICs in the active volume of the detector while the forward and backward sensors are readout by conventional APV25 chips located outside the acceptance.

To cope with the high luminosity environment at Belle II, the SVD radius coverage is enlarged to 135 mm, which allows the SVD to to track low-momentum particles that do not reach the central-drift-chamber (CDC), for example the pions from K_S^0 decays or slow pions from D^* decays.

2.4.2 Central Drift Chamber (CDC)

The CDC is the the primary tracking device of the Belle II detector. It is a large volume gas drift chamber with tiny drift cells. The CDC reconstructs charged particle trajectories to accurately estimate their momenta, and uses energy loss in the CDC volume to enable particle identification in the low-momentum region. It also provides reliable trigger information about charged particle events.

The CDC is based on its predecessor's design: the same structure is utilised, as well as the same material and gas combination. The most significant changes concern:

- the readout electronics, in order to accommodate higher trigger rates;
- the innermost cylinder radii must be greater to accommodate the larger SVD, while the outermost radius must account for the more compact barrel detector needed for PID, resulting in 160 mm and 1130 mm radii, respectively. The wiring arrangement are adjusted accordingly. The polar angular coverage is $17°$ to $150°$;

The CDC is made up of 56 layers that are grouped into nine super-layers. The squared cells range in length from 10 mm for the innermost super-layer to 18.2 mm for the outermost super-layer. A total of 14336 tungsten sensing wires with a diameter of 30 μm are inserted into the gas mixture of 50$\%$ helium and 50$\%$ ethane. Aluminum wires with a diameter of 126 μm are utilised to generate the required electric field gradient. Lastly, the CDC has a measured spatial resolution of approximately 100 μm, with a relative accuracy of about 12$\%$ on dE/dx measurements for particles with an incidence angle of 90°.

2.4.3 Particle identification system

There are two particle identification subsystems at Belle II: *Time-of-propagation* counter in the barrel region and *Aerogel Ring-Imaging Cherenkov* counter in the end-cap. Both sub-detectors use the Cherenkov effect to identify the charged particle passing the spectrometer, but the operating principles are different. Ring imaging Cherenkov detectors work by measuring the angle θ_C of photons produced by relativistic charged particles traversing a radiator material and obtaining the velocity (β) of the particle using the relation $\cos\theta_C = 1/n\beta$, where n represents the refractive index of the material. The particle mass is determined by combining the PID detector information with the momentum measured by the tracking devices and the energy loss information measured by the CDC.

Time-Of-Propagation counter (TOP)

The Time-Of-Propagation (TOP) counter estimates the propagation time of Cherenkov photons reflected internally in the quartz bar, as demonstrated in Fig. 2.20. The arrival time, when combined with the detected arriving position along with the x coordinate of the quartz bar as shown in Fig. 2.20, allows for the reconstruction of the Cherenkov angle θ_C, from which the particle velocity can be inferred and the likelihood for various mass assignment hypotheses can be calculated.

The TOP is made up of 16 modules that encircle the exterior wall of the CDC. Each module is a quartz radiator made up of two quartz bars cemented together and having a length of 2500 mm and transverse area of 4420 mm^2. A mirror at the front end of the quartz bar reflects backwards photons that are produced in the forward direction. Depending on the angle of reflection, photons propagating backwards are captured by various PMT channels. The chromatic dispersion of Cherenkov photons is compensated using a focusing system consisting of a slightly concave-shaped mirror: parallel rays are

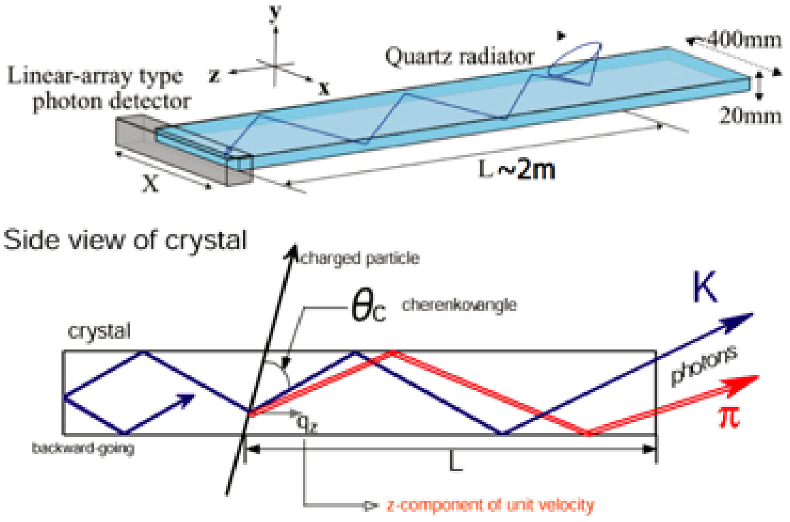

Figure 2.20: Conceptual representation of the time-of-propagation counter, which measures both the arriving time and position of the internally reflected Cherenkov photons [77].

focused onto the same pixel of a photo-sensor, where as, chromatically dispersed ones are detected by separate channels. A single-photon detection requires a time resolution of approximately 50 ps. The Multi-Channel Plate Photo Multipliers (MCP PMTs), two-stage amplification devices with a gain of 10^6 and an extremely rapid response, are used as photon detectors. The angular acceptance of TOP is $31^\circ < \theta < 128^\circ$.

Aerogel Ring-Imaging CHerenkov counter (ARICH)

The Aerogel Ring-Imaging Cherenkov counter (ARICH) provides particle identification in the front end-cap. When a charged particle travels through the volume of an aerogel radiator, Cherenkov photons are produced; a 20 cm expansion space separates the aerogel tile from the hybrid avalanche photon detector (HAPD) surface, allowing the Cherenkov photons to expand into rings; it is demonstrated in Fig. 2.21. The array of position sensitive photon detectors provides single photon detection in a high magnetic

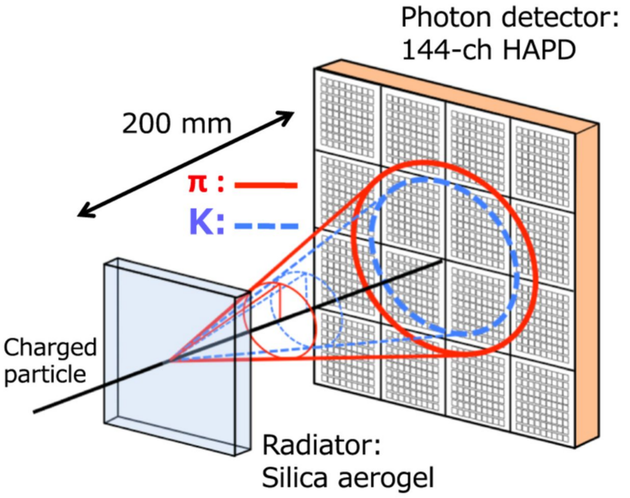

Figure 2.21: The principle of π/K identification for the ARICH counter. The solid-line and dotted-line cones illustrate the emitted Cherenkov light for a pion and a kaon, respectively [78].

field (1.5 T) with optimum resolution in two dimensions.

The number of detected photons N_γ and the single-photon resolution of the Cherenkov angle, σ_{θ_C}, are the two factors that influence the performance of the ARICH detector. N_γ rises with the radiator thickness; hence, the resolution per track improves as per the dependency, $\sigma_{\theta_C}/N_\gamma$. Two layers of aerogel with different refractive indexes ($n = 1.045,\ 1.055$) and 2 cm thickness are employed in the ARICH to maximise its performance: the two generated rings are overlapped over the detecting surface, providing N_γ equal to a two-fold radiator thickness.

The achieved resolution is $\sigma_{\theta_C} \approx 13$ mrad, which is optimal for charged tracks with velocity greater than 3.5 GeV/c, although it does not degrade much for tracks with lower momentum. The resolution of a single track is approximately $\sigma_{\theta_C} \approx 3$ mrad given $N_\gamma \approx 10$ per ring. The angular acceptance of ARICH is $14^\circ < \theta < 30^\circ$.

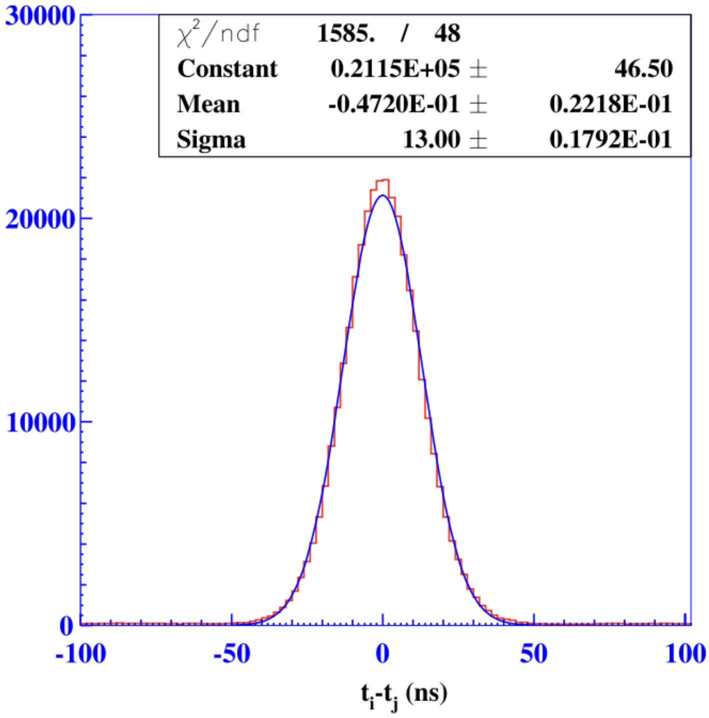

Figure 2.22: ECL timing distribution from the Belle II cosmic ray run [73].

2.4.4 Electromagnetic Calorimeter (ECL)

In Belle II, the ECL plays a number of key roles. First, it efficiently detects photons and provides their energy over a wide range, from 20 MeV to 4 GeV, and angle. Second, it detects electrons and helps with the K_L^0 detection. Third, it creates a photon trigger in both hardware and software. In addition, the ECL is used to monitor the luminosity of SuperKEKB, both online and offline.

The Belle II ECL utilises the same crystals as of Belle's calorimeter along with its configuration, but the readout electronics needed to be completely upgraded to handle the SuperKEKB's enhanced luminosity. The geometrical configuration is also same as of Belle; it is given in Table 2.2.

The energy resolution obtained with this calorimeter at Belle is discussed in Sec. 2.2.5.

A similar performance is also expected at Belle II in the absence of background. However, with the higher background levels anticipated at Belle II, the relatively long decay time of CsI(Tl) crystals (1 μs) would significantly enhance the overlapping of pulses from adjacent (background) events. The readout electronics have been changed to reduce the significant pile-up background [79]. The "Shaper-DSP board" reduces the shaping time from 1 μs to 0.5 μs and adds a pipelined readout with waveform sampling analysis, where the raw signal after amplification from each crystal is constantly digitised with a 2 MHz clock frequency. The ECL timing distribution from the Belle II cosmic ray run is demonstrated in Fig. 2.22.

2.4.5 K_{L}^{0}-muon detector (KLM)

The K_{L}^{0} and muon detector (KLM) consists of 4.7 cm thick iron plates and active material detectors and is located outside the superconducting solenoid. It is used for long-lived particle momentum measurements. The iron is required for the solenoid's magnetic flux return and has a material budget of 3.9 interaction lengths, which allows the K_{L}^{0} to shower in its volume hadronically. The KLM has an angular acceptance of $20^{\circ} < \theta < 155^{\circ}$. The Belle KLM system, based on glass-electrode resistive plate chambers, performed well during the Belle experiment's data taking period. In contrast to Belle, significant background rates are anticipated in certain parts of the KLM detection system at Belle II (both endcaps and the innermost layers in the barrel area) because of the neutrons generated mostly by the background processes in electromagnetic showers (e.g., radiative Bhabha scattering). Because of the large hit rate, the longer dead-time of RPCs increases the muon misidentification probability.

Scintillator strips with silicon photomultipliers (SiPM), which are tolerant to higher rates, are installed in the inner two layers and endcaps to avoid this problem.

The usage of scintillator strips with SiPMs provides the best time resolution, measured using a cosmic ray event as a trigger; the time dispersion difference yields $\sigma_t \approx 0.7$ ns. Because of the excellent timing performance, the KLM endcaps may be used as a time of flight detector for K^0_{L}. The K^0_{L}-reconstruction efficiency is observed to increase linearly with particle momentum in the barrel section, reaching a plateau of approximately 80% for momenta greater than 3 GeV/c.

2.4.6 Trigger

The trigger mechanism selects events of interest while rejecting the enormous background caused by intra-beam scattering and Bhabha scattering. The Belle II trigger is significantly enhanced over the Belle trigger, providing greater sensitivity and decreased systematic uncertainty for the low multiplicity final states. The major modifications are in the level-1 (L1) trigger and the processing pace of the high-level trigger (HLT). In the case of massive QED backgrounds, the Belle II trigger is capable of triggering on any neutral exotic physics signatures such as $e^+e^- \to \gamma +$ nothing or $e^+e^- \to \gamma A(\to \gamma\gamma)$, where A stands for an Axion-Like-Particle. It can also provide excellent efficiency, stability, and minimal systematics for 1-prong vs 1-prong $+\tau^+\tau^-$ events that offer significant input for $g-2$ results, such as $e^+e^- \to \pi^+\pi^-\gamma$.

The important features of the L1 trigger are:

- high efficiency for hadronic events as well as low multiplicity events;

- a maximum average trigger rate of 30 kHz;
- a fixed latency of about 5 μs;
- a timing precision of less than 10 ns;
- a minimum two-event separation of 200 ns; and
- a trigger configuration that is flexible and robust.

The goal of HLT is to decrease the L1 trigger's 30 kHz event rate to a maximum storable rate of 10 kHz. The HLT utilises all of the information from all sub-detectors except for PXD and conducts a rapid reconstruction; the events are fully reconstructed using the same software used for the offline analysis (except the PXD information). The trigger then applies the physics requirements to the reconstructed events and lowers the event rate to 10 kHz.

Following the HLT reduction, the tracks reconstructed in the fast reconstruction using the SVD and the CDC information are then extended to the PXD layers, where the region-of-interest (ROI) is assessed, and the pixels inside the specified areas are read. Finally, the exclusive events are constructed before the final storage by merging the rapid reconstruction events with the PXD data.

Table 2.3 summarizes the basic performance of Belle II in comparison to Belle [73].

Table 2.3: Summary of Belle and Belle II detector performances [73].

Measurement	Belle	Belle II
B vertex reconstruction	$\sigma_z = 61$ mm	$\sigma_z = 26$ mm
Tracking	$\sigma_{p_t}/p_t = 0.0019 p_t$ [GeV/c] $\oplus\ 0.0030/\beta$	$\sigma_{p_t}/p_t = 0.0011 p_t$ [GeV/c] $\oplus\ 0.0025/\beta$
K, π ID	Kaon efficiency $\epsilon_K \simeq 0.85$ with pion fake rate $\epsilon_\pi \simeq 0.10$ for $p = 2$ GeV/c	$\epsilon_K \simeq 0.9$ with $\epsilon_\pi \simeq 0.04$ for $p = 2$ GeV/c
Calorimetry	$\dfrac{\sigma_E}{E} = \dfrac{0.0066}{E} \oplus \dfrac{1.53}{E^{1/4}} \oplus 1.18(\%)$	$\dfrac{\sigma_E}{E} = 7.7\%$ at 0.1 GeV, 2.25% at 1 GeV
Muon ID	Muon efficiency $\epsilon_\mu \simeq 0.90$ with fake rate $\epsilon = 0.02$ for $p_t > 0.8$ GeV/c tracks	$\epsilon_\mu = 0.92 - 0.98$ with $\epsilon = 0.02 - 0.06$ for $p_t > 1$ GeV/c
L1 Trigger	500 Hz typical average, Efficiency for hadronic events $\epsilon_{\mathrm{hadron}} \simeq 1$	30 kHz max. average rate, $\epsilon_{\mathrm{hadron}} \simeq 1$
DAQ	∼5% dead time at 500 Hz L1 rate	<3% dead time at 30 kHz L1 rate

CHAPTER 3

Selection of $B^{\pm} \to D(K_S^0 h^- h^+)h^{\pm}$, $h = K, \pi$ events at Belle and Belle II

This chapter describes the reconstruction of $B^+ \to DK^+$ and $B^+ \to D\pi^+$ decays, where D decays to $K_S^0\pi^+\pi^-$ and $K_S^0K^+K^-$, for the model-independent BPGGSZ measurement of CKM angle ϕ_3 described in Chapter 1. This measurement requires simultaneous analysis of $B^+ \to DK^+$ and $B^+ \to D\pi^+$. The $B^+ \to DK^+$ sample is the signal mode of interest and $B^+ \to D\pi^+$ is used to calculate the F_i and F_{-i} fractions required for ϕ_3 extraction as given in Equation 1.34. The branching fraction of $B^+ \to D\pi^+$ decays is an order of magnitude higher than that of $B^+ \to DK^+$ decays [8], and hence serves as a very good calibration sample because of its identical topological structure to that of $B^+ \to DK^+$, if a common selection is applied. Also, the $K-\pi$ misidentified background in data can be directly extracted from the simultaneous analysis of these two decay channels. The event selections are slightly different for Belle and Belle II because of the non-identical sub-detector configurations of these two experiments, as explained in Chapter 2. The detailed description of these selections are described in this chapter.

The remainder of this chapter is structured as follows: the data samples used for this analysis are described in Sec. 3.1. The event selections in Belle and Belle II are summarized in Sec. 3.2 and Sec. 3.3, respectively. Section 3.4 describes the procedure followed to reject different background components. Section 3.5 explains the best-candidate selection and presents the signal efficiencies. Lastly, the data-MC comparison studies are described in Sec. 3.6.

3.1 DATA SAMPLE

The analysis uses e^+e^- collision data collected at a c.m. energy corresponding to the mass of the $\Upsilon(4S)$ resonance. The integrated luminosities of the samples collected by Belle and Belle II are 711 fb^{-1} and 128 fb^{-1}, respectively.

Simulation samples are used to optimise the selection criteria, estimate signal efficiencies, train multivariate discriminants, identify various sources of background and develop a model to fit data. The signal and $e^+e^- \to \Upsilon(4S) \to B\bar{B}$ simulation samples are generated using the EVTGEN software package [80]. The Belle simulation samples of continuum background events $e^+e^- \to q\bar{q}$, where $q = u, d, s, c$, are generated by PYTHIA [81]. The Belle II $e^+e^- \to q\bar{q}$ simulation sample is generated using the KKMC [82] generator interfaced with PYTHIA. The EVTGEN package also simulates the decay of short-lived particles. The Belle (Belle II) simulation samples use a GEANT3-based simulation package [83] (GEANT4 [84]) to model the detector response to the final-state particles. Final-state radiation effects are taken into account by including the PHOTOS model [85]. Belle simulation includes the effect of beam background by overlaying data taken that is unrelated to e^+e^- collisions (random triggers). Belle II simulation samples include the effect of simulated beam-induced background caused by the Touschek effect (scattering and loss of beam particles) and by beam-gas scattering, as well as luminosity-dependent backgrounds caused by Bhabha scattering and two-photon quantum electrodynamic processes [86]. Cross-sections of the physics processes, related to the analysis, used for the MC generation are given in

Table 3.1.

Table 3.1: Total production cross-section of various physics processes from collisions at $\sqrt{s} = 10.58$ GeV.

Physics process	Cross-section [nb]
$\Upsilon(4S)$	1.11
$u\bar{u}$	1.61
$d\bar{d}$	0.40
$s\bar{s}$	0.38
$c\bar{c}$	1.30

The Belle II analysis software framework (basf2) [87] is used for decay-chain reconstruction. The Belle II data are processed using this framework, whereas the tracks and clusters in the processed Belle data are converted to the basf2 format using the B2BII software package [88]. Hence, the reconstruction software is identical for both the data samples.

3.2 SELECTION APPLIED TO BELLE DATA

There are six streams of independent generic Monte Carlo (MC) simulation samples available within the Belle software framework, each stream has a luminosity corresponding to the full data set of Belle. The structure of these samples are equivalent to real data. Hence, these are used to estimate efficiency, train multivariate discriminant to suppress continuum background and validate the signal extraction procedure. Signal MC events are generated for the channel $B^+ \to D(K^0_S h^- h^+)h^+$ considering the final-state particles do not decay via a resonance and are distributed according to the allowed phase space. The decay is modeled using the PHSP model implemented from EvtGen package; the Gsim simulation tool, which is based on the Geant3 simulation package, models the detector response to the final-state particles. The final-state radiation (FSR) effects have been simulated by including the PHOTOS model. The decay chain is as follows:

$$e^+e^- \to \Upsilon(4S) \to B^+B^-;\ B^+ \to Dh^+;\ D \to K_S^0 h^- h^+, \tag{3.1}$$

where one B from $\Upsilon(4S)$ decays generically.

The selections of the tracks and kinematic variables are given in the following subsections.

3.2.1 Selection of tracks

Charged particle tracks are selected by requiring $|dr| < 0.2$ cm and $|dz| < 1$ cm, where dr and dz represent the distance of the closest approach to the interaction point (IP) in the plane transverse to the beam direction and in the beam direction, respectively. These requirements eliminate poorly-reconstructed tracks that do not come from the IP region. These tracks are then identified as either a kaon or pion using the information from some sub-detectors: CDC, TOF and ACC. The likelihood that the particle is either a pion or a kaon is constructed from ionization-energy-loss information in the tracking detectors and information from the dedicated PID detectors, as described in Chapter 2, and is given by

$$\mathcal{L}(K/\pi) = \frac{\mathcal{L}(K)}{\mathcal{L}(K) + \mathcal{L}(\pi)}, \tag{3.2}$$

where, $\mathcal{L}(K)$ and $\mathcal{L}(\pi)$ are the likelihood ratios for K and π, respectively. The $\mathcal{L}(K/\pi)$ distributions for π^+ and K^+ tracks in signal MC sample is shown in Fig. 3.1. A requirement of $\mathcal{L}(K/\pi) > 0.6$ is used to separate the kaons from pions coming directly

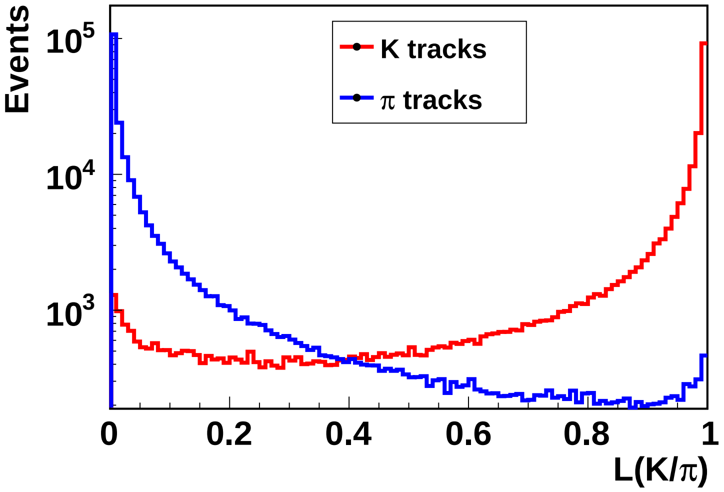

Figure 3.1: $\mathcal{L}(K/\pi)$ distribution for charged kaon and pion tracks in the signal MC sample.

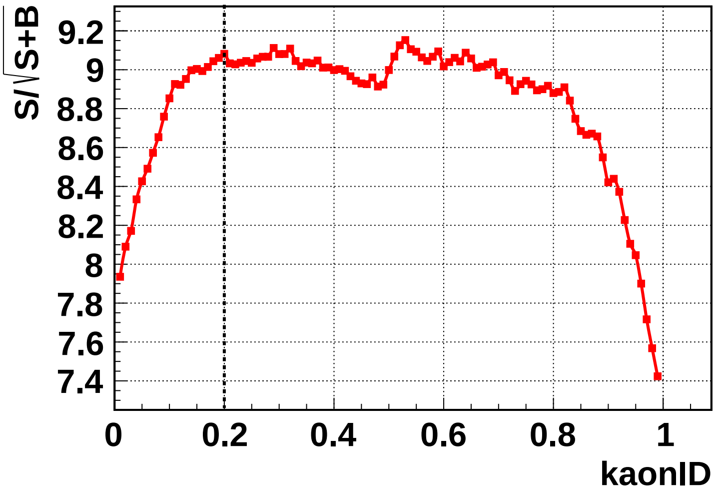

Figure 3.2: Distribution of $S/\sqrt{S+B}$ for PID selection optimization for kaon tracks coming from D in $B^+ \to D(K^0_S K^- K^+)K^+$ decays. The black dash line shows where the selection is applied.

from the $B^+ \to Dh^+$ decays. For $D \to K^0_{\rm S} K^- K^+$ final state, a rather loose criteria $\mathcal{L}(K/\pi) > 0.2$ has been applied for D daughters in $B^+ \to D(K^0_S K^- K^+)K^+$ decays, which is optimized using the metric $S/\sqrt{S+B}$, where S and B represent the total signal and background events present in the window $|\Delta E| < 0.05$ GeV, with a particular condition on $\mathcal{L}(K/\pi)$. The $S/\sqrt{S+B}$ optimization is shown in Fig. 3.2.

3.2.2 Selection of K_S^0 candidates

$K_{\rm S}^0$ candidates are reconstructed from pairs of oppositely charged pion tracks that originate from a common vertex and have dipion mass consistent with the nominal $K_{\rm S}^0$ mass [8]. No likelihood conditions are applied to these tracks. The dipion mass is required to be within the range (0.487, 0.508) GeV/c^2, which is nearly $\pm 3\sigma$ about the known $K_{\rm S}^0$ mass [8], where σ is the dipion mass resolution. To remove the backgrounds due to random combination of pion tracks, a neural network (NN) based selection is applied [89]. The following variables are used as inputs to the NN:

- $K_{\rm S}^0$ momentum in the lab frame;
- the distance between the two track helices along the z-axis;
- the flight length of the $K_{\rm S}^0$ candidate in the plane transverse to the beam direction;
- the azimuthal angle between the momentum vector and the vector between the IP and the decay vertex of the $K_{\rm S}^0$ candidate;
- the smaller (longer) distance of the closest approach between the extrapolated track of one of the pion candidates and the IP;
- the angle between the $K_{\rm S}^0$ momentum in the lab frame and pion momentum in the $K_{\rm S}^0$ rest frame;
- the number of CDC hits for each pion track; and
- presence of SVD hits for each pion track.

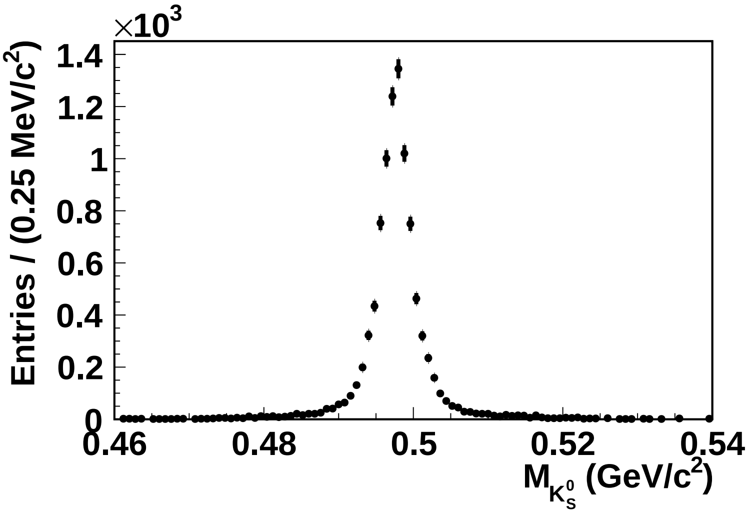

Figure 3.3: $M_{K^0_S}$ distribution after applying the selection criteria in $B^+ \to D(K^0_S\pi^-\pi^+)K^+$ generic MC sample.

The K^0_S selection efficiency in this analysis is 87%. The dipion invariant mass distribution after applying all these selections is given in Fig. 3.3. The estimate of the K^0_S candidate's four-momentum is improved by using a kinematic fit that constrains the reconstructed mass to the known mass and the decay products to originate from a common vertex point.

3.2.3 Selection of D candidates

The D mesons are reconstructed from a pair of oppositely charged pion (kaon) tracks and a K^0_S candidate. The invariant mass of the daughter particles $M_{K^0_S h^- h^+}$ is required to be in the range (1.85, 1.88) GeV/c^2, which corresponds to $\pm 3\sigma$ region around the D meson nominal mass [8], where σ is the $M_{K^0_S h^- h^+}$ resolution. To improve the resolution of the selected D candidates four-momentum, it is reconstructed using a kinematic fit that constraints the reconstructed mass to the known D mass [8] and the decay products to a common vertex point. The D invariant mass distributions of $K^0_S\pi^-\pi^+$

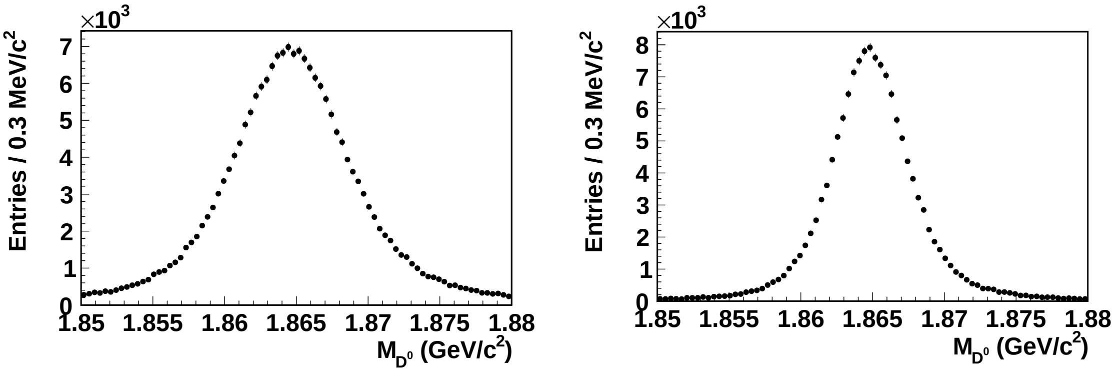

Figure 3.4: M_{D^0} distribution after applying the selection criteria in $B^+ \to D(K^0_S\pi^-\pi^+)K^+$ signal MC sample (left) and $B^+ \to D(K^0_S K^- K^+)K^+$ signal MC sample (right).

and $K^0_S K^- K^+$ final states in signal MC sample are shown in Fig. 3.4. The resolution of $M_{K^0_S K^- K^+}$ is better as compared to $M_{K^0_S\pi^-\pi^+}$ because of the comparatively lower momentum of the kaon tracks in $D \to K^0_S K^- K^+$ decays. The typical momentum range of these tracks are between $0.5 - 2$ GeV/c. The momentum resolution in this range is better as compared to very high or low momentum tracks, leading to better resolution, as for the high momentum tracks the curvature is less and for the low momentum tracks there is a high probability of multiple scattering.

3.2.4 Selection of B candidates

A B meson candidate is reconstructed by combining a D meson candidate with a charged kaon or pion track. The kinematic variables used to discriminate B decays from combinatorial or partially reconstructed background are the beam-constrained mass

$$M_{\rm bc} = \sqrt{E^2_{\rm beam} - (\sum_i^{N_{\rm daughter}} \overrightarrow{p_i})^2}, \tag{3.3}$$

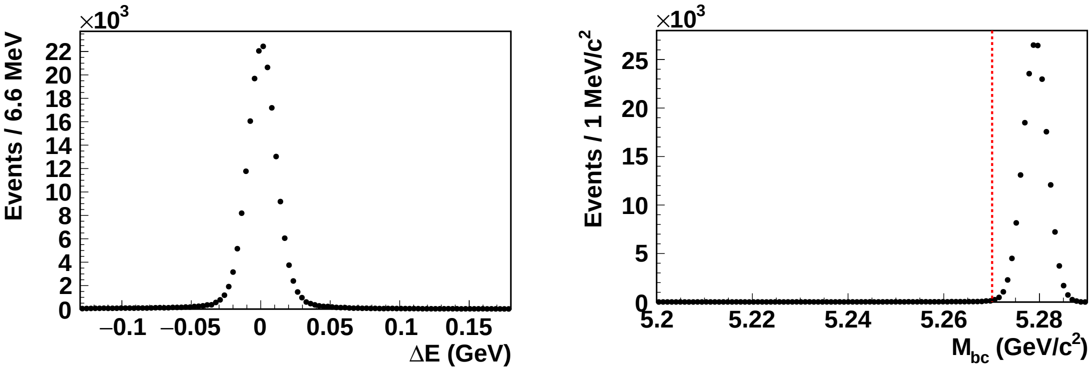

Figure 3.5: ΔE (left) and $M_{\rm bc}$ (right) distributions in $B^+ \to D(K^0_S\pi^-\pi^+)K^+$ signal MC sample in Belle. The red dotted line shows where the selection is applied.

and the beam energy difference

$$\Delta E = \sum_{i}^{N_{\rm daughter}} E_i - E_{\rm beam}, \tag{3.4}$$

where $E_{\rm beam}$ is the beam energy in the c.m. frame and E_i and $\overrightarrow{p_i}$ are the energy and momenta of the $N_{\rm daughter}$ particles in the c.m. frame. For correctly reconstructed signal the value of $M_{\rm bc}$ peaks at the nominal B meson mass [8], and ΔE at zero. The candidates that satisfy the conditions, $-0.13 < \Delta E < 0.18$ GeV and $M_{\rm bc} > 5.27$ GeV/c^2, are chosen. The sideband regions of ΔE are included in the selection as it is one of the signal extraction variables. These variable distributions in signal and generic background MC events are shown in Figs. 3.5 and 3.6. The ΔE selection is asymmetric to avoid partially reconstructed D^* mesons coming from the $B^\pm \to D^{(*)}K^{(*)\pm}$ decays in the lower sideband of ΔE, which requires a non-trivial description in the signal extraction fit. A vertex fit is performed to constrain the B daughters to a common vertex.

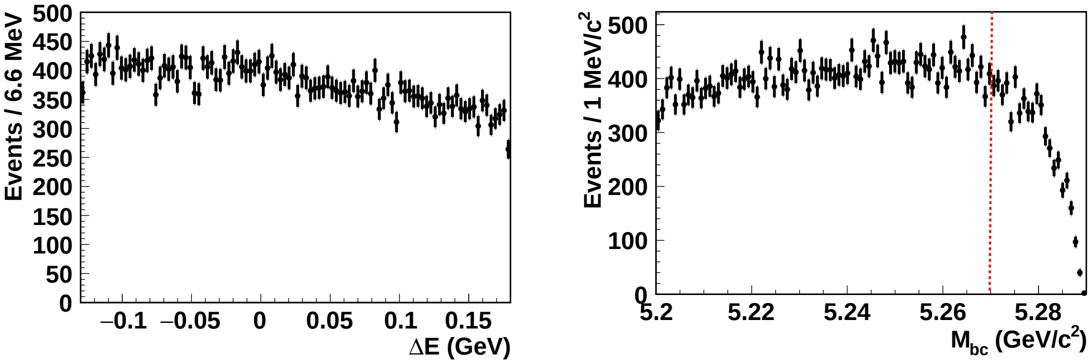

Figure 3.6: ΔE (left) and $M_{\rm bc}$ (right) distributions in $B^+ \to D(K^0_{\rm S}\pi^-\pi^+)K^+$ generic background MC sample in Belle. The red dotted line shows where the selection is applied.

3.3 SELECTION APPLIED TO BELLE II DATA

In Belle II, the MC samples, both signal and generic, are produced in official MC production campaigns. These production campaigns are based on the latest software version, detector geometry and beam-background conditions. The samples of so-called MC14 campaign is used for this analysis. The luminosity of the generic MC used, to model the background shapes and to estimate the signal yields, in our analysis is 500 fb^{-1}. The size of the signal MC sample used (generated with `PHSP` model), to model the signal shape and calculate signal efficiencies, is two million. The signal MC samples generated with both resonant (`D_DALITZ`) and non-resonant (`PHSP`) models are studied. In `PHSP` model, the events are distributed uniformly over the D phase-space whereas in `D_DALITZ` the events are distributed according to different resonances. For example, in the case of $K^0_{\rm S}\pi^+\pi^-$ final state, the resonances are $K^{*0}(\to K^0_{\rm S}\pi^-)\pi^+$ and $K^0_{\rm S}\rho^0(\to \pi^-\pi^+)$, and for $K^0_{\rm S}K^+K^-$ final states, the resonances are $\phi^0(\to K^+K^-)K^0_{\rm S}$ and $a^0(\to K^+K^-)K^0_{\rm S}$. Both of these models led to identical conclusions about the acceptance over the Dalitz plot and resolution.

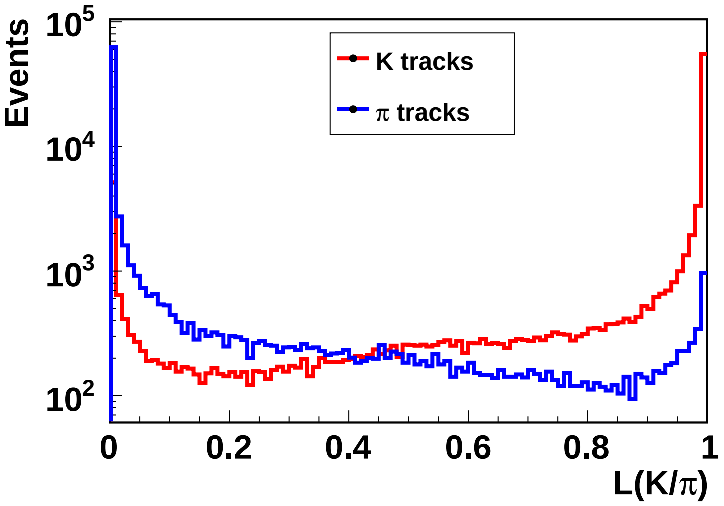

Figure 3.7: $\mathcal{L}(K/\pi)$ distribution for charged kaon and pion tracks in signal MC sample (Belle II).

Most of the event selection criteria are identical to those described in Sec. 3.2. There is an additional selection applied for the tracks, which is described in Sec. 3.3.1. The K_S^0 selection is also different to that of reported in Sec. 3.2.2, and it is explained in Sec. 3.3.2.

3.3.1 Selection of tracks

The impact parameter selections, $|dr|$ and $|dz|$, and the likelihood ratio criteria ($\mathcal{L}(K/\pi)$), to identify whether a charged track is kaon or pion, is analogous to the Belle selections. Here, the likelihood ratio is constructed from dedicated Belle II PID sub-detectors, as specified in Chapter 2. The $\mathcal{L}(K/\pi)$ distributions in Belle II signal MC sample is shown in Fig. 3.7. There is an additional selection $\cos\theta > -0.6$, where θ is the polar angle in lab frame, for the prompt track (the π or K tracks directly coming from the B meson decay) is applied. This criteria removes the backward tracks (outside the PID sub-detectors: TOP or ARICH acceptance), which helps in reducing the $K-\pi$ misidentification rate [90]. A comparison of the $\cos\theta$ distributions for Belle and Belle II

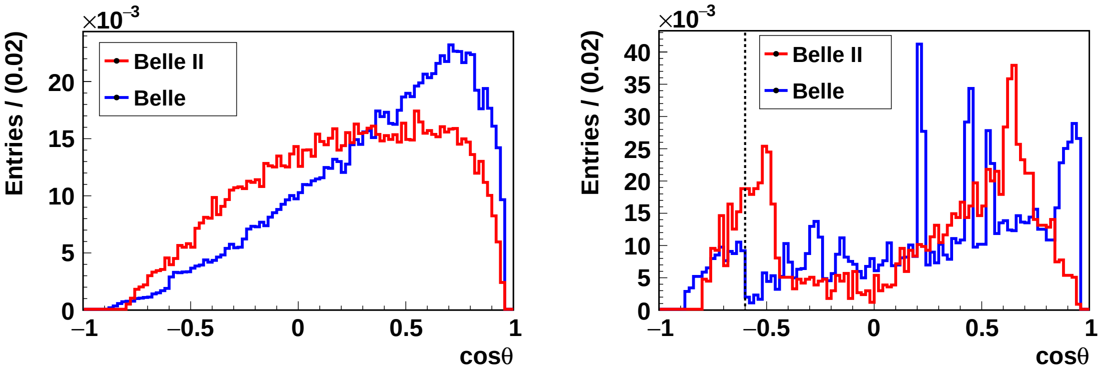

Figure 3.8: Comparison of $\cos\theta$ distribution for Belle and Belle II signal MC sample for $\mathcal{L}(K/\pi) > 0.6$ for true signal (left) and fake-pion (right) candidates. The black dash line shows where the selection is applied.

data is shown in Fig. 3.8. The misidentification rate is clearly high in the case of Belle II, which motivates this selection only for Belle II analysis.

3.3.2 K_S^0 selection

A Fast Boosted Decision Tree (FBDT), from multivariate analysis package embedded in the `BASF2` framework, based K_S^0 selection was developed to improve the K_S^0 signal efficiency and purity at Belle II. The motivation comes from the NN based K_S^0 selection implemented for Belle sample, described in Sec. 3.2.2.

The K_S^0 candidates are reconstructed from a pair of oppositely charged pion tracks that originate from a common vertex. No particle identification criteria are applied to these tracks. A pre-selection has been applied to reject the poorly reconstructed candidates: mass difference between the dipion invariant mass and nominal K_S^0 mass should be less than 20 MeV. The following variables are taken as inputs to the BDT training:

- $d\phi$, which is the azimuthal angle between the momentum vector and the vector between the IP and the decay vertex of the K_S^0 candidate;

- dr_{min}, which is the shortest distance between IP and one of the pion helix;
- dr_{max}, which is the longest distance between IP and the other pion;
- flight length of K^0_{S} candidate in the $x-y$ plane; and
- M_{pull}, which is the deviation of the measured mass from the nominal K^0_{S} mass divided by error in K^0_{S} mass.

The distributions of these variables are shown in Fig. 3.9. Generic MC is used as a training sample to take into account the full range of K^0_{S} momentum. The performance of this K^0_{S} selection is verified by applying the weight from the training to an independent sample, and the FBDT probability output of this independent sample is shown in Fig. 3.10; the separation between the signal and background candidates is very good. The receiver operating characteristic (ROC) curve is plotted by obtaining the number of signal and background events while varying the criteria on the FBDT output. The area of the ROC curve determines the amount of improvement in terms of rejecting more background while retaining most of the signal. The figure-of-merit (FoM) curve is also plotted by calculating $S/\sqrt{S+B}$ for different selections on FBDT output, where S is the number of signal events and B is the number of background events in the sample after the requirement, respectively, in the range $M_{\pi^+\pi^-} \in (0.487, 0.508)$ GeV/c^2. The maximum value of $S/\sqrt{S+B}$ is obtained with a criterion of greater than 0.95. Hence, the BDT output is required to be greater than 0.95 to select the K^0_{S} candidates, which has 91% signal efficiency with 97% background rejection. Figure 3.11 shows the ROC curve and FoM curves. The dipion invariant mass is selected in the range $(0.487 - 0.508)$ GeV/c^2, which is 3σ from the K^0_{S} nominal mass, where σ is the K^0_{S} in

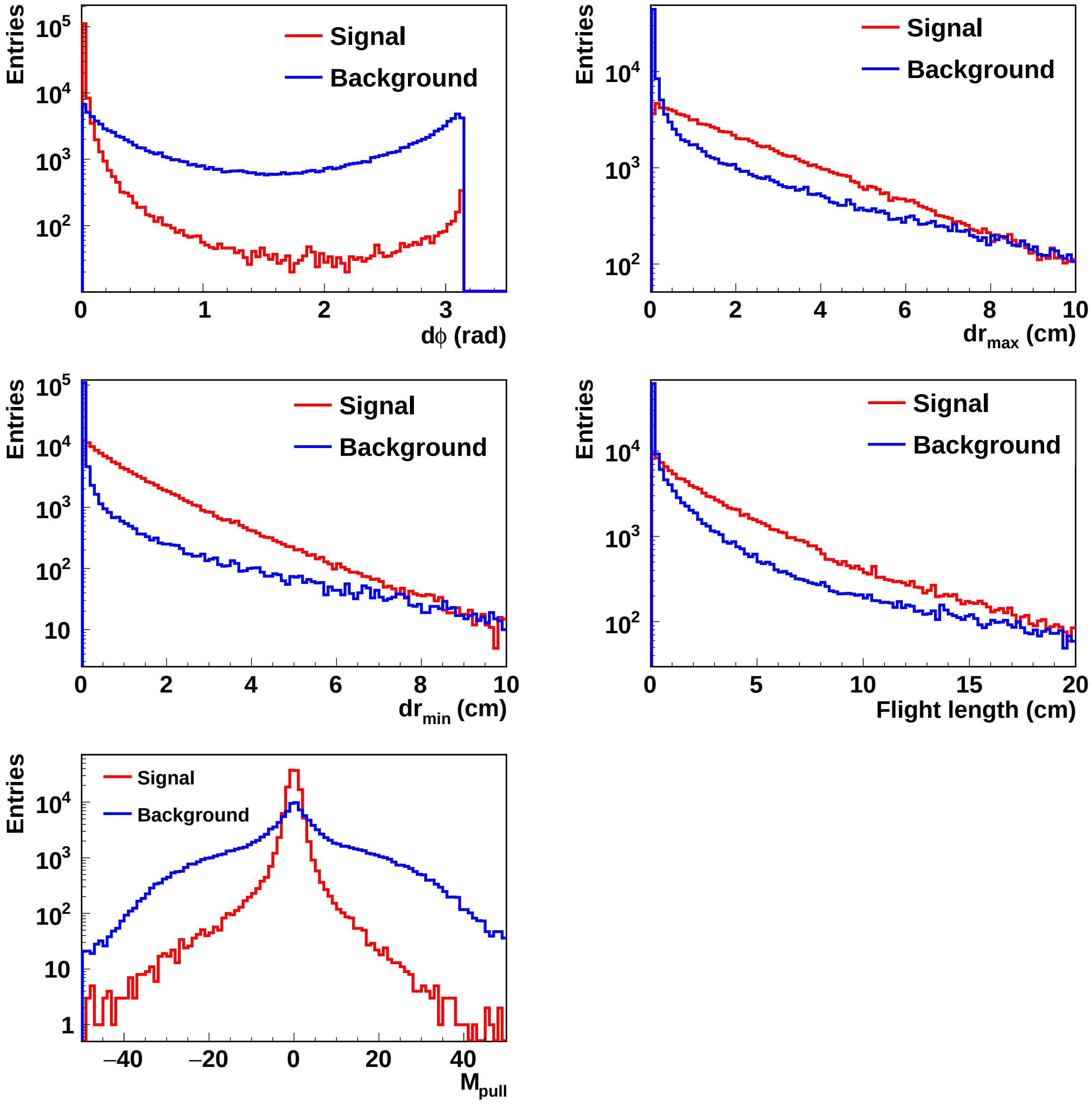

Figure 3.9: Distributions of $d\phi$ (top left), dr_{max} (top right), dr_{min} (middle left), flight length (middle right) and $M_{\rm pull}$ (bottom left) in generic MC sample (Belle II). The red and blue histograms represent the true K_S^0 candidates and combinatorial background candidates, respectively.

invariant mass resolution. The invariant mass distribution in the signal MC sample is shown in Fig. 3.12.

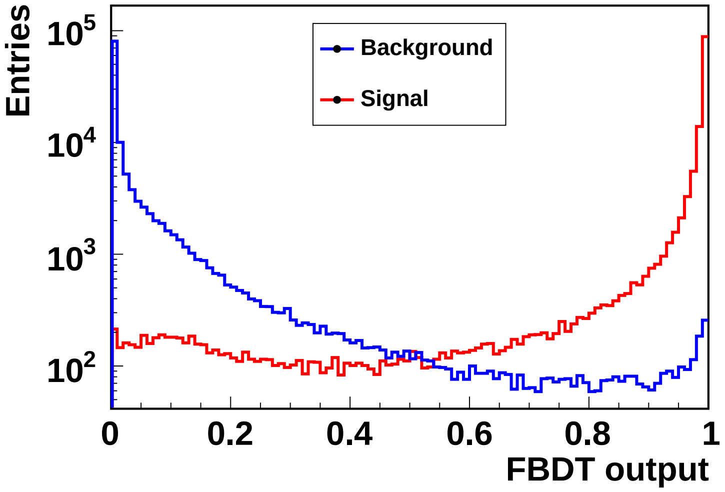

Figure 3.10: FBDT output of K_S^0 selection from an independent sample.

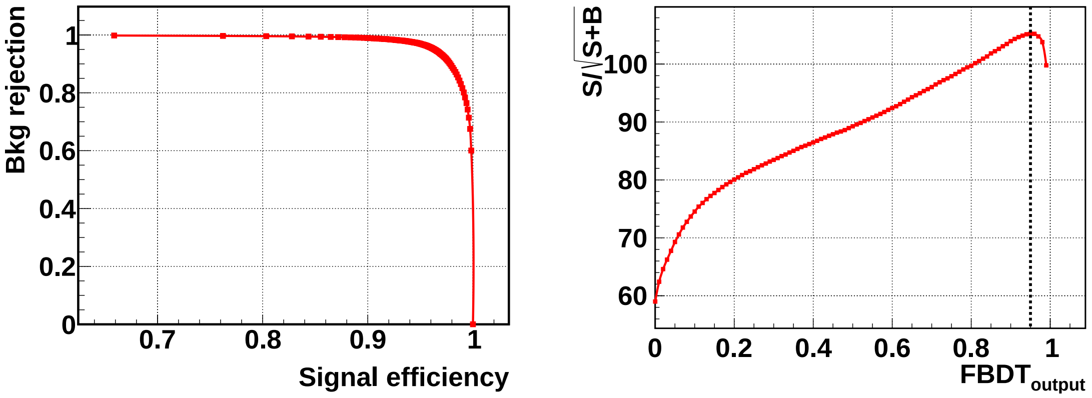

Figure 3.11: ROC curve (left) indicating the signal efficiency *vs.* background rejection of the FBDT output and the $S/\sqrt{S+B}$ distribution (right) with different selection requirements on FBDT output. The black dash line shows where the selection is applied.

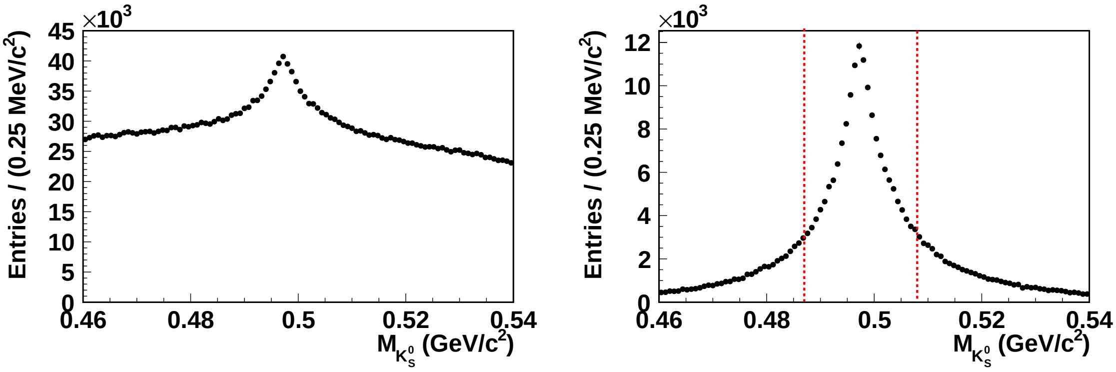

Figure 3.12: $M_{K_S^0}$ distribution before (left) and after (right) applying the FBDT K_S^0 selection criteria in generic MC sample (Belle II).

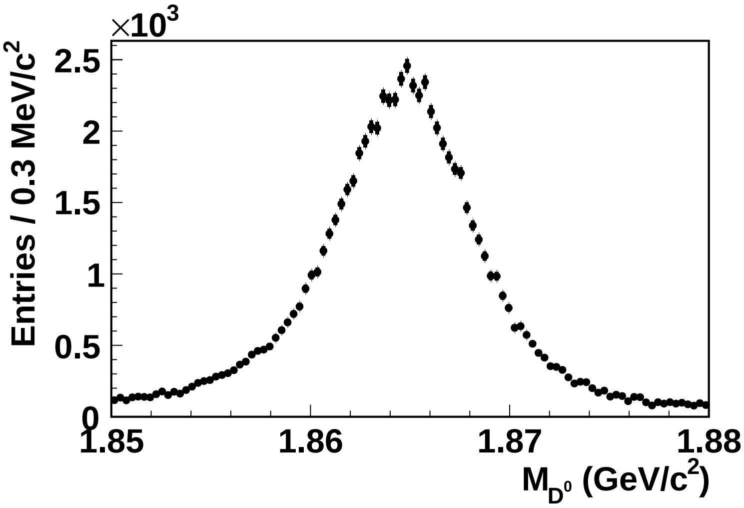

Figure 3.13: M_{D^0} distribution after applying the selection criteria in $B^+ \to D(K^0_S\pi^-\pi^+)K^+$ signal MC sample (Belle II).

3.3.3 Selection of D and B candidates

The D and B meson reconstructions are identical to those described in Secs. 3.2.3 and 3.2.4, respectively. The D meson invariant mass distribution in Belle II signal MC sample is shown in Fig. 3.13, and the ΔE distributions in signal and generic background MC sample is shown in Fig. 3.14. A one-dimensional maximum likelihood fit is performed to ΔE variable to estimate the resolution in both Belle and Belle II signal MC sample; the model used is a sum of a Gaussian and an asymmetric Gaussian function. The clear and detail definition of these functions are provided later in Chapter 4. The fit projections are shown in Fig. 3.15. The resolution better in Belle II MC as compared to Belle because of the improved vertexing capability of Belle II, as described in Chapter 2.

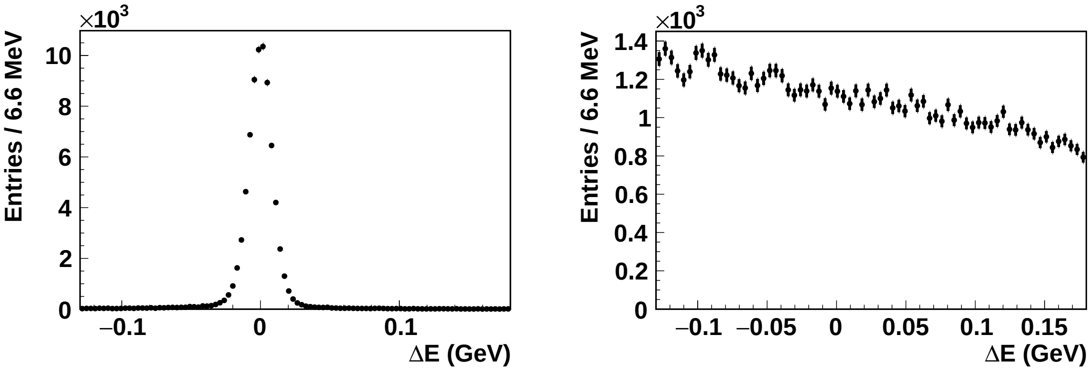

Figure 3.14: ΔE distributions in $B^+ \to D(K^0_S\pi^-\pi^+)K^+$ signal (left) and generic background (right) MC sample in Belle II.

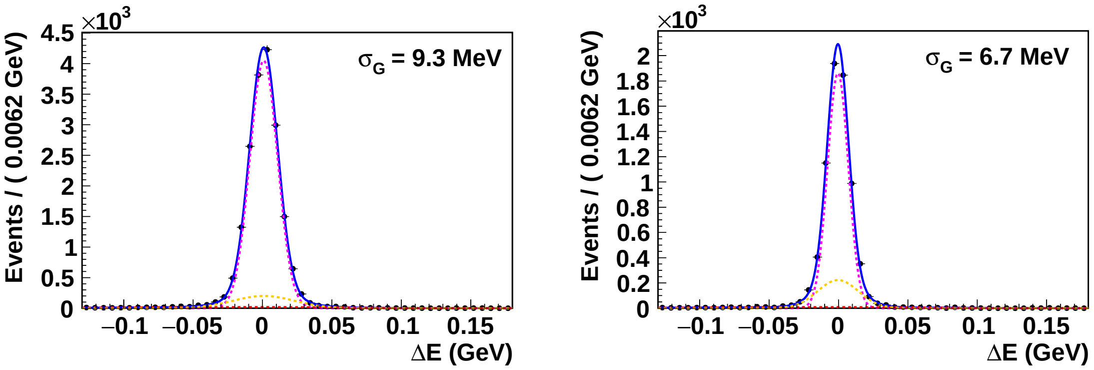

Figure 3.15: ΔE distributions in $B^+ \to D(K^0_S\pi^-\pi^+)K^+$ signal MC sample for Belle (left) and Belle II (right). Black points with error bar are signal MC sample and blue soild curve represent the total fit. σ_G is the resolution of core Gaussian function shown by the magenta dotted curve. The asymmetric Gaussian is shown by orange dotted curve.

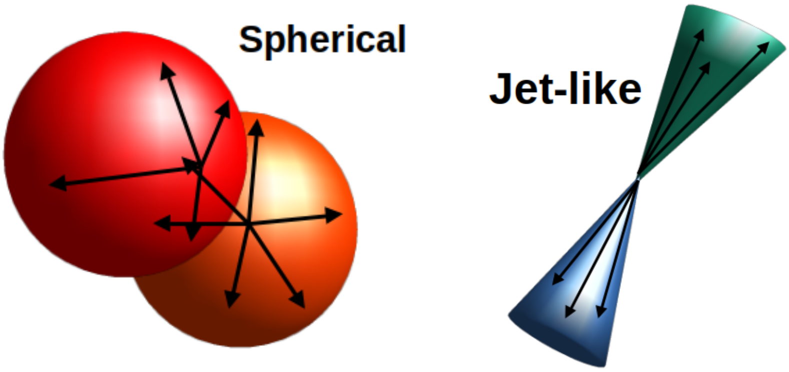

Figure 3.16: Event topology of $e^+e^- \to \Upsilon(4S) \to B\overline{B}$ (left) and $e^+e^- \to q\overline{q}$ (right) events.

3.4 CONTINUUM BACKGROUND SUPPRESSION

The cross section of $e^+e^- \to q\overline{q}$ continuum events is almost three times larger than that of $e^+e^- \to B\overline{B}$. Hence, these events are usually the dominant background for any B meson decay. The topological differences between these two processes is exploited to suppress this background. The decay products coming from $e^+e^- \to \Upsilon(4S) \to B\overline{B}$ are distributed uniformly over the 4π solid angle as the B mesons do not have significant momentum in the c.m. frame, whereas, the events from $e^+e^- \to q\overline{q}$ are highly boosted and have relatively larger momenta because of their small masses, as they are produced back-to-back this results in a jet-like structure, as shown in Fig. 3.16. Eight topological variables, based on angular configuration, displaced vertices and information associated to flavor of the other B meson, are fed as inputs to the FBDT to reject the continuum background. At first, the training was performed with many input variables, later, the lesser discriminating variables were removed those have negligible impact on the FBDT performance.

3.4.1 Variables used to suppress continuum

The following variables are given as inputs to the FBDT.

- **KSFW moments**: The Fox-Wolfram moments [91] are defined by

  $$H_l = \sum_{i,j} |p_i||p_j| P_l \left(\cos\theta_{ij}\right), \tag{3.5}$$

  where p_i and p_j are the momenta of reconstructed particle in an event, P_l is the Legendre Polynomial of order l and $\cos\theta_{ij}$ is the angle between momenta of particles i and j. These moments are used to characterize the shape of the event. It is observed that the discrimination between continuum and $B\bar{B}$ can be improved if the reconstructed tracks are classified according to whether they belong to the "signal" B meson and the remainder belong to the "opposite" (tagging side) B meson [92]. Thus, the modified Super Fox-Wolfram sub-moments are defined separately for "signal-opposite" and "opposite-opposite" combinations as

  $$H_l^{\mathrm{so}} = \sum_{i,j} |p_i||p_j| P_l \left(\cos\theta_{ij}\right), \tag{3.6}$$

  $$H_l^{\mathrm{oo}} = \sum_{j,k} |p_j||p_k| P_l \left(\cos\theta_{jk}\right), \tag{3.7}$$

  where i runs over all signal particles, and j and k run over all opposite particles. The moments H_0^{oo}, H_{02}^{so} and H_{12}^{so} have been used to attain better discriminating power as compared to other available moments. The distribution of these moments are shown in Fig. 3.17.

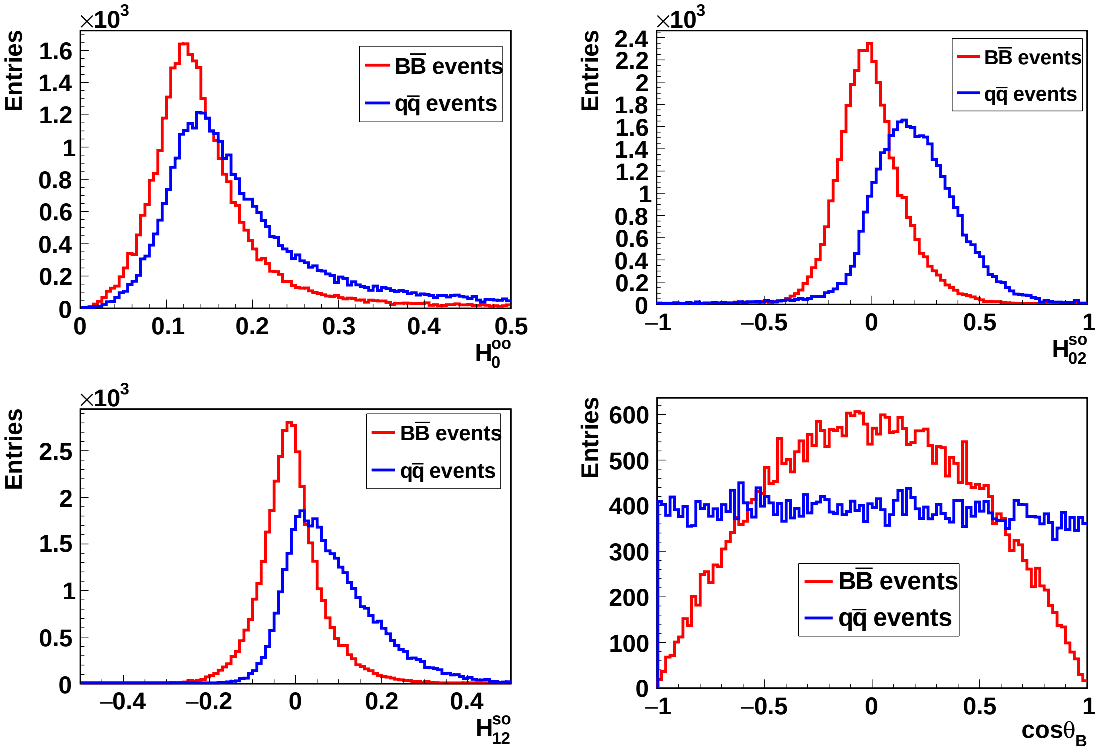

Figure 3.17: Distributions of H_0^{oo} (top left), H_{02}^{so} (top right), H_{12}^{so} (bottom left) and $\cos\theta_B$ (bottom right) in MC sample (Belle). The red and blue histograms represent the simulated $B\bar{B}$ and $q\bar{q}$ events, respectively.

- ***B* meson direction**: The polar angle θ_B in the center-of-mass frame serves as an independent discriminant variable. The decay of the spin-1 parent particle $\Upsilon(4S)$ to the two spin-0 B mesons has a $1 - \cos^2\theta_B$ angular distribution with respect to the beam axis to conserve the angular momentum, but the spin-$\frac{1}{2}$ $q\bar{q}$ and the resultant jets have uniform distribution in $\cos\theta_B$. Hence, the variable $\cos\theta_B$ allows one to distinguish between signal B decays and the continuum background by using the polar angle between the reconstructed momentum of the B candidates (computed in the $\Upsilon(4S)$ reference frame) and the beam axis. The distribution of this variable is shown in Fig. 3.17.

- **Thrust**: The thrust axis $\vec{T}$ is defined as the unit vector along which the total projection of a collection of N momenta p_i is maximum, p_i being the momentum of i^{th} particle. The magnitude of the thrust axis is defined as:

$$T = \frac{\sum_i^N |\vec{T}.\vec{p_i}|}{\sum_i^N |\vec{p_i}|} \tag{3.8}$$

Both, the signal B and rest-of-event (ROE) thrusts, provide signal and continuum discrimination. The magnitude of signal B thrust T_{signal} is used as input; the distribution is shown in Fig. 3.18.

- **Thrust angle**: The angle between the thrust axis of the momenta of the B candidate decay particles and the thrust axis of the ROE is a valuable discriminating variable. Both B mesons are almost at rest in $\Upsilon(4S)$ rest frame for a $B\bar{B}$ like event, thus their decay particles are isotropically dispersed and are randomly distributed following a uniform distribution of $|\cos\theta_B^{\text{ROE}}|$ in the range $(0, 1)$. In $q\bar{q}$ events, however, particle momenta follow the direction of the jets in the event, resulting an extremely collimated thrusts, with the $|\cos\theta_B^{\text{ROE}}|$ distribution largely peaking towards higher value (here it is one). The distribution of this variable is shown in Fig. 3.18.

- **Vertex position**: Because of the boost, the B mesons have comparably longer lifetime of B mesons as compared to lighter mesons, thus resulting a larger average flight distance. The quantity $\Delta z = z_{B_{\text{sig}}} - z_{B_{\text{tag}}}$, difference of decay vertex longitudinal components between the signal B and ROE vertex, which is wider for $B\bar{B}$ events as compared to continuum events, is utilized in the FBDT classifier. The variable distribution is shown in Fig. 3.18.

- **Flavour tagging**: The flavour tagger (FT) uses an algorithm where many

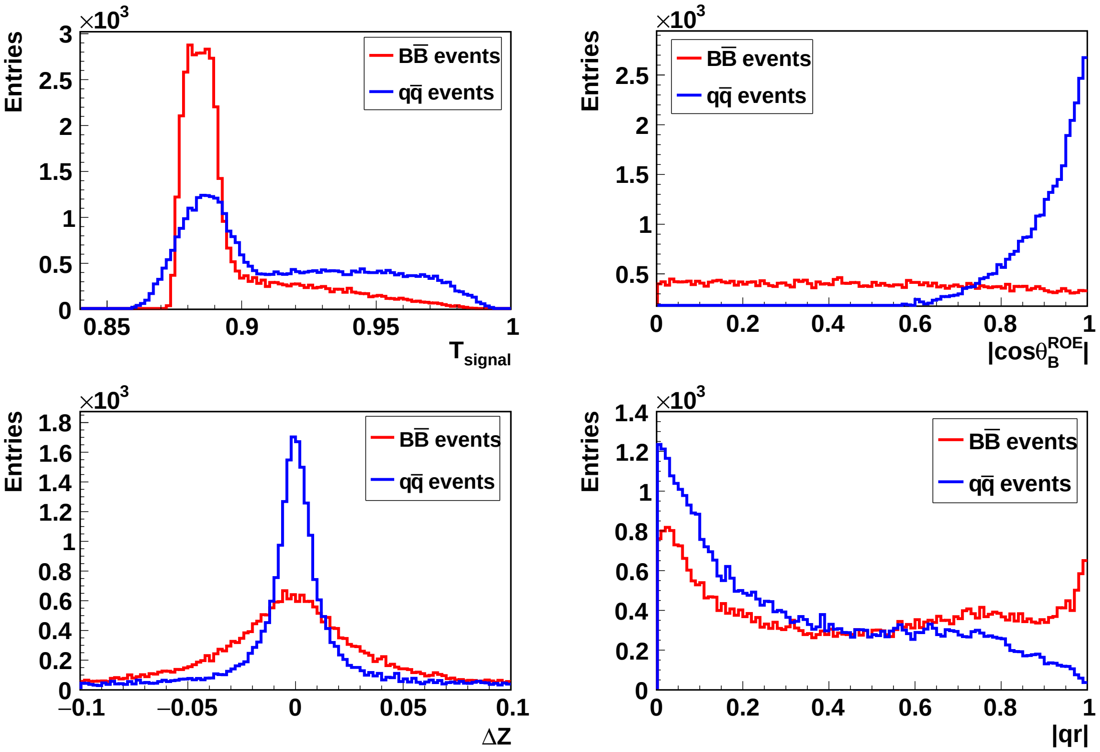

Figure 3.18: Distributions of $|B_{\text{thrust}}|$ (top left), $|\cos\theta_B^{\text{ROE}}|$ (top right), ΔZ (bottom left) and $|qr|$ (bottom right) in MC sample (Belle). The red and blue histograms represent the $B\bar{B}$ and $q\bar{q}$ events, respectively.

multivariate classifiers are combined into a single fast boosted decision tree using the information about charge of leptons and kaons not associated with the signal B decay. It identifies the flavor q of the signal B candidates with an effective tagging efficiency expressed as $\sum \varepsilon_i \times (1 - 2w_i)^2$, where ε_i represents the efficiency of the i^{th} classifier and w_i is the flavor mis-tag fraction [93]. The output of this algorithm is denoted by $|q.r|$, where r is the quality factor, which ranges from zero (for an event where the B-tag flavor cannot be determined accurately) to one (for known B-tag events), and the flavour q is given by $+1$ (if the signal and tagging B mesons seem to have the same flavor) or -1 otherwise. The $|q.r|$ distribution for signal and continuum events are shown in Fig. 3.18.

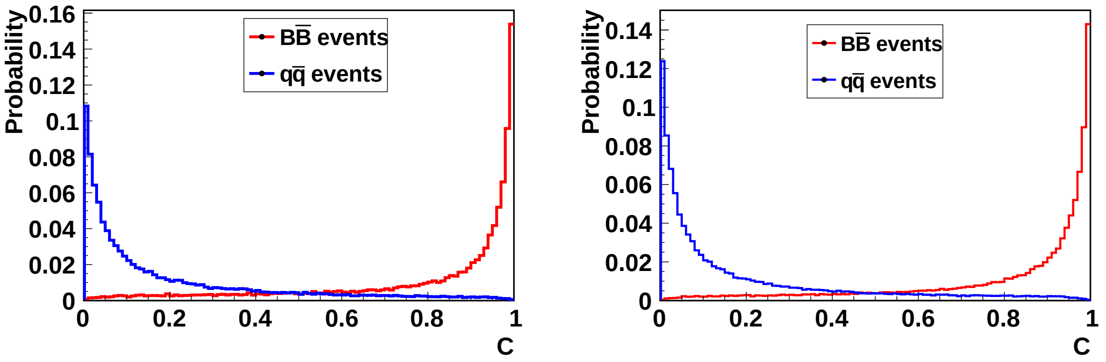

Figure 3.19: FBDT output (C) from independent MC sample: Belle (left) and Belle II (right). The red and blue lines represent $B\bar{B}$ and $q\bar{q}$ events, respectively.

The variable distributions are similar in Belle II. The FBDT is trained using 100,000 events of signal and continuum MC samples. Independent MC samples are used to assess its performance and ensure that it is not overtrained, i.e., the FBDT is not picking up on statistical fluctuations within the training sample. As seen in Fig. 3.19, the FBDT output (C) peaks at 0 for continuum and at 1 for $B\bar{B}$ events. The ROC curve, shown in Fig. 3.20, depicts the FBDT's signal efficiency $vs.$ background rejection performance. The FBDT rejects 91% (92%) of background at 20% signal loss for Belle (Belle II). The selection on the $C > 0.15(0.2)$ is applied for Belle (Belle II), which rejects 61% (68%) of the background at 4% signal loss.

3.4.2 Background from D^* events

There might be combinatorial background events arising from $D^{*\pm} \to D\pi^{\pm}$, $D \to K^0_S h^+ h^-$ decays originating in $c\bar{c}$ events. The ΔM variable, the mass difference between D^* and D candidates, can be used to veto these background events. The possible D^* candidates are reconstructed from a signal side D and a π from ROE. The ΔM value that is closest to the nominal value is chosen to reject the multiple candidates.

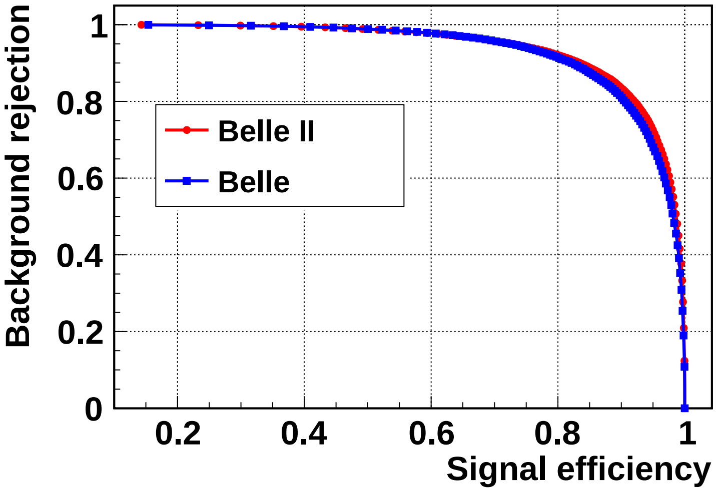

Figure 3.20: The ROC comparison for Belle (blue line) and Belle II (red line). The performance is slightly better at Belle II.

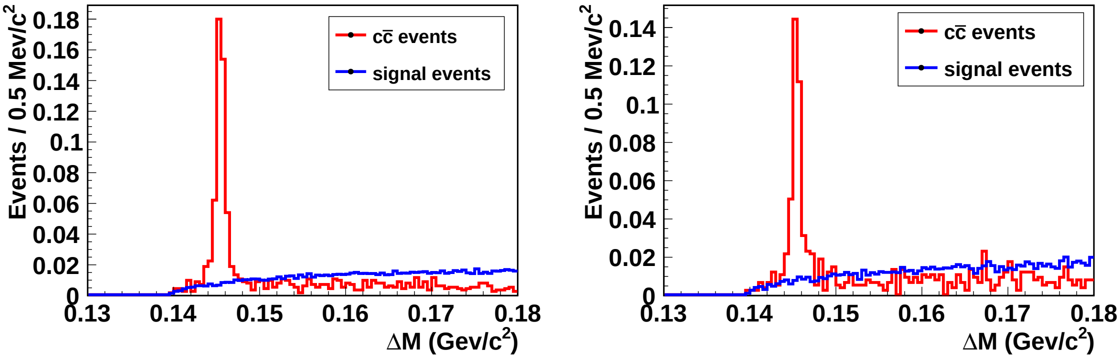

Figure 3.21: ΔM distributions of $B^+ \to D^0(K^0_S\pi^+\pi^-)K^+$ in the MC sample shown for Belle (left) and Belle II (right). The red and blue lines represent $c\bar{c}$ and signal events, respectively.

No PID requirements are applied to the pion tracks because of their low momentum. To exclude these D^* backgrounds, the events in the range $0.143 < \Delta M < 0.148$ GeV/c^2 are eliminated, which is $\pm 3\sigma$ around nominal value. With this selection, the total background rejection is 8.9% with a 0.65% reduction in relative signal efficiency. The ΔM distributions for $c\bar{c}$ events and signal events are displayed in Fig. 3.21.

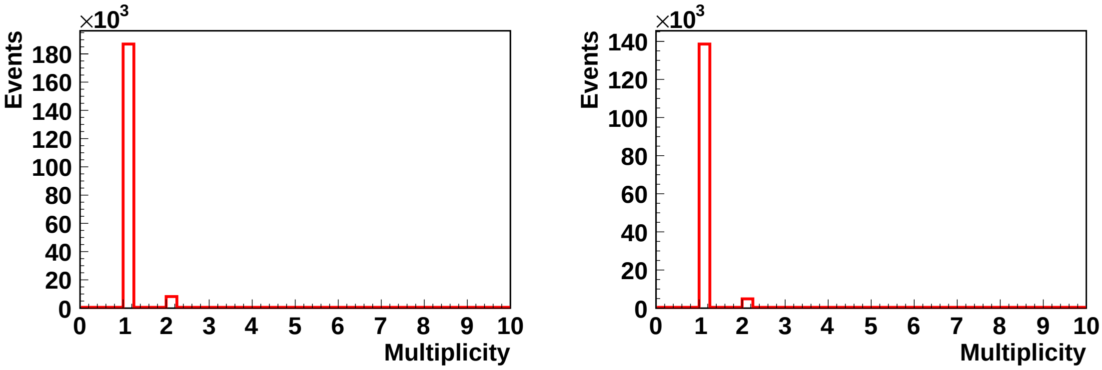

Figure 3.22: B candidate multiplicities after applying all the selection criteria for the channel $B^+ \to D^0(K^0_S\pi^+\pi^-)K^+$ (left) and $B^+ \to D^0(K^0_S K^+K^-)K^+$ (right) in Belle signal MC sample.

3.5 MULTIPLICITY, BEST-CANDIDATE SELECTION AND EFFICIENCY

There can be a potential for more than one candidate in some event caused by the soft momentum tracks. In an event, randomly misreconstructed tracks can provide a false candidate alongside the real ones. Figures. 3.22 and 3.23 depict the multiplicity distributions for B candidates after applying all the optimized selection criteria to the Belle and Belle II datasets, respectively. The average multiplicity is 1.022 (1.029) and 1.018 (1.025) for the final states $K^0_S\pi^+\pi^-$ and $K^0_S K^+K^-$, respectively, for Belle (Belle II). A best-candidate selection (BCS) is performed in each event to remove the duplicate candidates.

Different metrics involving $M_{\rm bc}$ and M_{D^0} are investigated for the BCS using signal MC sample. The resolution of M_{bc} and M_{D^0} are determined from simple fits in signal MC samples. A single Gaussian PDF is used for M_{bc} and a sum of two Gaussian is used for M_{D^0}. The effective resolution obtained is 2.5 MeV/c^2 and 5.25 MeV/c^2 for M_{bc} and M_{D^0}, respectively, for the channel $B^+ \to D^0(K^0_S\pi^+\pi^-)K^+$ in Belle signal MC sample. The fit projections are shown in Fig 3.24. Different BCS metrics and their

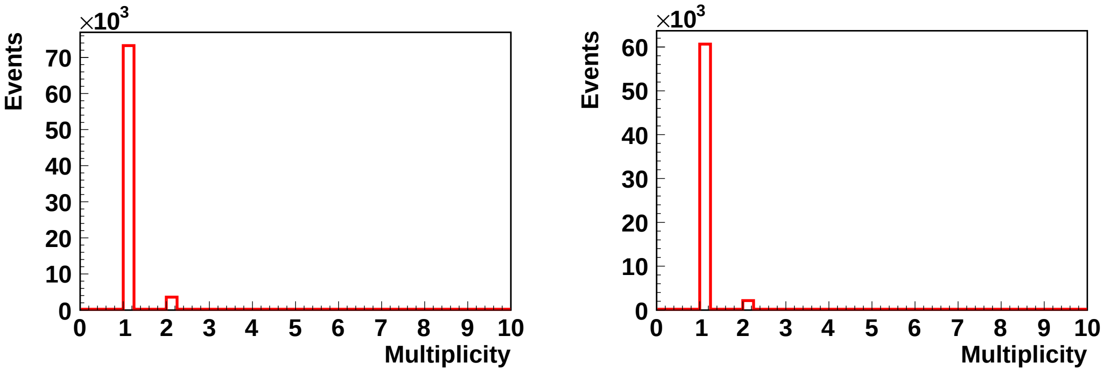

Figure 3.23: B candidate multiplicities after applying all the selection criteria for the channel $B^- \to D^0(K_S^0\pi^+\pi^-)K^-$ (left) and $B^- \to D^0(K_S^0K^+K^-)K^-$ (right) in Belle II signal MC sample.

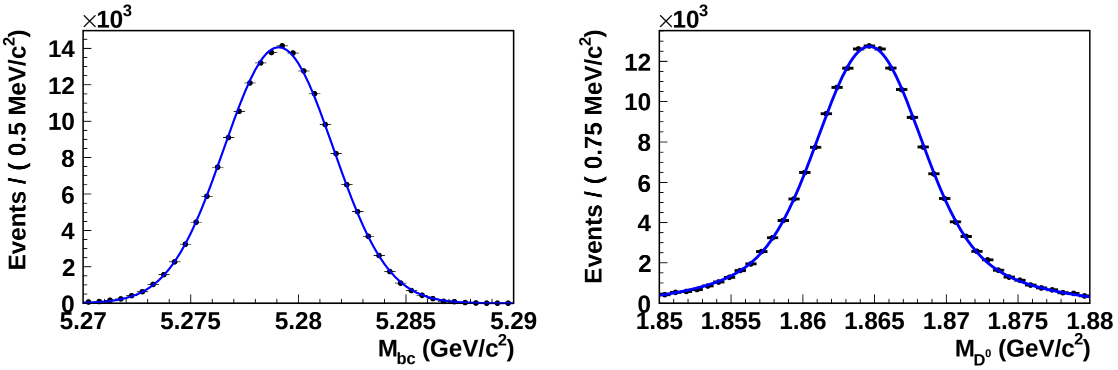

Figure 3.24: M_{bc} (left) and M_{D^0} (right) distributions in $B^+ \to D^0(K_S^0\pi^+\pi^-)K^+$ Belle signal MC sample. The black points with error bars represent data and the solid blue line represents the fit model.

corresponding efficiencies are listed in Table 3.2.

Table 3.2: Different BCS metrics and their corresponding efficiencies.

BCS metric	efficiency (%)
$(\frac{M_{\rm bc}-M_B^{\rm PDG}}{\sigma_{M_{\rm bc}}})^2$	61.35 ± 0.04
$(\frac{M_{D^0}-M_{D^0}^{\rm PDG}}{\sigma_{M_{D^0}}})^2$	58.02 ± 0.04
$(\frac{M_{\rm bc}-M_B^{\rm PDG}}{\sigma_{M_{\rm bc}}})^2 + (\frac{M_{D^0}-M_{D^0}^{\rm PDG}}{\sigma_{M_{D^0}}})^2$	63.32 ± 0.04

The χ^2 metric defined as $(\frac{M_{bc}-M_B^{PDG}}{\sigma_{M_{bc}}})^2 + (\frac{M_{D^0}-M_{D^0}^{PDG}}{\sigma_{M_{D^0}}})^2$, where $\sigma_{M_{bc}}$ and $\sigma_{M_{D^0}}$ are the resolutions of M_{bc} and M_{D^0}, respectively, has been chosen. Studies using signal MC samples show that this metric selects the correctly reconstructed candidate approximately 63% of the time for all the decay modes. The signal efficiencies after all the selections and best-candidate selection are summarized in Table 3.3. The $B^+ \to D\left(K_S^0\pi^+\pi^-\right)h^+$ selection efficiency is marginally improved at Belle II compared to Belle, whereas there is a significant improvement in the $B^+ \to D\left(K_S^0K^+K^-\right)h^+$ selection efficiency. This increase is due to the $\mathcal{L}(K/\pi) > 0.2$ requirement on the D-decay products being more efficient when applied to Belle II data compared to Belle data.

Table 3.3: Signal efficiencies of all the decay channels of interests. The $B^+ \to D\pi^+$ and $B^+ \to DK^+$ channels are separated by $\mathcal{L}(K/\pi) < 0.6$ and $\mathcal{L}(K/\pi) > 0.6$ selections, respectively.

Decay mode	Efficiency (%)	
	Belle	Belle II
$B^+ \to D(K_S^0\pi\pi)\pi^+$	21.77 ± 0.03	22.13 ± 0.05
$B^+ \to D(K_S^0\pi\pi)K^+$	19.11 ± 0.03	19.79 ± 0.05
$B^+ \to D(K_S^0KK)\pi^+$	16.26 ± 0.03	18.16 ± 0.05
$B^+ \to D(K_S^0KK)K^+$	14.29 ± 0.03	16.73 ± 0.05

3.6 DATA-MC COMPARISON STUDY

As the MC sample is used for optimizing the selection criteria and PDF modeling, the data sample must be checked to ensure that its relevant distributions match those in MC before applying the selection and fit model to it. The control sample $B^+ \to D\pi^+, D \to K_S^0\pi^-\pi^+$ has been used for this purpose. After applying all the selection criteria described in Sec. 3.2, the B candidate multiplicity is compared for generic MC and data, shown in Fig. 3.25. The agreement is very good. Fig. 3.26 shows a comparison of the ΔE distribution in generic MC samples before and after the best-candidate selection. They are in good agreement with one another, indicating

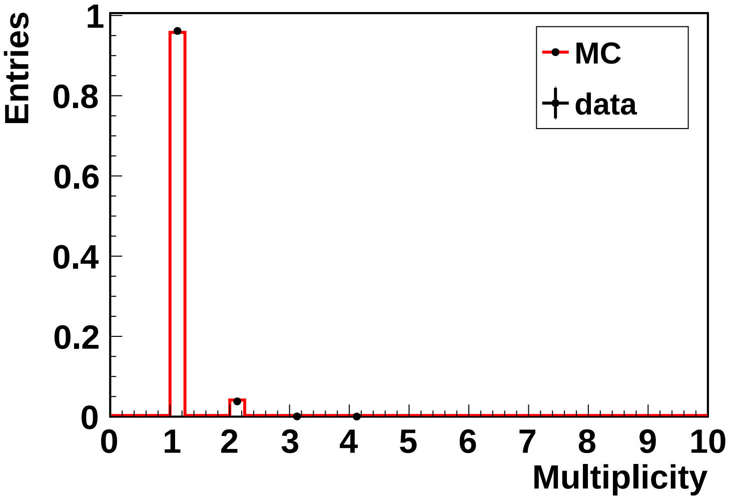

Figure 3.25: Comparison of candidate multiplicity distribution in Belle generic MC sample and data for the channel $B^+ \to D\pi^+, D \to K^0_S\pi^+\pi^-$. The luminosity of the generic MC and data are exactly the same. The black points with uncertainty represent data and the red and histogram represent the MC.

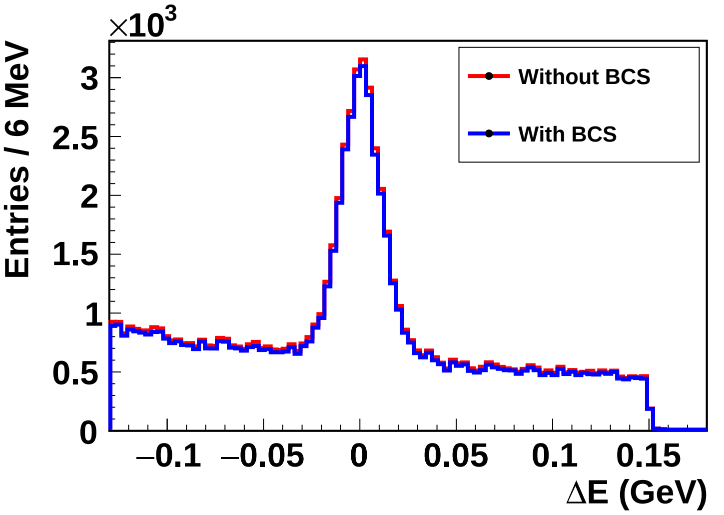

Figure 3.26: ΔE distribution in $B^+ \to D\pi^+, D \to K^0_S\pi^+\pi^-$ generic MC sample before and after the best-candidate selection.

that the BCS has no bias on the fit variable distributions. The similar checks have been performed for Belle II samples as well, and there is no bias observed for any of the cases. The data-MC comparison is also performed for the continuum suppression input variables. The comparison plots are shown in Figs. 3.27-3.30. All these distributions are background subtracted through $\mathcal{S}\mathcal{P}lot$ technique [94]; it is a statistical tool that can

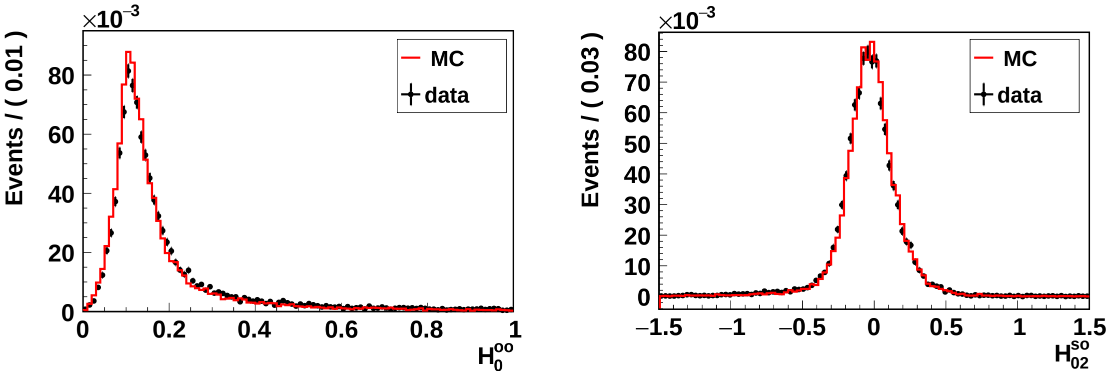

Figure 3.27: Comparison of distributions of H_0^{oo} (left) and H_{02}^{so} (right) in Belle generic MC sample and data for the channel $B^+ \to D\pi^+, D \to K_S^0\pi^+\pi^-$. The luminosity of the generic MC and data are exactly the same. The black points with uncertainty represent data and the red and histogram represent the MC.

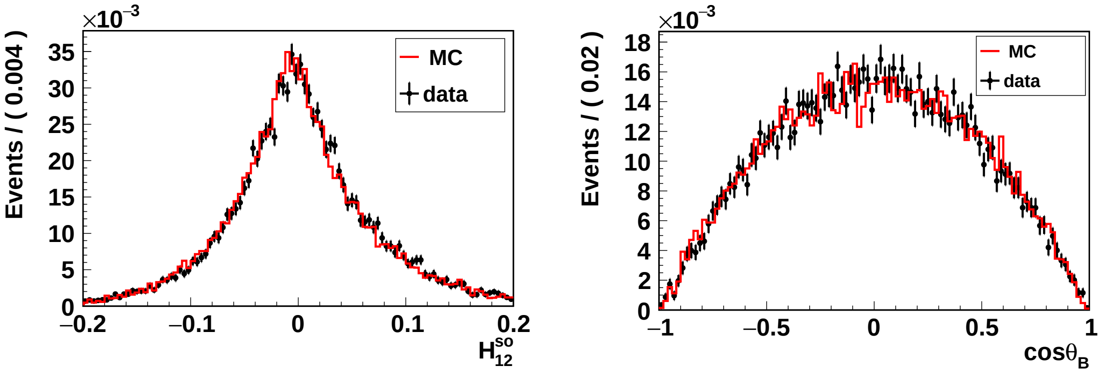

Figure 3.28: Comparison of distributions of H_{12}^{so} (left) and $\cos\theta_B$ (right) in Belle generic MC sample and data for the channel $B^+ \to D\pi^+, D \to K_S^0\pi^+\pi^-$. The luminosity of the generic MC and data are exactly the same. The black points with uncertainty represent data and the red and histogram represent the MC.

identify contribution of different sources in a given variable using the weights from the likelihood fits. The variable ΔE is used as a fit variable for this purpose. Only the ΔZ distribution in data shows a large deviation; the effect of this has been taken into account in the final fit through the free parameter of transformed FBDT output (C') signal component, which is described in Sec. 4.2. This discrepancy has not been observed for Belle II samples. The data-MC comparison of the variable ΔZ in Belle II is shown in Fig. 3.31.

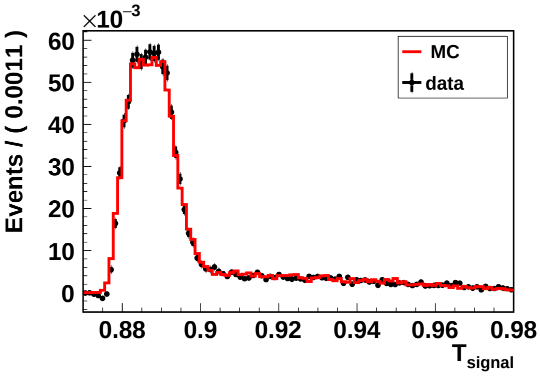

Figure 3.29: Comparison of distributions of $|B_{\text{thrust}}|$ (left) and $|\cos\theta_B^{\text{ROE}}|$ (right) in Belle generic MC sample and data for the channel $B^+ \to D\pi^+, D \to K_S^0\pi^+\pi^-$. The luminosity of the generic MC and data are exactly the same. The black points with uncertainty represent data and the red and histogram represent the MC.

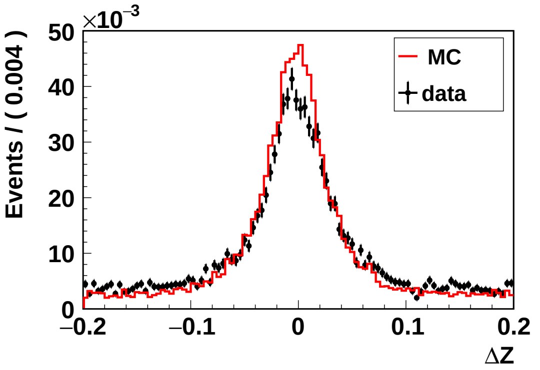

Figure 3.30: Comparison of distributions of ΔZ (left) and $|qr|$ (right) in Belle generic MC sample and data for the channel $B^+ \to D\pi^+, D \to K_S^0\pi^+\pi^-$. The luminosity of the generic MC and data are exactly the same. The black points with uncertainty represent data and the red and histogram represent the MC.

The event selection optimization ends here. The next step of the analysis, signal yield extraction procedure and strategy, is described in Chapter 4.

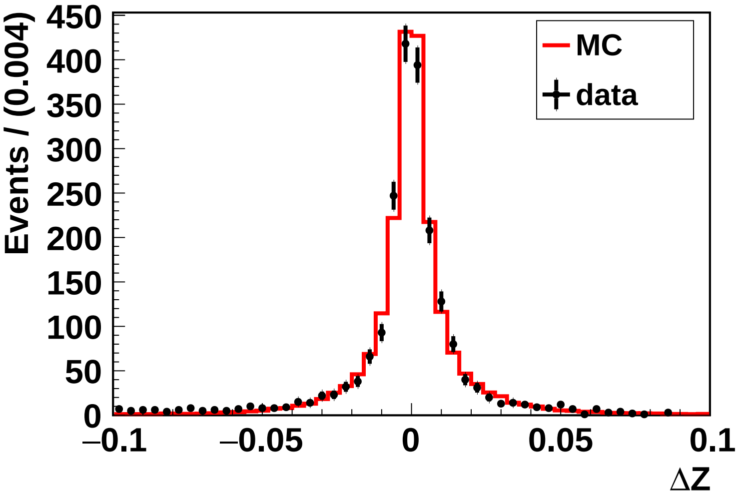

Figure 3.31: Comparison of distributions of ΔZ in Belle II generic MC sample and data for the channel $B^+ \to D\pi^+, D \to K^0_{\rm S}\pi^+\pi^-$. The data luminosity is normalized to the MC luminosity. The black points with uncertainty represent data and the red and histogram represent the MC.

CHAPTER 4

Signal yield determination

In this chapter, the description of the signal yield determination technique is given, which employs unbinned extended maximum-likelihood fits to ΔE and transformed FBDT output (C'). The definition of C' is described later in this chapter. The parametrization of the four distinct components is done in terms of two independent variables, ΔE and C'. Apart from $B \to Dh$ signal, there are three background components are also present in the sample

- $continuum$ background: events coming from $e^+e^- \to q\bar{q}$, $q = (u, d, s, c)$ processes;
- $combinatorial\ B\bar{B}$ background: events, other than signal, coming from $e^+e^- \to \Upsilon(4S) \to B\overline{B}$ decays; and
- $peaking\ background$: $B^+ \to Dh^+$, $(h = \pi$ or $K)$ decays due to the $K - \pi$ misidentification of the prompt hadron.

Each of these component probability density functions (PDFs) are fitted individually using corresponding MC samples, separately for Belle and Belle II.

A brief introduction to maximum likelihood fits is given in Sec. 4.1, the definition of the transformed FBDT output is given in Sec. 4.2, the fit strategy and PDF parametrization of each component are described in Sec. 4.3, and the signal extraction and yields are summarized in Sec. 4.4.

4.1 MAXIMUM LIKELIHOOD FIT METHOD

The maximum likelihood (ML) is a powerful approach for determining the parameters of a model. The parameters are estimated by varying them in a likelihood until a global minimum is reached. If x_i are the n measurements of the variable x, and $P(x_i;\alpha)$ is the model to describe the distribution, then

$$L(x_1, x_2, ..., x_n; \alpha) = \prod_{i=1}^{n} P(x_i; \alpha), \tag{4.1}$$

where α is the unknown parameter whose value is to be estimated and $L(x_i)$ is the likelihood function. The logarithm of the likelihood function is used for convenience, referred to as the log-likelihood function:

$$\mathrm{ln}L(x_1, x_2, ..., x_n; \alpha) = \sum_{i=1}^{n} \mathrm{ln}P(x_i; \alpha). \tag{4.2}$$

To get the most likely estimator for the parameter of interest α, the minimum of the negative log-likelihood function is utilised. Furthermore, if the data distribution has many components, such as signal and three background components in our case, each with its own model, an extension of the likelihood function is utilised. Considering this, the log-likelihood function of an unbinned extended ML fit is defined as

$$\mathcal{L}(\alpha) = \mathrm{ln}L(\alpha) = \sum_{i=1}^{n} \mathrm{ln}\left\{ \sum_{j=1}^{m} N_j P_j(x_i; \alpha) \right\} - \sum_{j=1}^{m} N_j - \mathrm{ln}(N!), \tag{4.3}$$

where m represent the number of different components present in the dataset, N_j and P_j are the expected number of events and PDF of the j^{th} component, respectively, and

N is the total number of events present in the sample and is a constant. The value of α_k, for which extended $\mathcal{L}(\alpha_k)$ is maximum, is the estimator from the extended ML, which one can obtain by solving the following equation:

$$\frac{d\left(\mathcal{L}(\alpha_k)\right)}{d\alpha_k} = 0. \tag{4.4}$$

For the ML fit to operate effectively, a suitable PDF needs to be chosen carefully. The parametrization of the simulated data must be done for each component in order to obtain the right PDF for the data distribution. The ROOT [95] framework's maximum likelihood fitting module RooFit [96] is used for this purpose. The RooFit package contains a large number of PDFs that may be used to create a data distribution model. In addition, it normalizes the PDFs and provides tools to visualize the fit results.

The functional representation of the PDFs used for modeling different components of ΔE and C' in this analysis are given below.

1. Symmetric Gaussian function (G_S)

$$G_S(x;\mu,\sigma) = \frac{1}{\sqrt{2\pi}\sigma}\exp\left[-\frac{1}{2}\left(\frac{x-\mu}{\sigma}\right)^2\right], \tag{4.5}$$

   where μ is the mean and σ is the width.

2. Symmetric double Gaussian function (G_D)

$$G_D(x;\mu,\sigma_1,\sigma_2) = fG_S(x;\mu,\sigma_1) + (1-f)G_S(x;\mu,\sigma_2), \tag{4.6}$$

where μ is the mean, σ_1 and σ_2 are the width of the two Gaussian functions, and f is the fractional weight factor of the first Gaussian function.

3. Asymmetric Gaussian function ($G_\pm$)

$$G_\pm(x;\mu,\sigma_\pm) = \frac{\sqrt{2}}{\sqrt{\pi}(\sigma_+ + \sigma_-)} \begin{cases} \exp\left[-\frac{1}{2}\left(\frac{x-\mu}{\sigma_+}\right)^2\right], & \text{if } x \geq \mu \\ \exp\left[-\frac{1}{2}\left(\frac{x-\mu}{\sigma_-}\right)^2\right], & \text{if } x < \mu \end{cases} \tag{4.7}$$

where μ is the mean, σ_+ and σ_- are the widths for the cases $x \geq \mu$ and $x < \mu$, respectively.

4. Exponential function (E)

$$E(x;\lambda) = \lambda \mathrm{e}^{-\lambda x}, \tag{4.8}$$

where λ is a constant.

5. The Chebyshev polynomials are a set of orthogonal polynomials, and are defined as:

$$P_{n+1}(x) = 2xP_n(x) - P_{n-1}(x), \tag{4.9}$$

where n represent the order of the polynomial. These are the best choice to fit a curve because of their orthogonality and convergence properties.

In order to extract the signal, a two-dimensional ML fit is executed using the PDFs mentioned previously. As the variables ΔE and C' have negligible correlations, which will be shown in Sec. 4.2, the two-dimensional PDF is defined as a product of two

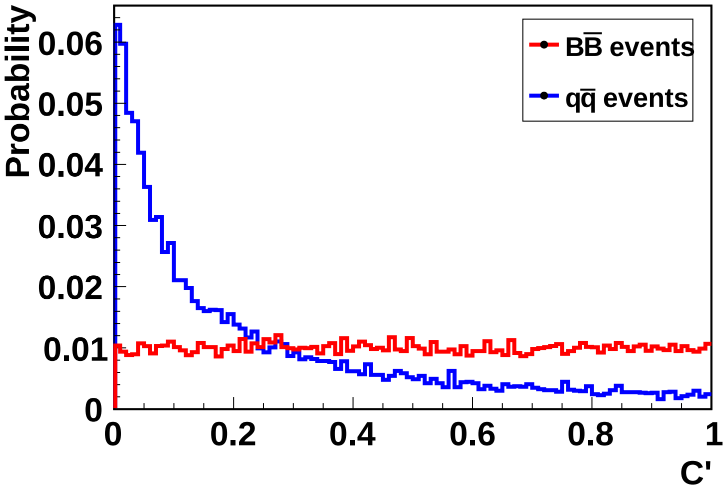

Figure 4.1: C' distribution of $B^+ \to D^0(K^0_S\pi^+\pi^-)K^+$ in MC sample. The red and blue lines represent $B\bar{B}$ and $q\bar{q}$ events, respectively.

one-dimensional PDFs ($\mathcal{F}_i$):

$$\mathcal{P}_i = \mathcal{F}_i(\Delta E) \times \mathcal{F}_i(C'). \tag{4.10}$$

4.2 TRANSFORMATION OF FBDT OUTPUT (C)

As C is difficult to model in an analytic way, the transformation of C to C' is done using a large ordered list of C signal values and calculating the fraction of signal events present in the given sample using that list, which is also known in the name of "μ-transformation" (probability integral transformation) [97, 98]. The C' distribution is shown in Fig. 4.1.

When compared to the traditional Gaussian-transformation [99], this transformation has some advantages: the signal and background shapes are clearly distinguishable and can be represented by easy analytic PDFs with fewer parameters in the final signal extraction fit. Furthermore, The maximum value of C used in the Gaussian-transformation is a arbitrary for each analysis, which is not the case for this transformation. The statistical stability and separation power [100] of both the transformations are also verified using one stream of Belle generic MC. The yields from μ-transformation are statistically comparable to the yields obtained from Gaussian-transformation. The separation power S is defined as:

$$S = \sqrt{f(1-f)\int \frac{(p_1(x) - p_2(x))^2}{p_{\text{tot}}(x)}dx}, \tag{4.11}$$

where, S is the separation power and varies from zero (no separation) to one (absolute maximum achievable with the given sample), f is the fraction of signal events in the sample, $p_1(x)$ is the signal PDF (histogram), $p_2(x)$ is the background PDF (histogram) and $p_{\text{tot}}(x)$ is the total PDF (histogram) $= fp_1(x) + (1-f)p_2(x)$. The separation power obtained are 0.512 and 0.517 for μ-transformation and Gaussian-transformation, respectively using the channel $B^+ \to D^0(K_S^0\pi^+\pi^-)K^+$ selected from the Belle MC sample.

The data-MC comparison is also checked for the C' distribution. The background subtracted C' distribution for the Belle dataset is shown in Fig. 4.2. A slope is observed for the shape of C' instead of a uniform distribution, and it arises due to small differences in the FBDT input variable distributions between data and MC. Hence, the signal component is described by a first-order Chebyshev polynomial.

Correlation with ΔE

Before moving on to signal extraction, the correlations between ΔE and C' for different sorts of events are investigated, as C' is the other signal extraction variable apart from

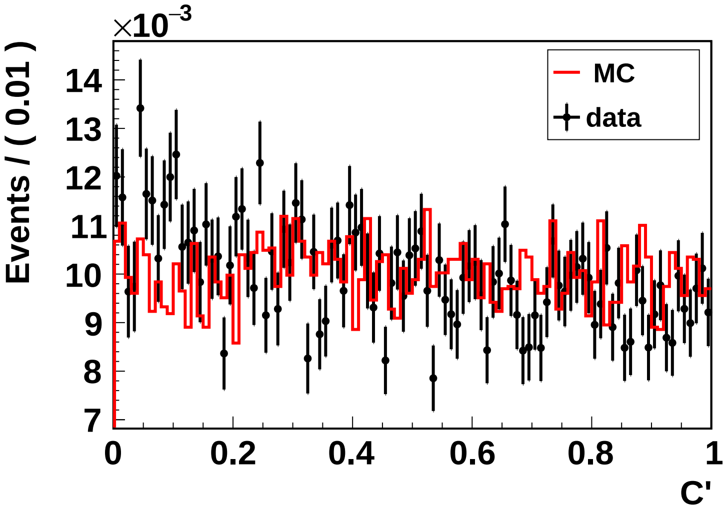

Figure 4.2: Comparison of distributions of C' in Belle generic MC sample and data for the channel $B^+ \to D\pi^+, D \to K_S^0\pi^+\pi^-$. The luminosity of the generic MC and data are exactly the same. The black points with uncertainty represent data, and the red and histogram represent the MC.

ΔE. The correlation coefficients are found to be -0.01, -0.09 and -0.02 for signal, $B\bar{B}$ and $q\bar{q}$ samples, respectively. These are negligible and can be ignored. To test whether there is any non-linear correlation, the fits are performed on simulated samples and no significant bias between the measured and generated parameters is observed, which also indicates there is negligible correlation. The two-dimesional histograms of ΔE vs C' for different components are demonstrated in Fig. 4.3.

4.3 FIT STRATEGY

A simultaneous extended maximum likelihood fit is carried out to $B^+ \to D\pi^+$ and $B^+ \to DK^+$ samples for this purpose. These two decay modes are identified with a PID $(\mathcal{L}(K/\pi))$ selection, defined in Sec. 3.2, on the kaon and pion tracks coming directly from the B meson, $\mathcal{L}(K/\pi) > 0.6$ for the kaons and $\mathcal{L}(K/\pi) < 0.6$ for the pions, and are referred as “pion-enhanced” and “kaon-enhanced” samples in this

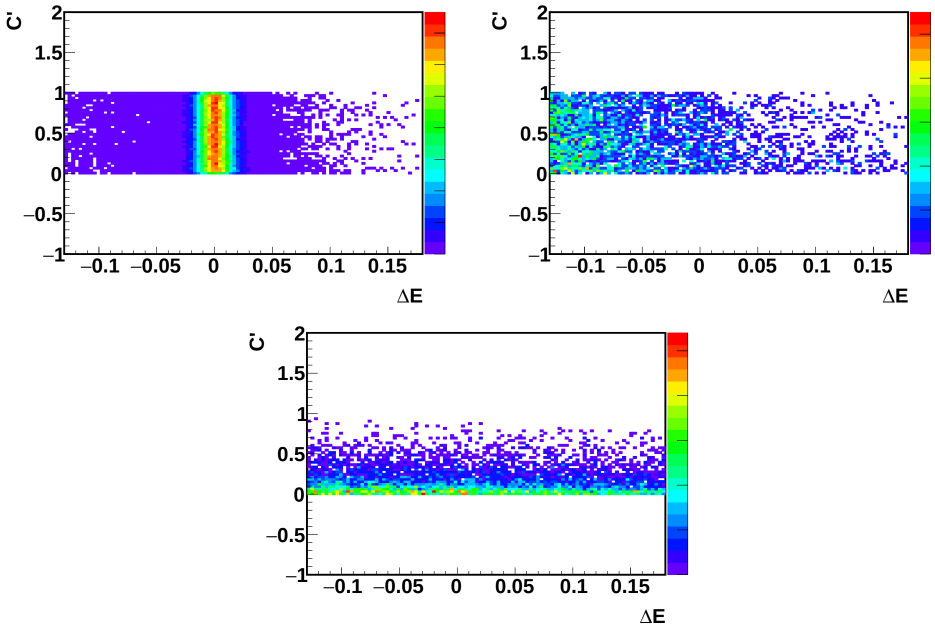

Figure 4.3: Two-dimensional histogram of ΔE and C' for different components: signal (up left), $B\bar{B}$ background (up right) and $q\bar{q}$ background (bottom).

thesis. In this way, one can directly extract the $K-\pi$ misidentification rate from data. The correlation between ΔE and C' has been checked for different components before proceeding towards signal extraction. The obtained correlation is less than 10% for all the components, irrespective of the D final states and different experiments.

The two-dimensional PDF is formed by combining one-dimensional PDFs of different components. The suitable shapes and parameters are obtained by doing the one-dimensional fit to the individual components in corresponding MC samples. The parametrization of the PDFs is described in Sec. 4.3.1. The two-dimensional PDFs are separate for $D \to K_S^0\pi^+\pi^-$ and $D \to K_S^0K^+K^-$ final states as well as for Belle and Belle II experiments. The PDF description of various components are identical between Belle and Belle II, but the parameter values are slightly different and are obtained from the MC samples corresponding to the respective experiments. Some parameters are fixed in the final fit to the values obtained from the MC samples, but enough are free to account for any data-MC differences. In some cases, a scale factor has also been introduced to account for this difference. The effect of these fixed parameters is studied as a source of systematic uncertainty. The detailed description of free and fixed parameters, as well as the signal extraction results are discussed in Sec. 4.4.

4.3.1 Parametrization of PDFs used in the fit

In this section, the discussion of the parametrization of ΔE and C' PDFs for different components is provided. The parameters are obtained by performing a one-dimensional fit to the corresponding MC samples. The majority of PDFs used are similar for all the $B^+ \to Dh^+$ modes for most of the components, though a few are different; any differences are noted. The summary of all the PDFs are listed in Table 4.9.

Models for the decay $B^+ \to D\pi^+, D \to K_S^0\pi^+\pi^-$

The ΔE signal component has been modeled with a sum of a double Gaussian (G_D) and an asymmetric Gaussian ($G_\pm$). To obtain these PDFs, the fit has been performed in large signal MC samples of respective experiments. The $B\bar{B}$ background component is modeled using the $B\bar{B}$ generic sample events after the removal of true signal events from it. An exponential function (E) is used to fit these events. A Chebyshev polynomial $(P_n(x))$ of first order is suitable for the $q\bar{q}$ background coming from $e^+e^- \to q\bar{q}$ continuum events. As the branching fraction of $B^+ \to DK^+$ is an order of magnitude small, the contribution of peaking background events from $B^+ \to DK^+$ to $B^+ \to D\pi^+$ is tiny compared to the signal yield. The wrong mass hypothesis associated with the $\pi^{\pm}$ causes a -50 MeV shift in the ΔE distribution. The suitable fit model, a double Gaussian, is obtained by performing the fit to the $B^+ \to D\pi^+$ reconstructed events in $B^+ \to DK^+$ signal MC sample.

The obtained value of all the parameteres are summarized in Table 4.1 and the fit projections are demonstrated in Fig. 4.4. As the PDF description is exactly the same for Belle and Belle II, only the projections in Belle MC samples are shown.

Table 4.1: Fit parameter information of ΔE distribution of the all the components of the mode $B^+ \to D\pi^+, D \to K_S^0\pi^+\pi^-$ in MC sample. The parameters μ represents the mean value, $\sigma_{0,1}$ represent the width of the first, second Gaussians, respectively. $\sigma_{L,R}$ is the left and right width of the asymmetric Gaussian PDF. The parameter $f_{(1)}$ represents the weight of the first Gaussian and f_2 is the weight of the asymmetric Gaussian. Paramter λ and b_0 are the free parameters of the exponential and polynomial functions, respectively.

Component	Parameter	Belle	Belle II
Signal	μ	$(\ 0.80 \pm 0.08) \times 10^{-3}$ GeV	$(\ 0.11 \pm 0.01) \times 10^{-3}$ GeV
	σ_0	$(\ 9.70 \pm 0.19) \times 10^{-3}$ GeV	$(\ 7.94 \pm 0.19) \times 10^{-3}$ GeV
	σ_1	$(17.60 \pm 1.20) \times 10^{-3}$ GeV	$(15.90 \pm 1.60) \times 10^{-3}$ GeV
	σ_L	$(76.80 \pm 6.80) \times 10^{-3}$ GeV	$(92.00 \pm 4.70) \times 10^{-3}$ GeV
	σ_R	$(41.00 \pm 1.70) \times 10^{-3}$ GeV	$(45.90 \pm 2.90) \times 10^{-3}$ GeV
	f_1	0.80 ± 0.03	0.85 ± 0.04
	f_2	0.95 ± 0.00	0.94 ± 0.01
$B\bar{B}$	λ	(-9.65 ± 0.19)	$-(8.06 \pm 0.24)$
$q\bar{q}$	b_0	(-0.29 ± 0.01)	$-(0.28 \pm 0.02)$
DK	μ	$-(48.46 \pm 0.30) \times 10^{-3}$ GeV	$-(48.75 \pm 0.22) \times 10^{-3}$ GeV
peaking	σ_0	$(14.87 \pm 0.28) \times 10^{-3}$ GeV	$(11.03 \pm 0.18) \times 10^{-3}$ GeV
background	σ_1	$(64.20 \pm 4.90) \times 10^{-3}$ GeV	$(77.00 \pm 5.00) \times 10^{-3}$ GeV
	f	0.92 ± 0.01	0.91 ± 0.02

For C', the signal component is fitted with a zeroth-order polynomial, and the $B\bar{B}$ background and cross-feed peaking background from $B^+ \to DK^+$ are modeled with a Chebychev polynomial of first order. A sum of two exponential functions is used to fit the $q\bar{q}$ component. The fit parameter information is given in Table 4.2 and projections of all these four components are shown in Fig. 4.4.

Table 4.2: Fit parameter information of C' distribution of the all the components of the mode $B^+ \to D\pi^+, D \to K_S^0\pi^+\pi^-$ in MC samples. The parameters a_0 and c_0 are the slopes of the polynomial function. $\lambda_{1,2}$ are the free parameters of the first and second exponential functions, respectively; f is the weight of the first exponential function.

Component	Parameter	Belle	Belle II
$B\bar{B}$	a_0	$-(0.44 \pm 0.02)$	$-(0.56 \pm 0.03)$
$q\bar{q}$	λ_1	$-(\ 5.84 \pm 0.12)$	$-(\ 5.95 \pm 0.18)$
	λ_2	$-(24.56 \pm 2.20)$	$-(30.73 \pm 2.70)$
	f	0.79 ± 0.02	0.68 ± 0.03
DK peaking	c_0	$-(0.06 \pm 0.01)$	$-(0.22 \pm 0.01)$

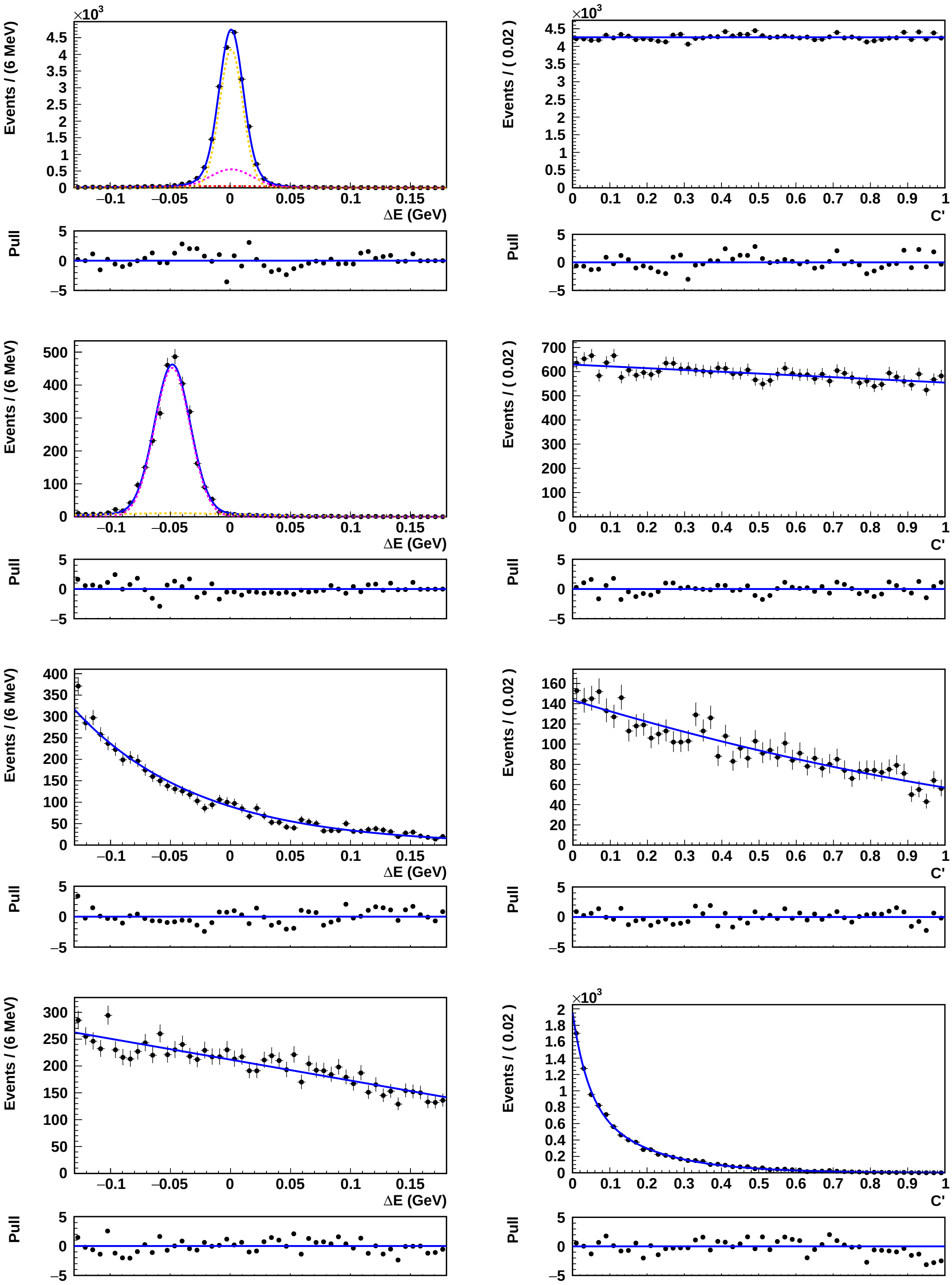

Figure 4.4: One-dimensional fit projection of the ΔE (left) and C' (right) distribution for signal (1st row), peaking background (2nd row), $B\bar{B}$ background (3rd row) and $q\bar{q}$ (4th row) components of the channel $B^+ \to D\pi^+, D \to K^0_\mathrm{S}\pi^+\pi^-$ in Belle MC samples. The black points with error bars represent data, and the blue solid curve shows the total fit. The pull distributions between data points and the fit are shown below the fit projections.

Models for the decay $B^+ \to DK^+, D \to K^0_S\pi^+\pi^-$

The suitable models of different components are identified by performing one-dimensional fits in the corresponding MC samples of $B^+ \to DK^+, D \to K^0_S\pi^+\pi^-$.

The PDF for the ΔE signal and $q\bar{q}$ components of this decay mode is similar to that described for the channel $B^+ \to D\pi^+$ in the previous section, i.e., a sum of double Gaussian and asymmetric Gaussian for the signal and first-order Chebyshev polynomial for the $q\bar{q}$ events. The slope of the combinatorial $B\bar{B}$ background events in the ΔE sample is steeper than in the $B^+ \to D\pi^+$ sample because of the presence of partially reconstructed $B \to D^{(*)}K^{(*)}$ events. The exponential PDF is then summed up with a first-order Chebyshev polynomial to describe this component. The cross-feed peaking background of $B^+ \to D\pi^+$ events are studied using signal MC sample. Due to the incorrect mass hypothesis ascribed to the kaon, the ΔE distribution of these events is displaced by $+50$ MeV. The percentage of this component is more significant in the kaon-enhanced sample due to the higher branching fraction of $B^+ \to D\pi^+$ decays. The ΔE distribution of these events is fitted using the same PDF as the signal component.

The fit parameter information are summarized in Table 4.3 and the projections of all the components of ΔE are shown in Fig. 4.5.

Table 4.3: Fit parameter information of ΔE distribution of the all the components of the mode $B^+ \rightarrow DK^+, D \rightarrow K_S^0\pi^+\pi^-$ in MC samples. The parameters μ represents the mean value, $\sigma_{0,1}$ represent the width of the first, second Gaussians, respectively. $\sigma_{L,R}$ is the left and right width of the asymmetric Gaussian PDF. The parameter f_1 represents the weight of the first Gaussian and f_2 is the weight of the asymmetric Gaussian. Paramter λ and b_0, d_0 are the free parameters of the exponential and polynomial functions, respectively. The parameter f represents the weight of the exponential function.

Component	Parameter	Belle	Belle II
Signal	μ	$(\ 0.85 \pm 0.08) \times 10^{-3}$ GeV	$-(\ 0.04 \pm 0.11) \times 10^{-3}$ GeV
	σ_0	$(10.03 \pm 0.14) \times 10^{-3}$ GeV	$(\ 7.51 \pm 0.23) \times 10^{-3}$ GeV
	σ_1	$(22.20 \pm 2.40) \times 10^{-3}$ GeV	$(14.70 \pm 1.40) \times 10^{-3}$ GeV
	σ_L	$(99.80 \pm 2.60) \times 10^{-3}$ GeV	$(99.00 \pm 2.60) \times 10^{-3}$ GeV
	σ_R	$(55.40 \pm 4.60) \times 10^{-3}$ GeV	$(66.20 \pm 5.80) \times 10^{-3}$ GeV
	f_1	0.90 ± 0.02	0.81 ± 0.05
	f_2	0.97 ± 0.00	0.96 ± 0.01
$B\bar{B}$	λ	$-(25.82 \pm 2.70)$	$-(31.11 \pm 4.6)$
	d_0	$-(\ 0.11 \pm 0.02)$	$-(0.42 \pm 0.14)$
	f	0.35 ± 0.06	0.54 ± 0.05
$q\bar{q}$	b_0	$-(0.22 \pm 0.02)$	$-(0.17 \pm 0.02)$
$D\pi$ peaking background	μ	$(51.52 \pm 0.25) \times 10^{-3}$ GeV	$(47.24 \pm 0.21) \times 10^{-3}$ GeV
	σ_0	$(24.90 \pm 5.20) \times 10^{-3}$ GeV	$(18.20 \pm 1.92) \times 10^{-3}$ GeV
	σ_1	$(14.38 \pm 0.52) \times 10^{-3}$ GeV	$(10.68 \pm 0.18) \times 10^{-3}$ GeV
	σ_L	$(76.30 \pm 8.40) \times 10^{-3}$ GeV	$(86.10 \pm 7.60) \times 10^{-3}$ GeV
	σ_R	$(49.40 \pm 4.30) \times 10^{-3}$ GeV	$(46.90 \pm 3.40) \times 10^{-3}$ GeV
	f_1	0.12 ± 0.08	0.10 ± 0.07
	f_2	0.94 ± 0.01	0.94 ± 0.00

For C', the only difference with respect to $B^+ \to D\pi^+$ models is that a second-order Chebyshev polynomial has been used for $B\bar{B}$ background instead of a first-order; all other PDFs descriptions are identical. The parameter values of the polynomials obtained from the respective MC samples are listed in the Table. 4.4. The fit projections of all the components of C' are shown in Fig. 4.5.

Table 4.4: Fit parameter information of C' distribution of the all the components of the mode $B^+ \to DK^+, D \to K^0_S\pi^+\pi^-$ in MC samples. The parameters e_0, e_1 and c_0 are the free parameters of the polynomial functions. $\lambda_{1,2}$ are the free parameters of the first and second exponential functions, respectively; f is the weight of the first exponential function.

Component	Parameter	Belle	Belle II
$B\bar{B}$	e_0	$-(0.48 \pm 0.05)$	$-(0.58 \pm 0.04)$
	e_1	0.12 ± 0.05	0.15 ± 0.07
$q\bar{q}$	λ_1	$-(\ 5.96 \pm 0.13)$	$-(\ 5.98 \pm 0.23)$
	λ_2	$-(27.76 \pm 2.80)$	$-(27.32 \pm 2.70)$
	f	0.81 ± 0.02	0.68 ± 0.03
peaking background	c_0	$-(0.11 \pm 0.02)$	$-(0.09 \pm 0.02)$

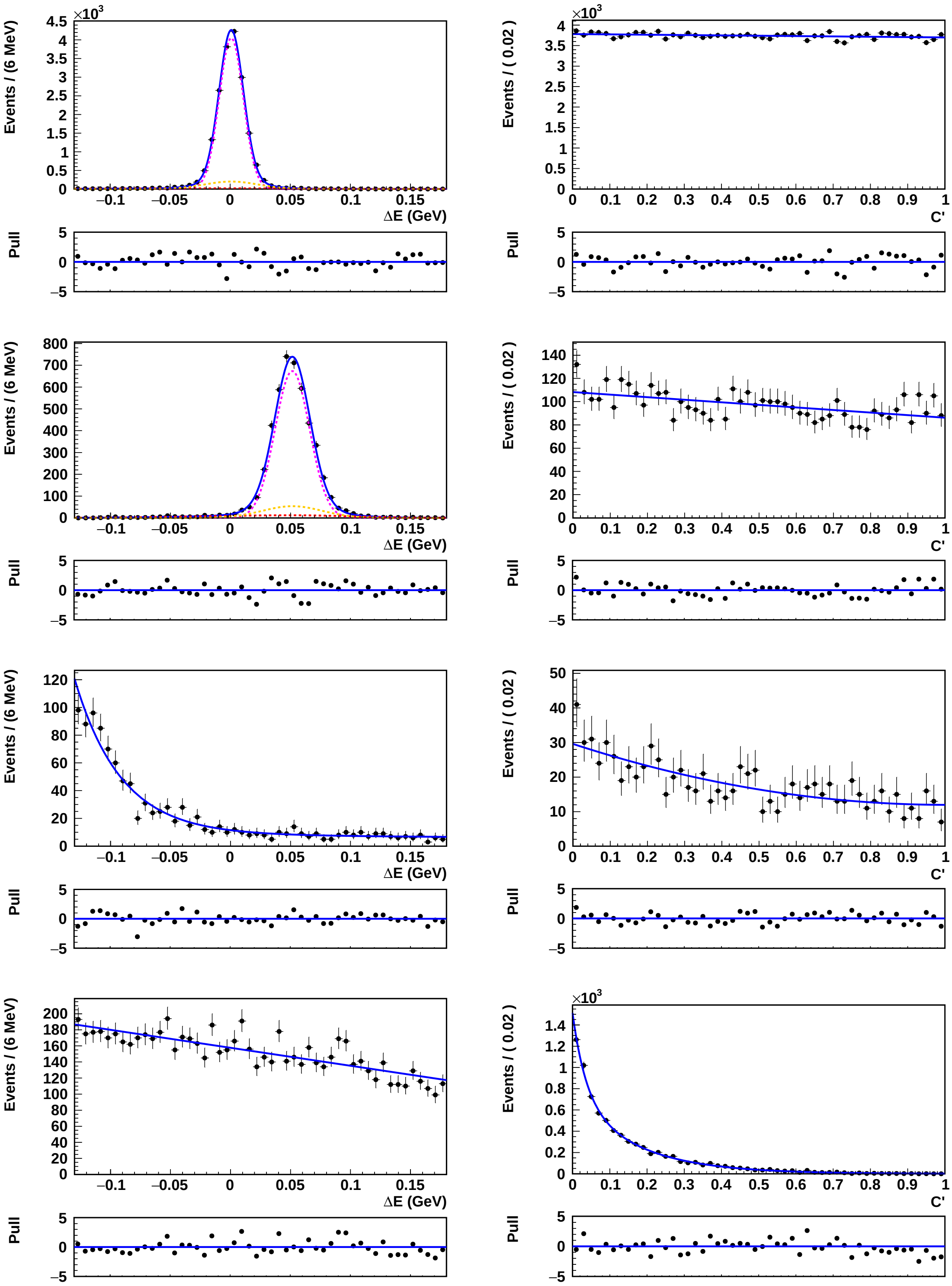

Figure 4.5: One-dimensional fit projection of the ΔE (left) and C' (right) distribution for signal (1st row), peaking background (2nd row), $B\bar{B}$ background (3rd row) and $q\bar{q}$ (4th row) components of the channel $B^+ \to DK^+, D \to K_S^0\pi^+\pi^-$ in Belle MC samples. The black points with error bars represent data, and the blue solid curve shows the total fit. The pull distributions between data points and the fit are shown below the fit projections.

Models for the decay $B^+ \to Dh^+, D \to K_S^0 K^+ K^-$

The respective components are fitted using MC samples of $K_S^0 K^+ K^-$ final state. Some component PDFs are modified compared to those described in the previous section. The $B\bar{B}$ background PDF that describes ΔE and C' for the $B^+ \to DK^+$ sample are an exponential and a first-order polynomial, respectively. The $B^+ \to D\pi^+$ peaking background component is modeled with the sum of a Gaussian and an asymmetric Gaussian. The $q\bar{q}$ background of both samples is modelled with just a single exponential function. All other component PDFs are the same as those for the $B^+ \to Dh^+$, $D \to K_S^0 \pi^+ \pi^-$ final state.

For $B^+ \to D\pi^+$, the parameter information of ΔE and C' are summarized in Tables 4.5 and 4.6, and the fit projections are shown in Fig. 4.6.

Table 4.5: Fit parameter information of ΔE distribution of the all the components of the mode $B^+ \to D\pi^+, D \to K^0_S K^+ K^-$ in MC samples. The parameters μ represents the mean value, $\sigma_{0,1}$ represent the width of the first, second Gaussians, respectively. $\sigma_{L,R}$ is the left and right width of the asymmetric Gaussian PDF. The parameter f_1 represents the weight of the first Gaussian and f_2 is the weight of the asymmetric Gaussian. Paramter λ and b_0 are the free parameters of the exponential and polynomial functions, respectively.

Component	Parameter	Belle	Belle II
Signal	μ	$(0.82 \pm 0.09) \times 10^{-3}$ GeV	$(0.30 \pm 0.12) \times 10^{-3}$ GeV
	σ_0	$(10.30 \pm 0.24) \times 10^{-3}$ GeV	$(8.22 \pm 0.21) \times 10^{-3}$ GeV
	σ_1	$(19.30 \pm 2.40) \times 10^{-3}$ GeV	$(17.80 \pm 1.80) \times 10^{-3}$ GeV
	σ_L	$(89.00 \pm 4.40) \times 10^{-3}$ GeV	$(85.00 \pm 9.20) \times 10^{-3}$ GeV
	σ_R	$(49.10 \pm 3.00) \times 10^{-3}$ GeV	$(44.90 \pm 3.50) \times 10^{-3}$ GeV
	f_1	0.86 ± 0.04	0.83 ± 0.03
	f_2	0.96 ± 0.01	0.95 ± 0.01
$B\bar{B}$	λ	$-(16.92 \pm 0.88)$	$-(14.55 \pm 1.30)$
$q\bar{q}$	b_0	$-(0.26 \pm 0.07)$	$-(0.66 \pm 0.14)$
DK peaking background	μ	$-(45.86 \pm 0.77) \times 10^{-3}$ GeV	$-(46.70 \pm 0.67) \times 10^{-3}$ GeV
	σ_0	$(13.50 \pm 0.38) \times 10^{-3}$ GeV	$(15.70 \pm 0.54) \times 10^{-3}$ GeV
	σ_1	$(50.04 \pm 4.10) \times 10^{-3}$ GeV	$(32.80 \pm 4.80) \times 10^{-3}$ GeV
	σ_L	$(19.80 \pm 2.20) \times 10^{-3}$ GeV	$(12.18 \pm 4.60) \times 10^{-3}$ GeV
	σ_R	$(10.20 \pm 2.60) \times 10^{-3}$ GeV	$(9.90 \pm 4.80) \times 10^{-3}$ GeV
	f_1	0.91 ± 0.02	0.85 ± 0.02
	f_2	0.75 ± 0.12	0.74 ± 0.10

Table 4.6: Fit parameter information of C' distribution of the all the components of the mode $B^+ \to D\pi^+, D \to K^0_S K^+ K^-$ in MC samples. The parameters a_0 and c_0 are the free parameters of the polynomial functions. λ_1 is the free parameter of the exponential function.

Component	Parameter	Belle	Belle II
$B\bar{B}$	a_0	$-(0.17 \pm 0.08)$	$-(0.39 \pm 0.14)$
$q\bar{q}$	λ	$-(5.48 \pm 0.24)$	$-(6.52 \pm 0.58)$
peaking background	c_0	$-(0.08 \pm 0.01)$	$-(0.18 \pm 0.01)$

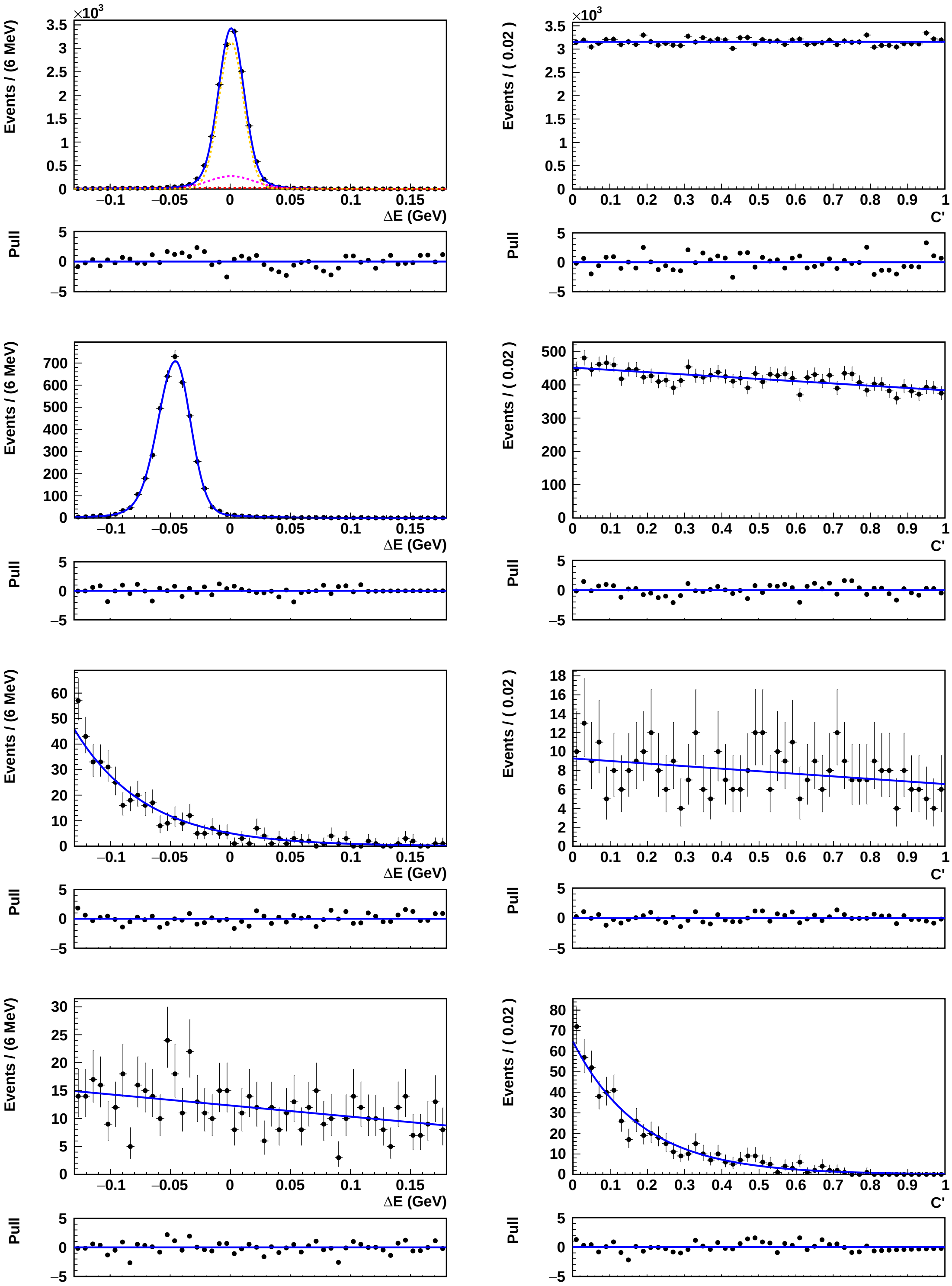

Figure 4.6: One-dimensional fit projection of the ΔE (left) and C' (right) distribution for signal (1st row), peaking background (2nd row), $B\bar{B}$ background (3rd row) and $q\bar{q}$ (4th row) components of the channel $B^+ \to D\pi^+, D \to K^0_S K^+ K^-$ in Belle MC samples. The black points with error bars represent data, and the blue solid curve shows the total fit. The pull distributions between data points and the fit are shown below the fit projections.

The $B^+ \to DK^+$ parameter information are given in Tables 4.7 and 4.7; fit projections are shown in Fig. 4.7.

Table 4.7: Fit parameter information of ΔE distribution of the all the components of the mode $B^+ \to DK^+, D \to K^0_S K^+ K^-$ in MC samples. The parameters μ represents the mean value, $\sigma_{0,1}$ represent the width of the first, second Gaussians, respectively. $\sigma_{L,R}$ is the left and right width of the asymmetric Gaussian PDF. The parameter f_1 represents the weight of the first Gaussian and f_2 is the weight of the asymmetric Gaussian. Paramter λ and b_0 are the free parameters of the exponential and polynomial functions, respectively.

Component	Parameter	Belle	Belle II
Signal	μ	$(\ 0.95 \pm 0.09) \times 10^{-3}$ GeV	$(\ 0.58 \pm 0.12) \times 10^{-3}$ GeV
	σ_0	$(18.70 \pm 1.60) \times 10^{-3}$ GeV	$(16.70 \pm 1.50) \times 10^{-3}$ GeV
	σ_1	$(\ 9.77 \pm 0.21) \times 10^{-3}$ GeV	$(\ 7.53 \pm 0.26) \times 10^{-3}$ GeV
	σ_L	$(78.00 \pm 9.00) \times 10^{-3}$ GeV	$(94.00 \pm 6.50) \times 10^{-3}$ GeV
	σ_R	$(48.70 \pm 3.40) \times 10^{-3}$ GeV	$(61.30 \pm 6.10) \times 10^{-3}$ GeV
	f_1	0.16 ± 0.03	0.21 ± 0.04
	f_2	0.97 ± 0.00	0.96 ± 0.01
$B\bar{B}$	λ	$-(19.34 \pm 1.80)$	$-(14.52 \pm 2.6)$
$q\bar{q}$	b_0	$-(0.20 \pm 0.07)$	$-(0.26 \pm 0.07)$
$D\pi$ peaking background	μ	$(50.25 \pm 0.30) \times 10^{-3}$ GeV	$(46.29 \pm 0.23) \times 10^{-3}$ GeV
	σ_0	$(15.15 \pm 0.27) \times 10^{-3}$ GeV	$(10.78 \pm 0.20) \times 10^{-3}$ GeV
	σ_L	$(81.60 \pm 8.30) \times 10^{-3}$ GeV	$(83.00 \pm 7.10) \times 10^{-3}$ GeV
	σ_R	$(44.80 \pm 3.80) \times 10^{-3}$ GeV	$(45.20 \pm 3.30) \times 10^{-3}$ GeV
	f	0.92 ± 0.01	0.90 ± 0.01

Table 4.8: Fit parameter information of C' distribution of the all the components of the mode $B^+ \to DK^+, D \to K^0_S K^+ K^-$ in Belle II MC sample. The parameters a_0 and c_0 are the free parameters of the polynomial functions. λ_1 is the free parameter of the exponential function.

Component	Parameter	Belle	Belle II
$B\bar{B}$	a_0	$-(0.54 \pm 0.18)$	$-(0.32 \pm 0.06)$
$q\bar{q}$	λ	$-(5.78 \pm 0.30)$	$-(6.44 \pm 0.69)$
peaking background	c_0	$-(0.07 \pm 0.03)$	$-(0.06 \pm 0.01)$

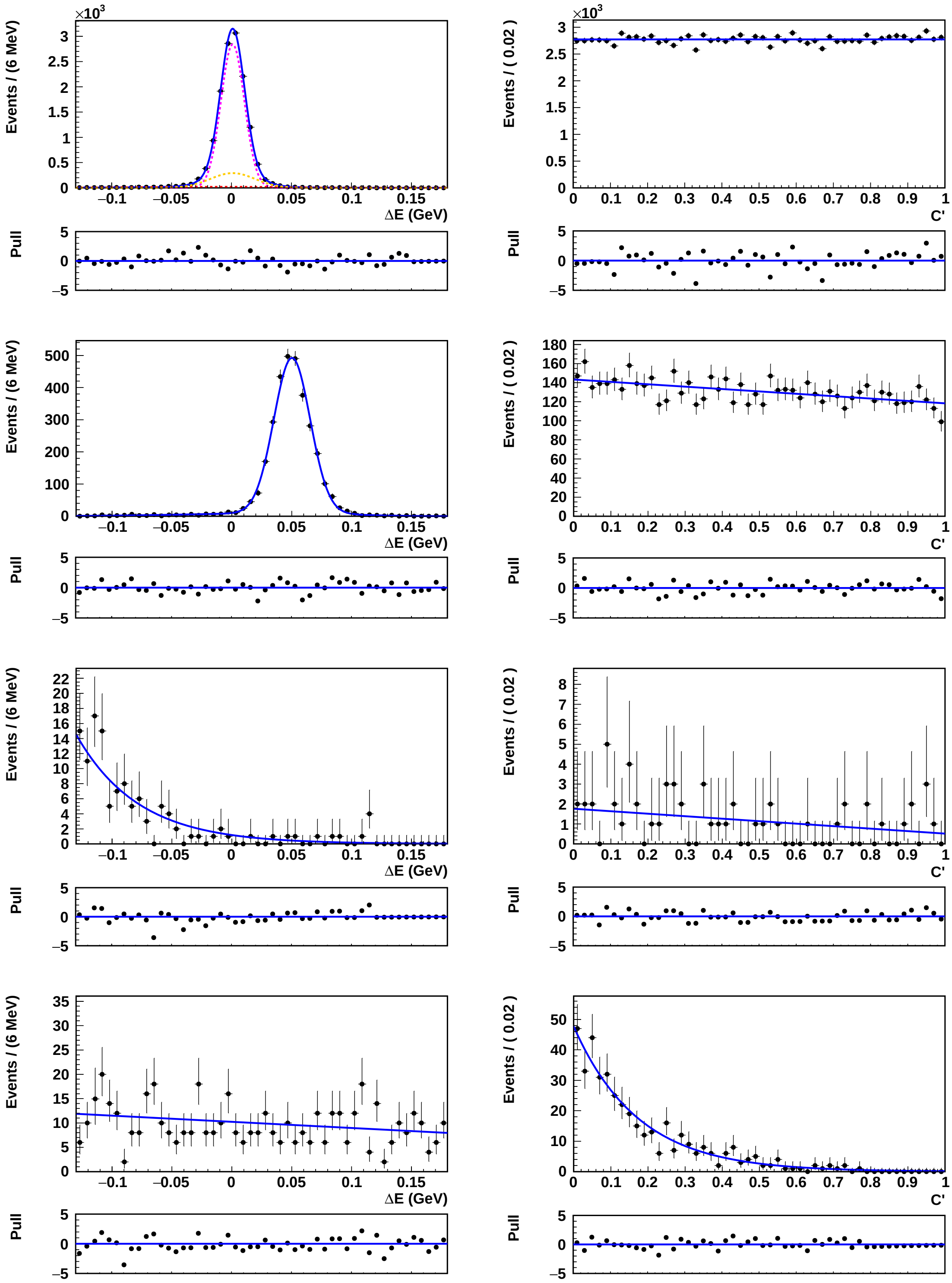

Figure 4.7: One-dimensional fit projection of the ΔE (left) and C' (right) distribution for signal (1st row), peaking background (2nd row), $B\bar{B}$ background (3rd row) and $q\bar{q}$ (4th row) components of the channel $B^+ \to DK^+, D \to K_S^0 K^+ K^-$ in Belle MC samples. The black points with error bars represent data, and the blue solid curve shows the total fit. The pull distributions between data points and the fit are shown below the fit projections.

Table 4.9: PDF information of all components of pion-enhanced and kaon-enhanced samples separated by D final states. The notations $G_S, G_D, G_\pm, E, P_n$ represent symmetric Gaussian, double Gaussian, asymmetric Gaussian, exponential and n^{th} order polynomial PDFs, respectively.

	component	pion-enhanced		kaon-enhanced	
D decay		ΔE	C'	ΔE	C'
$D \to K_S^0\pi^-\pi^+$	$B^+ \to D\pi^+$	$G_D + G_\pm$	P_0	$G_D + G_\pm$	P_0
	$B^+ \to DK^+$	G_D	P_1	$G_D + G_\pm$	P_1
	$B\overline{B}$ background	E	P_1	$E + P_1$	P_2
	$q\overline{q}$ background	P_1	$E + E$	P_1	$E + E$
$D \to K_S^0K^-K^+$	$B^+ \to D\pi^+$	$G_D + G_\pm$	P_0	$G_S + G_\pm$	P_0
	$B^+ \to DK^+$	$G_D + G_\pm$	P_1	$G_D + G_\pm$	P_1
	$B\overline{B}$ background	E	P_1	E	P_1
	$q\overline{q}$ background	P_1	E	P_1	E

4.4 SIGNAL EXTRACTION

In Sec. 4.3.1, it is observed that the PDF descriptions and parameters are similar between $B^+ \to D\pi^+$ and $B^+ \to DK^+$ with only minor differences. So, this fact will be exploited in the simultaneous fit; few PDFs are kept common to both $B^+ \to D\pi^+$ and $B^+ \to DK^+$ with a common free parameter in the fit to describe the differences between the two samples. The description of these common PDFs, free and fixed-parameter information are summarized in Table 4.10. The fixed parameters are taken from the one-dimensional component fits described in the previous section. This configuration of the simultaneous fit is identical for the D final states and the two experiments.

The signal component of C' is described with a 1^{st} order polynomial to account for any data-MC difference of the continuum suppression input variables. Similarly, a multiplicative factor $f_{\Delta E}$ is introduced on the principal σ of ΔE signal component, also known as "fudge factor", to account for the data-MC resolution difference. It tells us how better or worse the resolution in data is compared to the MC.

There are two categories in the simultaneous fit, pion-enhanced and kaon-enhanced samples. The four different yields, $D\pi$ and DK signal and peaking-background yields, can be represented in terms of the kaon-identification efficiency (ϵ) and $K-\pi$ misidentification rate (κ) using the relations

- $N^{D\pi}_{\text{pion enhanced}} = (1-\kappa)N^{D\pi}_{\text{tot}}$,
- $N^{\text{DK}}_{\text{pion enhanced}} = (1-\epsilon)N^{DK}_{\text{tot}}$,
- $N^{DK}_{\text{kaon enhanced}} = \epsilon N^{DK}_{\text{tot}}$,
- $N^{\text{D}\pi}_{\text{kaon enhanced}} = \kappa N^{D\pi}_{\text{tot}}$,

where $N^{D\pi}_{\text{tot}}$ and N^{DK}_{tot} represent the total $D\pi$ and DK yields without any PID selection, respectively. The value of ϵ is fixed to the value 0.84 ± 0.08 [101] and 0.78 ± 0.08 for Belle and Belle II, respectively, which were obtained using the PID correction tables of data [101]. The value of κ is directly extracted from data. The effect of all the fixed parameters are discussed in Chapter 5.

The total signal and other component yields are extracted using the simultaneous fit separately for Belle and Belle II and are referred to as “combined fit” in this thesis. The $K-\pi$ misidentification rate is obtained to be $(7.65 \pm 0.26)\%$ and $(6.86 \pm 0.49)\%$ in Belle and Belle II dataset, respectively. The signal enhanced fit projections are shown in Fig. 4.8 and 4.9, where the signal region is defined as $|\Delta E| < 0.05$ GeV and $0.65 < C' < 1$, and the obtained free parameter values are listed in Table 4.11

Table 4.10: PDF used in the simultaneous fit of pion- and kaon-enhanced samples and the parameter information. The notations $G_S, G_D, G_\pm, E, P_n$ represent symmetric Gaussian, double Gaussian, asymmetric Gaussian, exponential and n^{th} order polynomial PDFs, respectively.

Component	Category	ΔE	C'
Signal	$D\pi$	$G_D + G_\pm$ $f_{\Delta E}$, mean free other parameters fixed	P_1 slope free
	DK	same PDF mean separate other parameters common	same PDF common
$B\bar{B}$ background	$D\pi$	E slope fixed	P_1 slope fixed
	DK	$E + P_1$ slope of E free, other fixed	P_2 slopes fixed
Continuum background	$D\pi$	P_1 slope free	$E + E$ one slope of one E free other parameters fixed
	DK	same PDF common parameters	same PDF common parameters
peaking background	$D\pi$	G_D all parameters fixed	P_1 slope fixed
	DK	$G_D + G_\pm$ mean diff free other parameters fixed	P_1 slope fixed

Table 4.11: Fit parameter results from simultaneous fit in Belle data set.

Parameter	D final state	
	$K_S^0\pi\pi$	K_S^0KK
ΔE mean (GeV)	$(0.10 \pm 0.10) \times 10^{-3}$	$-(1.60 \pm 0.20) \times 10^{-3}$
$f_{\Delta E}$	(1.18 ± 0.01)	(1.19 ± 0.02)
a_0 of C' signal	$-(0.10 \pm 0.01)$	$-(0.14 \pm 0.03)$
b_0 of ΔE $q\bar{q}$	$-(0.25 \pm 0.02)$	$-(0.07 \pm 0.11)$
λ of C' $q\bar{q}$	$-(5.60 \pm 0.14)$	$-(4.44 \pm 0.35)$
λ of ΔE $B\bar{B}$	$-(29.80 \pm 2.60)$	$-(37.18 \pm 7.10)$
Mean diff (GeV)	$(50.80 \pm 0.70) \times 10^{-3}$	$(52.80 \pm 1.80) \times 10^{-3}$

and 4.12. The total signal and background yields obtained for both these experiments are summarized in Table 4.13. The obtained total signal yield is 67% higher as compared to the previous Belle analysis [45].

Table 4.12: Fit parameter results from simultaneous fit in of Belle II dataset.

Parameter	D final state	
	$K_S^0\pi\pi$	K_S^0KK
ΔE mean (GeV)	$(1.70 \pm 0.10) \times 10^{-3}$	$-(0.90 \pm 0.50) \times 10^{-3}$
$f_{\Delta E}$	(1.09 ± 0.01)	(1.20 ± 0.06)
a_0 of C' signal	$-(0.01 \pm 0.03)$	$-(0.02 \pm 0.08)$
b_0 of ΔE $q\bar{q}$	$-(0.21 \pm 0.04)$	$-(0.06 \pm 0.05)$
λ of C' $q\bar{q}$	$-(5.08 \pm 0.51)$	$-(6.26 \pm 0.77)$
λ of ΔE $B\bar{B}$	$-(26.63 \pm 5.30)$	$-(33.10 \pm 12.00)$
Mean diff (GeV)	$(47.10 \pm 0.90) \times 10^{-3}$	$(47.10 \pm 3.20) \times 10^{-3}$

Table 4.13: Total signal and background yields obtained from the two-dimensional fit of ΔE and C' in Belle and Belle II datasets.

	Sample	Pion-enhanced		Kaon-enhanced	
D decay	Component	Belle	Belle II	Belle	Belle II
$D \to K_S^0\pi^+\pi^-$	$B^+ \to D\pi^+$	21325 ± 162	4193 ± 70	1764 ± 64	308 ± 23
	$B^+ \to DK^+$	140 ± 29	62 ± 11	1467 ± 53	280 ± 21
	$B\bar{B}$ background	5040 ± 155	1223 ± 68	1309 ± 85	387 ± 42
	$q\bar{q}$ background	9022 ± 172	1657 ± 69	6295 ± 122	1021 ± 47
$D \to K_S^0K^+K^-$	$B^+ \to D\pi^+$	2740 ± 56	519 ± 21	211 ± 18	50 ± 10
	$B^+ \to DK^+$	17 ± 4	2.1 ± 0.2	194 ± 17	34 ± 7
	$B\bar{B}$ background	333 ± 31	77 ± 12	110 ± 18	22 ± 7
	$q\bar{q}$ background	409 ± 37	124 ± 14	309 ± 28	92 ± 11

To determine the CP-violating observables, the fit categories are further divided according to the charge of B candidates and the D-decay Dalitz bins, which is described in Chapter 5.

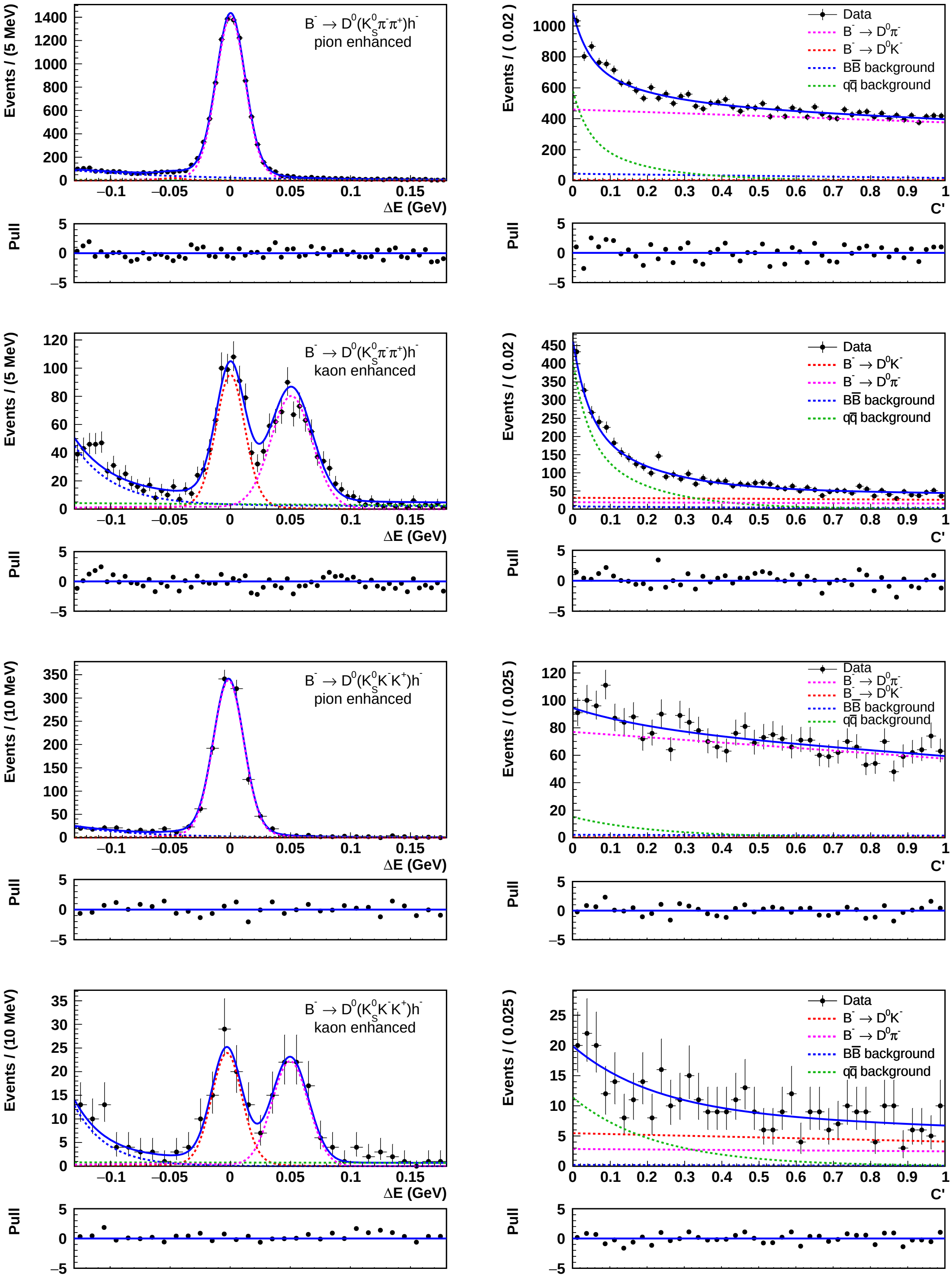

Figure 4.8: Signal-enhanced fit projections of ΔE (left) and C' (right) in Belle dataset. The first two rows represent $D \to K^0_S\pi^-\pi^+$ and the last two rows $D \to K^0_S K^- K^+$ final state, respectively. The black points with error bars represent data, and the solid blue line is the total fit. The dotted magenta, red, blue, and green curves represent $B^+ \to D\pi^+$, $B^+ \to DK^+$ continuum and combinatorial $B\bar{B}$ background components, respectively. The pull between the data and the fit are shown for all the projections.

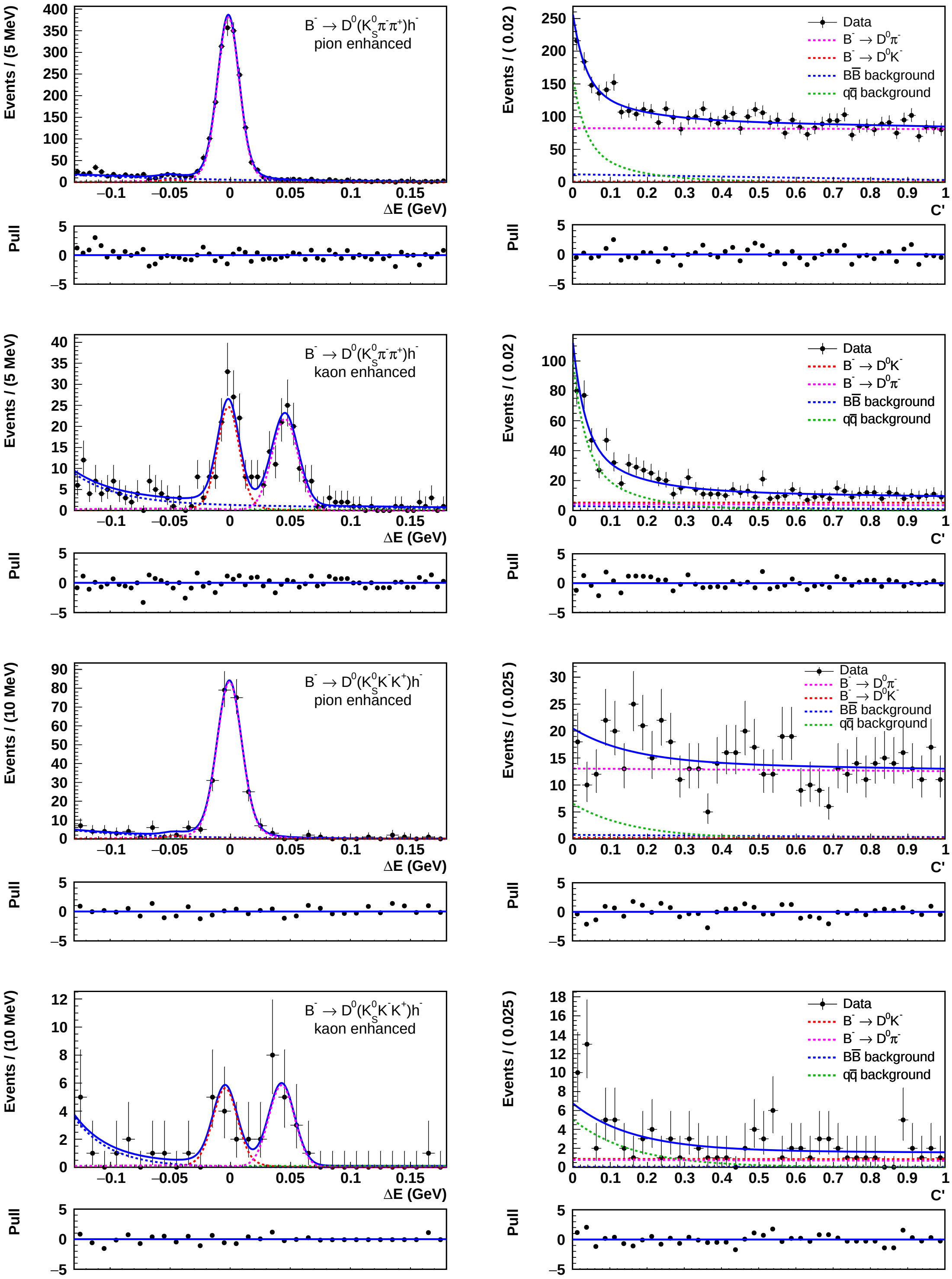

Figure 4.9: Signal-enhanced fit projections of ΔE (left) and C' (right) in Belle II dataset. The first two rows represent $D \to K_S^0\pi^-\pi^+$ and the last two rows $D \to K_S^0K^-K^+$ final state, respectively. The black points with error bars represent data, and the solid blue line is the total fit. The dotted magenta, red, blue, and green curves represent $B^+ \to D\pi^+$, $B^+ \to DK^+$ continuum and combinatorial $B\bar{B}$ background components, respectively. The pull between the data and the fit are shown for all the projections.

CHAPTER 5

Measurement of CKM angle ϕ_3 at Belle and Belle II

In the previous chapter the signal extraction fit models and the results of the fit parameters were described, and yields obtained from the simultaneous fit of Dh samples were also given. This chapter describes the second part of the fit, in which the CP-observables of interest are determined along with the extraction of hadronic parameters ϕ_3, r_B and δ_B.

The signal yields in different regions of D phase space are required to extract ϕ_3. So, the D phase space is binned using the binning scheme described in Chapter 1. There are a total of 16 bins in $D \to K_S^0\pi^+\pi^-$ final state and four bins in $D \to K_S^0K^+K^-$ final state. A combined fit with a common likelihood in all the bins is used, i.e. a simultaneous fit in all the $(16 + 4)$ bins, and is referred as "binned-fit" in this chapter. Thus, there are 80 categories in total ($(16 + 4)$ bins $\times$ 2 for charge of $B\times$ 2 for $D\pi/DK$) for each experiment. Furthermore, as the statistics of the Belle II dataset is small, a combined Belle + Belle II fit is performed to extract the parameters of interest. Hence, there are a total of 160 sub-categories in the simultaneous fit.

The fit in D Dalitz bins and the extraction of the CP-observables are discussed in Sec. 5.1, systematics sources and uncertainties are explained in Sec. 5.2 and the determination of ϕ_3 and the hadronic parameters is described in Sec. 5.3.

5.1 FIT IN D DALITZ BINS AND EXTRACTION OF CP OBSERVABLES

The signal yield in each D Dalitz bin is extracted from the binned-fit. The description of the PDFs in each bin is the same as described in the previous chapter. Almost the same set of parameters are free and fixed, which are common to all the bins of the respective D final states and experiments, in the binned-fit. The expectation is the $K-\pi$ misidentification rate. It is fixed to the value obtained from the first part of the fit, i.e., $(7.65 \pm 0.26)\%$ and $(6.86 \pm 0.49)\%$ for Belle and Belle II dataset, respectively, as the prompt hadron momentum is independent of position on the Dalitz plot. The obtained signal yields in each bin are summarized in Tables 5.1 and 5.2.

Table 5.1: Signal yields in D phase space bins of the decay modes $B \to D\pi$ and $B \to DK$ in Belle dataset.

Mode	Bin	$B \to D\pi$		$B \to DK$	
		B^+	B^-	B^+	B^-
$K_S^0\pi\pi$	-8	252 ± 18	642 ± 28	19 ± 6	63 ± 9
	-7	1189 ± 38	525 ± 26	53 ± 10	42 ± 9
	-6	678 ± 28	51 ± 8	39 ± 7	2 ± 2
	-5	542 ± 26	327 ± 20	47 ± 8	14 ± 5
	-4	1178 ± 38	660 ± 29	102 ± 13	45 ± 9
	-3	1492 ± 41	31 ± 7	104 ± 12	5 ± 3
	-2	1461 ± 41	45 ± 8	103 ± 12	10 ± 4
	-1	1108 ± 36	175 ± 16	85 ± 11	25 ± 7
	1	237 ± 18	1136 ± 36	8 ± 5	55 ± 9
	2	72 ± 10	1365 ± 39	0 ± 2	100 ± 11
	3	31 ± 7	1507 ± 41	4 ± 4	89 ± 11
	4	702 ± 30	1159 ± 38	63 ± 10	51 ± 10
	5	311 ± 19	521 ± 25	31 ± 7	31 ± 8
	6	58 ± 9	699 ± 28	3 ± 2	42 ± 8
	7	532 ± 26	1186 ± 38	32 ± 8	93 ± 12
	8	666 ± 28	269 ± 18	49 ± 9	15 ± 6
K_S^0KK	-2	233 ± 16	302 ± 18	16 ± 5	13 ± 5
	-1	341 ± 19	401 ± 21	18 ± 5	25 ± 6
	1	387 ± 21	304 ± 18	25 ± 6	19 ± 6
	2	283 ± 18	283 ± 18	16 ± 5	21 ± 5
Total		11503 ± 118	11588 ± 116	817 ± 35	760 ± 34

Table 5.2: Signal yields in D phase space bins of the decay modes $B \to D\pi$ and $B \to DK$ in Belle II dataset.

Mode	Bin	$B \to D\pi$		$B \to DK$	
		B^+	B^-	B^+	B^-
$K_S^0\pi\pi$	-8	38 ± 7	59 ± 8	2 ± 2	5 ± 3
	-7	235 ± 17	218 ± 16	15 ± 4	21 ± 5
	-6	159 ± 13	132 ± 12	11 ± 4	6 ± 2
	-5	108 ± 11	102 ± 11	8 ± 3	7 ± 3
	-4	230 ± 16	206 ± 16	9 ± 4	10 ± 4
	-3	297 ± 18	310 ± 18	29 ± 6	14 ± 4
	-2	264 ± 17	318 ± 18	17 ± 5	23 ± 5
	-1	240 ± 16	225 ± 16	11 ± 4	6 ± 3
	1	53 ± 8	52 ± 8	4 ± 3	5 ± 3
	2	11 ± 4	12 ± 4	1 ± 2	0 ± 2
	3	9 ± 4	7 ± 3	0 ± 2	0 ± 1
	4	106 ± 12	138 ± 13	16 ± 5	8 ± 4
	5	63 ± 9	71 ± 9	2 ± 2	8 ± 3
	6	5 ± 2	14 ± 4	2 ± 1	0 ± 2
	7	86 ± 11	98 ± 11	7 ± 3	6 ± 3
	8	139 ± 13	124 ± 12	11 ± 4	4 ± 3
K_S^0KK	-2	33 ± 6	52 ± 7	10 ± 4	4 ± 3
	-1	57 ± 8	50 ± 8	3 ± 2	1 ± 2
	1	92 ± 10	78 ± 9	2 ± 2	8 ± 3
	2	61 ± 8	69 ± 9	4 ± 2	3 ± 2
Total		2286 ± 48	2335 ± 48	164 ± 15	139 ± 14

The signal yield in each bin is parameterised according to the expressions in Eq. 1.34, that depend on the CP observables, $x_\pm^{DK}, y_\pm^{DK}, x_\xi^{D\pi}$ and $y_\xi^{D\pi}$, which are common to all the bins, as well as the external input values of c_i and s_i [49, 50]. The required flavour-tag fractions F_i and F_{-i} are extracted directly from the fit and common to $B^+ \to DK^+$ and $B^+ \to D\pi^+$ channels. As these fractions must satisfy $\sum F_i = 1, F_i \in [0, 1]$, there can be fit instability induced due to large correlations among the F_i parameters. Hence, following Ref. [42], the F_i fractions are reparameterised as a series of recursive fractions with parameters, $\mathcal{R}_i$, that are extracted from the fit. The $\mathcal{R}_i$ fractions are defined as

$$F_i = \begin{cases} \mathcal{R}_i & , \; i = -\mathcal{N} \\ \mathcal{R}_i \prod_{j<i}(1 - \mathcal{R}_j) & , \; -\mathcal{N} < i < +\mathcal{N} \\ \prod_{j<i}(1 - \mathcal{R}_j) & , \; i = +\mathcal{N}. \end{cases} \tag{5.1}$$

The values of $\mathcal{R}_i$ are independent for Belle and Belle II such that any difference in the acceptance profile is accounted for. The values of $\mathcal{R}_i$ are found to be compatible between Belle and Belle II within the current statistical uncertainties; the obtained values are listed in Table 5.3. However, if common $\mathcal{R}_i$ parameters are used, there is little statistical advantage in determining the CP-violating observables and an additional systematic uncertainty would be introduced related to the assumption.

Table 5.3: $\mathcal{R}_i$ values obtained for Belle and Belle II from the binned-fit.

Mode	Parameter	Belle	Belle II
$K_S^0\pi\pi$	$\mathcal{R}_1$	0.8218 ± 0.0077	0.8212 ± 0.0177
	$\mathcal{R}_2$	0.3206 ± 0.0073	0.3505 ± 0.0168
	$\mathcal{R}_3$	0.2015 ± 0.0058	0.2020 ± 0.0128
	$\mathcal{R}_4$	0.3064 ± 0.0056	0.2888 ± 0.0122
	$\mathcal{R}_5$	0.2805 ± 0.0043	0.2920 ± 0.0099
	$\mathcal{R}_6$	0.2086 ± 0.0035	0.2186 ± 0.0079
	$\mathcal{R}_7$	0.1425 ± 0.0028	0.1448 ± 0.0063
	$\mathcal{R}_8$	0.0635 ± 0.0017	0.0625 ± 0.0038
	$\mathcal{R}_9$	0.0545 ± 0.0018	0.0477 ± 0.0038
	$\mathcal{R}_{10}$	0.0055 ± 0.0006	0.0050 ± 0.0012
	$\mathcal{R}_{11}$	0.0350 ± 0.0014	0.0367 ± 0.0032
	$\mathcal{R}_{12}$	0.0786 ± 0.0022	0.0698 ± 0.0045
	$\mathcal{R}_{13}$	0.0041 ± 0.0006	0.0048 ± 0.0013
	$\mathcal{R}_{14}$	0.0070 ± 0.0007	0.0072 ± 0.0017
	$\mathcal{R}_{15}$	0.0261 ± 0.0014	0.0322 ± 0.0033
K_S^0KK	$\mathcal{R}_1$	0.5712 ± 0.0147	0.5502 ± 0.0364
	$\mathcal{R}_2$	0.2349 ± 0.0084	0.2622 ± 0.0197
	$\mathcal{R}_3$	0.4095 ± 0.0122	0.4616 ± 0.0265

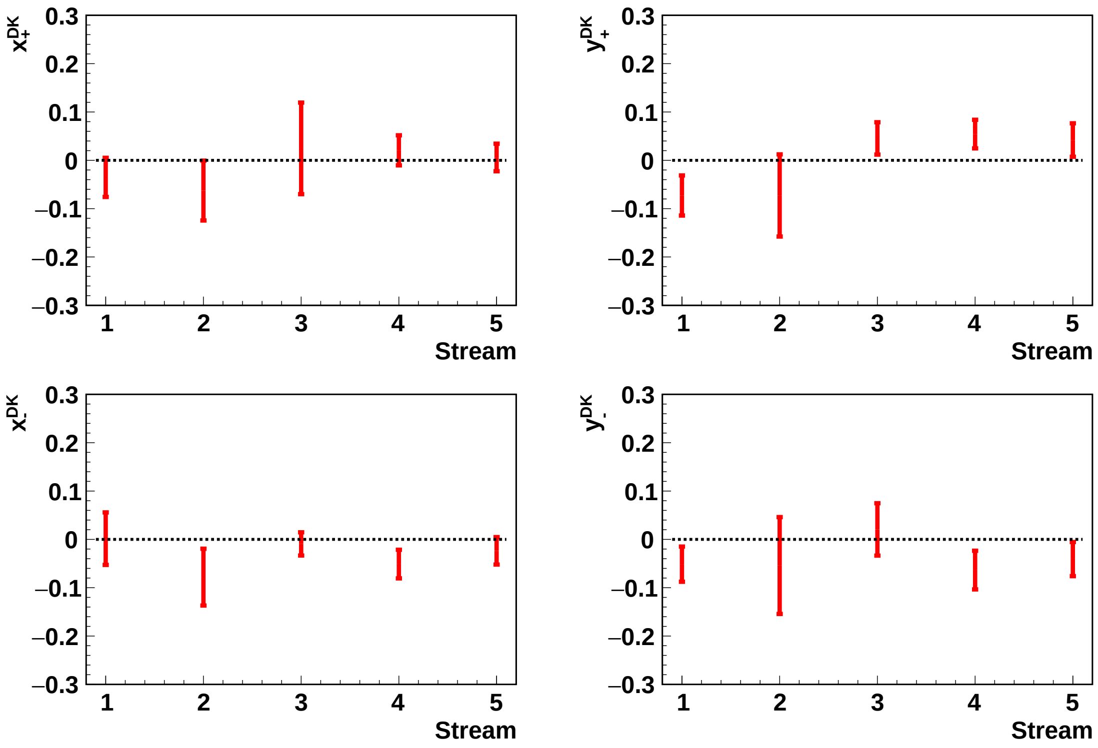

Figure 5.1: x_+^{DK} (top left), y_+^{DK} (top right), x_-^{DK} (bottom left) and y_+^{DK} (bottom right) parameter values obtained in five independent streams for Belle + Belle II combined fit. Each stream corresponds to $(711 + 128)$ fb^{-1} of independent generic MC samples.

At first, the binned fit is performed on the generic MC samples. For this purpose, five independent samples having luminosity $(711 + 128)$ fb^{-1} are used, which is equivalent to the statistics of the datasets used for the analysis, which are referred to as streams. As there is no CP-violation present in the MC samples, the expected values of the CP-observables are zero. The obtained values of the CP-observables are shown in Figs. 5.1 and 5.2; there is no bias observed for any of the parameters of interest, and the obtained values are in agreement with zero within the uncertainty.

Furthermore, a 1000 pseudo-experiments are also performed to determine if the fit model introduces any bias in the measurement of the CP-violation parameters. In order to verify the outcomes, samples are produced according to the fitted model with world

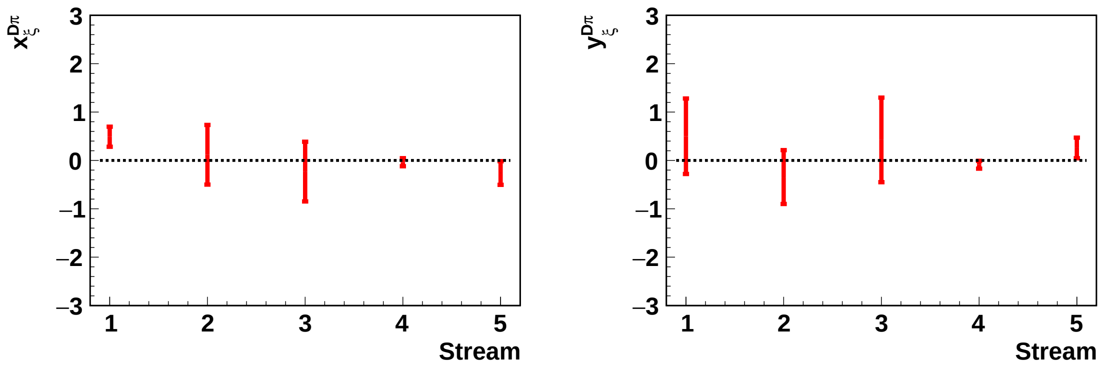

Figure 5.2: $x_\xi^{D\pi}$ (left) and $y_\xi^{D\pi}$ (right) parameter values obtained in five independent streams for Belle + Belle II combined fit. Each stream corresponds to (711 + 128) fb^{-1} of independent generic MC samples.

average values of $(x_\pm, y_\pm)$ as input, and then fitted back. The pull distributions of the output are compatible with Gaussian PDF with mean and spread values of 0 and 1, respectively. The values are shown in Table 5.4. The fit model produces no bias and is ready to be utilised on the datasets. The width of the parameter $x_\xi^{D\pi}$ is found to be smaller; it has been verified that the width becomes closer to one once the statistics of the sample increased. The pull, error and parameter values returned by the fit are shown in Appendix A.

Table 5.4: Mean and width of the pull distributions of CP-violating parameters from 1000 pseudo-experiments.

Parameter	Pull mean	Pull width
x_+^{DK}	-0.021 ± 0.022	0.967 ± 0.017
y_+^{DK}	0.003 ± 0.022	0.952 ± 0.016
x_-^{DK}	-0.024 ± 0.023	1.009 ± 0.016
y_-^{DK}	0.000 ± 0.023	1.006 ± 0.017
$x_\xi^{D\pi}$	0.076 ± 0.029	0.893 ± 0.014
$y_\xi^{D\pi}$	0.003 ± 0.023	0.975 ± 0.016

The binned fit is then performed in the combined datasets of Belle and Belle II. The fit results along with their statistical and systematic uncertainties are summarised in Sec. 5.3, and the statistical likelihood contours are shown in Fig. 5.3. The statistical and

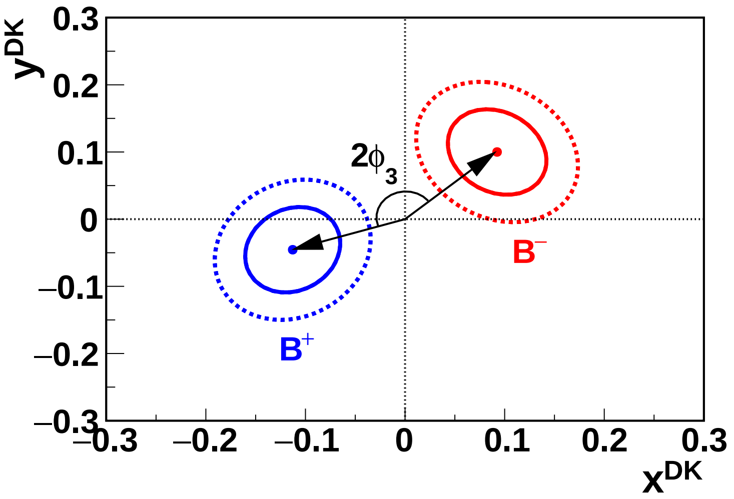

Figure 5.3: Statistical confidence levels at 68.2% and 95.5% probability for $\left(x_+^{DK}, y_+^{DK}\right)$ (blue) and $\left(x_-^{DK}, y_-^{DK}\right)$ (red) as measured in $B^+ \to DK^+$ decays from a profile likelihood scan. The dots represent central values.

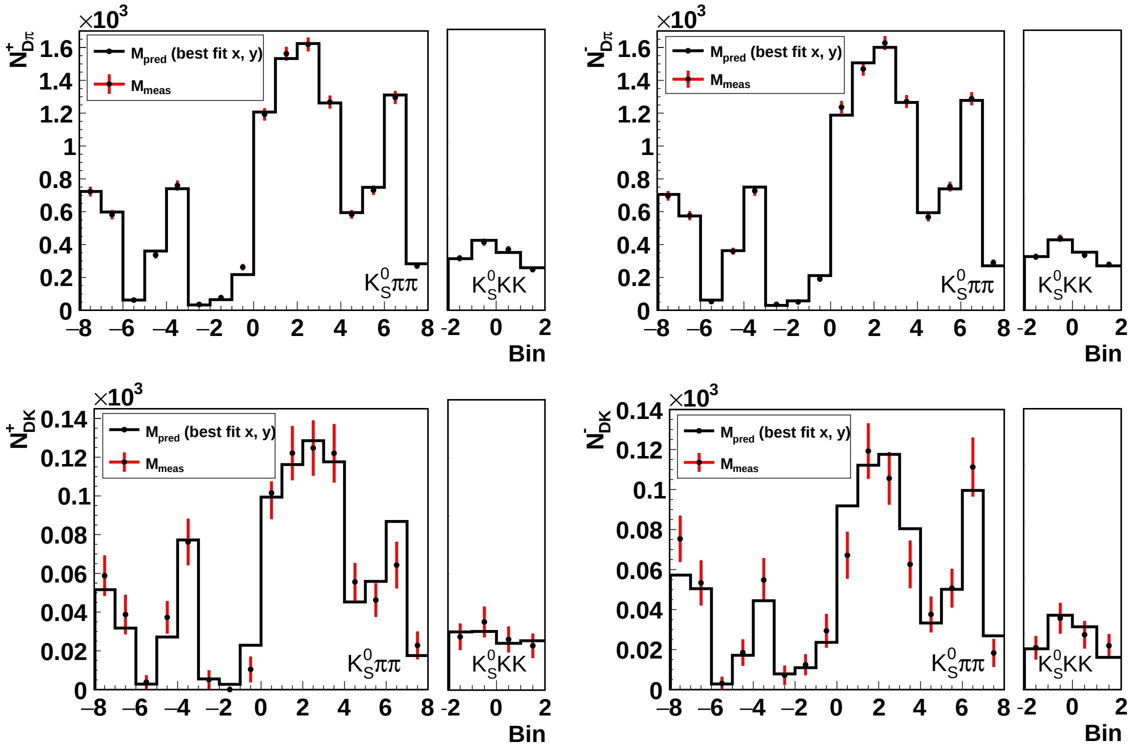

Figure 5.4: Measured and predicted yields in bins of the decays $B^+ \to D\pi^+$ (top left), $B^- \to D\pi^-$ (top right), $B^+ \to DK^+$ (bottom left) and $B^- \to DK^-$ (bottom right) in Belle dataset. The data points with error bars are the measured yields and the solid histogram is the expected yield from the best fit $(x_\pm, y_\pm)$ parameter values.

systematic correlation matrices are given in Appendix B.

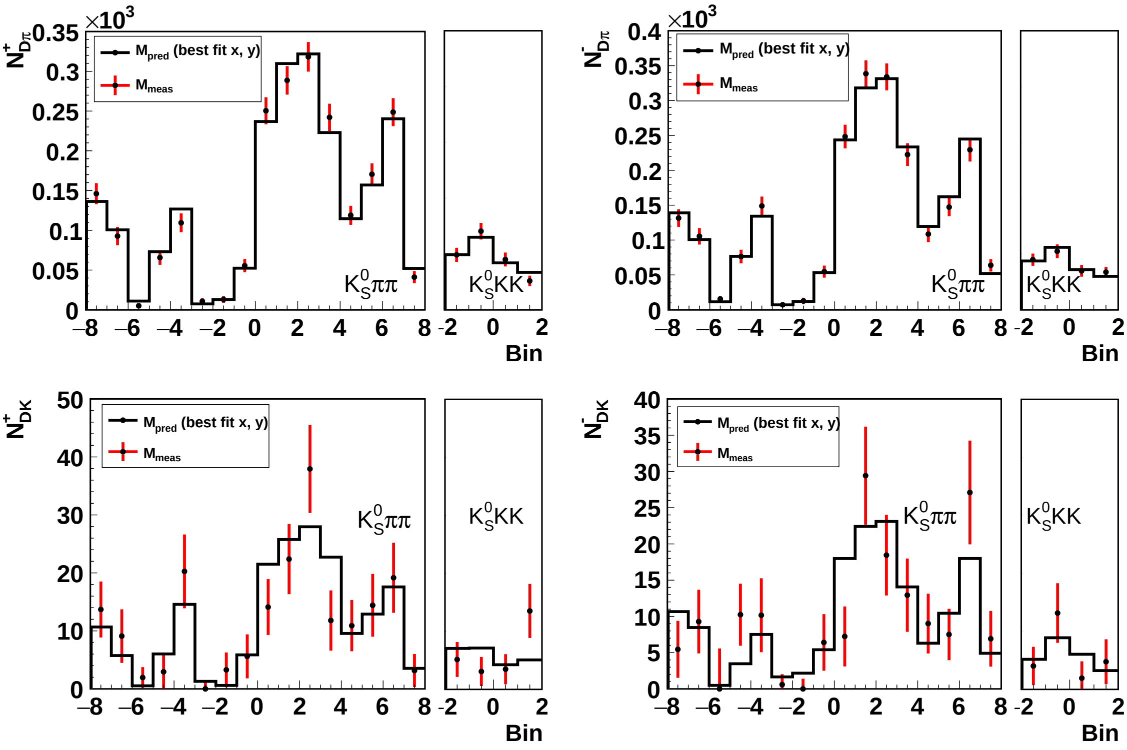

Figure 5.5: Measured and predicted yields in bins of the decays $B^+ \to D\pi^+$ (top left), $B^- \to D\pi^-$ (top right), $B^+ \to DK^+$ (bottom left) and $B^- \to DK^-$ (bottom right) in Belle II dataset. The data points with error bars are the measured yields and the solid histogram is the expected yield from the best fit $(x_\pm, y_\pm)$ parameter values.

The measured and predicted yield in each bin, from the default value of (x, y), have also been compared for all the samples as a cross check, shown in Figs. 5.4 and 5.5. The agreement between the two yields is seen to be excellent. Furthermore, the bin-by-bin asymmetries $\left(N^-_{-i} - N^+_{+i}\right) / \left(N^-_{-i} + N^+_{+i}\right)$ are also measured in each Dalitz plot bin i, which are shown in Fig. 5.6. Clear evidence for CP-violation, i.e. the non-zero value of the CP asymmetry, can be seen in the $B^+ \to DK^+$ datasets of Belle (bottom left plot of Fig. 5.6). The significance of the observed *CP* violation is assessed by comparing the likelihood to that from a fit under the no *CP*-violation hypothesis of $x^{DK}_+ = x^{DK}_-$ and $y^{DK}_+ = y^{DK}_-$. Considering only the statistical uncertainties the significance is found to be 5.8 standard deviations.

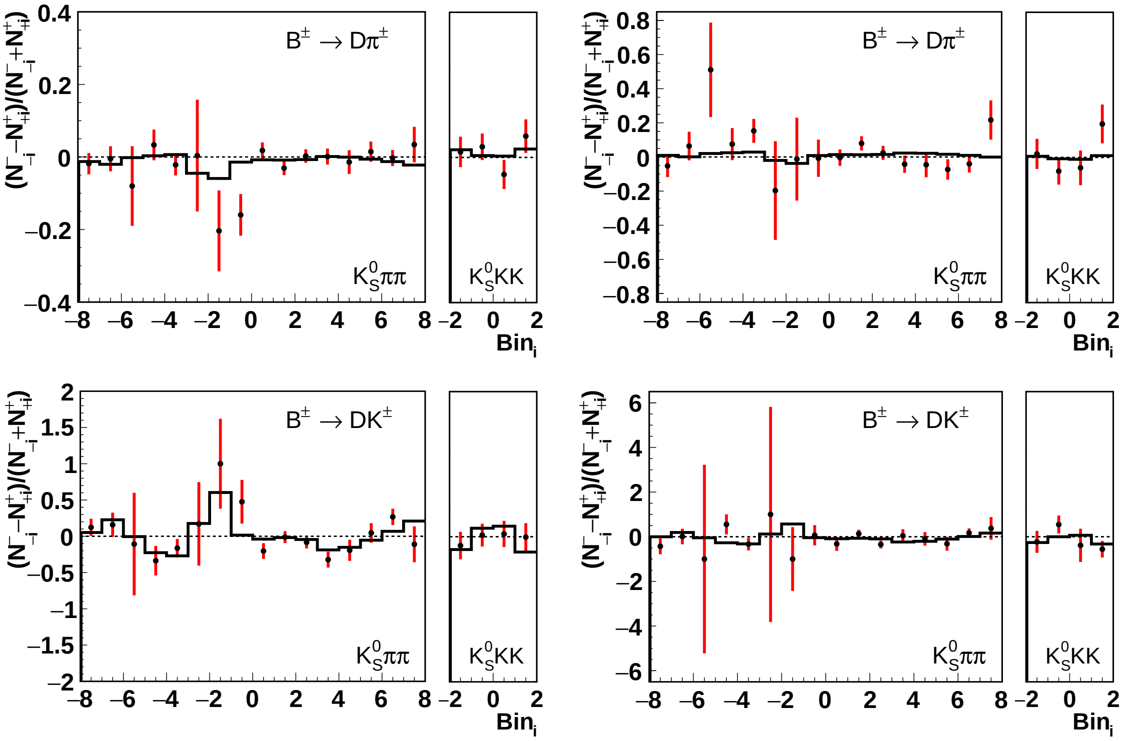

Figure 5.6: Bin-by-bin asymmetries $\left(N^-_{-i} - N^+_{+i}\right) / \left(N^-_{-i} + N^+_{+i}\right)$ in each Dalitz plot bin i for $B^+ \to D\pi^+$ (top) and $B^+ \to DK^+$ (bottom) for Belle (left) and Belle II (right) dataset. The asymmetries produced in fits with independent bin yields are given with error bars, and the prediction from the best-fit values of the (x, y) parameters is displayed with a solid line. A dotted line depicts the anticipated asymmetries in a fit that does not allow for CP violation.

5.2 SYSTEMATIC UNCERTAINTIES

Several possible sources of systematic uncertainties are considered, which are listed in Table 5.5. This section explains each source and the methodology adopted to compute the systematic uncertainties. The only correlated sources of systematic uncertainty between Belle and Belle II are the input c_i and s_i values, as well as the fit bias. All other systematic uncertainties are computed independently for Belle and Belle II, and are summed in quadrature. In general, the input nominal values are smeared with their uncertainties to calculate the systematic uncertainties. The fit is then repeated 1000 times and the resulting width of the fit physics parameter distribution

Table 5.5: Different sources of systematic uncertainties and the corresponding magnitudes. All values are multiplied by 10^{-2}.

Source	$\sigma_{x_+^{DK}}$	$\sigma_{y_+^{DK}}$	$\sigma_{x_-^{DK}}$	$\sigma_{y_-^{DK}}$	$\sigma_{x_\xi^{D\pi}}$	$\sigma_{y_\xi^{D\pi}}$
Fit bias	0.16	0.06	0.12	0.16	0.49	0.10
PDF parametrisation	0.07	0.08	0.12	0.16	0.12	0.12
PID	< 0.01	< 0.01	< 0.01	0.01	< 0.01	< 0.01
Peaking bkg	0.03	0.05	0.03	0.04	0.02	0.10
Bin-migration	< 0.01	< 0.01	< 0.01	< 0.01	< 0.01	0.03
Total	0.18	0.11	0.17	0.23	0.51	0.19
Input c_i, s_i	0.22	0.55	0.23	0.67	0.73	0.82
Statistical	3.15	4.20	3.27	4.20	4.75	5.44

is considered as systematic uncertainty. If the input values are correlated, the Cholesky decomposition [102] of the covariance matrix has been used to smear the uncertainties, which takes the correlation into account. It is a numerical optimization technique widely used in linear algebra, which decomposes an Hermitian, positive definite matrix into a lower triangular and its conjugate component and can later be used for optimally performing algebraic operations. If α is the vector of central values of parameters, A is the Cholesky decomposition of covariance matrix for elements in α and Z is the vector of Gaussian random variables with mean zero and standard deviation one, the vector of correlated variables X is obtained from α as $X = \alpha + AZ$. Since the covariance matrices are always symmetric and positive definite, the Cholesky decomposition is guaranteed. The matrix A is the decomposition of statistical and systematic covariance matrix added together. This approach is used to compute the contributions of the external inputs c_i and s_i and any correlated fixed parameters used to describe the PDFs. The correlations of the external inputs are taken from the Refs. [49, 50], and for the fixed parameters, are considered from the individual component fits to the simulated samples. The results are listed in Table 5.5. The corresponding uncertainties are less than 20% and 5% of the total statistical uncertainty for the external inputs and the fixed parameters, respectively. The systematic uncertainties related to PID are also calculated using this same strategy, where the efficiency and $K - \pi$ misidentification rates are varied within their uncertainty, independently for Belle and Belle II.

The possible contribution of peaking background from charmless decays has been ignored in the analysis so far. The possible effect is studied by performing the analysis on the sidebands of the D candidate invariant mass distribution. Only a small fraction of peaking events appeared for $B^+ \to D\pi^+$ whereas for $B^+ \to DK^+$, there is no events observed; the distributions in Belle data set are shown in Fig. 5.7. Studies of the simulated samples indicate that the main contributions arise from $B^+ \to K^{*+}\pi^-\pi^+$ and $B^+ \to K^{*+}\rho^0$ decays. The yields are obtained from fits to sideband data and then the peaking background yields are fixed in a fit to data; the peaking background is modelled using the same PDF distributions as the signal component. The obtained yields (scaled to the width of the selected D mass window) are 155 ± 15 for Belle, and 112 ± 11 for Belle II. The peaking background yield in Belle II is relatively higher than that in Belle; the extra events are $B \to K^* J/\psi$ decays because the muon to pion fake-rate is higher in Belle II. The resulting bias in the central values of the physics parameters, which is two orders of magnitude smaller than the statistical uncertainty, is considered as a systematic uncertainty.

Any bias in the fit is investigated using linearity tests. Many simulated data sets of bin yields are generated for five different values of $x_\pm^{DK}$, $y_\pm^{DK}$, $x_\xi^{D\pi}$ and $y_\xi^{D\pi}$: $0, \pm 0.05$ and ± 0.1. Each sample is then fit to determine the parameters. For an unbiased sample a graph of generated versus fit values should be linear with slope one and intercept zero.

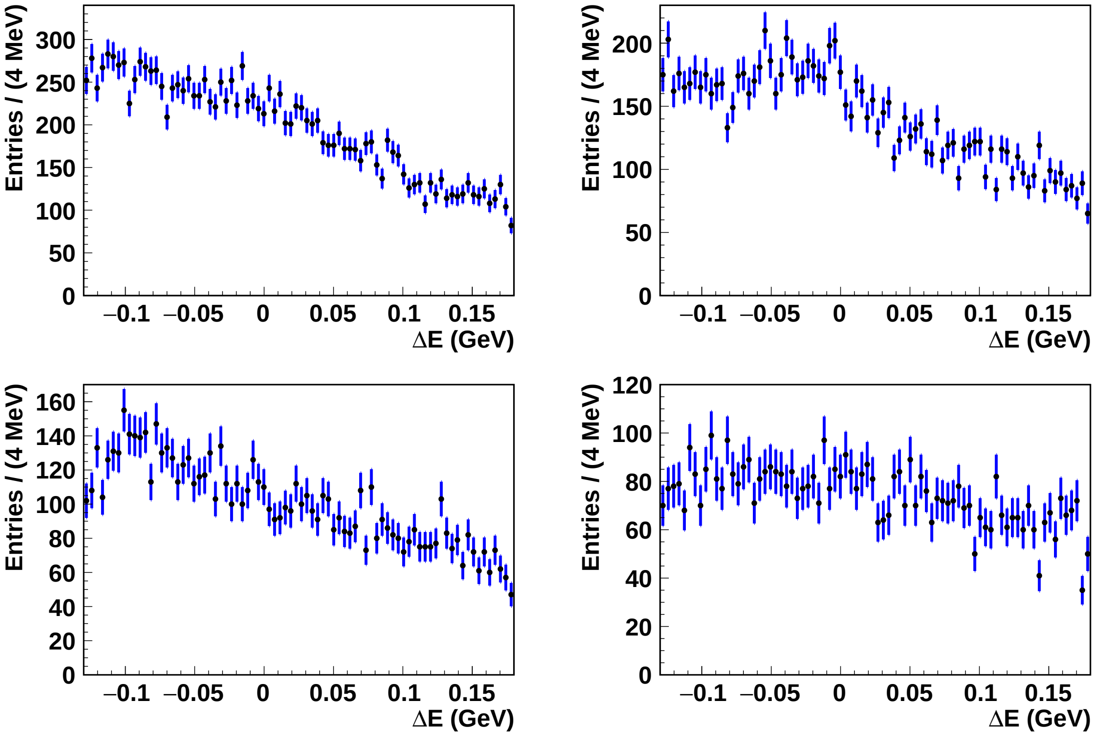

Figure 5.7: D invariant distributions of $B^+ \to D\pi^+$ (top) and $B^+ \to DK^+$ (bottom) in lower sideband, $1.80 < M_D < 1.85$ (left), and upper sideband, $1.88 < M_D < 1.92$ (left), in Belle data set.

The obtained results are shown in Figs. 5.8, 5.9 and 5.10. There is no significant bias observed for any of the parameters. The slopes agree with unity except for $x_\xi^{D\pi}$, which differs by a three standard deviations. As this is a nuisance parameter in the fit, it has no impact on the final ϕ_3 extraction. The systematic uncertainty is considered as the deviation of the slope from one times the obtained data central values.

The contribution of migration between D-decay Dalitz plot bins due to the finite resolution of $m_\pm^2$ has also been checked. The definition of F_i includes the effect of migration if it is the same in the $B^+ \to D\pi^+$ and $B^+ \to DK^+$ samples. However, the presence of *CP* violation means the Dalitz plot densities of the two samples are different, which can lead to differing levels of migration. Therefore, samples of events including *CP* violation are generated and fitted, with and without the effect of $m_\pm^2$ resolution

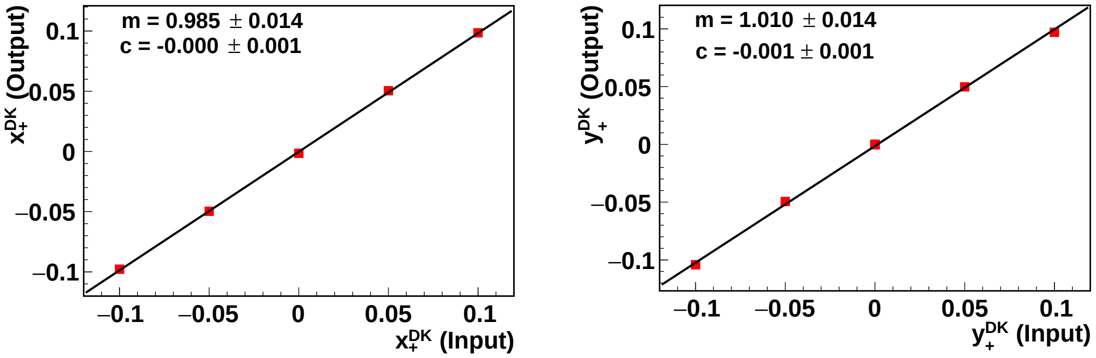

Figure 5.8: x_+^{DK} (left) and y_+^{DK} (right) results for different input values in 1000 pseudo-experiment sets each.

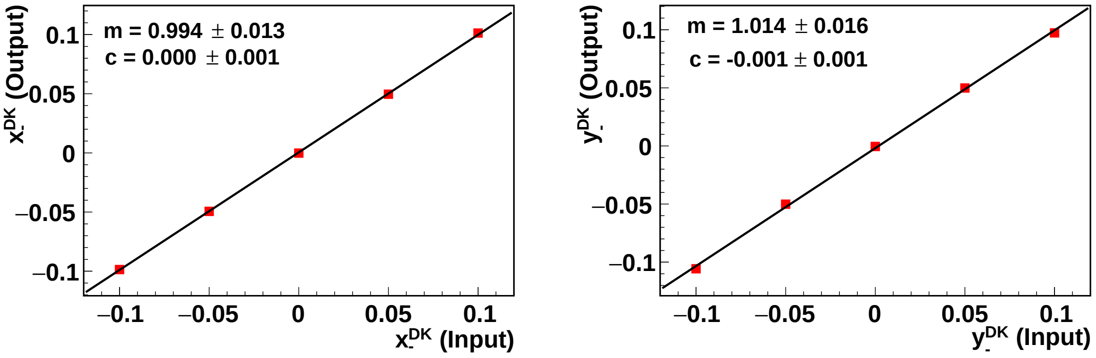

Figure 5.9: x_-^{DK} (left) and y_-^{DK} (right) results for different input values in 1000 pseudo-experiment sets each.

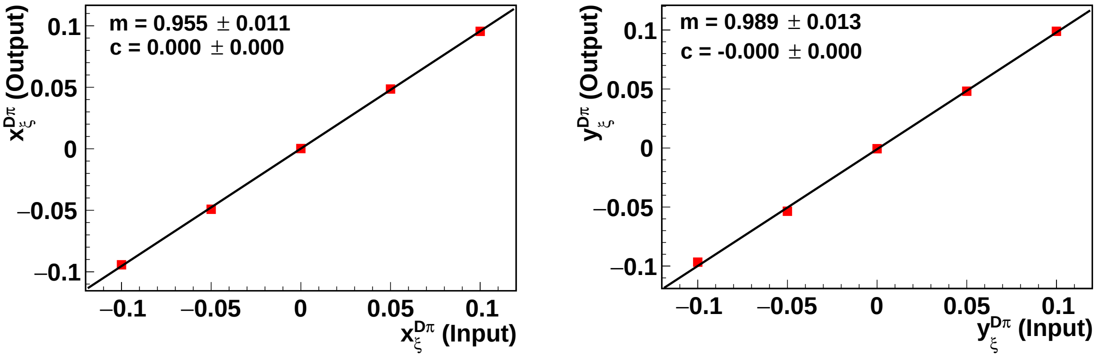

Figure 5.10: $x_\xi^{D\pi}$ (left) and $y_\xi^{D\pi}$ (right) results for different input values in 1000 pseudo-experiment sets each.

included. The parameter values shift less than 10^{-4} except for $y_\xi^{D\pi}$; the full bias is associated as a systematic uncertainty on $y_\xi^{D\pi}$.

The values of F_i are assumed to be the same for $B^+ \to D\left(K_S^0 h^+ h^-\right) K^+$ and

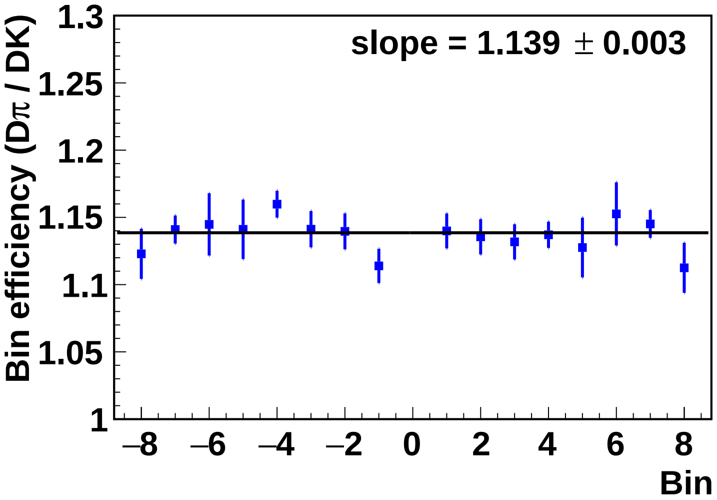

Figure 5.11: Ratio of efficiencies of $B^+ \to D\pi^+$ to $B^+ \to DK^+$ over Dalitz plot bins in Belle signal MC sample.

$B^- \to (K^0_S h^+ h^-)\pi^+$ decays. In principle a small difference exists due to the altered kinematics induced by the differing pion and kaon masses. The validity of the assumption is investigated in large simulated samples. No significant difference is observed in the values of F_i so no related systematic uncertainty is assigned. The efficiency ratio $D\pi/DK$ is demonstrated in Fig. 5.11 and it is constant over the Dalitz plot bins. The consideration of how the Belle and Belle II Dalitz plot acceptance might distort the effective values of c_i and s_i is also taken into account, which are measured assuming a uniform acceptance. The values are calculated with and without the Belle (Belle II) acceptance included. The deviations in the values of c_i and s_i are at most an order of magnitude smaller than the reported uncertainties [49, 50], which are already considered in our measurement. Therefore, this potential source of systematic uncertainty is ignored.

As a further check of the fit performance, a total of 1000 pseudo-experiments are generated with mean signal yields that correspond to the measured values of CP-

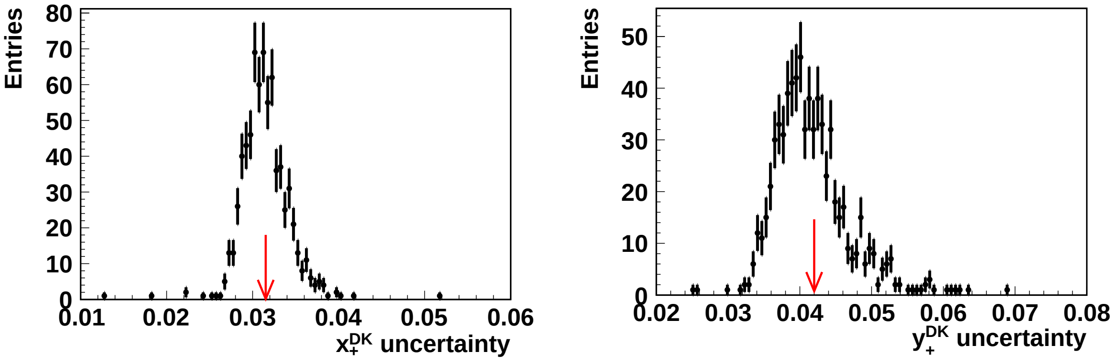

Figure 5.12: Uncertainties of the x_+^{DK} (left) and y_+^{DK} (right) parameters obtained from the 1000 pseudo-experiments. The red arrows show the acquired uncertainty in data.

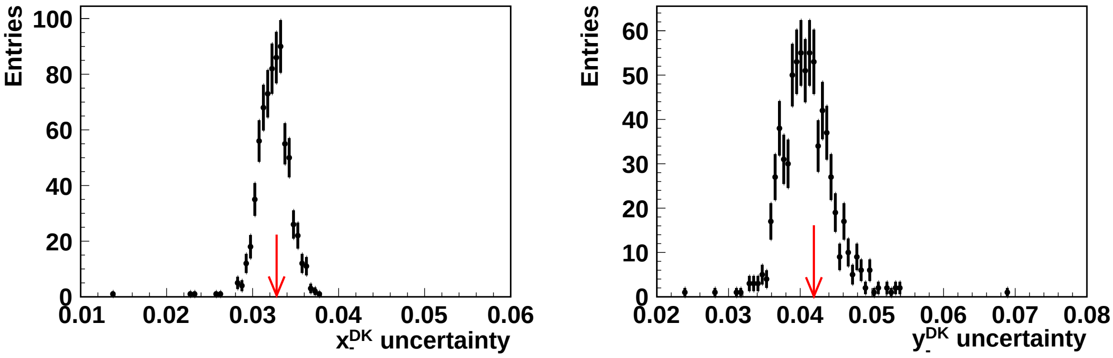

Figure 5.13: Uncertainties of the x_-^{DK} (left) and y_-^{DK} (right) parameters obtained from the 1000 pseudo-experiments. The red arrows show the acquired uncertainty in data.

violating parameters. These samples are then fit in an identical manner to the data. The results verify the fit is stable and unbiased with the current sample size, as well as providing the appropriate statistical coverage. The uncertainties on measured CP-violating parameters in data are found to be lie within the distribution of uncertainties generated by these pseudo-experiments. The resulting distribution of the uncertainties are shown in Figs. 5.12, 5.13 and 5.14.

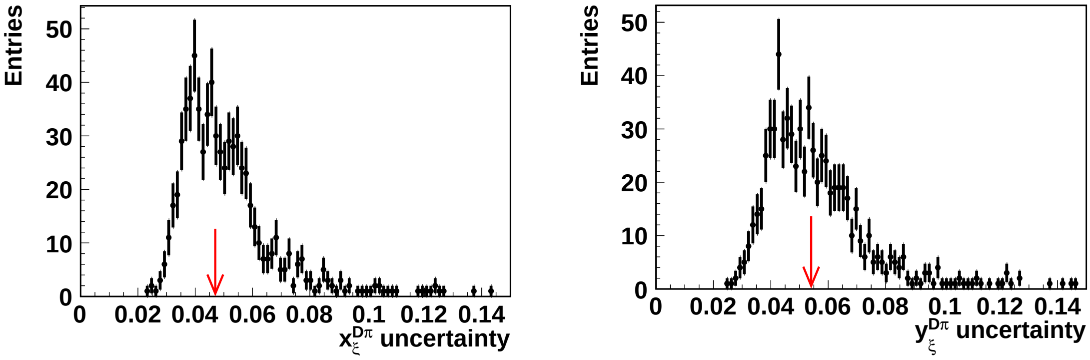

Figure 5.14: Uncertainties of the $x_\xi^{D\pi}$ (left) and $y_\xi^{D\pi}$ (right) parameters obtained from the 1000 pseudo-experiments. The red arrows show the acquired uncertainty in data.

5.3 DETERMINATION OF ϕ_3, r_B AND δ_B

The parameters obtained from the fit are

$$\begin{aligned} x_-^{DK} &= (9.24 \pm 3.27 \pm 0.13 \pm 0.23) \times 10^{-2}, \\ y_-^{DK} &= (10.00 \pm 4.20 \pm 0.22 \pm 0.67) \times 10^{-2}, \\ x_+^{DK} &= (-11.28 \pm 3.15 \pm 0.18 \pm 0.22) \times 10^{-2}, \\ y_+^{DK} &= (-4.55 \pm 4.20 \pm 0.10 \pm 0.55) \times 10^{-2}, \\ x_\xi^{D\pi} &= (-11.09 \pm 4.75 \pm 0.51 \pm 0.73) \times 10^{-2}, \\ y_\xi^{D\pi} &= (-7.90 \pm 5.44 \pm 0.18 \pm 0.82) \times 10^{-2}, \end{aligned} \tag{5.2}$$

where the first uncertainty is statistical, the second uncertainty is the total experimental systematic uncertainty, and the third uncertainty is the systematic uncertainty due to the external strong-phase difference inputs [49, 50].

The parameters, $\phi_3, r_B^{DK}, \delta_B^{DK}, r_B^{D\pi}$ and δ_B^{DK}, are determined from $x_\pm^{DK}, y_\pm^{DK}, x_\xi^{D\pi}$ and $y_\xi^{D\pi}$, where the frequentist approach described in Ref. [103] is used. The best central values are obtained via a maximum likelihood fit in this approach. The statistical approach used to calculate the best value of the physics parameters and confidence regions are discussed below.

If the collection of all observables for which a measurement has been performed is denoted A, and the set of underlying physics parameters are denoted α, then for a specific set of measurement results A_{obs}, the likelihood function is defined as

$$\mathcal{L}(\alpha|A_{\text{obs}}) = f(A_{\text{obs}}|\alpha), \tag{5.3}$$

where $f(A|\alpha)$ represent the probability density function of the measurement results A. The estimation of α is done by maximizing the likelihood function. In practice, a χ^2 function defined as

$$\chi^2(\alpha|A_{\text{obs}}) = -2\ln\mathcal{L}(\alpha|A_{\text{obs}}) \tag{5.4}$$

is minimized instead. If the likelihood profile is Gaussian, it can be expressed as

$$\chi^2(\alpha|A_{\text{obs}}) = (A_{\text{obs}} - A(\alpha))^T V^{-1}(A_{\text{obs}} - A(\alpha)) + c, \tag{5.5}$$

where V represent the experimental covariance matrix for the observables, $A(\alpha)$ denotes the value of the observables expressed in terms of the underlying physics parameters, and c is a constant that is independent of α. In our analysis,

$$\begin{aligned} A &= (x_-^{DK}, y_-^{DK}, x_+^{DK}, y_+^{DK}) \\ \alpha &= (\phi_3, r_B, \delta_B). \end{aligned} \tag{5.6}$$

The χ^2 function defined in Eq. 5.5 is minimized to give best estimate of ϕ_3. The confidence levels (CL) are calculated using a pseudo-experiment based frequentist method [104], which is based on the approach by Feldman and Cousins [105] and has been extended by introducing the concept of nuisance parameters. To evaluate the confidence level, a new minimum, $\chi^2(\alpha'_{\text{min}})$, is considered for a given value of a certain parameter, say $\phi_3 = \phi_3^0$. This changes the profile likelihood function to $\mathcal{L} = \exp(-\chi^2(\alpha'_{\text{min}})/2)$. Then a test statistic is defined as

$$\Delta\chi^2 = \chi^2(\alpha'_{\text{min}}) - \chi^2(\alpha_{\text{min}}). \tag{5.7}$$

The p-value, or $1 - \text{CL}$, is calculated by means of a Monte Carlo procedure, described in Ref. [106]. For each value of ϕ_3^0:

1. $\Delta\chi^2$ is calculated;
2. a set of pseudo-experiments $\{A_{\text{toy}}\}$ is generated using Eq. 5.3 with parameters α set to α'_{min} as the PDF;
3. $\Delta\chi^{2'}$ of the pseudo-experiment is calculated by replacing $A_{\text{obs}} \to A_{\text{toy}}$ and minimising with respect to α, once with ϕ_3 as a free parameter, and once with ϕ_3 fixed to ϕ_3^0;
4. $1 - \text{CL}$ is calculated as the fraction of pseudo-experiments which perform worse ($\Delta\chi^2 < \Delta\chi^{2'}$) than the measured data.

This method is sometimes known as the "$\hat{\mu}$", or the "plug-in" method. The `GammaCombo` software package [104] follows this procedure to calculate the

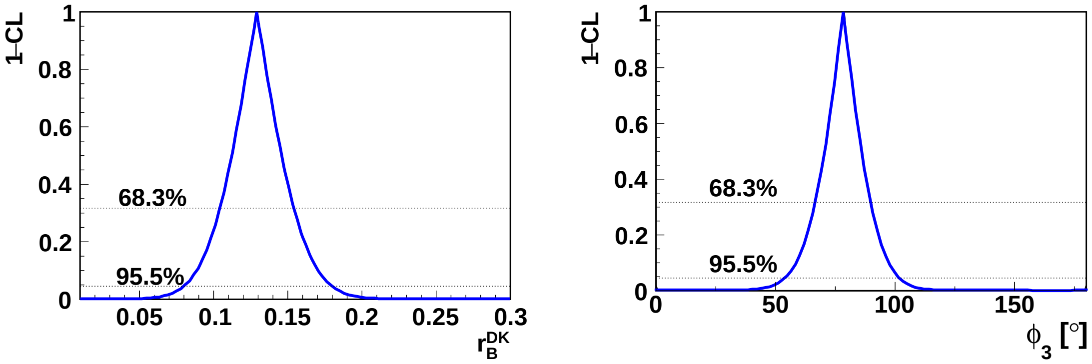

Figure 5.15: Statistical confidence limits obtained for r_B^{DK} (left) and ϕ_3 (right) using the methods described in Ref. [103].

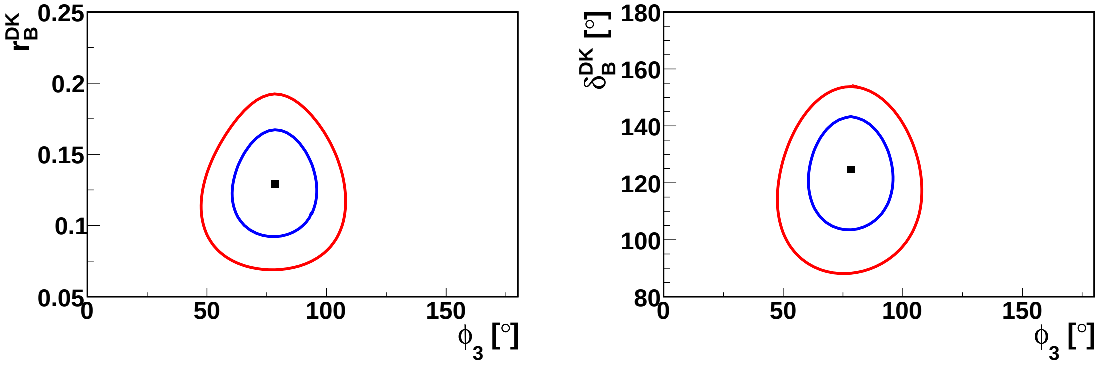

Figure 5.16: Two-dimensional statistical confidence regions, 68% and 95%, obtained for the $\phi_3 - r_B^{DK}$ (left) and $\phi_3 - \delta_B^{DK}$ (right) parameter combinations obtained using the methods described in Ref. [103].

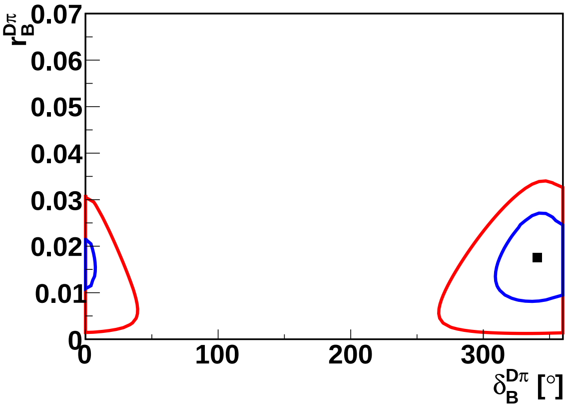

Figure 5.17: Two-dimensional statistical confidence regions, 68% and 95%, obtained for the $r_B^{D\pi} - \delta_B^{D\pi}$ parameter combinations obtained using the methods described in Ref. [103].

confidence regions; this software package is used for the best value estimation of the physics parameters and confidence regions.

Generally, there is a two-fold ambiguity in the results of these physics parameters as the Eqs. 1.34 are invariant under the substitutions of $\phi_3 = \phi_3 + 180^\circ$ and $\delta_B = \delta_B + 180^\circ$. The solution in the range $0^\circ < \phi_3 < 180^\circ$ is chosen that corresponds to the one favoured by other measurements of the unitarity triangle [33]. The measured values from ($x_{\pm}^{DK}, y_{\pm}^{DK}, x_{\xi}^{D\pi}$ and $y_{\xi}^{D\pi}$) are

$$\begin{aligned}
\phi_3(^\circ) &= 78.4 \pm 11.4\,(\text{stat.}) \pm 0.5\,(\text{syst.}) \pm 1.0\,(\text{ext. input}),\\
r_B^{DK} &= 0.129 \pm 0.024\,(\text{stat.}) \pm 0.001\,(\text{syst.}) \pm 0.002\,(\text{ext. input}),\\
\delta_B^{DK}(^\circ) &= 124.8 \pm 12.9\,(\text{stat.}) \pm 0.5\,(\text{syst.}) \pm 1.7\,(\text{ext. input}),\\
r_B^{D\pi} &= 0.017 \pm 0.006\,(\text{stat.}) \pm 0.001\,(\text{syst.}) \pm 0.001\,(\text{ext. input}),\\
\delta_B^{D\pi}(^\circ) &= 341.0 \pm 17.0\,(\text{stat.}) \pm 1.2\,(\text{syst.}) \pm 2.6\,(\text{ext. input}).
\end{aligned} \tag{5.8}$$

The systematic uncertainty is estimated by varying the ($x_{\pm}^{DK}, y_{\pm}^{DK}, x_{\xi}^{D\pi}$ and $y_{\xi}^{D\pi}$) parameters by their corresponding systematic uncertainties. The statistical confidence intervals for ϕ_3 and r_B^{DK} are illustrated in Fig. 5.15, while Fig. 5.16 shows the two-dimensional statistical confidence regions obtained for the (ϕ_3, r_B^{DK}) and (ϕ_3, δ_B) parameter combinations. Fig. 5.17 shows the two-dimensional statistical confidence region obtained for the ($\delta_B^{D\pi}, r_B^{D\pi}$) parameter combination; the 95% confidence region is compatible with the most precise values of these parameters reported [107]. The result is consistent with the previous Belle analysis [45] but the statistical precision is improved from 15°. The uncertainty related to strong-phase inputs has also decreased from 4° because of the new measurements reported by the BESIII collaboration [49, 50].

CHAPTER 6

Beam-energy calibration at Belle II

The desired center-of-mass (CM) energy at which the B mesons are produced corresponds to the mass of the Υ(4S) resonance, which is 10.58 GeV. An accurate determination of the CM energy is crucial for many physics analyses as it enters the two principal variables, ΔE and M_{bc}, that distinguish signal from background, along with being an input for calibrations of the momentum and energy scale. The determination of the beam energy in the CM frame is performed, which is half the CM energy. In some measurements, the shift in the beam energy can be the principal source of systematic uncertainty. For example, in the τ mass measurement at Belle, the systematic uncertainty due to the shift in beam-energy is 70% of the total systematic uncertainty [108]. The τ mass measurement at Belle II as a function of shift in beam-energy is shown in Fig. 6.1. The actual CM energy fluctuates because of run-by-run differences in the accelerator configuration. The average CM energy ($E_{\rm cms}$) is calculated along with its uncertainty and the spread of the distribution of the CM energy ($\sigma_{E_{\rm cms}}$) for the data recorded by Belle II detector during 2020 run.

The remainder of this chapter is structured as follows. In Sec. 6.1 the method for determining the correct beam-energy using the shift from the nominal value is discussed. Section 6.2 details the requirements used to select the hadronic decays of interest and Sec. 6.3 describes the fit to the $M_{\rm bc}$ distribution and the beam-energy values obtained for 2019 and 2020 collision data. The systematic uncertainties are discussed in Sec. 6.4. The results are summarized in Sec. 6.5.

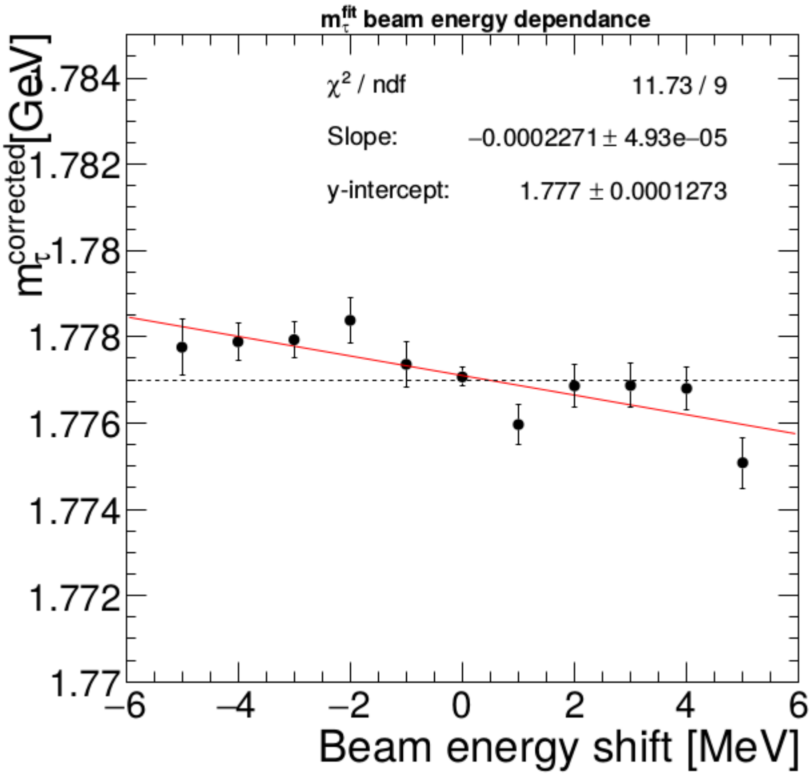

Figure 6.1: The τ mass measurement at Belle II as a function of shift in beam-energy.

6.1 METHOD TO DETERMINE BEAM-ENERGY SHIFT

One of the most important kinematic variables used for B-meson reconstruction is the beam-constrained mass ($M_{\rm bc}$), which is defined as

$$M_{\rm bc} = \sqrt{E^{*2}_{\rm beam} - \left(\overrightarrow{\mathbf{p}^*_B}\right)^2}, \tag{6.1}$$

where $E^*_{\rm beam}$ is the assumed beam-energy in the CM frame and $\overrightarrow{\mathbf{p}^*_B}$ is the momenta of the B meson in the CM frame. The nominal value of $M_{\rm bc}$ is either m_{B^+} or m_{B^0}. The resolution of $M_{\rm bc}$ is dominated by the beam-energy spread rather than the $\overrightarrow{\mathbf{p}^*_i}$ uncertainties [109].

Considering the error propagation of Eq. 6.1 (neglecting the uncertainty on $\overrightarrow{\mathbf{p}_B^*}$),

$$\frac{\delta M_{\rm bc}}{\delta E^*_{\rm beam}} = \frac{E^*_{\rm beam}}{\sqrt{E^{*2}_{\rm beam} - \overrightarrow{\mathbf{p}_B^{*2}}}}. \tag{6.2}$$

Hence, the shift in the beam energy $\delta E_{\rm beam}$ is calculated using the expression

$$\delta E^*_{\rm beam} = \frac{M_B}{E^*_{\rm beam}} \times \delta M_{\rm bc} \ , \tag{6.3}$$

where

$$\delta M_{\rm bc} = \mu\left(M_{\rm bc}\right) - M_B \ , \tag{6.4}$$

$$\delta E^*_{\rm beam} = E^*_{\rm beam} - E^{*\ \rm actual} \ , \tag{6.5}$$

where $\mu\left(M_{\rm bc}\right)$ is the measured mean of the $M_{\rm bc}$ signal peak. Here, the input is $E^*_{\rm beam} = \sqrt{s}/2$ = 5289.70 MeV, M_B is the nominal B meson mass and the value of is either 5279.31 ± 0.15 MeV$/c^2$ or 5279.62 ± 0.15 MeV$/c^2$ for B^+ or B^0 decays, respectively [8]. $E^{*\ \rm actual}$ is the correct beam-energy in the CM frame and is the final output of this study.

The beam energy spread $\sigma_{\rm E^*_{beam}}$ is defined as [109]:

$$\sigma^2_{\rm M_{bc}} \approx \sigma^2_{\rm E^*_{beam}} + \left(\frac{\overrightarrow{\mathbf{p}_B^*}}{M_B}\right)^2 \sigma^2_{\mathbf{p}_B^*}, \tag{6.6}$$

where $\sigma_{\rm M_{bc}}$ is the resolution of $M_{\rm bc}$, and $\sigma_{\mathbf{p}_B^*}$ is the uncertainty on p_B^*. The typical value of $\sigma_{\mathbf{p}_B^*}$ is of the order of 0.5 MeV. As the B mesons are almost at rest in the CM frame,

$|\overrightarrow{\mathbf{p}_B^*}|/M_B \approx 0.06$, the second term in the above equation is small. Hence, the resolution in $M_{\rm bc}$ is dominated by the spread in the beam energy [109].

The analysis proceeds as follows. First, the full run-range of any data set is divided into sub-ranges that have roughly equal luminosity. Second, $\mu\,(\rm M_{bc})$ is obtained from a one-dimensional maximum likelihood fit to the $M_{\rm bc}$ distribution of fully reconstructed B mesons within the different sub-ranges. Finally, the value of $\mu\,(\rm M_{bc})$ is used in Eq. 6.4 to determine $\delta M_{\rm bc}$, which when inserted in Eq. 6.3 gives $\delta E^*_{\rm beam}$ in each sub-range.

6.2 EVENT SELECTION AND RECONSTRUCTION

The following charged and neutral B decay modes are reconstructed for this measurement:

- $B^- \to D^0(K^-\pi^+, K^-\pi^+\pi^0, K^-\pi^+\pi^-\pi^+)\pi^-$,
- $\overline{B}^0 \to D^{*+}[D^0(K^-\pi^+, K^-\pi^+\pi^0, K^-\pi^+\pi^-\pi^+)\pi^+]\pi^-$, and
- $\overline{B}^0 \to D^+[K^-\pi^+\pi^+]\pi^-$.

These final states are Cabibbo favoured in nature and have comparatively larger branching fractions [8]. Hence, these channels are chosen to have sufficient sample size in each sub-range.

Charged particle tracks are selected by requiring $|dr| <$ 0.5 cm and $|dz| <$ 3 cm, where dr and dz represent the distance of the closest approach to the IP in the plane transverse to the beam direction and in the opposite direction to beam, respectively. The coordinate

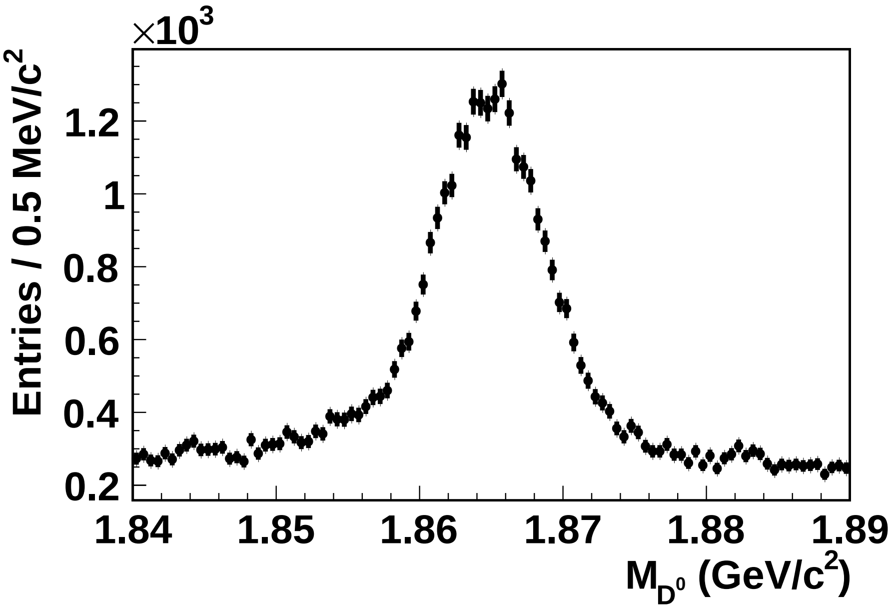

Figure 6.2: D^0 invariant mass distribution in the selected region for the channel $B^- \to D^0(K^-\pi^+)\pi^-$ in generic MC sample.

system of Belle II is defined in Chapter 2. These tracks are then identified as kaons and pions by PID selection $\mathcal{L}(K/\pi) > 0.6$ and $\mathcal{L}(K/\pi) < 0.6$, respectively. The π^0 candidates are reconstructed from photon pairs. The energy of each photon is required to be greater than 30, 80, and 60 MeV depending upon whether it is reconstructed in the barrel, forward, and backward end-cap region of the ECL, respectively; the differing thresholds are motivated by the different levels of beam-induced background within the regions. The D^0 and D^- invariant mass is restricted to $1.84 < M_{D^0} < 1.89$ GeV/c^2 and $1.844 < M_{D^-} < 1.894$ GeV/c^2, respectively, to reduce combinatorial backgrounds. These selections are corresponding to 4σ from the nominal mass of D^0 and D^- [8], respectively, where σ represents the invariant mass resolution. The invariant mass distributions of D^0 and D^- in the generic MC sample are shown in Figs. 6.2 and 6.3.

The mass difference $M(D^0\pi^+) - M(D^0)$, also known as ΔM, required to be in the interval $0.143 < \Delta M < 0.147$ GeV/c^2 to suppress the backgrounds coming from

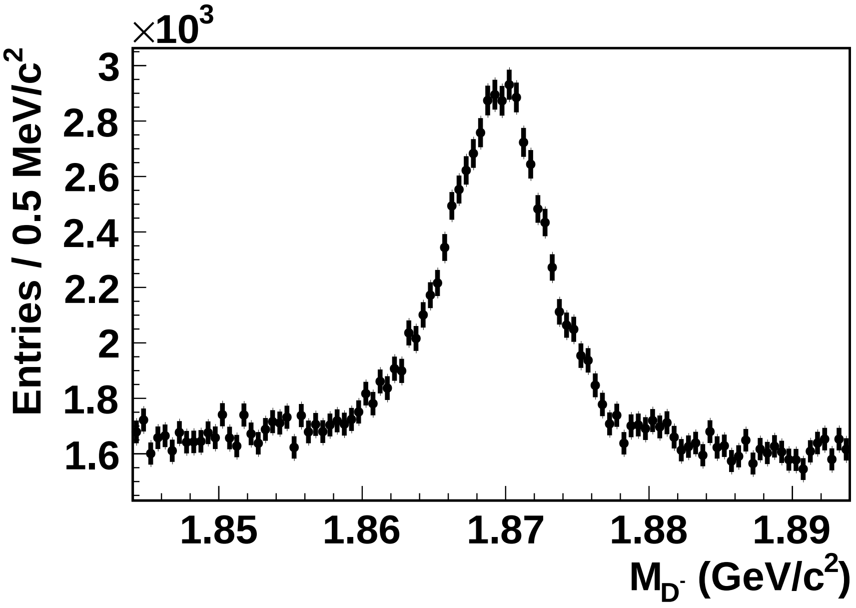

Figure 6.3: D^- invariant mass distribution in the selected range for the channel $B^0 \to D^-(K^-\pi^+\pi^-)\pi^+$ in generic MC sample.

$e^+e^- \to c\bar{c}$ events. The ΔM distribution for the channel $\overline{B}^0 \to D^{*+}[D^0(K^-\pi^+)\pi^+]\pi^-$ in generic MC sample is shown in Fig. 6.4. Generally, the value peaks at 145.4 MeV/c^2 for signal candidates [8] and the typical resolution is $\sigma = 0.6$ MeV/c^2. The 3σ window around the mean value is selected for this analysis. The continuum ($q\bar{q}$ events) background events are rejected by applying the cut on the ratio of second and zeroth Fox-Wolfram moment $R_2 <$ 0.3. The R_2 distribution for signal and background events is shown in Fig. 6.5. For $B\bar{B}$ events, the R_2 value is closer to zero because of its spherical topology, and for continuum events, R_2 takes higher values due to the back-to-back jet like structure [91]. The B meson kinematic variables ΔE and $M_{\rm bc}$ are chosen within the range $|\Delta E| < 0.05$ GeV and $5.2 < M_{\rm bc} < 5.29$ GeV/c^2, respectively. The ΔE and $M_{\rm bc}$ distributions in generic MC sample are shown in Figs. 6.6 and 6.7, respectively. These decay modes are high-statistics control channels for several analyses. The signal yields and efficiencies of these channels are reported

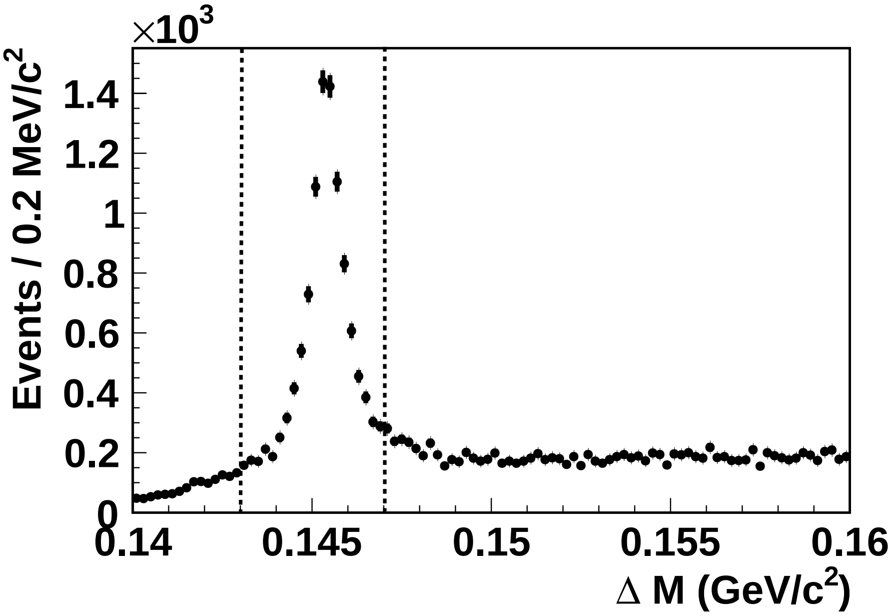

Figure 6.4: ΔM distribution for the channel $\overline{B}^0 \to D^{*+}[D^0(K^-\pi^+)\pi^+]\pi^-$ in generic MC sample. The black dotted lines represent where the selections have been applied.

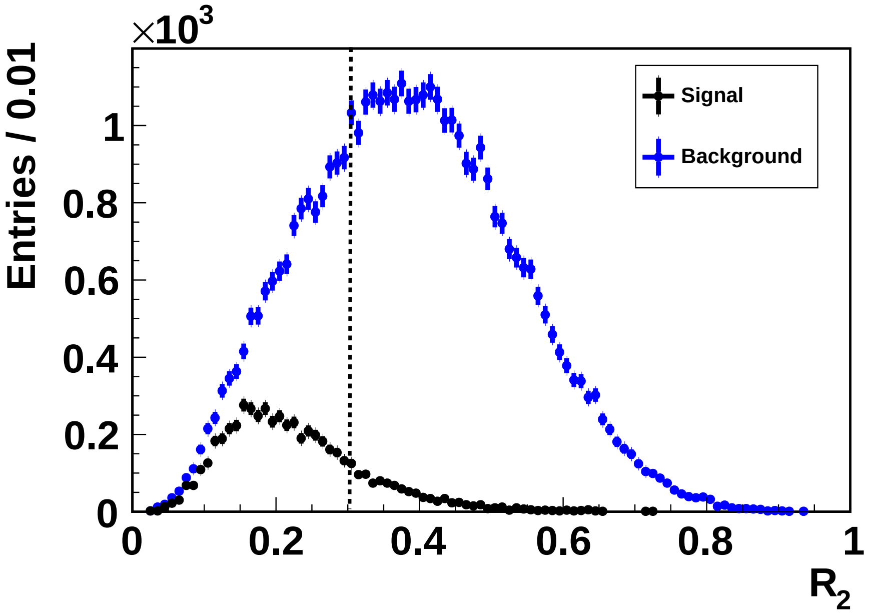

Figure 6.5: R_2 distribution for the channel $B^- \to D^0(K^-\pi^+)\pi^-$ in generic MC sample. The color black represents the true signal candidates and the color blue represents the background candidates coming from both $B\bar{B}$ and $q\bar{q}$ events. The dotted line shows where the selection has been applied.

in Ref. [90]. In this chapter, the calibration results of the data sample corresponding to an integrated luminosity of 26.5 fb^{-1}, collected during 2020 run of the Belle II

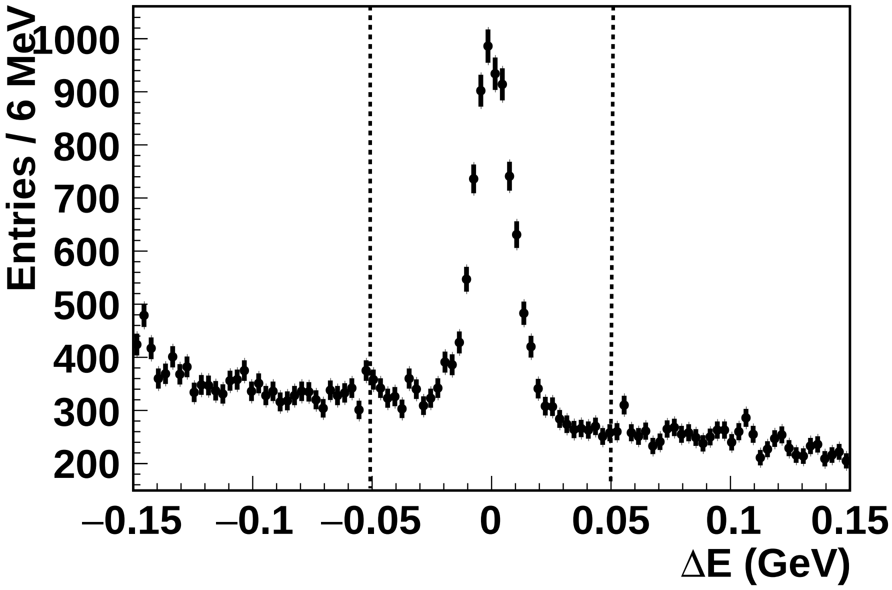

Figure 6.6: ΔE distribution for the channel $B^- \to D^0(K^-\pi^+)\pi^-$ in generic MC sample. The black dotted lines show where the selections have been applied.

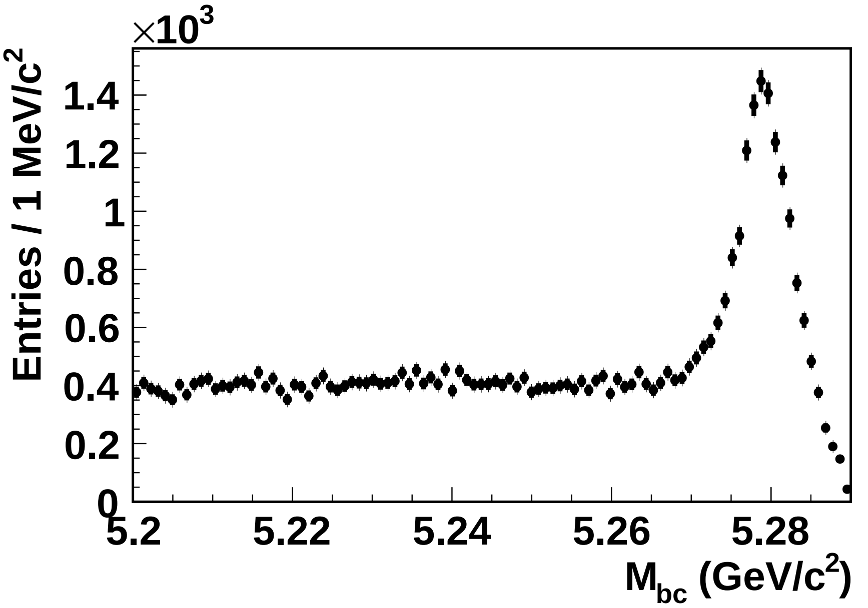

Figure 6.7: $\mathrm{M_{bc}}$ distribution for the channel $B^- \to D^0(K^-\pi^+)\pi^-$ in generic MC sample.

detector [110], are shown. This data set is divided into sub-samples of equal luminosity. These sub-samples, along with their corresponding integrated luminosity, are given in the Table 6.1. The beam-energy is determined in each of these sub-samples. As the method is based on reconstruction of B mesons, it is only applicable to the data

Table 6.1: Luminosity of the data sub-samples used. The experiment number correspond to the number used during the Belle II data-taking.

Experiment	Run range (label)	Luminosity (fb^{-1})
`exp12`	798 – 1969 (1)	2.95
	2143 – 2484 (2)	2.65
	2485 – 2589 (3)	2.65
	2590 – 2844 (4)	2.76
	2845 – 2890 (5)	2.49
	3103 – 3267 (6)	2.63
	3268 – 3349 (7)	2.62
	3355 – 3395 (8)	2.52
	3398 – 3473 (9)	2.63
	3474 – 3904 (10)	2.62

collected at Υ(4S) resonance. For off-resonance runs, a separate procedure based on dimuon events is followed, which is not part of our discussion.

6.3 SIGNAL EXTRACTION AND RESULTS

A one-dimensional maximum likelihood fit is performed on the $M_{\rm bc}$ distribution that is obtained from the reconstruction of the B channels described in Sec. 6.2. Gaussian and Argus functions are used as the probability density functions to model the signal and background distributions, respectively. The Argus function [111] is given by:

$$\mathrm{Argus}(x, x_0, \alpha) \propto t \cdot \sqrt{1-t^2} \cdot \exp[-\alpha(1-t^2)], \tag{6.7}$$

where $t = \frac{x}{x_0}$, x_0 is the end-point and α is the shape parameter of the Argus function. All the parameters along with x_0 and α are kept free in the fit to avoid any bias from the fixed parameter and eliminates sources of systematic uncertainty. Separate fits are performed for charged and neutral B decays. The weighted average of the mean and σ of both the B decays are used in the calculation to get the desired results.

Before looking at data, the fit was first validated with a MC sample of inclusive events, corresponding to an effective integrated luminosity of 50 fb^{-1}. The calculated values of the beam energy and the spread in beam energy should be consistent with the input values to the MC generator. The fit projections for MC sample are shown in Figs. 6.8 and 6.9. The obtained values from the calculation are shown in Table 6.2. The results are consistent with the input values within the uncertainty. As a further check, a linearity test has been performed to check for any systematic bias coming from the definitions of PDF shapes, which is described in Sec. 6.4. The beam-energy shift is calculated in this data-set using the same procedure described in Sec. 6.1. The full data-set is divided into sub ranges of $\sim$ 2.5 fb^{-1} as shown in the Table 6.1. The fits to the $M_{\rm bc}$

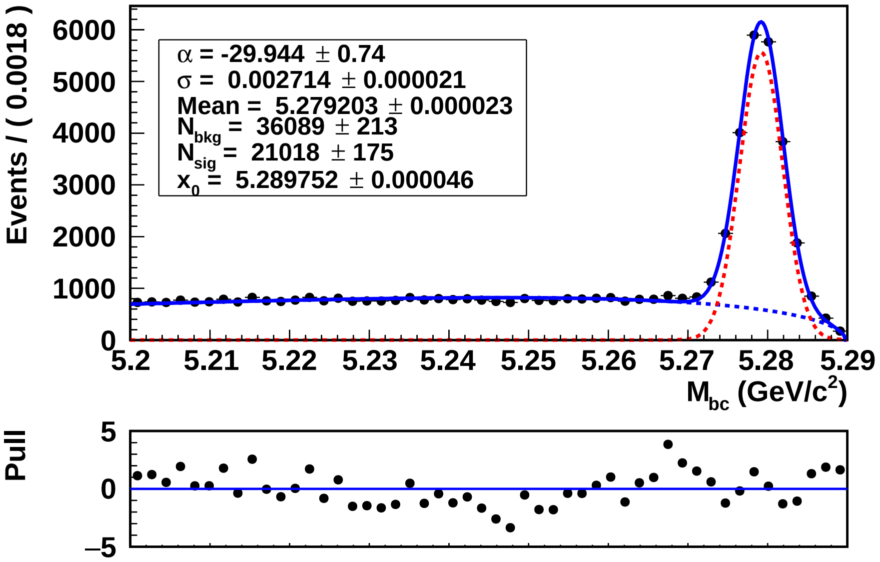

Figure 6.8: $M_{\rm bc}$ fit projection of charged B candidates in MC sample.

Table 6.2: Beam-energy and spread obtained in MC sample

Variable	Input (MeV)	Output (MeV)
$E^*_{\rm beam}$	10579.39	10579.37 ± 0.02
$\sigma_{E^*_{\rm beam}}$	2.60	2.68 ± 0.02

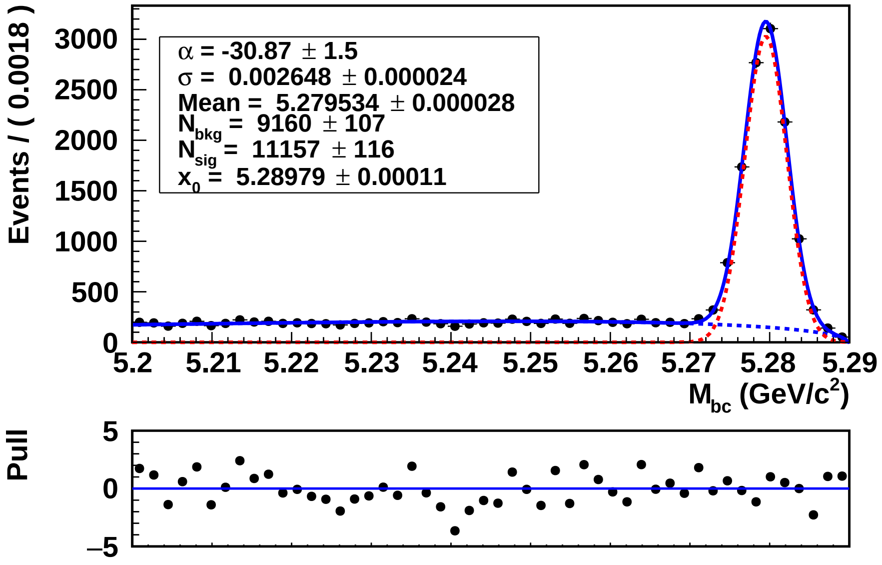

Figure 6.9: M_{bc} fit projection of neutral B candidates in MC sample.

distribution in two of the run-ranges are shown in Fig. 6.10. The shifts obtained from the data are tabulated in Table 6.3. Figures 6.11 and 6.12 show the obtained shift and the correct beam energy obtained after the calculation, respectively. As discussed in Sec. 6.1, the resolution of M_{bc} is dominated by the beam-energy uncertainty, which is also referred to as the beam-energy spread. The beam-energy spread is obtained from the width of M_{bc} signal peak, which is a free parameter in the fits. The obtained values of beam-energy spread values in the chunks of data are summarized in table 6.3 and are demonstrated in fig 6.13.

6.4 SYSTEMATIC UNCERTAINTIES

Any possible bias in the fit is studied with a set of 10 different generic MC sample generated with different input beam energies ($\sqrt{s}$), with ± 0.25, ± 0.5, ± 0.75, ± 1, ± 2 and ± 4 MeV shift from the nominal value. The shifts in beam energy are calculated

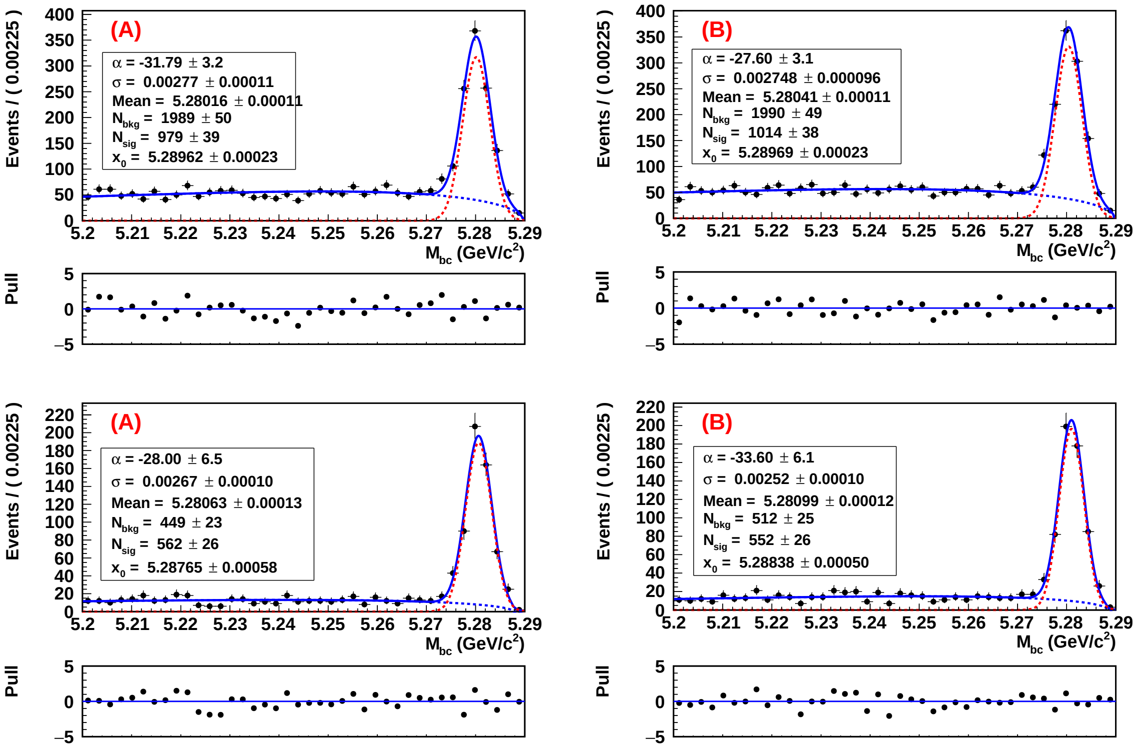

Figure 6.10: $\mathrm{M_{bc}}$ fit projection of charged (up) and neutral (down) B candidates in two different run-ranges. The labels (A) and (B) are corresponding to the run-range 1 and 2, respectively.

Table 6.3: Beam-energy shift and spread obtained in the sub-ranges of analyzed data-set of 26.52 fb^{-1}.

Run range	$\delta E^{*}_{\mathrm{beam}}$ (MeV)	$E^{*\mathrm{correct}}_{\mathrm{beam}}$ (MeV)	$\sigma_{M_{\mathrm{BC}}}$ (MeV)
1	-0.11 ± 0.13	5289.84 ± 0.11	2.70 ± 0.07
2	-0.32 ± 0.13	5290.06 ± 0.11	2.70 ± 0.07
3	-0.16 ± 0.13	5289.89 ± 0.11	2.66 ± 0.08
4	-0.25 ± 0.13	5289.98 ± 0.11	2.65 ± 0.07
5	-0.32 ± 0.13	5290.05 ± 0.12	2.78 ± 0.08
6	-0.30 ± 0.13	5290.03 ± 0.11	2.63 ± 0.07
7	-0.20 ± 0.13	5289.94 ± 0.12	2.87 ± 0.08
8	-0.20 ± 0.13	5289.94 ± 0.12	2.74 ± 0.08
9	-0.03 ± 0.13	5289.76 ± 0.12	3.01 ± 0.07
10	0.25 ± 0.13	5289.47 ± 0.11	2.86 ± 0.07

for each sample using the same procedure described in Sec. 6.1. A plot between the input value and the output value from the calculation is expected to be a linear function

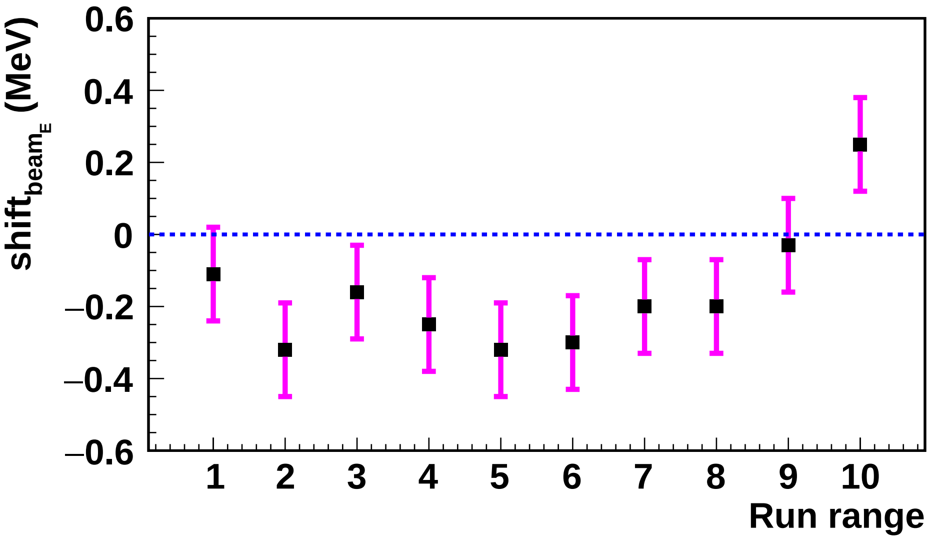

Figure 6.11: Beam energy shift values obtained in the sub-ranges of analyzed data-set of 26.52 fb^{-1}.

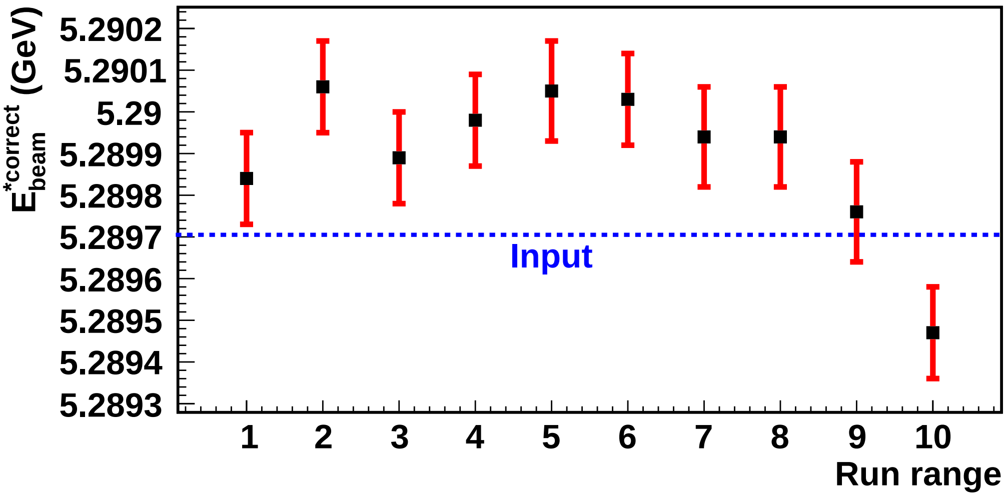

Figure 6.12: Correct beam energy values obtained in the sub-ranges of analyzed data-set of 26.52 fb^{-1}. The blue dotted line represents the value stored for the data-set and is considered as the input value in the calculation.

with slope, $m = 1$ and intercept, $c = 0$, and it is shown in Fig. 6.14. There is a bias of 127 keV was obtained, which is nearly 1σ deviation from the mean value; here σ corresponds to the statistical uncertainty on mean value of M_{bc} in each sub-range. The main reason of this bias is found to be the poor modeling of the signal shape. This value

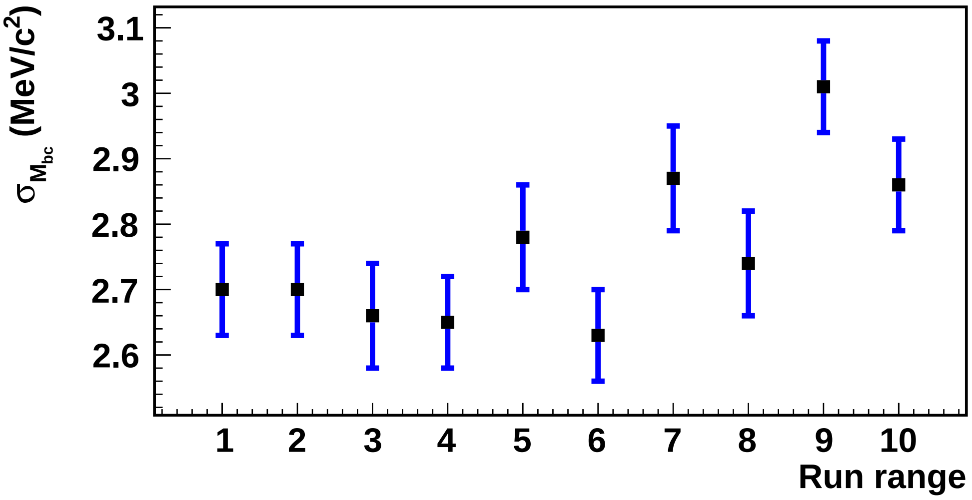

Figure 6.13: Beam energy spread values obtained in the sub-ranges of analyzed data-set of 26.52 fb^{-1}.

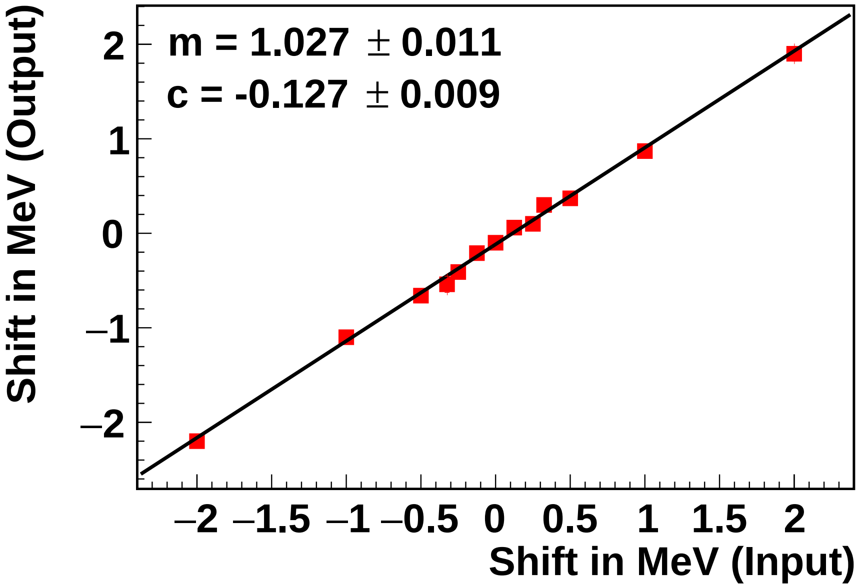

Figure 6.14: Shifts obtained for different input values of beam energy. The shift values are shown with respect to $\sqrt{s}/2$.

is added as an offset to the measured values given in table 6.3. The uncertainty on the B meson mass has not been propagated while calculating the shifts for these samples in order to achieve the pure bias caused solely due to the fit modeling. There is a high probability that the bias will be removed with alternative fit parametrization.

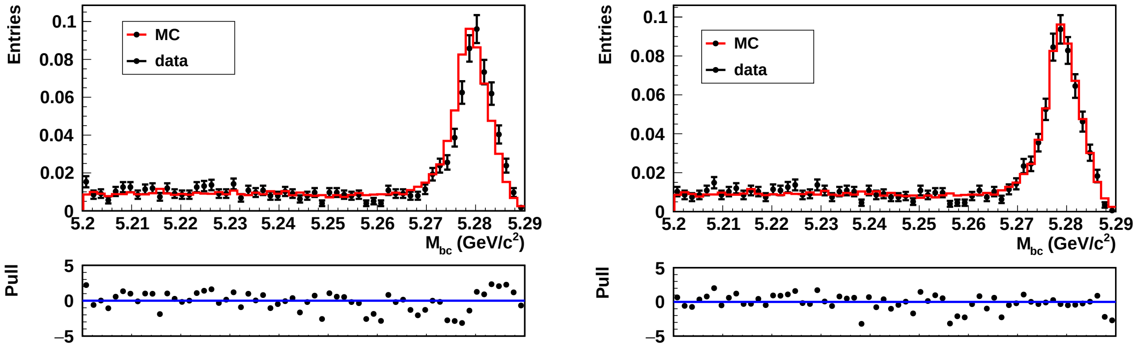

Figure 6.15: $\mathrm{M_{bc}}$ fit projections of the channel $B^- \to D^0(K^-\pi^+)\pi^-$ before (left) and after (right) the beam energy calibration.

6.5 SUMMARY

The exact value of beam energy in the CM frame is important for Belle II analyses and calibration. The importance of this study is demonstrated in Fig. 6.15, which shows the data-MC comparison of the variable M_{bc}. The data-MC discrepancy is clearly visible in the distribution without the beam energy calibration, and the discrepancy has been removed after the calibration. The step-by-step procedures are discussed to determine shift in beam energy from the nominal value using the M_{bc} distribution obtained from fully reconstructed B decays. The shifts obtained are less than 0.5 MeV for all the sub-ranges. These values are provided as calibration constants to the Belle II collaboration. Any systematic bias is also studied using the linearity check and the obtained value id 127 keV, which is caused solely due to the poor fit modeling.

CHAPTER 7

Summary and outlook

A precise determination of the CKM unitarity triangle angle ϕ_3 offers a compelling path to gain a better understanding of SM *CP* violation and search for non-SM contributions. The present ϕ_3 precision of 4° [33] is the limiting factor in determining whether the observed *CP* violation is consistent with the SM or a sign of non-SM particles. The small sample size of the $B \to D^{(*)}K^{(*)}$ decays used to determine ϕ_3 dominates this uncertainty.

The results of the first Belle and Belle II combined model-independent measurement of the CKM unitarity triangle angle ϕ_3 are presented. The analysis uses $B^+ \to D(K_S^0 h^- h^+)h^+$ decays reconstructed from a combined sample of 711 fb^{-1} of Belle data and 128 fb^{-1} of Belle II data. Independently measured strong-phase difference parameters c_i and s_i are used, which come from a combination of results reported by the CLEO and BESIII collaborations [49, 50]. We measure $\phi_3 = (78.4 \pm 11.4 \pm 0.5 \pm 1.0)^\circ$, where the first uncertainty is statistical, the second is the total experimental systematic uncertainty and the third is the systematic uncertainty due to the external c_i and s_i measurements.

The measurement is also performed on the Belle data sample alone and the results are reported in Appendix C. The statistical uncertainty in ϕ_3 is 11°, which is significantly improved from the 15° reported in the previous Belle analysis with the same data set [45]. The improvements are primarily due to the improved background rejection and

K_S^0 reconstruction, as well as the addition of $B^+ \to D(K_S^0 K^+ K^-)h^+$ decays. The inclusion of Belle II data improves the precision of $x_\pm^{DK}$ and $y_\pm^{DK}$ parameters. However, the ϕ_3 statistical uncertainty does not improve despite introducing 17% more data. The reason is that the Belle II data favours a much smaller value of r_B^{DK}, which results in a central value of 0.129 for the combined fit compared to 0.144 for the Belle data alone. The uncertainty in ϕ_3 is inversely proportional to r_B, which explains the lack of improvement in ϕ_3 sensitivity when including the Belle II data. The world average value of r_B is 0.0996 ± 0.0026 [33] so it is not unexpected the value of r_B will regress towards this value as additional data is included.

The statistical precision on ϕ_3 is worse than the current world-average value [33]. However, the precision is limited by the size of the data sample, so a future analysis with a Belle II data set corresponding to 10 ab^{-1} will provide measurements with a precision of approximately $4°$ from the $B^+ \to D\left(K_S^0 \pi^+ \pi^-\right) h^+$ mode alone.[1] The use of other modes will give additional sensitivity to ϕ_3 [9].

The beam energy in the centre-of-mass frame is also precisely measured for the early data set of the Belle II experiment. The peak position of the M_{bc} distribution (defined in Eq. 3.3) obtained from charged and neutral B reconstructions are used for this study. A less than 0.5 MeV shift from the nominal beam energy is obtained for all the data sets.

---

[1] The world-average value of r_B^{DK} is assumed in these extrapolations.

APPENDIX A

Results from pseudo-experiments

The distributions of pull, error and parameter values of $x_\pm$ and $y_\pm$ obtained from 2000 pseudo-experiments are shown in Figs. A.1- A.6.

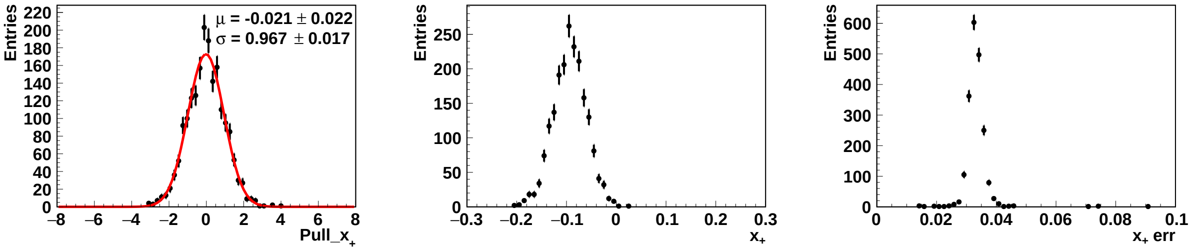

Figure A.1: Distribution of pull (left), parameter value (middle), and uncertainity of the parameter (right) of the variable x_{+}^{DK} returned from 2000 pseudo-experiments. The variable μ and σ represent the mean and resolution of the pull distribution.

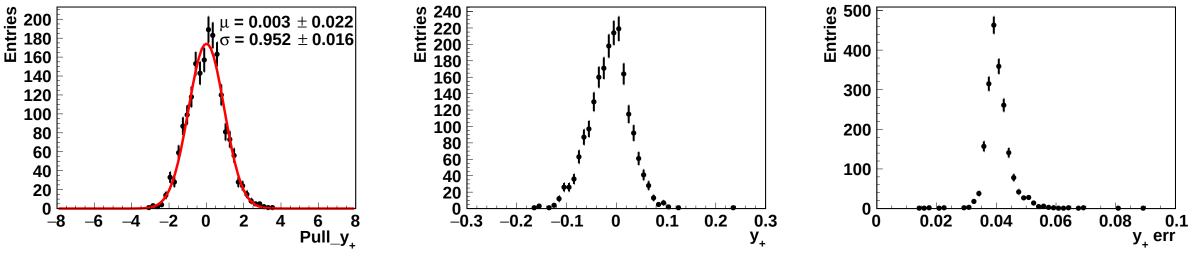

Figure A.2: Distribution of pull (left), parameter value (middle), and uncertainity of the parameter (right) of the variable y_{+}^{DK} returned from 2000 pseudo-experiments. The variable μ and σ represent the mean and resolution of the pull distribution.

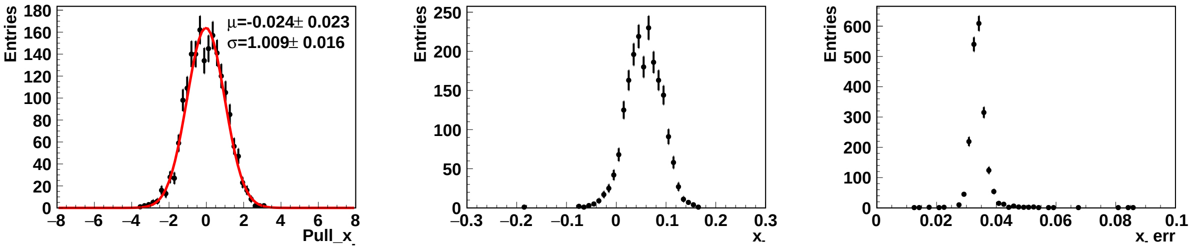

Figure A.3: Distribution of pull (left), parameter value (middle), and uncertainity of the parameter (right) of the variable x_{-}^{DK} returned from 2000 pseudo-experiments. The variable μ and σ represent the mean and resolution of the pull distribution.

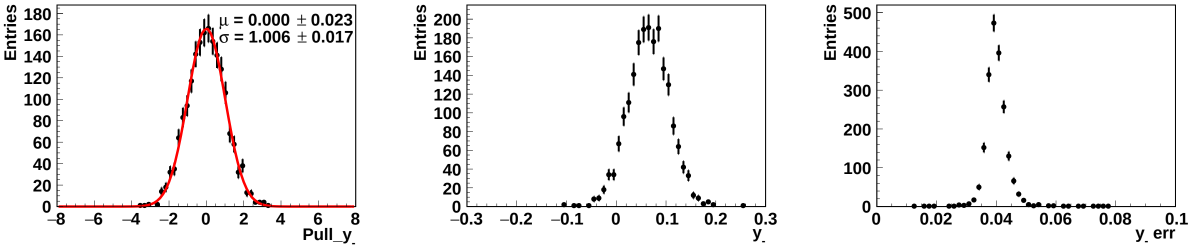

Figure A.4: Distribution of pull (left), parameter value (middle), and uncertainity of the parameter (right) of the variable y_{-}^{DK} returned from 2000 pseudo-experiments. The variable μ and σ represent the mean and resolution of the pull distribution.

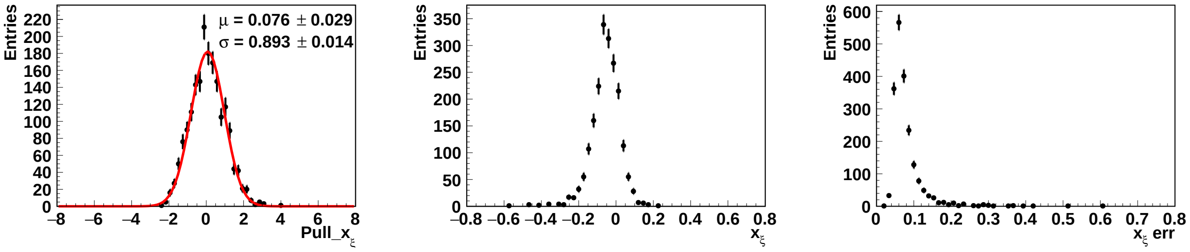

Figure A.5: Distribution of pull (left), parameter value (middle), and uncertainity of the parameter (right) of the variable $x_{\xi}^{D\pi}$ returned from 2000 pseudo-experiments. The variable μ and σ represent the mean and resolution of the pull distribution.

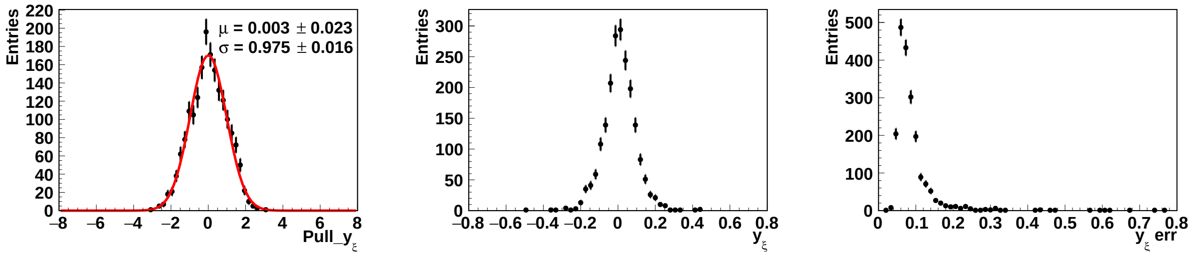

Figure A.6: Distribution of pull (left), parameter value (middle), and uncertainity of the parameter (right) of the variable $y_\xi^{D\pi}$ returned from 2000 pseudo-experiments. The variable μ and σ represent the mean and resolution of the pull distribution.

APPENDIX B

Correlation matrices

Tables B.1–B.3 represent the statistical, external strong phase input systematics and total experimental systematics correlation matrices for the combined data set of Belle and Belle II.

Table B.1: Statistical correlation matrix obtained for the combined Belle and Belle II data set.

	x_-^{DK}	y_-^{DK}	x_+^{DK}	y_+^{DK}	$x_\xi^{D\pi}$	$y_\xi^{D\pi}$
x_-^{DK}	1	-0.204	-0.051	0.063	0.365	-0.151
y_-^{DK}		1	0.014	-0.051	-0.090	0.404
x_+^{DK}			1	0.152	-0.330	-0.057
y_+^{DK}				1	0.026	-0.391
$x_\xi^{D\pi}$					1	0.080
$y_\xi^{D\pi}$						1

Table B.2: External inputs c_i, s_i systematics correlation matrix obtained for the combined Belle and Belle II data set.

	x_-^{DK}	y_-^{DK}	x_+^{DK}	y_+^{DK}	$x_\xi^{D\pi}$	$y_\xi^{D\pi}$
x_-^{DK}	1	-0.113	0.069	0.406	-0.016	0.114
y_-^{DK}		1	0.038	-0.196	-0.692	-0.106
x_+^{DK}			1	0.412	-0.226	-0.469
y_+^{DK}				1	0.180	-0.069
$x_\xi^{D\pi}$					1	0.622
$y_\xi^{D\pi}$						1

Table B.3: Experimental systematics correlation matrix obtained for the combined Belle and Belle II data set.

	x_-^{DK}	y_-^{DK}	x_+^{DK}	y_+^{DK}	$x_\xi^{D\pi}$	$y_\xi^{D\pi}$
x_-^{DK}	1	0.777	0.483	0.268	0.839	0.698
y_-^{DK}		1	0.411	0.504	0.802	0.797
x_+^{DK}			1	0.680	0.766	0.377
y_+^{DK}				1	0.480	0.303
$x_\xi^{D\pi}$					1	0.638
$y_\xi^{D\pi}$						1

APPENDIX C

Belle data results

The results obtained using only Belle data set are summarised in this section. The *CP* violation parameters are obtained to be

$$\begin{aligned}
x_-^{DK} &= (9.45 \pm 3.58 \pm 0.22 \pm 0.36) \times 10^{-2}, \\
y_-^{DK} &= (12.04 \pm 4.66 \pm 0.30 \pm 0.90) \times 10^{-2}, \\
x_+^{DK} &= (-11.94 \pm 3.46 \pm 0.23 \pm 0.37) \times 10^{-2}, \\
y_+^{DK} &= (-6.34 \pm 4.75 \pm 0.17 \pm 0.93) \times 10^{-2}, \\
x_\xi^{D\pi} &= (-8.76 \pm 4.50 \pm 0.50 \pm 0.69) \times 10^{-2}, \\
y_\xi^{D\pi} &= (-4.56 \pm 4.90 \pm 0.17 \pm 0.63) \times 10^{-2}.
\end{aligned} \tag{C.1}$$

The physics parameters are obtained to be

$$\begin{aligned}
\phi_3 &= (79.3 \pm 11.0 \pm 0.6 \pm 1.4)^\circ\,. \\
r_B^{DK} &= 0.144 \pm 0.028 \pm 0.002 \pm 0.004, \\
\delta_B &= (130.1 \pm 12.4 \pm 0.6 \pm 2.2)^\circ\,, \\
r_B^{D\pi} &= 0.014 \pm 0.007 \pm 0.001 \pm 0.001, \\
\delta_B^{D\pi} &= (337.5 \pm 22.0 \pm 1.3 \pm 2.9)^\circ\,.
\end{aligned} \tag{C.2}$$

The correlation matrices related to statistical, external strong phase input systematics, and total experimental systematics are given in Tables C.1–C.3.

Table C.1: Statistical correlation matrix obtained for the Belle standalone data set.

	x_-^{DK}	y_-^{DK}	x_+^{DK}	y_+^{DK}	$x_\xi^{D\pi}$	$y_\xi^{D\pi}$
x_-^{DK}	1	-0.205	-0.054	0.031	0.245	-0.167
y_-^{DK}		1	0.000	-0.045	0.033	0.315
x_+^{DK}			1	0.167	-0.298	-0.017
y_+^{DK}				1	0.103	-0.323
$x_\xi^{D\pi}$					1	0.184
$y_\xi^{D\pi}$						1

Table C.2: External inputs c_i, s_i systematics correlation matrix obtained for the Belle standalone data set.

	x_-^{DK}	y_-^{DK}	x_+^{DK}	y_+^{DK}	$x_\xi^{D\pi}$	$y_\xi^{D\pi}$
x_-^{DK}	1	0.095	0.333	0.575	0.383	0.396
y_-^{DK}		1	0.279	-0.054	-0.538	-0.328
x_+^{DK}			1	0.475	0.048	-0.222
y_+^{DK}				1	0.420	0.295
$x_\xi^{D\pi}$					1	0.862
$y_\xi^{D\pi}$						1

Table C.3: Experimental systematics correlation matrix obtained for the Belle standalone data set.

	x_-^{DK}	y_-^{DK}	x_+^{DK}	y_+^{DK}	$x_\xi^{D\pi}$	$y_\xi^{D\pi}$
x_-^{DK}	1	0.508	0.251	0.074	0.674	0.573
y_-^{DK}		1	0.109	0.071	0.661	0.683
x_+^{DK}			1	0.467	0.589	0.324
y_+^{DK}				1	0.254	0.125
$x_\xi^{D\pi}$					1	0.724
$y_\xi^{D\pi}$						1

REFERENCES

[1] G. L. Glashow, *Nucl. Phys.* **22**, 579 (1961).

[2] A. Salam and J. C. Ward, *Phys. Rev.* **13**, 168 (1964).

[3] S. Weinberg, *Phys. Rev. Lett.* **19**, 1264 (1967).

[4] J. Goldstone, A. Salam, and S. Weinberg, *Phys. Rev.* **127**, 965-970 (1962).

[5] P. W. Higgs, *Phys. Rev. Lett.* **12**, 132 (1964); P. W. Higgs, *Phys. Rev. Lett.* **13**, 508 (1964); F. Englert and R. Brout, *Phys. Rev. Lett.* **13**, 321 (1964); G. S. Guralnik, C. R. Hagen and T. W. B. Kibble, *Phys. Rev. Lett.* **13**, 585 (1964).

[6] G. Aad *et al.*, (ATLAS Collaboration), *Phys. Lett. B* **716**, 1 (2012), [`arXiv:1207.7214`].

[7] S. Chatrchyan *et al.*, (CMS Collaboration), *Phys. Lett. B* **716**, 30 (2012), [`arXiv:1207.7235`].

[8] P. A. Zyla *et al.* (Particle Data Group), *Prog. Theor. Exp. Phys.* 2020, 083C01 (2020).

[9] E. Kou *et al.*, *PTEP* **2019**, no.12, 123C01 (2019) [erratum: *PTEP* **2020**, no.2, 029201 (2020)].

[10] G. W. S. Hou, *Springer Tracts in Modern Physics*, Berlin/Heidelberg, *2nd ed.*, 2019.

[11] E. Noether, Gott. Nachr. **1918**, 235 (1918).

[12] J. F. Donoghue, E. Golowich, and B. R. Holstein, *Dynamics of the Standard Model*, Cambridge University Press, Cambridge, 2014.

[13] A. D. Sakarov, *JETP Letters* **5**, 24 (1966).

[14] C. S. Wu, E. Ambler, R. W. Hayward, D. D. Hoppes, and R. P. Hudson, *Phys. Rev. Lett.* **105**, 1413 (1957).

[15] T. D. Lee and C. N. Yang, *Phys. Rev.* **104**, 254 (1956).

[16] J. H. Christenson, J. W. Cronin, V. L. Fitch, and R. Turlay, *Phys. Rev. Lett.* **13**, 138 (1964).

[17] B. Aubert *et al.* (BaBar collaboration), *Phys. Rev. Lett.* **87**, 091801 (2001), [`arXiv:hep-ex/0107013`].

[18] K. Abe *et al.* (Belle collaboration), *Phys. Rev. Lett.* **87**, 091802 (2001), [`arXiv:hep-ex/0107061`].

[19] K. Trabelsi (Belle collaboration), [`arXiv:1301.2033`].

[20] R. Aaij *et al.* (LHCb collaboration), *Phys. Lett. B* **712**, 203 (2012), Erratum ibid. **B713** 351 (2012), [arXiv:1203.3662].

[21] R. Aaij *et al.* (LHCb collaboration), *Phys. Rev. Lett.* **122**, 211803 (2019), [arXiv:1903.08726].

[22] K. Abe *et al.* (T2K collaboration), *Nature* **580**, 339 (2020), [arXiv:1910.03887].

[23] I. I. Bigi and A. I. Sanda, *Phys. Rev. D* **29**, 1393 (1984).

[24] G. Lüders, Det. Kong. Danske Videnskabernes Selskab, *Mat.-fys. Medd.* **28**, 005 (1954).

[25] N. Cabibbo, *Phys. Rev. Lett.* **10**, 531 (1963).

[26] M. Kobayashi and T. Maskawa, *Prog. Theor. Phys.* **49**, 652 (1973).

[27] S. L. Glashow, J. Iliopoulos, and L. Maiani, *Phys. Rev. D.* **2**, 1285 (1970).

[28] J.-E. Augustin *et al.*, *Phys. Rev. Lett.* **33**, 1406 (1974); J. J. Aubert *et al.*, *Phys. Rev. Lett.* **33**, 1404 (1974).

[29] L. Wolfenstein, *Phys. Rev. Lett.* **51**, 1945 (1985).

[30] J. Charles *et al.*, (CKMfitter Group), *Eur. Phys. J. C* **41**, 1-131 (2005) [hep-ph/0406184], updated results and plots available at:http://ckmfitter.in2p3.fr/

[31] J. Brod and J. Zupan, *J. High Energ. Phys.* **01**, 051 (2014).

[32] M. Blanke and A. J. Buras, *Eur. Phys. J. C* **79**, 159 (2019) [arXiv:1812.06963]

[33] Y. S. Amhis *et al.* (HFLAV group) *Eur. Phys. J. C* **81**, 226 (2021), updated results and plots available at https://hflav.web.cern.ch/.

[34] M. Gronau and D. Wyler, *Phys. Lett. B* **265**, 172 (1991).

[35] D. Atwood, I. Dunietz and A. Soni, *Phys. Rev. Lett.* **78**, 3257 (1997).

[36] D. Atwood, I. Dunietz and A. Soni, *Phys. Rev. D* **63**, 036005 (2001).

[37] A. Giri, Y. Grossman, A. Soffer and J. Zupan, *Phys. Rev. D* **68**, 054018 (2003).

[38] A. Bondar, *Proceedings of BINP special analysis meeting on Dalitz analysis*, unpublished, 24–26 September 2002.

[39] A. Poluektov *et al.* (Belle collaboration), *Phys. Rev. D* **70**, 072003 (2004).

[40] P. del Amo Sanchez *et al.* (BaBar collaboration), *Phys. Rev. Lett.* **105**, 121801 (2010).

[41] A. Poluektov *et al.* (Belle collaboration), *Phys. Rev. D* **81**, 112002 (2010).

[42] R. Aaij *et al.*, (LHCb Collaboration), *JHEP* **02**, 169 (2021).

[43] J. Garra Ticó, [`arXiv:1804.05597`].

[44] J. Garra Ticó, V. Gibson, S.C. Haines, C.R. Jones, M. Kenzie and G. Lovell, *Phys. Rev. D* **102**, 053003 (2020).

[45] H. Aihara *et al.* (Belle Collaboration), *Phys. Rev. D* **85**, 112014 (2012).

[46] J. Libby *et al.* (CLEO Collaboration), *Phys. Rev. D* **82**, 112006 (2010).

[47] B. Aubert *et al.* (BaBar Collaboration), *Phys. Rev. D* **78**, 034023 (2008).

[48] P. del Amo Sanchez *et al.* (BaBar Collaboration), *Phys. Rev. Lett.* **105**, 121801 (2010).

[49] M. Ablikim *et al.* (BESIII Collaboration), *Phys. Rev. D* **101**, 112002 (2020).

[50] M. Ablikim *et al.* (BESIII Collaboration), *Phys. Rev. D* **102**, 052008 (2020).

[51] S. Kurokawa and E. Kikutani, *Nucl. Instrum. Meth. A.* **499**, 1 (2003), and other papers included in this volume.

[52] H. Kichimi *et al.*, JINST **5**, P03011 (2010).

[53] KEKB B-Factory Design Report, KEK Report 95-7, 1995.

[54] R. B. Palmer, SLAC-PUB 4707, 1988.

[55] K. Oide and K. Yokoya, *Phys. Rev. A* **40**, 315 (1989).

[56] `https://www.classe.cornell.edu/public/lab-info/upsilon.html`

[57] `http://belle.kek.jp/`

[58] A. Abashian *et al.*, (Belle Collaboration), *Nucl. Instrum. Meth. A.* **479**, 117 (2002).

[59] J. Brodzicka *et al.*, (Belle Collaboration), *Prog. Theor. Exp. Phys.* **2012**, 04D001 (2012), [`arXiv:1212.5342`].

[60] G. Alimonti *et al.*, (Belle Collaboration), *Nucl. Instr. Meth. A* **453**, 71 (2000).

[61] Y. Horii, PhD thesis, Tohoku University (2010) [`http://130.34.123.84/eeweb/paper/2011$_$Dthesis_yhorii.pdf`].

[62] E. Nygard *et al.*, *Nucl. Instrum. Meth. A* **301**, 506 (1991) .

[63] O. Toker *et al.*, *Nucl. Instrum. Meth. A* **340**, 572 (1994).

[64] `http://www.ideas.no/`

[65] H. Hirano *et al.*, *Nucl. Instrum. Meth. A* **455**, 294 (2000).

[66] H. Kichimi *et al.*, *Nucl. Instrum. Meth. A* **453**, 315 (2000).

[67] http://sabotin.ung.si/~sstanic/belle/nim/total/node65.html

[68] H. Ikeda *et al.* (Belle collaboration), *Nucl. Instrum. Meth. A* **441**, 401426 (2000).

[69] D. Mohapatra, Ph.D. Thesis, Virginia Tech (2006), [https://citeseerx.ist.psu.edu/viewdoc/download?doi=10.1.1.96.1930$&$rep=rep1$&$type=pdf]

[70] M. Nakao *et al.* (Belle collaboration), *IEEE Trans. Nucl. Sci.* **47**, 5660 (2000).

[71] K. Akai, K. Furukawa, and H. Koiso, *Nuclear Instruments and Methods in Physics Research Section A* **907**, 188 (2018).

[72] P. Lewis, I. Jaegle, H. Nakayama *et al., Nuclear Instruments and Methods in Physics Research Section A* **914**, 69 (2019).

[73] I. Adachi *et al.* (Belle II collaboration), textitNuclear Instruments and Methods in Physics Research Section A **907** 46 (2018).

[74] T. Bilka *et al.* (Belle II PXD and SVD Collaborations), *PoS Vertex2019*, **2020**, p. 001. 10.22323/1.373.0001 [https://doi.org/10.22323/1.373.0001].

[75] M.J. French *et al.*, *Nucl. Instrum. Methods A* **466**, 359 (2001).

[76] Gagan B. Mohanty, *Nucl. Instrum. Methods A* **831**, 80 (2016) [arXiv:1511.06197].

[77] https://www2.kek.jp/proffice/archives/feature/2010/BelleIIBPID.html

[78] S. Iwata *et al.*, *Progress of Theoretical and Experimental Physics* **2016** 033H01 (2016).

[79] V. Aulchenko *et al.*, JINST **12** C08001 (2017).

[80] D. J. Lange, *Nucl. Instrum. Meth. A* **462**, 152 (2001).

[81] T. Sjöstrand *et al.*, *Comput. Phys. Commun.* **178**, 852 (2008).

[82] B. Ward, S. Jadach and Z. Was, *Nucl. Phys. B Proc. Suppl.* **116**, 73 (2003).

[83] R. Brun *et al.* CERN-DD-EE-84-01 (1984).

[84] S. Agostinelli *et al.*, *Nucl. Instrum. Meth. A* **506**, 250 (2003).

[85] E. Barbiero and Z. Was, *Comp. Phys. Commun.* **79**, 291 (1994).

[86] P. M. Lewis *et al.*, *Nucl. Instrum. Meth. A* **914**, 69 (2019).

[87] T. Kuhr, C. Pulvermacher, M. Ritter, *Comput. Softw. Big Sci.* **3** (2019) no. 1, 1, [arXiv:1809.04299].

[88] M. Gelb *et al.*, *Comput. Softw. Big Sci.* **2** (2018) no. 1, 1, [arXiv:1810.00019].

[89] H. Nakano, Ph.D. Thesis, Tohoku University (2014) [https://inspirehep.net/files/d61e8ac40579522baba4da0f086e0887].

[90] F. Abudinén *et al.* (Belle II Collaboration), [arXiv:2104.03628].

[91] G. C. Fox and Stephen Wolfram. Phys. Rev. Lett., **41**, 1581 (1978).

[92] K. Abe *et al.* (Belle Collabolation), *Phys. Lett. B* **511**, 151 (2001).

[93] F. Abudinén *et al.* [Belle II Collaboration], [arXiv:2008.02707].

[94] M. Pivk, and F. R. Le Diberder, *Nucl. Instrum. Meth. A* **555**, 356 (2005) [arXiv:physics/0402083].

[95] R. Brun and F. Rademakers, *Nucl. Inst. & Meth.* in *Phys. Res. A* **389**, 81 (1997).

[96] W. Verkerke and P. D. Kirkby, *eConf* **C0303241** (2003) MOLT007 [arXiv:physics/0306116].

[97] https://tel.archives-ouvertes.fr/tel-00002991/document

[98] A. Hocker *et al.*, [arXiv:physics/0703039].

[99] P. K Resmi *et al.* (Belle Collaboration), *J. High Energy Phys.* **10**, 178 (2019).

[100] G. Punzi, *Notes on statistical separation of classes of events* [physics/0611219].

[101] Y. Horii *et al.* , (Belle Collaboration), *Phys. Rev. Lett.* **106**, 231803 (2011).

[102] W. H. Press, S. A. Teukolsky, W. T. Vetterling and B.P. Flannery, *"Numerical Recipes in C++ (Second Edition)"*, 99-101 (2002).

[103] R. Aaij *et al.*, (LHCb Collaboration), *JHEP* **12**, 087 (2016).

[104] https://gammacombo.github.io/

[105] G. J. Feldman and R. D. Cousins, *Phys. Rev. D* **57**, 3873 (1998).

[106] B. Sen, M. Walker, and M. Woodroofe, *Statistica Sinica* **19**, 301 (2009).

[107] R. Aaij *et al.* (LHCb collaboration), [arXiv:2110.02350].

[108] K. Belous *et al.* (Belle Collaboration), *Phys. Rev. Lett.* **99**, 011801 (2007).

[109] Ed. A.J. Bevan, B. Golob, Th. Mannel, S. Prell, and B.D. Yabsley, *Eur. Phys. J. C* **74** (2014) 3026, SLAC-PUB-15968, KEK Preprint 2014-3.

[110] https://confluence.desy.de/display/BI/Belle+II+Luminosity

[111] H. Albrecht *et al.* (ARGUS Collaboration), *Physics Letters B.* **241**, 278 (1990).

LIST OF PAPERS BASED ON THESIS

1. J. Libby, N. Rout and K. Trabelsi with the Belle II collaboration, *Combined analysis of Belle and Belle II data to determine the CKM angle ϕ_3 using $B^+ \rightarrow D(K_S^0 h^- h^+) h^+$ decays*, J. High. Energ. Phys. **02**, 063 (2022). [`arXiv:2110.12125`].

CURRICULUM VITAE

NIHARIKA ROUT

Contact Information

Indian Institute of Technology Madras
Chennai 600036, Tamilnadu, India
E-mail: niharikarout@physics.iitm.ac.in
Date of Birth: 02/04/1993
Citizenship: INDIAN

Education

PhD, *Experimental High Energy Physics*, Jul 2016 – present

Indian Institute of Technology Madras, Chennai, Tamilnadu, India
Supervisor: Prof. Jim Libby
Measurement of CKM angle ϕ_3 *from* $B^{\pm} \to D(K_S^0 h^- h^+)K^{\pm}$ *decays at Belle and Belle II*, submitted in Nov, 2021; defense scheduled in Jan, 2022.

MSc, *Physics*, Aug 2013 – Jul 2015

University of Mumbai, Kalina, Santacruz (E), Mumbai, Maharashtra, India
Scored 75.6% out of maximum marks
Assembly and characterization of resistive plate chambers and tracking of muons.
Supervisor: Dr. Lalit Mohan Pant

BSc, *Physics*, Jun 2013

Ravenshaw University, Cuttack, Odisha, India
Scored 80.0% out of maximum marks

PhD Research

I work in experimental flavour physics at electron-positron colliders.

Measurement of the quark-mixing angle γ using Belle and Belle II data

I performed the most precise determination of the quark-mixing angle γ in electron-positron collisions.
The present 4° precision of the CP-violating parameter γ ($\equiv \arg[-V_{ud}V_{ub}^{*}/V_{cd}V_{cb}^{*}]$) is the limiting factor in determining whether the observed violation of CP symmetry is consistent with the SM or a sign of non-SM particles. Hence any new measurements of γ are extremely impactful.
My PhD focuses on the measurement of the CKM angle γ from $B^{\pm} \to D(K_S^0 h^- h^+)K^{\pm}$ decays at Belle and Belle II. The angle γ is measured by studying the interference of $B^{\pm} \to DK^{\pm}$ decays, where D can either be a D^0 or $\bar{D}^0$. The interference is generated when D^0 and $\bar{D}^0$ decay to common $K_S^0 h^- h^+$ final states. I was the single student on this analysis, starting from the event selection, through optimisation, signal extraction, and up to the assessment of systematic uncertainties and writing of the paper, with just intellectual supervision of my supervisor and another senior colleague.
The principal challenge was to develop the fitter, which uses the distributions of signal and control-channel decays to determine the angle γ. This is a simultaneous fit of 2 observables in 160 different categories corresponding to the modes $B \to DK$ and $B \to D\pi$ (control mode) separated by charge, D final state, D Dalitz bins, and experiment (Belle or Belle II). Along with a global optimisation of other selections, I also developed

a novel K_S^0 selection based on boosted-decision-trees and obtained a 6% improvement in relative signal efficiency. The systematic uncertainty determination was also delicate as various effects were correlated between Belle and Belle II and had to be determined using Cholesky decomposition.

The results are the most precise achieved at B-factories owing to an improved simultaneous fit that determines from data themselves the relevant particle identification parameters and uses improved external inputs from experiments at the charm threshold that avoid model-dependent uncertainties in the final results. This is the first Belle II result in CP violation and the first-ever combined analysis made on Belle and Belle II data.

The uncertainty on γ is reduced from 15°, the previous best measurement of Belle, to 11°. This is not just due to the 17% increase in data from Belle II, but also to the inclusion of the $K_S^0 K^- K^+$ final state, which provided 10% more signal along with my improved K_S^0 selection and background rejection. The systematic uncertainty due to the external strong-phase input also reduced significantly by using updated inputs. The corresponding paper is currently under JHEP review.

In the context of my PhD work, I also pursued detector performance studies that were originally aimed at advancing on my own analysis, but become useful for the whole collaboration.

Beam energy calibration

An accurate determination of the beam energy is crucial for many Belle II analyses as beam energy enters the two principal variables that distinguish signal from background. I measured precisely the beam energy using fully reconstructed $B^\pm \to D^0(K\pi, K\pi\pi^0, K\pi\pi\pi)\pi^\pm$ and $B^0 \to D^{*\pm}(D^0(K\pi, K\pi\pi^0, K\pi\pi\pi)\pi^\pm, D^-(K\pi\pi)\pi^+)\pi^\mp$ decays. The peak position of the invariant B meson mass where the B energy is replaced by half of the collision energy ($M_{\rm bc}$) allows a calibration with 98% accuracy. I provided calibrations promptly and regularly as new data were collected, offering independent validation to the accelerator. A technical paper with the results of these calibrations is in preparation.

Reconstruction of hadronic B decays in early Belle II data

I contributed to the first reconstruction of hadronic B decays in early Belle II data to check the initial performances of the detector. The challenge was to extract the first-ever B signals in small data sets collected with a detector far from its optimal working point. I developed early analysis tools and validated data using signals from a variety of $B \to D^{(*)}h$ decays. I measured their branching fractions, which allowed assessing early detector performances in tracking, vertexing, alignment and particle identification. My results were shown at the EPS (2019), LP (2019), Beauty (2019), and Moriond (2021) conferences and are documented in various conference papers.

Undergraduate Research

I contributed to the assembly and characterization of the resistive plate chambers (RPC) for the fourth end-cap region of the CMS detector at LHC as a part of my MSc project. I assembled the gas-gaps and conducted the electrical and mechanical tests, such as HV test, leak rate measurements of the gas-gaps, and spacer test between the gas-gaps for an uniform electric field. I also characterized the RPC with efficiency scan and evaluation of strip profile, noise profile and cluster size. We assembled four RPCs. The second part focused on generating muon tracks passing through two RPCs, using python programming.

Leadership

Belle II Beam energy calibration leader (2019 – 2021)
Skim liaison of Belle II BtoCharm physics group (2017 – 2019)

Data skimming is aimed at reducing the data set to those sub-samples most likely to contain signals of interest, thus reducing the amount of CPU time and memory required to analyse data. The challenge is to define selections inclusive enough to maintain the flexibility to do physics downstream. I prepared skimming selection algorithms for four decay modes along with the validation scripts. The sample size was reduced by applying loose event-based selections that retain the signal and enough side band while reducing unnecessary backgrounds by a factor of ≈ 10. My skimmed samples were used by the Belle II BtoCharm group (10 analysts) to produce the 2016 – 2020 conference results.

Operations

Contributed to silicon vertex detector data monitoring during the early data taking, May, 2019 and May, 2018.
Served as experimental shifter during the early data taking, May, 2019.

Publications

Journal publications

1. N. Rout, J. Libby, and K. Trabelsi with the Belle II collaboration "*Determination of CKM angle ϕ_3 using $B^+ \to D(K_S^0 h^- h^+)h^+$ decays at Belle and Belle II*"; J. High. Energ. Phys. **02**, 063 (2022). [`arXiv:2110.12125`].

Primary author of Belle II public results

1. N. Rout *et al.* (8 primary authors and the Belle II Collaboration), "*Study of $B \to D^{(*)}h$ decays using 62.8 fb^{-1} of Belle II data*", [`arXiv:2104.03628`].
2. N. Rout *et al* (5 primary authors and the Belle II Collaboration) "*Hadronic B decay reconstruction in 5.15 fb^{-1} (2.62 fb^{-1}) of early Phase 3 data*", BELLE2-NOTE-PL-2019-028, BELLE2-NOTE-PL-2019-023.
3. N. Rout *et al.* (5 primary authors and the Belle II Collaboration) "*$B \to D^{(*)}h$ in 410 pb^{-1} of collision data.*", BELLE2-NOTE-PL-2019-005.
4. N. Rout *et al.* (8 primary authors and the Belle II Collaboration) "*Plots for $D^{*0} \to D\pi^0, D \to K^-\pi^+$ in 472 pb^{-1} collision data.*", BELLE2-NOTE-PL-2018-022, BELLE2-NOTE-PL-2018-021, BELLE2-NOTE-PL-2018-022, BELLE2-NOTE-PL-2018-012, BELLE2-NOTE-PL-2018-013, BELLE2-NOTE-PL-2018-014, BELLE2-NOTE-PL-2018-015, BELLE2-NOTE-PL-2018-019.
5. N. Rout *et al.* (8 primary authors and the Belle II Collaboration) "*Plots for $B \to D^{(*)}h, J/\psi K^{(*)}$ in 472 pb^{-1} collision data.*", BELLE2-NOTE-PL-2018-020.

Conference proceedings

1. N. Rout (on behalf of the Belle II collaboration), "*Measurement of ϕ_3 (γ) and first results on CP violation at Belle II*", PoS (ICHEP2020) **416** (2020).
2. N. Rout (on behalf of the Belle and Belle II collaboration), "*Determination of CKM angle ϕ_3 at Belle and Belle II*", Proceedings of XXIV DAE-BRNS High Energy Physics symposium, 2020.
3. E. Ganiev, N. Rout and B. Wach (on behalf of the Belle II collaboration), "*Hadronic B decay reconstruction in early Belle II data*", PoS (Beauty2019) **062** (2019).
4. N. Rout (on behalf of the Belle II collaboration), "*Measurement of CKM angle ϕ_3 at Belle II*", in Proceedings of the 17th Conference on Flavor Physics and CP Violation, 2019, eConf C190506 (2019).

5. N. Rout (on behalf of the Belle II collaboration), "*Rediscoveries from the first data of Belle II*", Proceedings of XXIII DAE-BRNS High Energy Physics symposium, 2018.
6. S. T. Sehgal, V. K. S. Kashyap, L.M. Pant, T. Kar, K.Dhanmeher, N. Rout, S. Padwal and A.K. Mohanty, "*G-10 read out panel (1m x 1m) as an option for RPCs in INO*", Proceedings of the DAE Symp. on Nucl. Phys. **59** (2014).

Belle II physics internal notes

1. J. Libby, N. Rout, K. Trabelsi, "*Determination of CKM angle ϕ_3 using the channel $B^\pm \to D(K^0_S h^- h^+)K^\pm$ at Belle and Belle II*", BELLE2-NOTE-PH-2021-016.
2. N. Rout *et al.* (8 primary authors) "*Hadronic B decay reconstruction to final states with charm mesons in the 2019-2020 data set (Moriond 2021)*", BELLE2-NOTE-PH-2020-035.
3. J. Libby, N. Rout, K. Trabelsi, "*Beam energy calibration*", BELLE2-NOTE-PH-2020-002.
4. N. Rout *et al.* (5 primary authors), "*Hadronic B decay reconstruction in Early Phase III data*", BELLE2-NOTE-PH-2019-039.
5. N. Rout *et al.* (5 primary authors), "*Study of R_2 distribution in early phase 2 data*", BELLE2-NOTE-PH-2018-009.

In addition I authored 70 papers and public notes as default member of the Belle and Belle II collaborations.

Conferences

International

1. Parallel talk "*First results of $B \to DK$ decays at Belle II*" at 11th International workshop on CKM Unitarity Triangle (CKM 2021), Melbourne, Australia, Nov, 2021.
2. Parallel talk "*Measurement of γ (ϕ_3) and first results on CP violation at Belle II*" at 40th International Conference on High Energy Physics (ICHEP 2020), Prague, Czech Republic, Aug, 2020.
3. Parallel talk "*Measurement of CKM angle ϕ_3 at Belle II*" at 17th conference on FPCP, Victoria, Canada, May, 2019.

National

1. Parallel talk titled "*Determination of CKM angle ϕ_3 at Belle and Belle II*" at XXIV DAE-BRNS High Energy Physics symposium, NISER, Bhubaneswar, Dec, 2020.
2. Parallel talk titled "*Rediscoveries from the first data of Belle II*" at XXIII DAE-BRNS High Energy Physics symposium, IIT Madras, Chennai, Dec, 2018.

Programming

C++, PYTHON, ROOT, git, LaTeX, grid computing, basics of machine learning.

Awards/ Scholarships/ Activities

Academic

1. Recipient of INSPIRE scholarship given by Department of Science and Technology, India from 2010 – 2015 ($1100 per year).

2. Selected for INSPIRE fellowship program.
3. Ranked 102^{nd} out of 1500 qualified candidates at the GATE physics exam administrated by IISc, Bangalore, India, 2016. GATE is an exam aimed at assessing the comprehensive understanding of various undergraduate subjects in engineering and science.

Teaching

1. Teaching assistant at IIT Madras for the courses “Introduction to Particle Physics”, “Mathematical Physics”, “Introduction to Classical Physics” and MSc lab experiments. (2016 – 2021)

REFERENCES

Prof. Alessandro Gaz (e-mail: alessandro.gaz@pd.infn.it)
- University of Padova, Padova, Italy

Dr. Diego Tonelli (e-mail: diego.tonelli@cern.ch)
- INFN Trieste, Trieste, Italy

Prof. James Libby (e-mail: libby@iitm.ac.in)
- IIT Madras, Adyar, Chennai

Dr. Karim Trabelsi (e-mail: karim.trabelsi@in2p3.fr)
- IJCLab, Orsay, France

DOCTORAL COMMITTEE

- **Dr. Suresh Govindarajan (Chair)**

  email: suresh@iitm.ac.in

  (Department of Physics, IIT Madras, Chennai-600036)

- **Dr. Prasanta Kumar Tripathy**

  email: prasanta@iitm.ac.in

  (Department of Physics, IIT Madras, Chennai-600036)

- **Dr. Chandra Kant Mishra**

  email: ckm@iitm.ac.in

  (Department of Physics, IIT Madras, Chennai-600036)

- **Dr. Rahul Sinha**

  email: sinha@imsc.res.in

  (The Institute of Mathematical Sciences, Chennai-600113)